Synthesis of Nanocrystal Quantum Dots with Enhanced Photoluminescence for Luminescent Optoelectronics

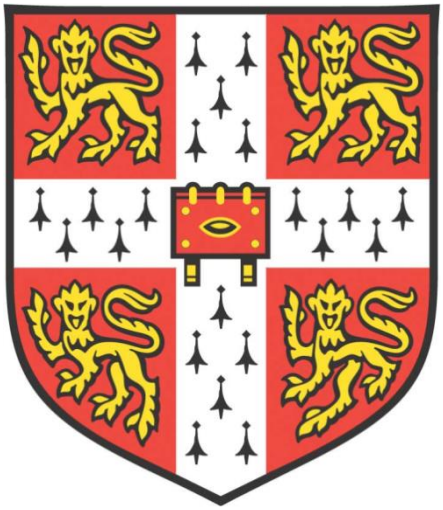

Zifan Xiao

Selwyn College
University of Cambridge

Optoelectronics Group
Department of Physics

This dissertation is submitted for the degree of

Doctor of Philosophy

January 2019

1.1 Declaration of Originality

This dissertation is the result of my own work and includes nothing which is the outcome of work done in collaboration except where specifically indicated in the text. The use of the first person plural is strictly a matter of style. It has not been previously submitted, in part or whole, to any university or institution for any degree, diploma, or other qualification.

In accordance with the Department of Physics guidelines, this thesis does not exceed 60,000 words.

Zifan (James) Xiao

1.2 Abstract

This thesis examines different approaches towards achieving greater luminescence efficiencies in colloidal nanocrystal quantum dots with primary focus towards application within singlet fission photon-multiplier down-conversion systems. Specific challenges to characterising their luminescent properties have been explored in detail, also applicable to other luminescent materials. Additionally, alternative applications for luminescent quantum dots have been investigated, and finally, the gap between small-scale synthesis and industrial production was explored for the material system of most interest.

PbS quantum dots were synthesised and their luminescence efficiencies were enhanced through cation exchange with cadmium. It was found that the luminescence improvement was sensitive to a multitude of factors, particularly reaction duration at hitherto unexplored short timescales. Time-resolved optical and structural characterisation was performed indicating a two-step mechanism consisting of cation adsorption followed by subsequent exchange. Halting the reaction to the adsorption stage resulted in the highest luminescence efficiencies.

The lead-free quantum dot systems InAs and $CuInSe_2$ were investigated as alternative near-infrared emitters for photon-multiplication. Core-shell approaches with a variety of materials and complex structures were employed to improve their otherwise poor luminescence.

The measurement of photoluminescence quantum efficiency is widely used for luminescent material characterisation. As a figure of merit for colloidal quantum dots, the method was examined in great detail. The sources of systematic error were identified and random measurement error quantified for a recognised measurement methodology in order to obtain accurate measurements with meaningful uncertainty bounds, applied for a photon-multiplier demonstrator system.

CdSe and InP core-shell quantum dots were synthesised for a novel voltage probe. Their stability under electrolytic environments and strong response to applied electric fields was demonstrated for a biological voltage sensor.

PbS quantum dots were synthesised using a commercially-available microfluidic flow reactor. The challenges to product quality and reproducibility upon scale-up were examined. Mitigation strategies against the problems encountered were proposed.

1.3 Acknowledgements

I would like to thank my supervisor, Neil Greenham, for his tremendous support and valuable feedback.

For funding, the opportunity to be here and all the fun activities, I thank the NanoDTC and their team.

I'd like to thank the friends and collaborators in Optoelectronics and elsewhere: Akshay Rao, Tom Jellicoe, Callum Benson, Nate Davis, Jesse Allardice, Heather Goodwin, Demelza Wright, Neddy Booker, Eight19, Simon Dowland, Jurjen Winkel, Chloe Francis, Zhilong Zhang, Andrew Pearson, Raj Pandya, Mustafa Calgar, Hope Bretscher, Zhaojun Li, Arfa Karani, Patrick Conaghan, Linjie Dai, Jeff Gorman, Maxim Tabachnyk, Matt Menke, Emrys Evans, Andrew Parnell, Dominic Wright, Felix Deschler, Dan Credgington, Mike Weir, Dan Toolan, Ashish Sharma, Anthony Barnett and Marcus Böhm, to name a few.

I would like to thank my family and all the friends along the way: D. R., J. M., J. M., A. D., A. B., J. L., W. R., T. M., R. B., D. W., I. D., T. O., C. C., D. O., B.W., L. Z., C. S., A. C., C. S., T. J., H. G., N. D., N. B., M. C., I. B., A. L., R. R., W. J., S. D. and D. W. to insinuate arbitrarily.

Table of Contents`

1.4 List of Publications

- Cole, M. T., Parmee, R. J, Kumar, A., Collins, C. M., Kang, M. H., **Xiao, J.**, Cepek, C., Yuan, X. and Milne, W. I., Conjugated polyelectrolyte nano field emission adlayers, Nanoscale Horizons 1, 304–312 (2016).
- Tabachnyk, M., Karani, A. H., Broch, K., Pazos-Outón, L. M., **Xiao, J.**, Jellicoe, T. C., Novák, J., Harkin, D., Pearson, A. J., Rao, A., Greenham, N. C., Böhm, Marcus L. and Friend, Richard H., Efficient singlet exciton fission in pentacene prepared from a soluble precursor, APL Materials 4, 116112 (2016).
- Amemori, S., Gupta, R. K., Böhm, M. L., **Xiao, J.**, Huynh, U., Oyama, T., Kaneko, K., Rao, A., Yanai, N. and Kimizuka, N., Hybridizing semiconductor nanocrystals with metal–organic frameworks for visible and near-infrared photon upconversion, Dalton Transactions 25–28 (2018).
- Rivett, J. P. H., Tan, L. Z., Price, M. B., Bourelle, S. A., Davis, N. J. L. K., **Xiao, J.**, Zou, Y. Middleton, R., Sun, B., Rappe, A. M., Credgington, D. and Deschler, F., Long-lived polarization memory in the electronic states of lead-halide perovskites from local structural dynamics, Nature Communications 9, 3531 (2018).
- Li, N., Subramanian, G. S., Matthews, P. D., **Xiao, J.**, Chellappan, V., Rosser, T. E., Reisner, E., Luo, H. K. and Wright, D. S., Energy transfer and photoluminescence properties of lanthanide-containing polyoxotitanate cages coordinated by salicylate ligands, Dalton Transactions 47, 5679–5686 (2018).
- Davis, N. J. L. K., Allardice, J. R., **Xiao, J.**, Petty, A. J., Greenham, N. C., Anthony, J. E. and Rao, A., Singlet Fission and Triplet Transfer to PbS Quantum Dots in TIPS-Tetracene Carboxylic Acid Ligands, Journal of Physical Chemistry Letters 9, 1454–1460 (2018).
- Davis, N. J. L. K., Allardice, J. R., **Xiao, J.**, Karani, A., Jellicoe, T. C., Rao, A. and Greenham, N. C., Improving the photoluminescence quantum yields of quantum dot films through a donor/acceptor system for near-IR LEDs, Materials Horizons 6, 137–143 (2019).

Chapter 1 Introduction

In the midst of ever-increasing world energy demands, greater focus has been applied towards renewable energy sources. Photovoltaic (PV) technologies have rapidly expanded in implementation and efficiency to help alleviate the mounting requirements of power generation networks. Extant single-junction photovoltaic technologies are limited by the Shockley-Queisser efficiency limit. One of the major loss mechanisms in this limit is thermalisation, where excess energy of incident photons above the bandgap is lost to heat. Carrier-multiplication systems such as singlet fission are one approach to circumvent the efficiency limit. A related system, photon-multiplication down-conversion is a more flexible approach that may be applied to existing PV generation capacity to increase efficiency. In a photon-multiplication system, high energy photons are converted by an organic layer into two lower-energy excitons per photon. The lower-energy excitons are transferred into quantum dots for reemission as two lower energy photons for absorption by a conventional photovoltaic, boosting its photocurrent and increasing efficiency. As highly luminescent colloidal quantum dots are a key element of a photon-multiplier system and are currently the limiting factor in their overall efficiency, measures to ensure their photoluminescence quantum yield and stability are essential.

This thesis addresses some of the challenges faced in the synthesis of colloidal quantum dots with high luminescence efficiency and their application in photon-multipliers and other optoelectronic systems. Following a chapter on the background of discussed concepts, four results chapters are presented with the structure as follows.

Colloidal lead sulfide quantum dots have demonstrated good near-infrared luminescence. They have been the preferred materials for applications requiring utmost near-infrared luminescence such as photon-multiplier down-conversion concepts for photovoltaics. A widely-utilised method to improve photoluminescence efficiency involves the exchange of lead with cadmium cations to form a nominally core-shell PbS/CdS structure. Despite significant literature, the reaction is not necessarily well-understood. In Chapter 3, the reaction's effect on photoluminescence efficiency has been investigated and linked to structural characterisation, focussing on previously overlooked short timescales. The optimal exchange parameters to maximise luminescence efficiency have been identified along with a proposed structural explanation.

Although the choice materials for high-luminescence near-infrared quantum dots have typically been lead chalcogenides, significant concerns remain concerning their potential toxicity. Near-infrared emitter materials not containing lead become attractive for study as potential alternatives, aided by environmental legislation. In Chapter 4, lead-free nanocrystals such as the III-V material indium arsenide have been investigated as near-infrared emitters. The sizable challenges in the improvement of their luminescence efficiencies have been tackled through core-shell passivation routes.

The measurement of photoluminescence quantum efficiency is critical to the evaluation of luminescent materials in light-emitting applications. Whilst conceptually simple for ideal samples in dilute solutions, the measurement becomes complicated by sample anisotropy. Absolute quantum efficiency measurements thus require precise calibration of instrument spectral response to a known radiometric source. The multitude of factors influencing spectral response creates numerous potential sources of systematic error. In addition, significant random errors may be introduced under certain conditions. Chapter 5 identifies and explores various aspects of photoluminescence quantum efficiency measurements to consider and control in the pursuit of accurate measurements. Following mitigation of systematic error sources, quantification of statistically-measurable random error sources has been performed on a case-study system in order to provide meaningful measurement uncertainty ranges and to validate a functional singlet fission photon-multiplier system.

In addition to the main focus of photon-multiplication systems in this thesis, other applications of colloidal quantum dots have been investigated. Luminescent nanocrystal quantum dots have an established presence in biological imaging applications. As fluorescent markers, they have allowed excellent spatial resolution and sensitivity to be achieved in tissue studies. In addition, they can be sensitive to the local chemical environment, creating another information channel. In the first section of Chapter 6, a quantum dot voltage sensor concept has been demonstrated following the synthesis of core-shell quantum dots with good luminescence and stability.

To expand the relevance of colloidal quantum dots within the context of scale, practical aspects of their synthesis was investigated. Industrial chemical syntheses have generally favoured continuous flow processes. As quantum dots secure more commercial applications, it becomes necessary to scale up production routes. The second half of Chapter 6 focusses on the conversion of existing wet-chemical batch quantum dot synthesis techniques to a microfluidic continuous flow system. The technical challenges encountered transitioning to flow chemistry have been described along with potential mitigation routes to improve product yield and quality.

Chapter 2 Background

2.1 Organic semiconductors

Organic semiconductors are organic molecules or polymers that possess good charge transport properties not normally associated with organic molecules.[1] Semiconductor properties arise from conjugated π-bonding systems. Separation between the highest-occupied molecular orbital (HOMO) and lowest-unoccupied molecular orbital (LUMO) energy levels provide defined electronic states. Photoexcitation of an electron from the HOMO to the LUMO or injection of an electron and a hole results in a bound excited electron-hole pair or exciton. The small dielectric constants of organic molecules result in large binding energies of the excitons. With large binding energies, excitons are confined to single molecules or small numbers of molecules resulting in large exchange energy from large overlap of electron and hole wavefunctions. Two distinct exciton spin states are thus generated: spin-0 singlets and spin-1 triplets. Generally, the first excited triplet state (T_1) is lower in energy than the first excited singlet state (S_1) because of the exchange interaction between electrons with parallel spin in the HOMO and LUMO.[2,3]

Transitions between energy levels are spin-conserving, thus photoexcitation results in promotion of an electron from the singlet ground state to a singlet excited state. For intersystem crossing between the excited singlet state and a triplet state, overall spin must be conserved through hyperfine interaction or spin-orbit coupling. Radiative recombination of the exciton to emit a photon is spin-allowed from the excited singlet state and spin-forbidden from the triplet state. The probability of triplet emission is low and triplet excitons are thus termed ‘dark’ or non-emissive.

In traditional organic optoelectronics, formation of triplet excitons leads to substantial device limitations. In organic photovoltaics, intersystem crossing of photoexcited singlet states to triplet states can result in large recombination losses reducing both voltage and photocurrent.[4] In light-emitting diodes (LEDs), electrically generated exciton populations follow spin statistics leading to 25% as emissive singlets and 75% as non-emissive triplets.[5,6]

Singlet fission polyacenes

Polyacenes are conjugated organic molecules consisting of fused benzene rings. Polyacenes such as pentacene and tetracene are one group of organic materials where the triplet exciton energy is around half the singlet energy.[7] The ultra-fast exciton multiplication process known as singlet fission (SF) occurs where a singlet exciton splits into two triplet excitons each with approximately half the energy.[8] A photogenerated singlet exciton on a molecule couples into a neighbouring chromophore on another molecule, forming a pair of triplets, one on each molecule. Some triplet pair states have

overall spin-0 or singlet character where spin is conserved, thus singlet fission is spin-allowed and can take place on timescales as fast as 80 fs in some organic materials with 200% efficiency.[7] Triplets generated by SF have been shown to have long lifetimes of milliseconds and diffusion lengths up to several micrometres.[9]

Several applications of polyacene SF have been investigated including LEDs, sensors and particularly photovoltaics, with the promise of greater quantum efficiencies.[10–13] Sensitisation of solar cells with singlet fission material may yield increased photocurrents from high-energy photons. A photogenerated singlet exciton from a high-energy photon in a sensitiser undergoes singlet fission. Both triplet excitons may be transferred into a suitable electron acceptor to dissociate into charges, resulting in two charge carriers obtained for a single photoexcitation and allowing for greater photocurrents. However, a main limitation of SF solar cells has been the requirement for thin layers to allow triplet diffusion at the cost of reduced absorption. In addition, the relative insolubility of polyacenes has mostly precluded solution-process techniques, requiring more costly vapour deposition. Singlet fission based solar cell devices have consisted of a SF material in conjunction with an electron acceptor material such as C_{60} or quantum dots to dissociate the triplet excitons and have so far only achieved maximum power conversion efficiencies of 4-5%, despite obtaining external quantum efficiencies in excess of 100% in certain spectral regions.[10,12]

Chemical modification of SF materials with solubilising functional groups has greatly improved ease of processing. Efficient singlet fission has also been shown in such materials, for example, 5,12-bis(triisopropylsilylethynyl)tetracene (TIPS-tetracene), which has good solubility in common solvents.[13,14] Alteration of the polyacene systems with other functional groups has been shown to alter the photophysics of the material, including triplet energies.[15] These include heterocycles to change energetics or coordinating functional groups like carboxylic acids to allow dative bonding as a ligand.[16,17] The tuneable physical properties of SF materials have demonstrated their flexibility for incorporation into optoelectronic device applications.

2.2 Singlet fission downconversion

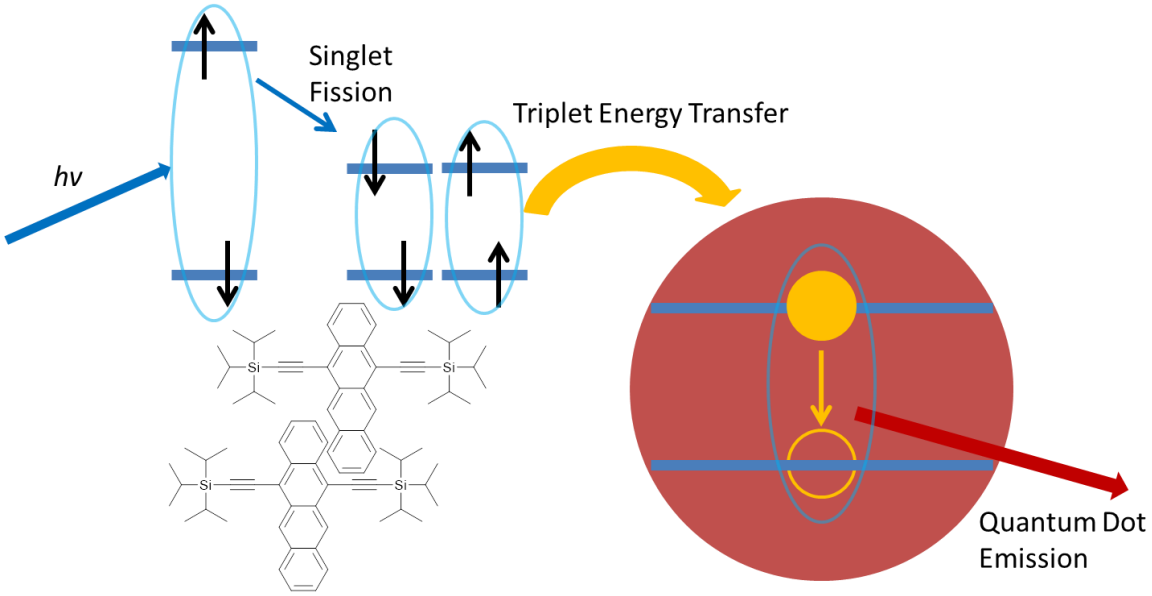

Figure 2-1 Cartoon schematic of a singlet fission down-conversion assembly. A high-energy blue photon hv is absorbed in the sensitiser TIPS-tetracene molecules to produce a high energy singlet exciton. This is rapidly converted into two lower-energy triplet excitons which are non-emissive. The triplet excitons are then transferred into quantum dots and radiative recombination occurs resulting in the emission of a photon. Two near-infrared photons are emitted for each blue photon absorbed.

Another approach for the incorporation of singlet fission in photovoltaics is the conversion of high energy photons into two low-energy photons i.e. down-conversion. The emitted low-energy photons can then be absorbed in a conventional inorganic photovoltaic solar cell such as silicon. In conventional photovoltaics, the excess energy of high-energy photons is lost as heat through thermalisation to the bandgap, limiting single-junction silicon cells to a theoretical maximum of 32% power conversion efficiency (PCE).[18] Down-conversion instead allows the excess energy to be harvested. The photon-multiplication process provides additional photocurrent in the host solar cell, thus increasing efficiency. A down-conversion unit consists of two key components, shown in Figure 2-1: a singlet fission sensitiser material to absorb high-energy photons and convert each into two triplet excitons. An acceptor/emitter component then converts the triplet excitons into lower-energy photons which can be absorbed by the solar cell, potentially enabling gains of 4% absolute PCE for current real-world cells.[19]

Triplet Energy Transfer

As the singlet fission generated triplet excitons in the organic molecules are non-emissive, it is necessary to transfer the energy into a suitable emitter material. However, Förster resonance energy transfer (FRET) is not possible because the zero oscillator strength of triplet excitons prevents dipolar

coupling.[20] Instead, wavefunction overlap must occur between the triplet exciton and the emitter/acceptor, with energy transfer occurring through an electron transfer process or Dexter transfer. Dexter transfer has been shown to be far slower than FRET, however transfer efficiency into quantum dots (QDs) has been shown to greater than 95%.[21,22] SF-generated triplet energy transfer into QDs has been demonstrated at high efficiencies with potential application in SF down-conversion.

Luminescent emitters

A suitable emitter material is required to convert non-emissive triplet excitons into photons. In inorganic semiconductors, the greater spin-orbit coupling mixes spin states such that excitons do not have defined singlet or triplet states. Thus an organic triplet exciton transferred via Dexter transfer to a luminescent inorganic emitter, where it becomes an exciton without defined singlet or triplet states, could then undergo radiative recombination without violating spin conservation.[23] Inorganic quantum dots can be highly luminescent with tuneable bandgaps thus can serve as suitable emitters for down-conversion.[19]

The singlet fission down-conversion process thus relies on a combination of efficiencies: the singlet fission triplet yield, the triplet energy transfer efficiency, the luminescence efficiency of the emitter and the out-coupling efficiency of emitted photons into the photovoltaic cell. Singlet fission and triplet energy transfer have both been demonstrated at near-complete efficiencies and out-coupling efficiency may be maximised through optical engineering.[7,21] Critical to the efficiency of the down-conversion process is thus the luminescence efficiency of the emitter quantum dots. For matching to extant photovoltaic technologies, near-infrared quantum dot emitters are required. Near-infrared QDs have received less attention and have correspondingly demonstrated lower luminescence efficiencies compared to their visible counterparts.[24–26] Investigation into improvement of near-infrared QD luminescence efficiency is thus paramount for down-conversion applications.

2.3 Confined semiconductors

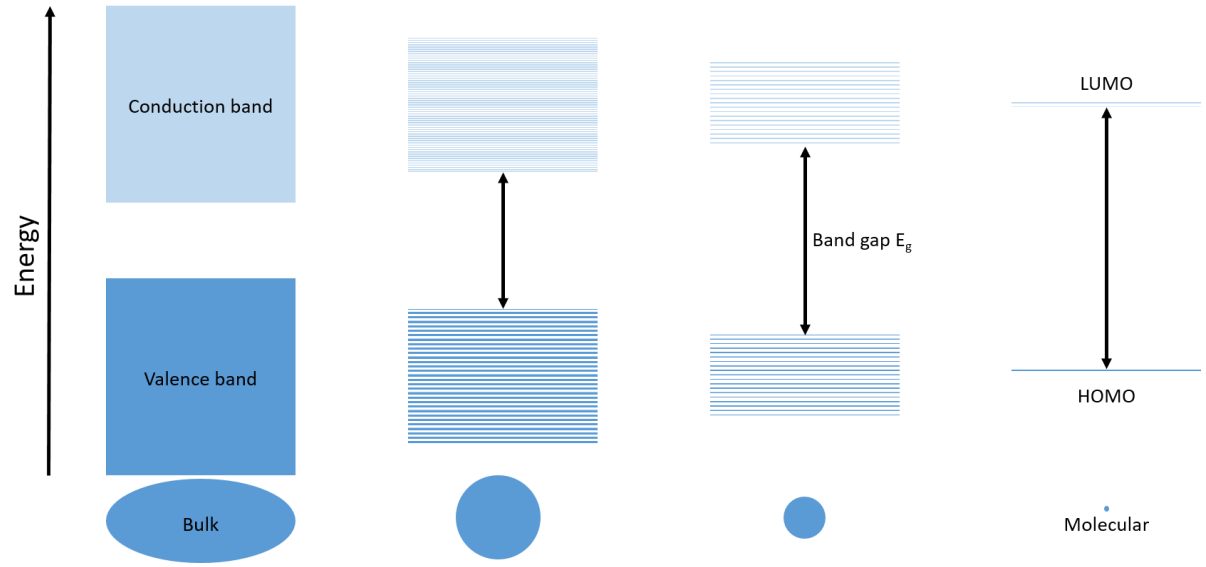

Figure 2-2 – Cartoon of available energy levels in different sized systems. As the number of energy states decrease due to decrease in system size from the bulk, the corresponding bandgap increases. The extreme case of a molecular system with a single bond is shown, showing the maximal energy gap between highest occupied molecular orbital (HOMO) and lowest unoccupied molecular orbital (LUMO).

In inorganic semiconductors, large dielectric constants result in lowered Coulombic attraction in exciton electron-hole pairs leading to large exciton Bohr radii. Quantum dots are semiconductor nanoscale crystals where the physical size approaches or becomes smaller than the material exciton Bohr radius. The system becomes quantum-confined as the exciton experiences restriction from the spatial confinement of the nanocrystal. The band structure or available energy states become more discrete leading to an increase in band gap, illustrated in the cartoon Figure 2-2 showing change in available energy states and band gap with change in crystal size. The band gap is thus controlled by size and shape, with spherical nanocrystals behaving like zero-dimensional quantum wells with quantised energy states hence the term quantum dot. Smaller quantum dots experience greater confinement and possess larger bandgaps compared to larger dots or bulk material.[27]

Colloidal QDs

Conventional techniques for semiconductor fabrication such as gas-phase epitaxy and lithographic methods have produced many varieties of quantum dots.[28,29] QDs produced through these methods are typically affixed to substrates and cannot be solution processed. Conventional methods also possess other significant disadvantages such as cost and processing difficulty. Wet-chemical colloidal synthesis methods have attracted great interest and have demonstrated the ability to create large quantities of quantum dots. The resulting colloidal nanocrystals may be dispersed in solvents and easily processed as solutions or inks.[30–33]

Wet chemical synthesis

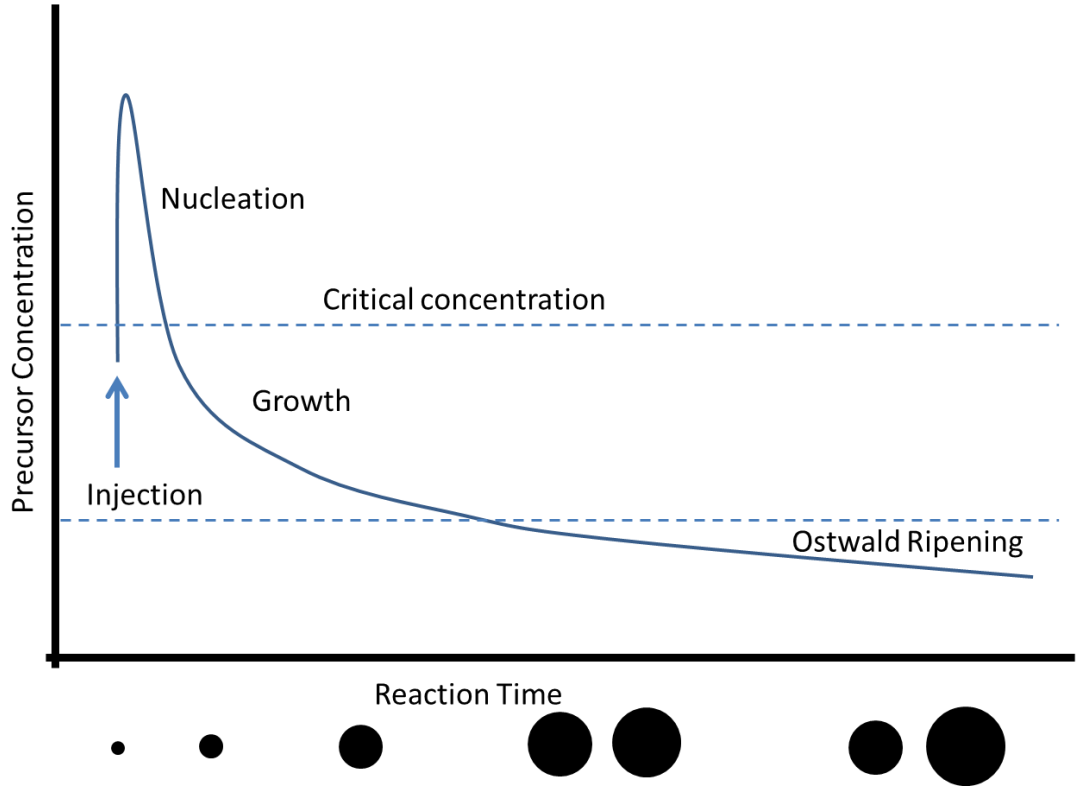

Figure 2-3 – Concentration profile of precursors in nanocrystal growth, known as a LaMer diagram.[32] At point of injection, precursor concentration is maximised and increased above the critical concentration for crystal nucleation. Rapid nucleation decreases the concentration below the critical concentration, and further nucleation is arrested. At intermediate precursor concentration, crystal growth is faster than dissolution and particle sizes increase. At low precursor concentration, growth is inhomogeneous. Smaller crystals dissolve more quickly into precursors than larger crystals and fuel the growth of the larger crystals, resulting in size distribution increase.

The synthesis of colloidal semiconductor nanocrystals has typically occurred through a solution-based hot-injection method.[35–37] A solution of one component precursor is injected into a heated solution of a different precursor to induce crystal nucleation and growth; a conceptual concentration profile is illustrated in Figure 2-3. The growth solution contains precursors and solubilising ligands in addition to the nucleated nanocrystals. The initial temperature is typically highest at point of injection to assist nucleation and is subsequently lowered for growth to minimise additional nucleation.[38] The suppression of additional nucleation events after the initial burst of nucleation assists with the minimisation of size distribution, by ensuring all nuclei formed to experience the same conditions throughout the complete reaction process.[34] As quantum dot bandgap is determined by size, a narrow size distribution is desirable for well-defined absorption and emission profiles.[39,40] The hot injection method has been applied to synthesise a wide range of semiconductor quantum dots, including more complex ternary and quaternary compositions.[36,41,42]

Surface chemistry and ligand coordination

The small size of colloidal nanocrystals results in a very high surface area-to-volume ratio, with a high proportion of surface atoms. Surface atoms are particularly reactive because of unsaturated coordination with neighbouring atoms, leaving 'dangling' bonds.[43] Electronic passivation of these orbitals is typically achieved by electron density-donating ligands 'coordinating' to the surface atoms. Insufficient electronic passivation may result in reactions with the environment such as surface oxidation. Bulky ligands may sterically hinder additional ligands from coordinating with the surface, resulting in incomplete electronic passivation.[44]

The colloidal stability of nanocrystals is aided by the capping of solubilising ligands on their surface.[45–47] Ligands can provide a steric or Coulombic barrier against aggregation of nanocrystals. Nanocrystal aggregation causes precipitation from solvent and can be prevented through physically limiting minimum separation or by electrostatic repulsive forces. Ligands also reduce interfacial energies, allowing dispersion in a solvent. As-synthesised, nanocrystal surfaces are capped with ligands present in the reaction solution.[48] Commonly, these have been long-chain alkyl species with a carboxylic acid or amine group for surface bonding. Long-chain alkyl ligands provide hydrophobic interactions with common non-polar organic solvents such as toluene or hexane, allowing colloidal stability. Halide anions and alkylphosphines have also been commonly utilised as synthesis ligands.[49–51] The ligand environment around a colloidal quantum dot is dynamic and exchange may occur with different ligands to modify and tune physiochemical behaviour of the nanocrystals. Attachment of polar ligands can allow dispersion in polar organic solvents or water, and functionalised proteins can provide targeted binding sites for biological systems.[44,52–54]

Passivation and luminescence

Luminescence efficiency of colloidal nanocrystals is primarily governed by passivation efficacy. Un-passivated surface states or defects can cause intra-band energy states.[55,56] Instead of radiative recombination, an exciton may instead populate the intra-band state and become trapped. In a single quantum-confined system, the presence of a trap results in a non-emissive nanocrystal. The trap increases the non-radiative recombination rate compared to the radiative recombination rate. Radiative recombination thus becomes out-competed and non-radiative recombination becomes the dominant mechanism. The overall photoluminescence quantum efficiency of a population of nanocrystals may be regarded as the emissive proportion.[57] To maximise luminescence efficiency, improvement of nanocrystal surface passivation is paramount.

Although ligands provide a degree of passivation, they rarely provide complete passivation or protection of the exciton wavefunction.[50,58,59] Substantial research has been carried out to improve luminescence efficiency and stability of colloidal quantum dots for a variety of applications. For different environments such as atmospheric conditions, additional passivation techniques are required

for chemical and optical stability. A common approach has been the growth of a shell of wider-bandgap semiconductor material around the nanocrystals to create core-shell structures.[42,60–63] Core-shell colloidal quantum dots have demonstrated near-100% luminescence quantum efficiencies and have found extensive commercial applications.[24,25,64]

Extant applications

Visible-emitting colloidal QDs have notably attained widespread incorporation in display technologies.[65] The sharp emission properties of QDs have enabled higher colour purity and brightness compared to organic LED technologies, making them particularly attractive for television displays. Typically, highly luminescent QDs are photo-excited with an efficient conventional blue LED and re-emit monochromatic red, green and blue (RGB) light in a display matrix. In contrast, electroluminescent polymers in organic LED materials often feature broad emission spectra. Visible emitting materials such as CdSe and InP have been extensively studied and have achieved high luminescence efficiencies.[64,66,67]

Colloidal QDs have been researched extensively for biological imaging applications as fluorescent markers as their emission properties offer large advantages over conventional organic dyes.[52] In particular, near-infrared emitting QDs such as InAs have been studied for deep tissue imaging, where their emission lies in a region where biological tissue is largely transparent.[68,69] Further introduction to colloidal quantum dots in biological applications is presented in the first half of Chapter 6, where an application is demonstrated in principle.

Colloidal near-infrared QDs have also been studied for photovoltaic applications, such as the lead chalcogenide materials PbS and PbSe.[70–72] The characteristic properties of high absorption, tuneable bandgaps and ability for solution processing have offered an attractive prospect for low-cost photovoltaics.[33,41,45]

2.4 References

1. Coropceanu, V., Cornil, J., da Silva Filho, D. A., Olivier, Y., Silbey, R. & Brédas, J.-L. *Chemical Reviews* **107**, 926–952 (2007).

2. Reineke, S. & Baldo, M. a. *Scientific reports* **4**, 3797 (2014).

3. Köhler, A. & Bässler, H. *Materials Science and Engineering: R: Reports* **66**, 71–109 (2009).

4. Etherington, M. K., Wang, J., Chow, P. C. Y. & Greenham, N. C. *Applied Physics Letters* **104**, 063304 (2014).

5. Forrest, S. R., Baldo, M. A., O'Brien, D. F., You, Y., Shoustikov, A., Sibley, S. *et al. Nature* **395**, 151–154 (1998).

6. Cho, H., Jeong, S.-H., Park, M.-H., Kim, Y.-H., Wolf, C., Lee, C.-L. *et al. Science* **350**, 1222–1225 (2015).

7. Wilson, M. W. B., Rao, A., Clark, J., Kumar, R. S. S., Brida, D., Cerullo, G. *et al. Journal of the American Chemical Society* **133**, 11830–11833 (2011).

8. Smith, M. B. & Michl, J. *Chemical Reviews* **110**, 6891–6936 (2010).

9. Tabachnyk, M., Ehrler, B., Bayliss, S., Friend, R. H. & Greenham, N. C. *Applied Physics Letters* **103**, (2013).

10. Lee, J., Jadhav, P., Reusswig, P. D., Yost, S. R., Thompson, N. J., Congreve, D. N. *et al. Accounts of Chemical Research* **46**, 1300–1311 (2013).

11. Ehrler, B., Wilson, M. W. B., Rao, A., Friend, R. H. & Greenham, N. C. *Nano Letters* **12**, 1053–1057 (2012).

12. Congreve, D. N., Lee, J., Thompson, N. J., Hontz, E., Yost, S. R., Reusswig, P. D. *et al. Science* **340**, 334–337 (2013).

13. Yang, L., Tabachnyk, M., Bayliss, S. L., Böhm, M. L., Broch, K., Greenham, N. C. *et al. Nano Letters* **15**, 354–358 (2015).

14. Tabachnyk, M., Karani, A. H., Broch, K., Pazos-Outón, L. M., Xiao, J., Jellicoe, T. C. *et al. APL Materials* **4**, 116112 (2016).

15. Garakyaraghi, S., Mongin, C., Granger, D. B., Anthony, J. E. & Castellano, F. N. *The Journal of Physical Chemistry Letters* 1458–1463 (2017).

16. Anthony, J. E. *Chemical Reviews* **106**, 5028–5048 (2006).

17. Davis, N. J. L. K., Allardice, J. R., Xiao, J., Petty, A. J., Greenham, N. C., Anthony, J. E. *et al. The Journal of Physical Chemistry Letters* **9**, 1454–1460 (2018).

18. Shockley, W. & Queisser, H. J. *Journal of Applied Physics* **32**, 510–519 (1961).

19. Futscher, M. H., Rao, A. & Ehrler, B. *ACS Energy Letters* **3**, 2587–2592 (2018).

20. Mahboub, M., Huang, Z. & Tang, M. L. *Nano Letters* **16**, 7169–7175 (2016).

21. Tabachnyk, M., Ehrler, B., Gélinas, S., Böhm, M. L., Walker, B. J., Musselman, K. P. *et al. Nature Materials* **13**, (2014).

22. Thompson, N. J., Wilson, M. W. B., Congreve, D. N., Brown, P. R., Scherer, J. M., Bischof, T.

S. *et al. Nature Materials* **13**, 1039–1043 (2014).

23. Chiu, Y. *The Journal of Chemical Physics* **56**, 4882–4898 (1972).

24. McBride, J., Treadway, J., Feldman, L. C., Pennycook, S. J. & Rosenthal, S. J. *Nano Letters* **6**, 1496–1501 (2006).

25. Jeong, B. G., Park, Y.-S., Chang, J. H., Cho, I., Kim, J. K., Kim, H. *et al. ACS Nano* **10**, 9297–9305 (2016).

26. Solomeshch, O. & Tessler, N. *APL Materials* **4**, (2016).

27. Brus, L. E. *The Journal of Chemical Physics* **80**, 4403 (1984).

28. Oliver, R. A., Briggs, G. A. D., Kappers, M. J., Humphreys, C. J., Yasin, S., Rice, J. H. *et al. Applied Physics Letters* **83**, 755–757 (2003).

29. Benyoucef, M. & Reithmaier, J. P. *Semiconductor Science and Technology* **28**, (2013).

30. Liu, M., Voznyy, O., Sabatini, R., García de Arquer, F. P., Munir, R., Balawi, A. H. *et al. Nature Materials* **1**, (2016).

31. Giansante, C., Carbone, L., Giannini, C., Altamura, D., Ameer, Z., Maruccio, G. *et al. Thin Solid Films* **560**, 2–9 (2014).

32. Konstantatos, G., Howard, I., Fischer, A., Hoogland, S., Clifford, J., Klem, E. *et al. Nature* **442**, 180–183 (2006).

33. Cademartiri, L., Montanari, E., Calestani, G., Migliori, A., Guagliardi, A. & Ozin, G. A. *Journal of the American Chemical Society* **128**, 10337–10346 (2006).

34. LaMer, V. K. & Dinegar, R. H. *Journal of the American Chemical Society* **72**, 4847–4854 (1950).

35. Murray, C. B., Norris, D. & Bawendi, M. G. *Journal of the American Chemical Society* **115**, 8706–8715 (1993).

36. Song, J. M., Liu, Y., Niu, H. L., Mao, C. J., Cheng, L. J., Zhang, S. Y. *et al. Journal of Alloys and Compounds* **581**, 646–652 (2013).

37. Zhang, L. J., Shen, X. C., Liang, H., Guo, S. & Liang, Z. H. *Journal of Colloid and Interface Science* **342**, 236–242 (2010).

38. Peng, X., Wickham, J. & Alivisatos, a. P. *Journal of the American Chemical Society* **120**,

5343–5344 (1998).

39. Moreels, I., Lambert, K., Smeets, D., De Muynck, D., Nollet, T., Martins, J. C. *et al. ACS Nano* **3**, 3023–3030 (2009).

40. Jasieniak, J., Califano, M. & Watkins, S. E. *ACS Nano* **5**, 5888–5902 (2011).

41. Wei, H., Guo, W., Sun, Y., Yang, Z. & Zhang, Y. *Materials Letters* **64**, 1424–1426 (2010).

42. Kim, S. W., Zimmer, J. P., Ohnishi, S., Tracy, J. B., Frangioni, J. V & Bawendi, M. G. *J. Am. Chem. Soc.* **127**, 10526–10532 (2005).

43. Neo, D. C. J., Cheng, C., Stranks, S. D., Fairclough, S. M., Kim, J. S., Kirkland, A. I. *et al. Chemistry of Materials* **26**, 4004–4013 (2014).

44. Boles, M. A., Ling, D., Hyeon, T. & Talapin, D. V. *Nature Materials* **15**, 141–153 (2016).

45. Giansante, C., Carbone, L., Giannini, C., Altamura, D., Ameer, Z., Maruccio, G. *et al. Journal of Physical Chemistry C* **117**, 13305–13317 (2013).

46. Hines, M. A. & Scholes, G. D. *Advanced Materials* **15**, 1844–1849 (2003).

47. Mourdikoudis, S. & Liz-Marzán, L. M. *Chemistry of Materials* **25**, 1465–1476 (2013).

48. Dong, A., Ye, X., Chen, J., Kang, Y., Gordon, T., Kikkawa, J. M. *et al. Journal of the American Chemical Society* **133**, 998–1006 (2011).

49. Kim, K., Yoo, D., Choi, H., Tamang, S., Ko, J.-H., Kim, S. *et al. Angewandte Chemie International Edition* **55**, 3714–3718 (2016).

50. Guzelian, a a, Katari, J. E. B., Kadavanich, a V, Banin, U., Hamad, K., Juban, E. *et al. Journal of Physical Chemistry* **100**, 7212–7219 (1996).

51. Shakeri, B. & Meulenberg, R. W. *Langmuir* **31**, 13433–13440 (2015).

52. Parak, W. J., Pellegrino, T. & Plank, C. *Nanotechnology* **16**, R9–R25 (2005).

53. Gerion, D., Pinaud, F., Williams, S. C., Parak, W. J., Zanchet, D., Weiss, S. *et al. The Journal of Physical Chemistry B* **105**, 8861–8871 (2001).

54. Reinhart, C. C. & Johansson, E. *Chemistry of Materials* **27**, 7313–7320 (2015).

55. Ip, A. H., Thon, S. M., Hoogland, S., Voznyy, O., Zhitomirsky, D., Debnath, R. *et al. Nature Nanotechnology* **7**, 577–582 (2012).

56. Morgenstern, F. S. F., B??hm, M. L., Kist, R. J. P., Sadhanala, A., G??linas, S., Rao, A. *et al. Journal of Physical Chemistry C* **120**, 19064–19069 (2016).

57. Efros, A. L. & Nesbitt, D. J. *Nature Nanotechnology* **11**, 661–671 (2016).

58. Cao, Y. & Banin, U. *Journal of the American Chemical Society* 9692–9702 (2000).

59. Guzelian, a. a., Banin, U., Kadavanich, A. V., Peng, X. & Alivisatos, a. P. *Applied Physics Letters* **69**, 1432 (1996).

60. Manna, L., Scher, E. C., Li, L. S. & Alivisatos, a. P. *Journal of the American Chemical Society* **124**, 7136–7145 (2002).

61. Pietra, F., De Trizio, L., Hoekstra, A. W., Renaud, N., Prato, M., Grozema, F. C. *et al. ACS Nano* **10**, 4754–4762 (2016).

62. Zimmer, J. P., Kim, S., Ohnishi, S., Tanaka, E., Frangioni, J. V & Bawendi, M. G. 2526–2527 (2006).

63. Talapin, D. V, Mekis, I., Go, S., Kornowski, A., Benson, O. & Weller, H. 18826–18831 (2004).

64. Coropceanu, I., Rossinelli, A., Caram, J. R., Freyria, F. S. & Bawendi, M. G. *ACS Nano* **10**, 3295–3301 (2016).

65. Tamang, S., Lincheneau, C., Hermans, Y., Jeong, S. & Reiss, P. *Chemistry of Materials* **28**, 2491–2506 (2016).

66. Li, L. & Reiss, P. *Journal of the American Chemical Society* **130**, 11588–11589 (2008).

67. Wang, N., Koh, S., Jeong, B. G., Lee, D., Kim, Y., Lee, B. *et al. Nanotechnology* **185603**, 185603 (2017).

68. Benayas, A., Ren, F., Carrasco, E., Marzal, V., Del Rosal, B., Gonfa, B. A. *et al. Advanced Functional Materials* **25**, 6650–6659 (2015).

69. Zhu, C. N., Jiang, P., Zhang, Z. L., Zhu, D. L., Tian, Z. Q. & Pang, D. W. *ACS Applied Materials and Interfaces* **5**, 1186–1189 (2013).

70. Ma, W., Swisher, S. L., Ewers, T., Engel, J. H., Ferry, V. E., Atwater, H. A. *et al. ACS Nano* **5**, 8140–8147 (2011).

71. Clark, P. C. J., Radtke, H., Pengpad, A., Williamson, A. I., Spencer, B. F., Hardman, S. J. O. *et al. Nanoscale* **9**, 6056–6067 (2017).

72. Zarghami, M. H., Liu, Y., Gibbs, M., Gebremichael, E., Webster, C. & Law, M. *ACS Nano* **4**, 2475–2485 (2010).

Chapter 3 Optimising Photoluminescence Enhancement in PbS/CdS Core-Shell Quantum Dots

3.1 Introduction

Near-infrared quantum dot emitters

Near-infrared (NIR) emitters have well-established applications within the fields of optical telecommunications, medical imaging and spectroscopy. [1–4] Emergent applications also include night-vision imaging and biometric sensing. Colloidal nanocrystal quantum dots have shown promise as NIR emitter materials; however they have lacked the stability and efficiency of commercial devices.[5,6] Recent advances in the stability and luminescence of visible-emitting colloidal QDs have been accompanied by widespread commercial incorporation in display technologies.[7,8] Similar work has progressed for the improvement of NIR QDs.[2,3,5]

Lead chalcogenides

Lead chalcogenides are compounds of lead and group VI chalcogenide materials such as sulfur, selenium and tellurium. The bulk materials demonstrate narrow-bandgap semiconducting properties and typically adopt the cubic rocksalt structure. Bulk lead sulfide (PbS) has a bandgap of around 0.41 eV and has been widely utilised for infrared detector applications.[9,10]

Lead chalcogenide colloidal quantum dots have been shown to be efficient near-infrared emitters.[11–13] The facile synthesis and bandgap tunability in the near-infrared have made them attractive materials for photovoltaics applications.[14,15] Lead sulfide has been the preferred material over selenide or telluride because of its greater resistance to surface oxidation and lower sensitivity to atmospheric conditions.[16–18] Pure PbS QDs suffer from emission efficiency losses upon exposure to atmospheric conditions.[19] Halide-passivated PbS has been shown to provide greater surface passivation and atmospheric stability.[20–22]

Surface passivation through cation exchange

Cation exchange of Pb with Cd cations in lead chalcogenide QDs has attracted considerable study for the improvement of photoluminescence efficiency.[23–27] This involves the substitution of lattice atoms inwards from the surface of the nanocrystal, contrary to conventional shell growth methods where a higher-bandgap semiconductor material is deposited on the surface growing outwards. Substitution of lattice atoms ostensibly allows for epitaxial shell layers and minimisation of core-shell interfacial defects.

Previous studies of cation-exchanged core-shell PbS/CdS nanocrystals have provided insight into the surface chemistry and structure-property relationships exhibited in these systems.[28] The cation exchange reaction has been observed to progress with time-dependence in literature.[29] However, work has been centred on slow processes at extended reaction times. In other work, synchrotron-enabled studies have demonstrated annealing of thick CdS shell material, associating with observed crystal phase transitions.[29] The key observations in these studies were the emergence of different CdS material phases within the nanocrystal shell where with increasing reaction time, the CdS shell sequentially transformed from the cubic rocksalt to cubic zincblende then finally to the favoured hexagonal wurtzite structure. The observation demonstrated that the rocksalt-structure kinetic product gradually transformed to the wurtzite-structure thermodynamic product through atomic rearrangement under reaction conditions. Phase transformation of the shell from an epitaxial layer to a different crystal structure creates strain between the core and shell material. This generated strain can induce the formation of defects at the nanocrystal core-shell interface. The observation of photoluminescence decrease after cation exchange has been typically attributed to development of interfacial defects arising between the PbS core and CdS shell.[29]

The work presented here focuses on the fast reaction kinetics of Cd cation exchange in PbS nanocrystal QDs and its effect on the optical properties. Through understanding the surface chemistry and its effect on structure-property relationships, optimisation of reaction parameters may be performed to maximise the photoluminescence efficiencies obtained. Portions of this work were performed in collaboration; my primary contributions were all the synthesis and most of the analysis. Ultrafast optical measurements, blinking, small-angle X-ray scattering (SAXS) and elemental analysis experiments were performed by collaborators Jesse Allardice, Ashish Sharma, Andrew Pearson and Andrew Parnell as specified in the text.

3.2 Methods

PbS synthesis

The synthesis of PbS QDs was carried out following modified versions of the method of Hines & Scholes.[11] A typical synthesis was as follows:

Lead oxide (0.625 g, 99.999%, Sigma Aldrich), oleic acid (OA, 2 mL, 90%, Sigma Aldrich) and 1-octadecene (ODE, 25 mL, 90%, Sigma Aldrich) were placed in a three-necked round bottomed flask and degassed under vacuum at 110 °C for 2 hours with stirring, forming a colourless solution. Subsequently, the flask was put under nitrogen flow and heated to 115 °C. In a nitrogen glovebox, a syringe was prepared containing ODE (13.9 mL), diphenylphosphine (DPP, 144 µL, 99%, Sigma Aldrich) and bis(trimethylsilyl)sulfide (TMS_2S, 296 µL, 95%, Sigma Aldrich). The syringe containing the sulfur precursor was rapidly injected into the reaction flask, which was allowed to cool. Upon

cooling to 60 °C, the reaction mixture was transferred to an argon glovebox. The synthesised nanocrystals were twice purified by precipitation with a mix of anhydrous ethanol/1-butanol, centrifugation and resuspension in hexane. The purified QDs were redispersed in toluene for storage in an argon glovebox. The product QD bandgaps were tuned by modifying reaction parameters of injection temperature and oleic acid concentration.

PbS/CdS cation exchange

Cadmium cation exchange of PbS QDs was performed following a modified method of Neo et al.[26] A typical procedure was as follows:

Cadmium oxide (1.03 g, 99.999%, Sigma Aldrich), OA (6.35 mL) and ODE (25 mL) was placed in a three-necked round bottomed flask and degassed under vacuum for 110 °C. The vessel was switched to nitrogen and heated to 230 °C for 2 hours, resulting in the formation of a colourless solution of cadmium oleate. The solution was cooled and degassed under vacuum for 15 minutes. The flask was switched to nitrogen and the solution was transferred to a nitrogen glovebox for storage.

Cation exchange was performed with the addition of Cd-oleate solution to PbS nanocrystals. A typical reaction is as follows. In a nitrogen glovebox, a suspension of PbS nanocrystals in toluene (50 mg, 50 mg mL^{-1}) was heated to 100 °C. Cadmium oleate in ODE (0.35 mL, 0.26 M) was added to the nanocrystal suspension and maintained at 100 °C. The reaction was cooled and quenched after the desired time with the addition of anhydrous acetone. The cation-exchanged nanocrystals were twice precipitated, centrifuged and re-suspended with acetone and toluene.

Characterisation

Transmission electron microscopy (TEM) imaging was performed with a FEI Tecnai 20 TEM with LaB_6 cathode at 200 kV operating voltage. Samples were diluted and drop-cast onto 200-mesh carbon-coated Cu grids (Agar AGS160).

Photoluminescence quantum efficiency measurements were performed according to the integrating sphere method of de Mello et al.[30,31] The excitation light source was a Coherent OBIS laser at 405 nm. The optical system was a 6-inch Labsphere with diffusely-reflective $BaSO_4$ coating fibre-coupled into an Andor Shamrock SR-303i imaging spectrograph with iDus Si CCD and InGaAs PDA detectors. Detailed explanations of the measurement are described in Chapter 5, and the therein identified precautions to achieve accurate measurements were performed for all PLQE values explicitly shown. However, full random error analysis was not performed as the samples measured in this Chapter were sufficiently absorbing this was deemed unnecessary.

Inductively-coupled plasma mass spectrometry (ICP-MS) was performed on digested nanocrystal samples. Dried nanocrystals were digested in 4.5 M aqueous analytical grade nitric acid (70%, Fisher,

15.7 M). The solutions were then diluted to 0.45 M nitric acid concentration with deionised water. The digested mass concentration was between 10-1000 ppm w/w. ICP-MS was performed at the Department of Chemistry, University of Sheffield as a technical service.

3.3 Results and Discussion

PbS synthesis

The bandgap of PbS QDs synthesised was widely tuneable between 1.7 eV and 0.9 eV through modification of the synthesis conditions through two primary parameters: injection temperature and oleic acid concentration. The photoluminescence peak position was generally used to indirectly indicate bandgap, rather than directly by measured by absorption. This was because the luminescence characteristics were the desired properties of these materials. As a result of quantum confinement, bandgap decreased with increasing nanocrystal size. The general strategy for nanocrystal size tuning was the modification of the reaction kinetics to favour faster or slower growth thus larger or smaller resulting sizes. The synthesised PbS QDs were stored in toluene for reasons of both convenience and stability. The follow-up cation exchange reaction described in Section 3.5 required a higher boiling point thus it was convenient to keep batches in toluene for follow-up experiments. It was also found that vials of QDs dissolved in other solvents such as hexane or octane were prone to leakage and drying whilst in storage over time. The use of toluene meant that solvent absorption peaks at 1150 nm and 1200 nm were present in PL spectra. PLQE values quoted were thus considered to be underestimates, as explained in Chapter 5, however this was deemed to be acceptable.

Reaction temperature

Increased injection temperatures resulted in smaller bandgaps observed in PbS QDs. At higher temperatures, the reaction rate between precursors is higher thus both nucleation and growth of nanocrystals occur more rapidly. Faster nucleation was evident in the colour change of the solution upon injection – an almost immediate colour change was observed at 180 °C, whilst the same change took several seconds at 80 °C.

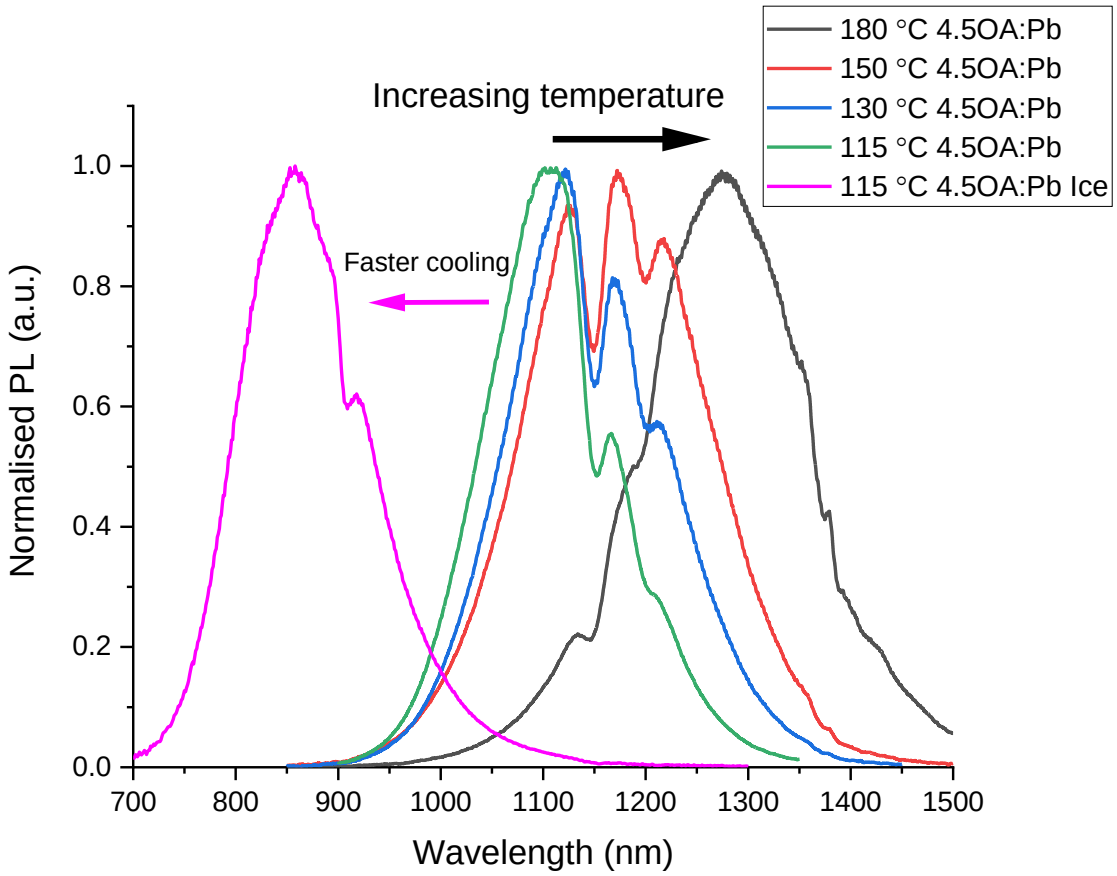

Figure 3-1 - PL emission spectra of PbS QDs in toluene synthesised at different injection temperatures and cooling profiles. The dips at 1150 and 1200 nm were a result of absorption from the toluene solvent.

As the reaction vessels were typically allowed to cool naturally in air after injection, increase of injection temperature had the additional effect of increasing overall reaction time. Nanocrystals nucleated at higher injection temperatures thus spent longer times within the reaction growth medium at elevated temperatures before purification. Increased nanocrystal size was because of combined lengthened reaction time and increased reactivity at higher temperature. The injection temperature did not uniquely determine the resulting QD bandgap, as demonstrated by alternative cooling profiles, shown in Figure 3-1. At fixed injection temperature, rapid cooling through use of an ice-water bath resulted in higher observed bandgaps corresponding to smaller QD sizes. It was speculated that lower injection temperatures combined with faster cooling would achieve even higher bandgaps than 1.7 eV, however this was not explored in this work.

Oleic acid concentration

The concentration of oleic acid within the precursor solution had considerable effect on the resulting nanocrystal size and bandgap, shown in Figure 3-2. Essentially, the OA:Pb ratio and ligand concentration determined the reactivity of the solubilised lead oleate species. Solubilisation of the PbO occurs through coordination by oleic acid ligands to form the ODE-soluble lead oleate complex.

In syntheses where insufficient ligand was present, namely at OA:Pb molar ratios less than 2:1, the lead precursor solution developed a cloudy off-white colour, indicating incomplete dissolution of the lead oxide. Increase in oleic acid concentration resulted in larger nanocrystals and smaller resulting bandgaps. The increased reactivity at higher ligand concentrations was explained by the greater solubility and thus availability of mobile Pb cationic species in solution during the nucleation and growth phases.[11,32,33] Greater mobility and availability of soluble Pb species resulted in more rapid attachment of monomer species leading to faster growth of nanocrystals.

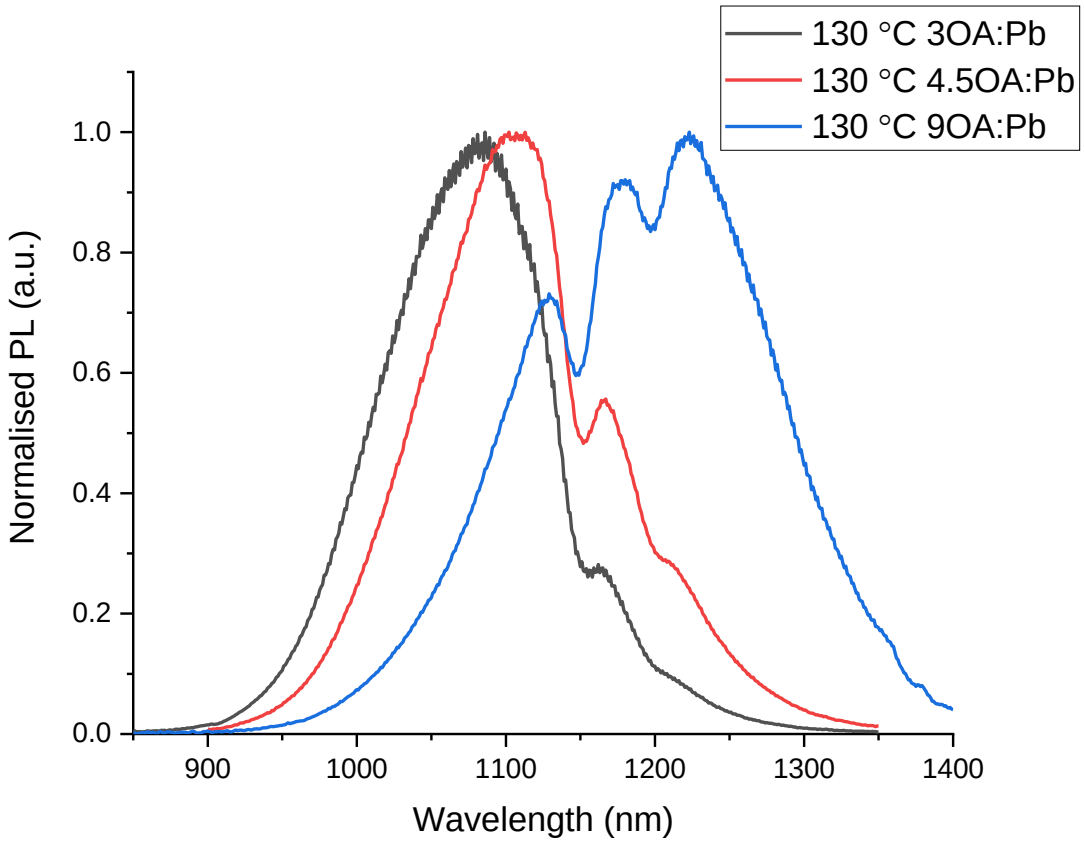

Figure 3-2 - PL emission of PbS QDs in toluene synthesised with different oleic acid ligand ratios. The dips at 1150 and 1200 nm were a result of absorption from the toluene solvent.

Controlled synthesis of a particular target QD bandgap could be achieved by different combinations of the main control parameters: oleic acid concentration and injection temperature. It was possible to achieve the same bandgap at high ligand concentration with low temperature, high injection temperature with low ligand concentration, or with intermediate conditions for both parameters. Generally for a given bandgap, larger emission bandwidths were observed at higher injection temperatures, indicating less desirable larger size distributions. This was attributed to several factors: the variation between injections was more apparent at higher injection temperatures, where greater sensitivity to finite injection speed and initial precursor mixing lengthened the period of the initial

nucleation burst. Higher temperatures also lengthened the period where the precursor concentrations were greater than the critical concentration. In addition, higher temperatures resulted in longer cooling times following injection, leading to lengthened total reaction time. Lengthened reaction times may have resulted in depletion of growth monomer within the reaction mixture. Depletion of growth monomer may have resulted in size defocusing effects within the nanocrystal population as a result of Ostwald ripening processes.[11,34,35] The greater reactivity of smaller nanocrystals resulted in their dissolution whilst larger nanocrystals experienced growth in conditions of low growth monomer concentration.

3.4 Characterisation

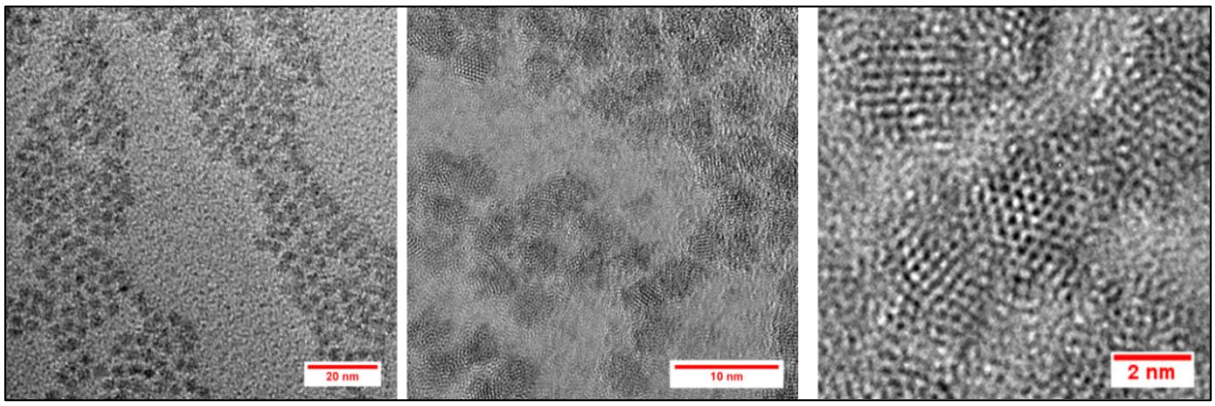

Figure 3-3 –TEM images of 1.2 eV PbS nanocrystals emitting at 1050 nm

Transmission electron microscopy (TEM) was used to verify nanocrystal size and shape with a direct measurement. As shown in Figure 3-3, TEM of PbS nanocrystals showed small crystalline objects with 3-4 nm size with individually faceted shapes. The contrast of nanocrystals with the supporting carbon film rendered quantitative measurement of size to be ambiguous and dependent on thresholding parameters for edge detection particle counting. The small sample observable in TEM was also a hindrance for overall size distribution assessment. The size distribution analysis of the PbS QDs shown in Figure 3-3 is shown in Figure 3-4, showing a mean size of 3.4 nm with a standard deviation of 0.3 nm. Measurement was performed manually by taking the mean of perpendicular dimensions for each visible particle. Optical measurements of bandgap and PL energy were used instead for relevant size assessment.

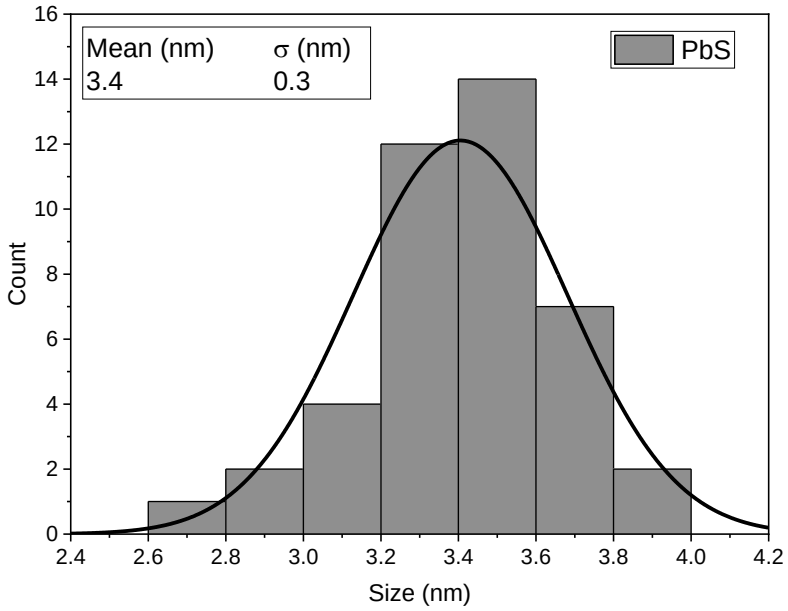

Figure 3-4 – TEM size distribution analysis of 1.2 eV PbS QDs emitting at 1050 nm shown in Figure 3-3. Sizes were measured by manually taking the mean length along perpendicular axes. The mean size was 3.4 nm with a standard deviation of 0.3 nm.

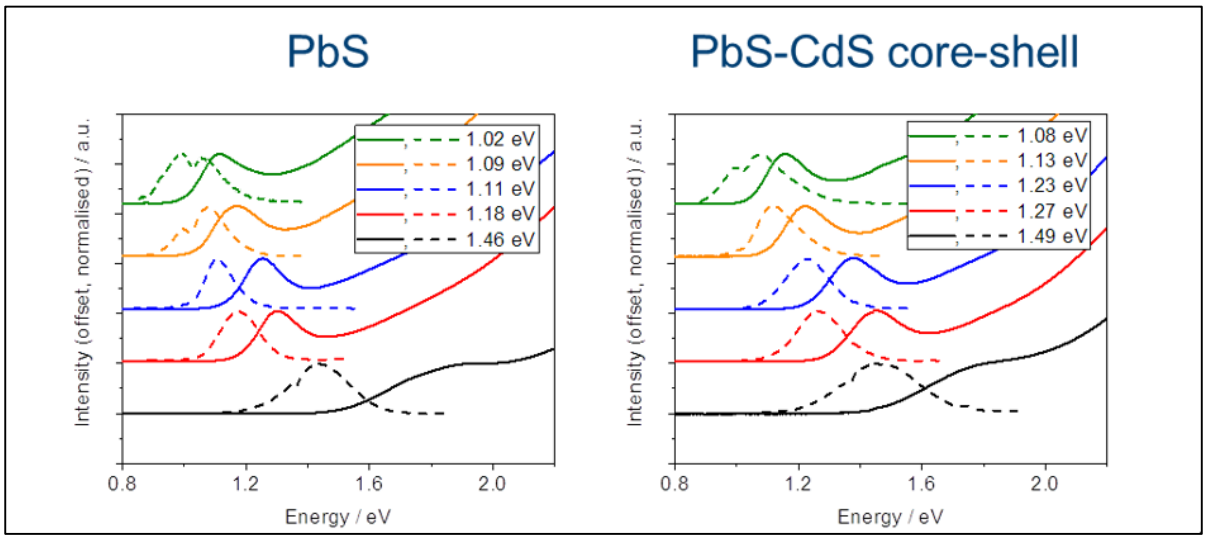

Figure 3-5 - UV-Vis-NIR absorption (solid) and PL (dashed) of PbS and PbS/CdS QDs of different sizes identified by emission energy in eV.

As-synthesised PbS QDs displayed varying photoluminescence peak position depending on size and bandgap defined as the first excitonic absorption peak as shown in Figure 3-5. The highest photoluminescence quantum efficiencies (PLQE) achieved were for nanocrystals emissive around 1.2 eV, corresponding to a bandgap at around 1.3 eV.[36] Larger and smaller bandgaps displayed lower PLQEs, as shown in Figure 3-6.

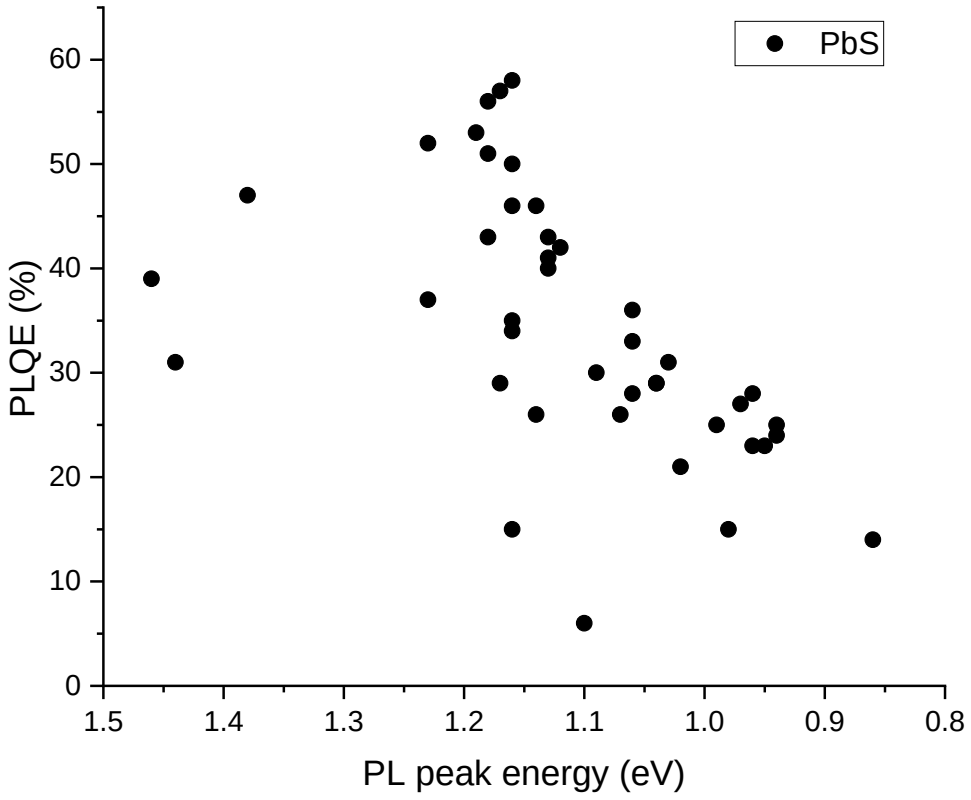

Figure 3-6 - Measured PLQE against PL peak emission of synthesised PbS QD batches, highlighting the strong bandgap and size-dependence of maximum achievable PLQE in PbS QD batches for this synthesis method.

Decreased PLQE with decreasing bandgap was explained by larger nanocrystal sizes lessening exciton confinement. Larger nanocrystals possessed larger surface area and greater probability of possessing a surface defect.[21,37] The probability of an individual nanocrystal possessing a trap state arising from a surface defect was thus greater for smaller bandgap nanocrystal populations. The ensemble effect was the decreased PLQE with increasing nanocrystal size. At the other end of the scale, smaller nanocrystals possessed larger curvature with more high-energy exposed facets leading to more dangling bonds resulting in higher defect density.[38] The increased defect density resulted in decreased PLQE despite possessing a smaller total surface area compared to larger QDs.

3.5 Cadmium cation exchange

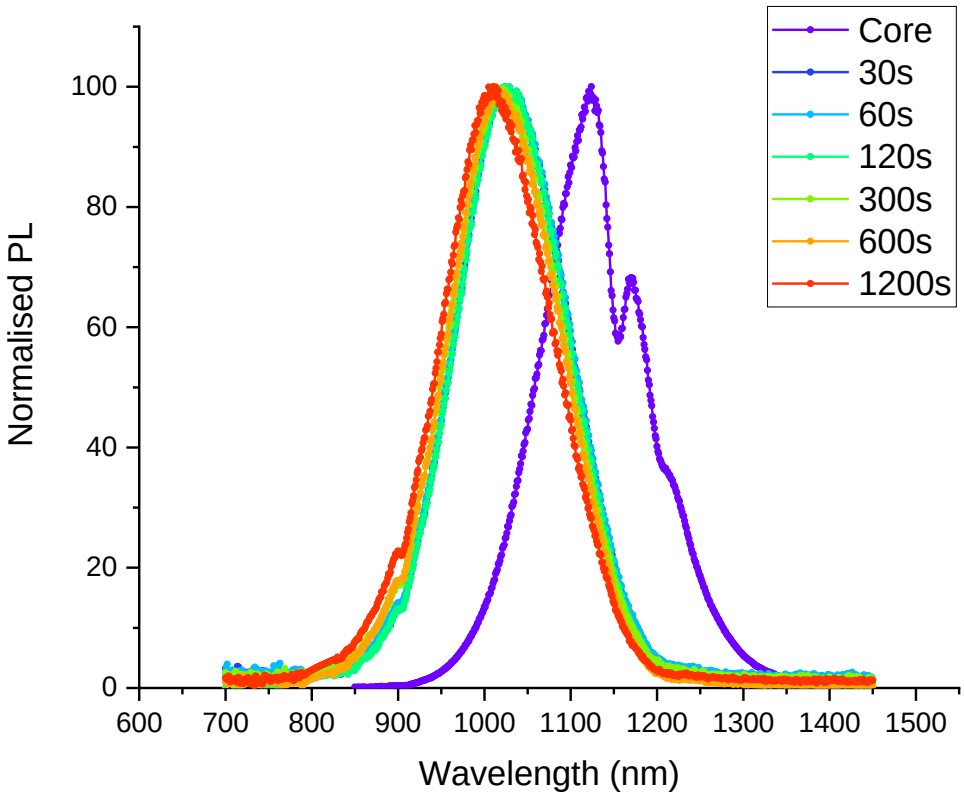

Figure 3-7 – Progression of photoluminescence from PbS and PbS/CdS with varying reaction time illustrating the blue shift. Dips in the PbS emission peak were caused by absorption by the toluene solvent. The PbS/CdS QDs were redispersed in octane and did not show the absorption features.

Cation exchange of PbS QDs to PbS/CdS core-shell QDs resulted in a blue-shift in absorption and photoluminescence, as illustrated in Figure 3-7. The blue-shift has been attributed to shrinking of the PbS core and the associated increased confinement resulting from a smaller quantum 'box'. The blue shift was apparent for all QD sizes after cation exchange and the magnitude was generally around 100 meV. A photoluminescence quantum efficiency increase was generally observed after cation exchange to PbS/CdS. This was explained as a result of greater passivation of the nanocrystal surface and reduction in surface trap states.[39] Exchange of Cd atoms in the place of Pb causes removal of un-passivated Pb surface dangling bonds which would create intra-band trap states. The higher bandgap CdS shell would also help confine the exciton wavefunction with a high conduction band energy offset. If present after cation exchange, states associated with un-passivated Cd surface dangling bonds would lie away from the band gap within the PbS conduction and valence bands. These states become relatively benign instead of a trapping route for non-radiative decay processes.

Ultrafast optical characterisation

Time-resolved spectroscopy was used to investigate the exciton dynamics in 1.2 eV PbS and cation-exchanged PbS/CdS nanocrystals to probe the mechanisms of photoluminescence enhancement. Time-correlated single photon counting (TCSPC) measured the photoluminescence lifetime of QDs. A TCSPC measurement consisted of excitation of a sample followed by time-resolved observation of photoluminescence through a single-photon avalanche diode. The histogram of accumulated photon detection events with corresponding delays allows interpretation of photoluminescence decay routes.

A transient absorption (TA) experiment consists of time-resolved absorption spectroscopy of ground and excited states of an optically excited sample. Briefly, the sample was initially excited with a narrow-band pump excitation followed by a broadband probe pulse at controlled time delay to obtain the resulting change in the absorption spectrum. The measured component is change in absorption between the unexcited and excited spectrum that allows observations of excited state transitions and bleaching of the ground state spectrum. Excited state absorptions are termed photo-induced absorptions (PIA) and decrease in absorption of the ground state spectrum are termed ground state bleaches (GSB).

Transient absorption and TCSPC in this chapter was both performed by Jesse Allardice.

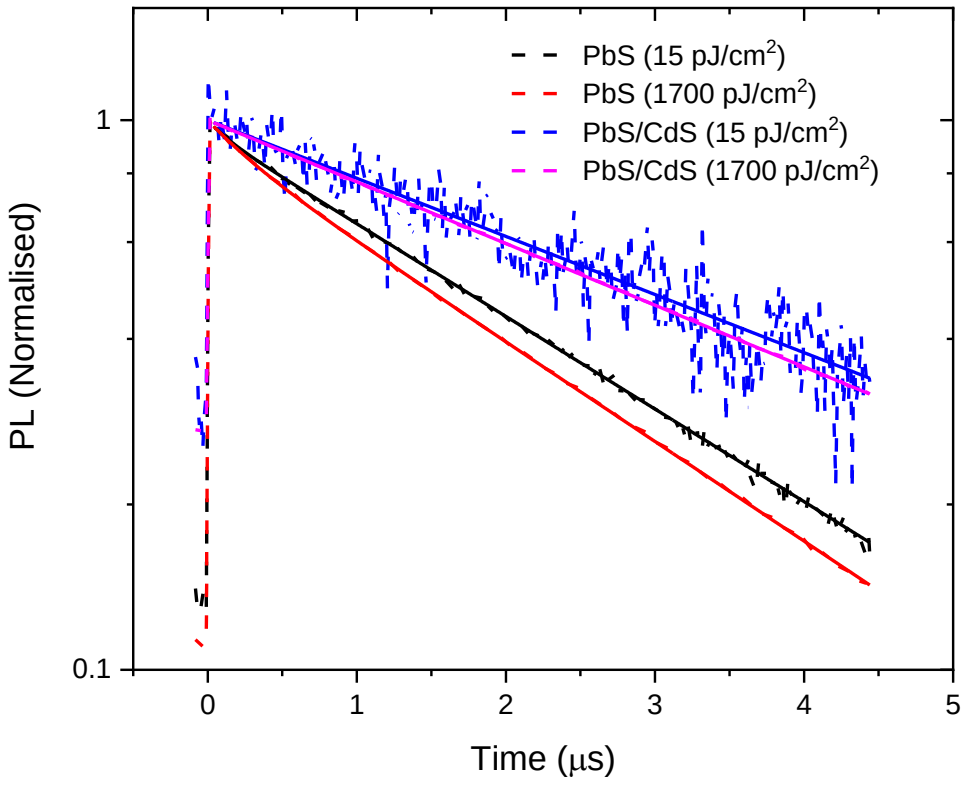

Figure 3-8 - IR TCSPC data for 1.2 eV PbS and cation-exchanged PbS/CdS solutions at 0.5 mg mL^{-1}. Excitation was provided with a pulsed white light laser with 2x Schott KG3 IR-blocking filters. The high baseline for PbS/CdS was because of incomplete PL decay before incidence of subsequent excitation pulses at the slowest laser repetition frequency (200 kHz). Laser energy quoted per pulse.

Infrared TCSPC measurements on PbS and PbS/CdS nanocrystal suspensions displayed longer photoluminescence lifetimes for core-shell QDs of 4.1 μs compared to the cores of 2.6 μs, shown in Figure 3-8 at low excitation fluence. Some power dependence in the decay slope was observed for both samples, but less for core-shell QDs. As photoluminescence lifetime is a combination of radiative and non-radiative decay, comparison with the measured photoluminescence quantum efficiencies (54% and 65% for PbS and PbS/CdS respectively) indicated that both the radiative and non-radiative lifetimes increased following cation exchange. The calculated radiative lifetime increased from 4.7 μs to 6.3 μs and the non-radiative lifetime increased from 5.8 μs to 11.7 μs for PbS and PbS/CdS respectively. The large increase in non-radiative lifetime relative to the non-radiative lifetime indicated the likely mechanism for photoluminescence increase was through better passivation of non-radiative decay routes and has been previously observed in PbS/CdS.[28] The observed lifetimes for all samples were longer than the slowest repetition rate of the pulsed excitation white light laser (200 kHz) which resulted the photoluminescence not fully decaying before incidence

of the next excitation, leading to substantial measured luminescence at the fiducial time datum. The observed high baseline was not caused by a normalisation artefact in noisy data following division by the largest value, as several samples demonstrated good signal, thus it was indicative of a long-lived emissive state.

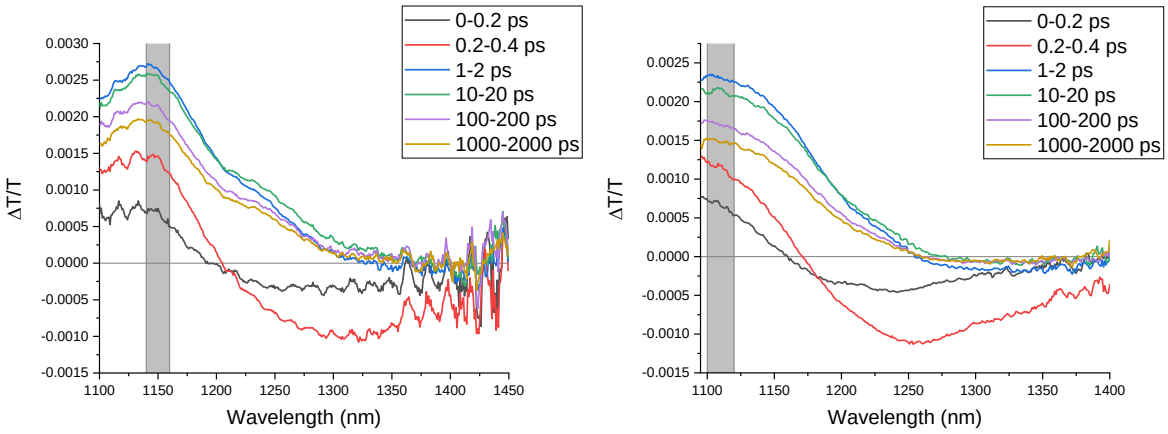

Figure 3-9 – Transient absorption spectra for films of 1.2 eV PbS (left) and PbS/CdS (right) after cation exchange. The excitation wavelength was 530 nm and the excitation density was 72 µJ/cm^2. The highlighted bar indicates the probed spectral region for the ground state bleach (GSB) kinetics plots in Figure 6.

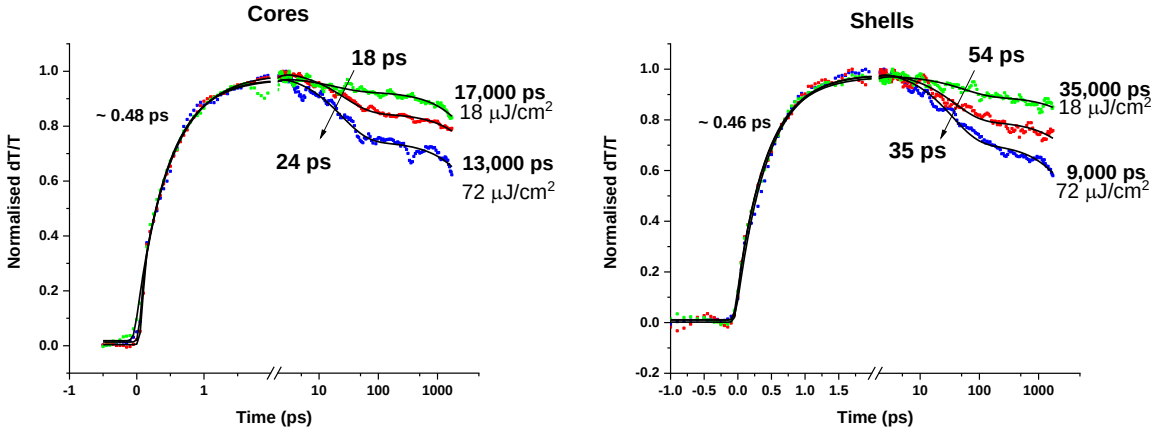

Figure 3-10 – Transient abosrption kinetics of 1.2 eV PbS and PbS/CdS ground state bleach (GSB) feature with different excitation fluences (18, 36, 72 µJ/cm^2) at 530 nm. The spectral region shown was at 1150 nm for PbS cores and 1110 nm for PbS/CdS core-shell QDs. Lifetimes shown for(in ps) rise slope, decrease slope on Auger timescale (10-100 ps) and slope at extended times.

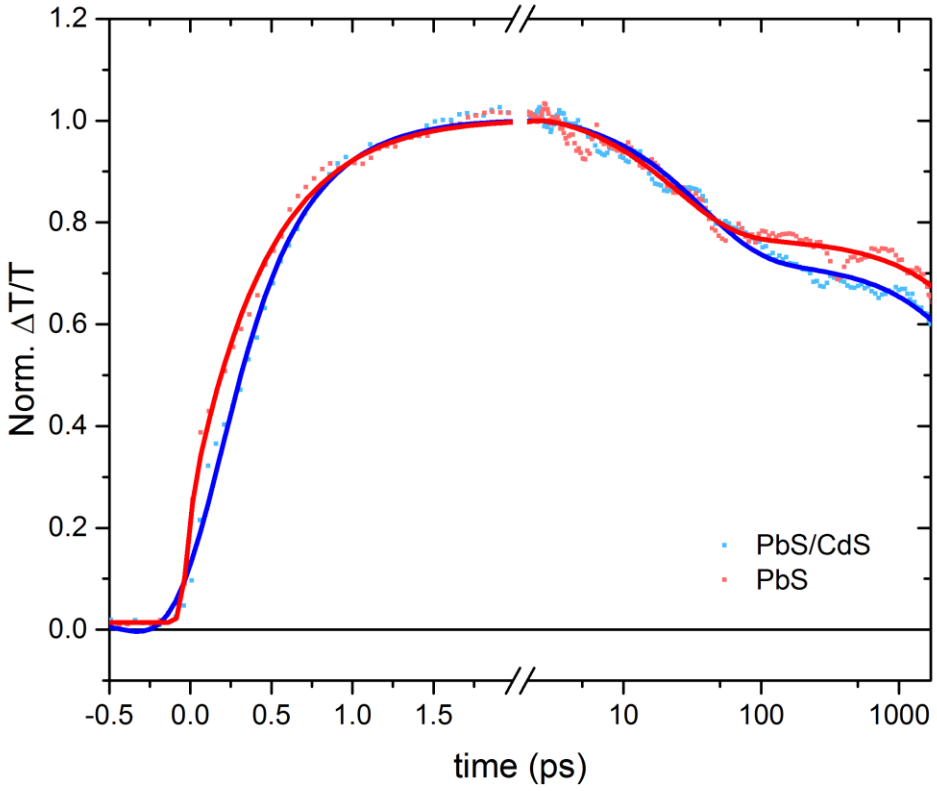

Figure 3-11 – Comparison of PbS and PbS/CdS transient absorption kinetics of the GSB signal at high excitation fluence.

Transient absorption spectra of films, shown in Figure 3-9, showed a ground state bleach feature around 1150 nm in 1.2 eV PbS and around 1110 nm in cation-exchanged PbS/CdS. Transient absorption kinetics of the ground-state bleach feature shown in Figure 3-10 displayed small differences between core and core-shell QDs. The ground state bleach arises due to increase in transmission caused by of depopulation of carriers at the valence band edge and the filling of states near the conduction band edge after the pump excitation. The slow rise time of approximately 0.5 ps for both samples was possibly because of the relaxation of hot carriers to the conduction band edge at excitation energies high above the bandgap.[40,41] Both PbS and PbS/CdS nanocrystals possessed similar kinetics, shown in Figure 3-11, on the Auger timescale of 10-100 ps at high excitation fluences. The long extended lifetimes (μs) for the band edge states in both PbS and PbS/CdS indicated relatively slow decay processes from the conduction band edge. The slow decay indicated that very fast, non-radiative decay processes to depopulate the excited carriers were limited. This was consistent with the general observation of good (non-zero) photoluminescence quantum efficiencies and relatively long photoluminescence lifetimes of both PbS and PbS/CdS.

Single nanocrystal blinking

To help explain the photoluminescence quantum efficiency differences between cation-exchanged PbS/CdS and core PbS nanocrystals, single particle blinking experiments were performed by Ashish Sharma at the University of Sydney, Australia. In short, a suspension of QDs was sequentially diluted to reduce concentration, spin coated into films then encapsulated to prevent atmospheric degradation. Time-resolved photoluminescence was measured with a microscope with excitation at 640 nm at high fluence. At low concentrations, single QDs may be observed as being in either the 'bright', emissive state or the 'dark', non-emissive state. Individual nanocrystals may switch between emission states as a time-variable property, termed blinking. Literature reports have suggested two primary mechanisms for blinking behaviour of QDs. Auger-recombination assisted blinking arises from charging of a nanocrystal through interaction of an exciton with an electron in a multiply-excited QD.[42–44] In a doubly-excited QD, each exciton may recombine radiatively. Trapping or ejection of an individual charge carrier, electron or hole, from the two pairs of carriers results in a remainder net charge. The charged exciton formed creates a fast non-radiative decay route competing with radiative decay. The charged state may return to the neutral state through de-trapping or ejection of a carrier of opposite charge. Events of the Auger-assisted blinking mechanism persist until a characteristic cut-off, up to dozens of milliseconds. Surface trap-assisted blinking arises from non-radiative recombination centres associated with surface states such as a crystal defect or unfilled atomic orbitals. The surface trap becomes activated by a preceding event such as desorption of a passivating ligand.[42,45] Events of the trap-assisted blinking mechanism may persist for much longer, up to several seconds and more. Both main types of blinking behaviour may be expressed together in a population of QDs.

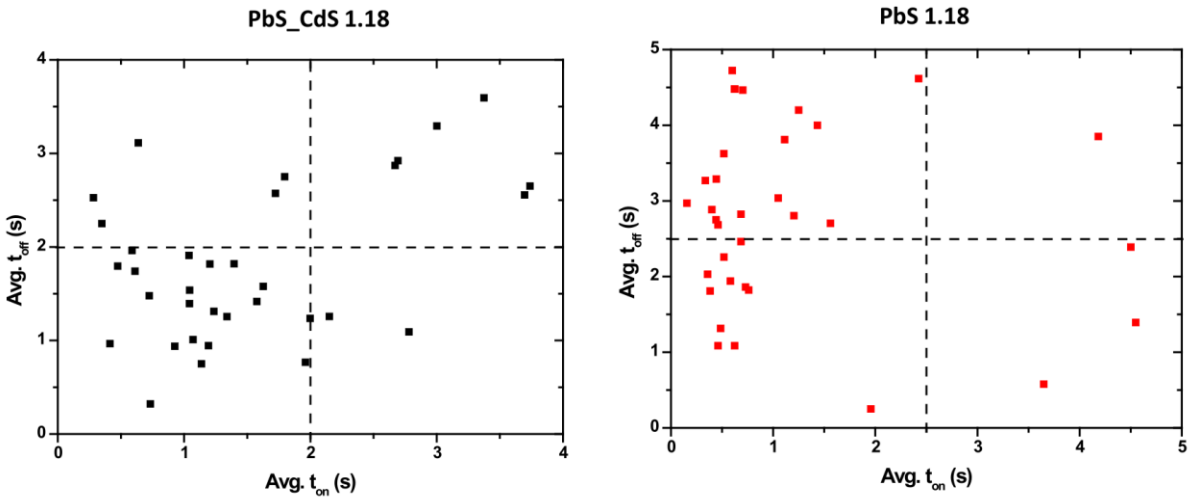

Figure 3-12 – Distribution of the average time duration spent in the off (non-emissive) against on (emissive) states for 40 individual PbS and PbS/CdS nanocrystals. The PL energy was 1.18 eV before (right) and 1.26 eV after (left) cation exchange. PbS generally spent longer in the off state regardless of time spent in the on state, in contrast to PbS/CdS, which displayed stronger correlation between on/off times.

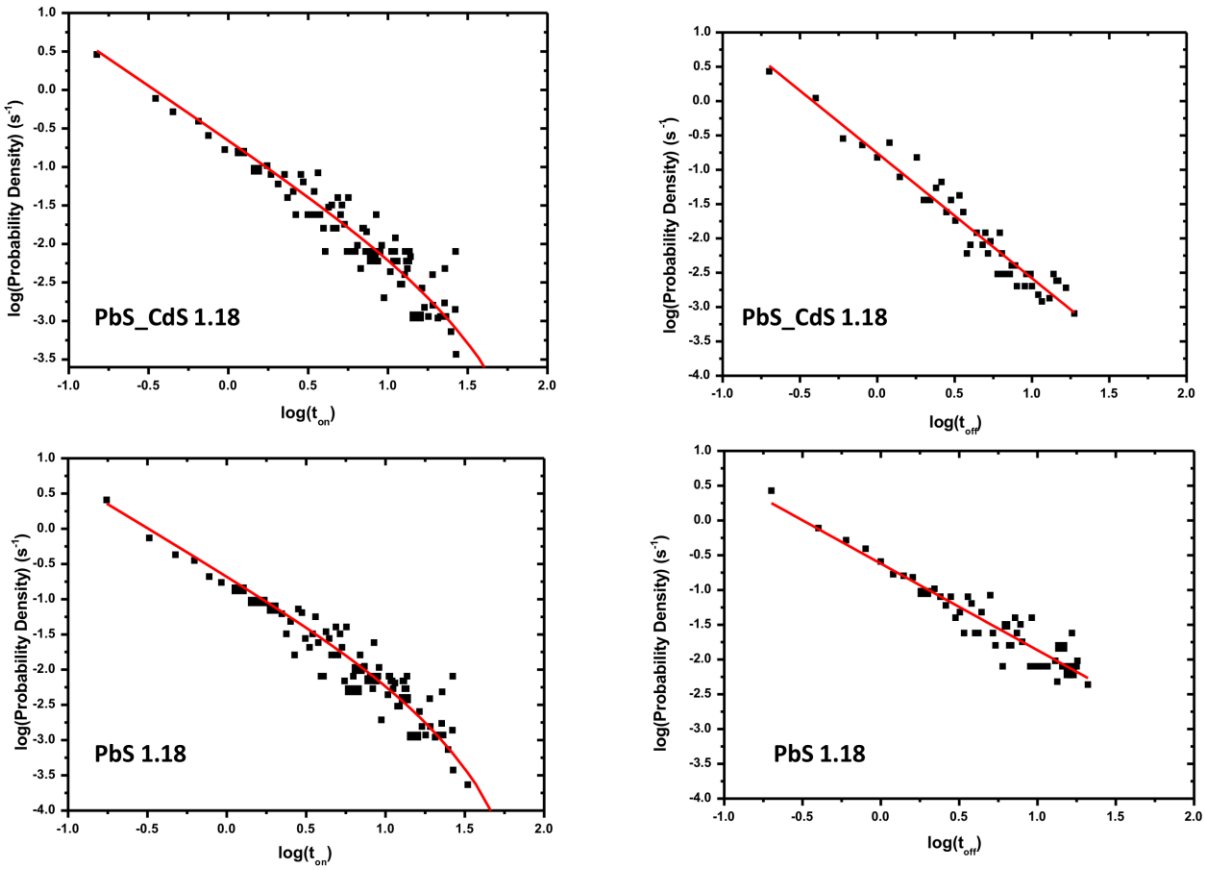

Figure 3-13 – Blinking statistics for on (left) and off (right) states for PbS (bottom) and PbS/CdS (top) nanocrystals of 1.18 eV and 1.26 eV emission energy respectively. The probability densities for the on state were fitted to an exponential with time cut-off giving a mostly linear trace with a curve after the cut-off time of 1.3 s. The probability densities for the off state were fitted to an exponential without cut-off resulting in a linear trace. The exponential factors (α) were α_{on}=-1.41 and α_{off}=-1.82 for PbS/CdS and α_{on}=-1.35 and α_{off}=-1.25, which corresponds to literature values of 1<α<2.[42,44–46]

From blinking experiments, both PbS and PbS/CdS showed binary blinking with an emissive on state and a non-emissive off state. Core-shell PbS/CdS displayed greater correlation between average on and off time durations unlike the PbS cores, shown in Figure 3-12. PbS cores displayed long off time durations when compared to their on time durations. The long uncorrelated off times displayed by PbS indicated dependence of its blinking behaviour to random dynamic surface events such as ligand adsorption and desorption. An explanation for the unexpected correlation of on and off state time durations for PbS/CdS was the passivation of surface trap states through cation exchange. The suppression of surface trap states reduced the prevalence of the transient trap-assisted non-radiative recombination pathway, resulting in a decrease of surface-trap assisted blinking. The observed decrease in trap-assisted blinking did not necessarily eliminate non-radiative recombination processes. The probability density distributions for on and off state in PbS and PbS/CdS QDs, shown in Figure 3-13, followed power-law distributions with similar exponential factors to reported literature values, indicating that Auger-assisted blinking was observed in both populations.[42,44–46] The time durations for

each state were similar for PbS and PbS/CdS, further indicating Auger-assisted blinking pathway was largely unaffected by cation exchange.

As observed in transient absorption measurements, the excited state kinetics on the characteristic Auger timescale of 10-100 ps were similar for PbS and PbS/CdS at high excitation densities. Supporting this observation, the Auger-assisted blinking pathway was not suppressed following cation exchange, being observed in both PbS and PbS/CdS. The observed increase in photoluminescence quantum efficiency was thus unlikely to be a result of differences in Auger processes between PbS and PbS/CdS. Near-infrared TCSPC also showed a longer photoluminescence lifetime for PbS/CdS than PbS, indicating with significantly lengthened non-radiative lifetime associated with surface trap passivation. The observed change in blinking characteristics following cation exchange to a duration correlated on-off behaviour suggested that surface trap-assisted blinking was reduced. The reduction this blinking mechanism possibly contributed to the observed increased PLQEs in PbS/CdS. However, fluorescence measurements such as TCSPC and blinking do not provide information on any permanently non-emissive sub-population of QDs, which contribute to decreasing observed PLQE.

Small-angle X-ray scattering

To associate the observed photophysical effects to physical changes, structural characterisation was required. Small-angle X-ray scattering (SAXS) measurements were performed by Andrew Pearson and Andrew Parnell at the University of Sheffield to characterise structural changes in nanocrystals upon cation exchange. SAXS is an X-ray scattering method where a sample is illuminated with a monochromatic, collimated beam of X-rays, and scattered at small angles to strike a planar detector behind the sample. The technique operates at smaller angles than X-ray diffraction (XRD) techniques and is able to probe larger length scales of non-crystalline materials. The resulting scattering curve can be fitted with models to provide a physical interpretation. Unlike grazing-incidence SAXS (GISAXS), the standard SAXS geometry is not a surface sensitive measurement for colloids.

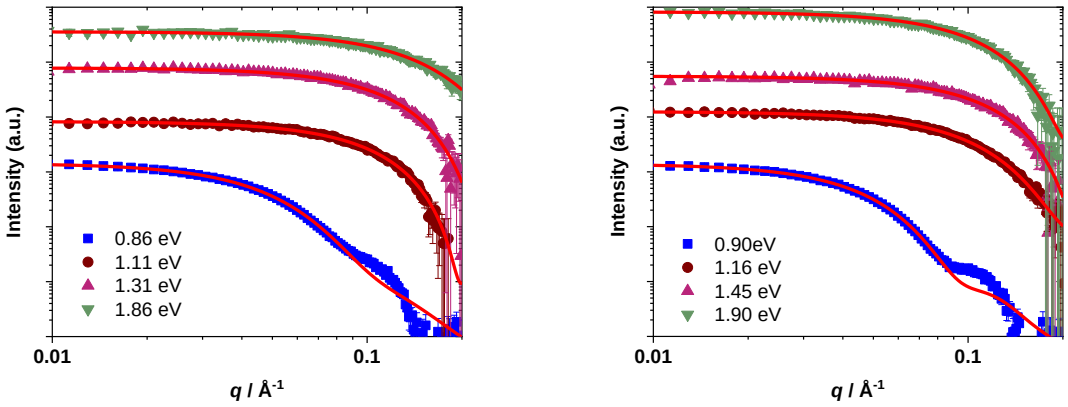

Figure 3-14 – Measured SAXS data for PbS (left) and corresponding PbS/CdS (right) offset for clarity. The indicated band gaps were derived from the photoluminescence peak energy using an empirically-derived linear fit from Zhao *et. al.*[47] The red lines indicate fitted curves according to a simple hard sphere model. The discrepancy between fitted model and data for the low bandgap sample was because of the large nanocrystal size distribution.

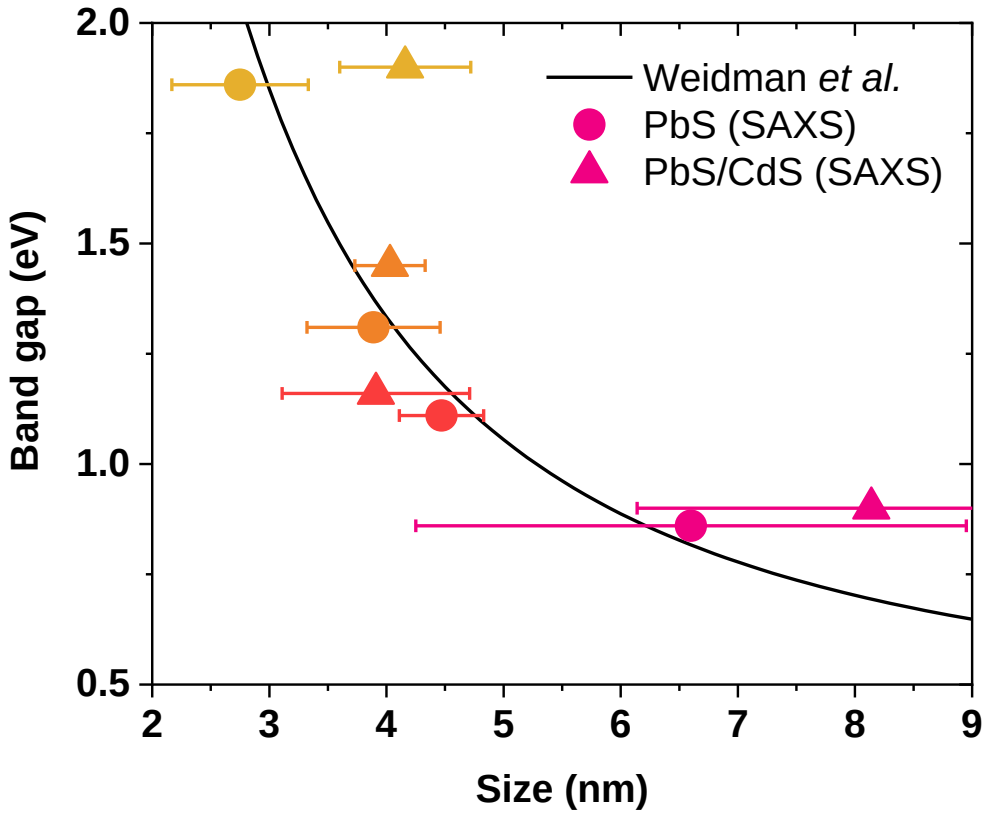

Figure 3-15 – Modelled SAXS nanocrystal sizes for PbS and corresponding PbS/CdS compared to band gap. The nanocrystal band gap was obtained from the photoluminescence energy through an empirically-derived linear fit from Zhao *et. al.*[47] The black curve represents the empirically-derived sizing curve

obtained in part with SAXS by Weidman *et. al.*[48] The error bars were obtained from modelled size distributions based on the photoluminescence bandwidths.

The data, shown in Figure 3-14, were fitted to a spherical model despite the faceted shape of individual nanocrystals for reasons of simplicity as well as population averaging to be a roughly spherical shape. The resulting sizes obtained through SAXS, shown in Figure 3-15, of PbS nanocrystals were in good agreement with the empirically-derived sizing curve obtained by Weidman *et. al.* which in part utilised SAXS.[48] For cation-exchanged PbS/CdS core-shell nanocrystals, general agreement was obtained for the corresponding cores and the sizing curve except for the largest bandgap i.e. the smallest nanocrystals. Generally, bandgaps, nanocrystal size did not appear to change significantly after cation exchange. The sizes obtained by SAXS for the largest bandgap nanocrystals indicated significant growth in nanocrystal size following cation exchange, with increases of over 1 nm indicated for approximately 3 nm sized nanocrystals, shown in Figure 3-15. Cation exchange to form PbS/CdS has been widely perceived as exchange of lattice atoms inwards from the outer nanocrystal surface, thus the suggested significant increase in overall nanocrystal size was unexpected and likely spurious.[24,25] The discrepancy was explained as a result of the spherical model fitting parameters poorly describing the nanocrystals after cation exchange. The large surface area to volume ratio of small nanocrystals resulted in a greater exchanged fraction of material. The greater relative proportion of the nanocrystal composition with a smaller scattering length density distorted the resulting fitted size.[49] Additionally for small nanocrystals, shape deviation from population-averaged spherical assemblies towards shape-anisotropic faceted polygonal species could have contributed in skewing the fitted size.[11]

Cation exchange – Effect of bandgap

Photoluminescence increase was determined to have resulted from increased passivation of PbS nanocrystal surfaces after Cd cation exchange. To better understand the kinetics of the cation exchange reaction, a size-series with reaction time dependence was performed for cation exchange on PbS nanocrystals.

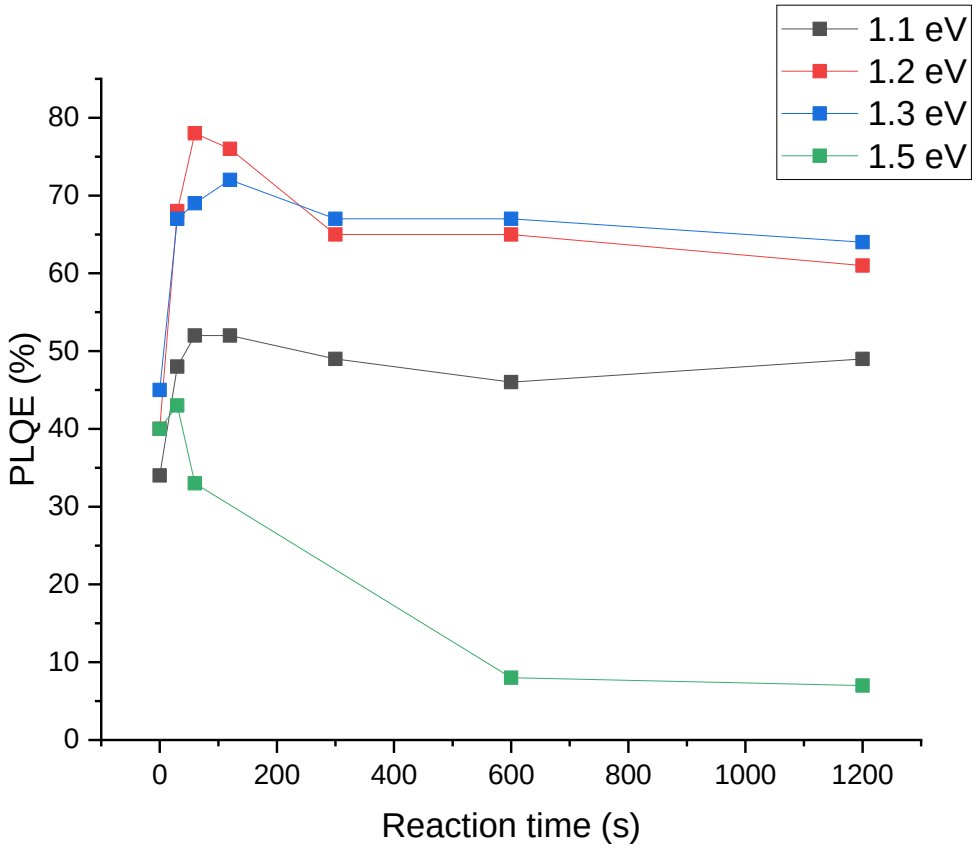

Figure 3-16 – Photoluminescence quantum efficiency (PLQE) of PbS and PbS/CdS with varying cation exchange reaction time at different initial sizes indicated by peak PL energy.

The magnitude of the PLQE increase after cation exchange was dependent on original bandgap, with a smaller change observed for smaller bandgap nanocrystals, as shown in Figure 3-16. In the case of small, high-bandgap QDs, an initial small increase in PLQE was observed followed by a severe decrease upon lengthened cation exchange reaction times, going well below the luminescence efficiency of the PbS cores before treatment. This behaviour was not observed for lower-bandgap QDs, where luminescence improvement was largely maintained. Maximum luminescence efficiency increase was observed at short reaction times for all QD sizes investigated. A slight decrease from the peak PLQE was generally observed with reaction times exceeding 1-2 minutes up to 20 minutes.

ICP-MS - Elemental compositions with reaction time resolution

The explanations presented in previous works of crystal phase transformations within the CdS shell were insufficient to understand the observed time dependence of cation exchange and its effect on photoluminescence efficiency.[29] Compared to previous work focussing on slow thermodynamic lattice rearrangement processes, the timescales explored here were far shorter and indicated the presence of much faster kinetic processes. For better characterisation of nanocrystal composition, inductively-

coupled-plasma mass spectrometry (ICP-MS) was performed to obtain elemental components for different nanocrystal sizes and cation exchange times.

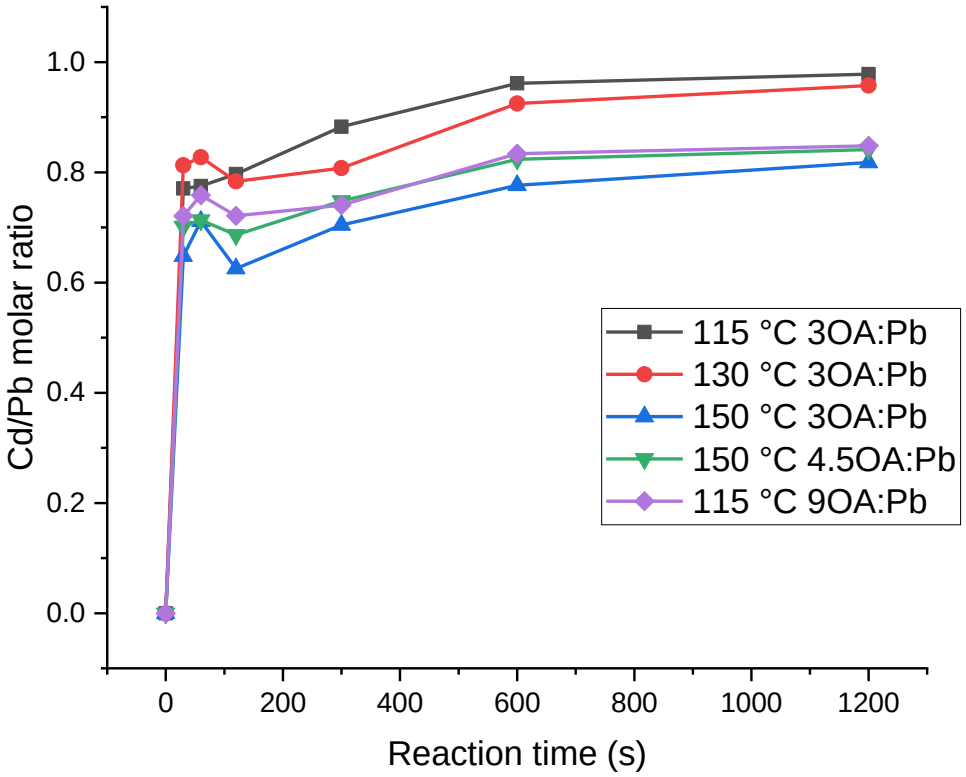

Figure 3-17 – Cd/Pb molar ratios of PbS and PbS/CdS samples at different synthesis conditions and reaction times obtained via ICP-MS.

The relative ratios of cation-anion and Cd:Pb provide a measurement of the extent of exchange and can track reaction progression. For one-to-one exchange to occur, the total cation-to-anion ratio should remain constant as the cation exchange reaction progresses. In the absence of additional anion precursors, further growth of nanocrystal size is unlikely.

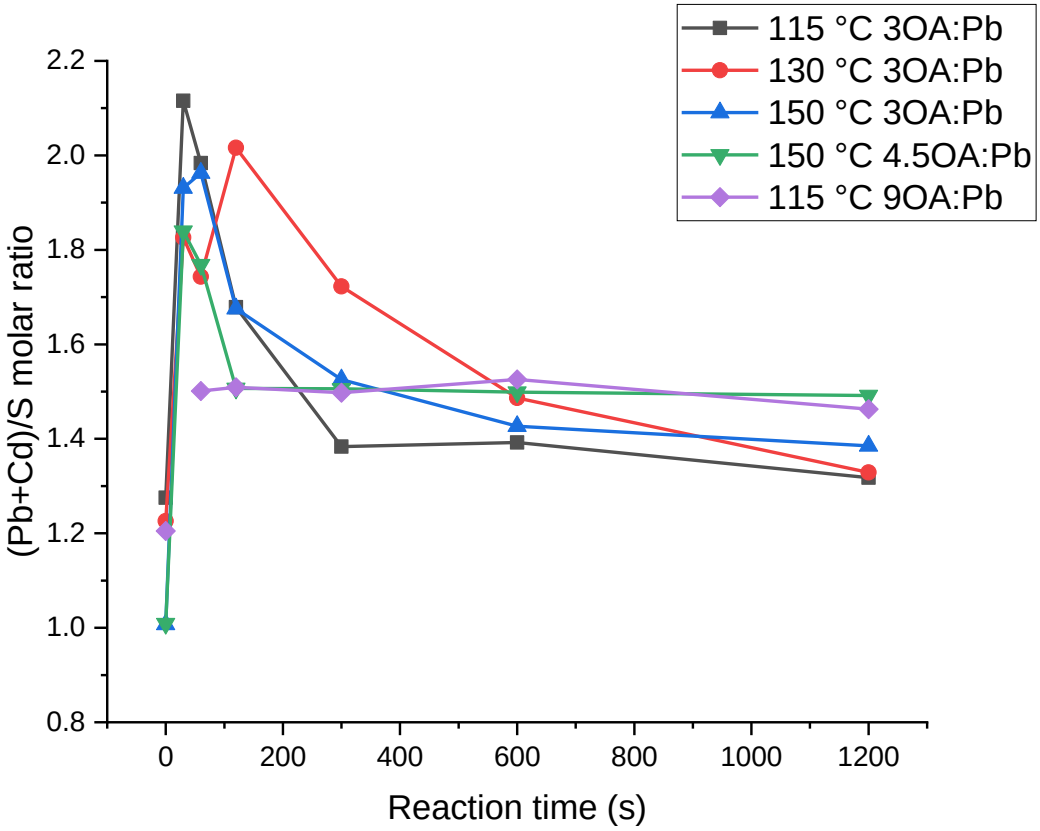

Figure 3-18 – (Pb+Cd)/S (total cation/anion) molar ratios of PbS and PbS/CdS samples at different synthesis conditions and reaction times obtained via ICP-MS.

For all nanocrystal sizes, the Cd/Pb ratio increased from zero rapidly after addition of the cadmium oleate precursor, as observed in the first time aliquot, shown in Figure 3-17. At extended reaction times, the ratio increased more slowly compared to the initial jump after addition. The Cd/Pb ratio increased with increased reaction time, consistent with gradual exchange of Pb with Cd cations. However, the cation/anion ratios (shown in Figure 3-18) did not remain constant, which was expected for 1:1 cation exchange. Upon addition of cadmium oleate, the total cation fraction (Cd+Pb) increased greatly, reaching a maximum after 1-2 minutes reaction time. The ratio decreased slowly after 2 minutes with extended reaction time up to 20 minutes. The nanocrystals at the final time point had a higher cation content compared to before addition of Pb. A spurious sample has been removed for clarity where no Pb or Cd was detected in the sample.

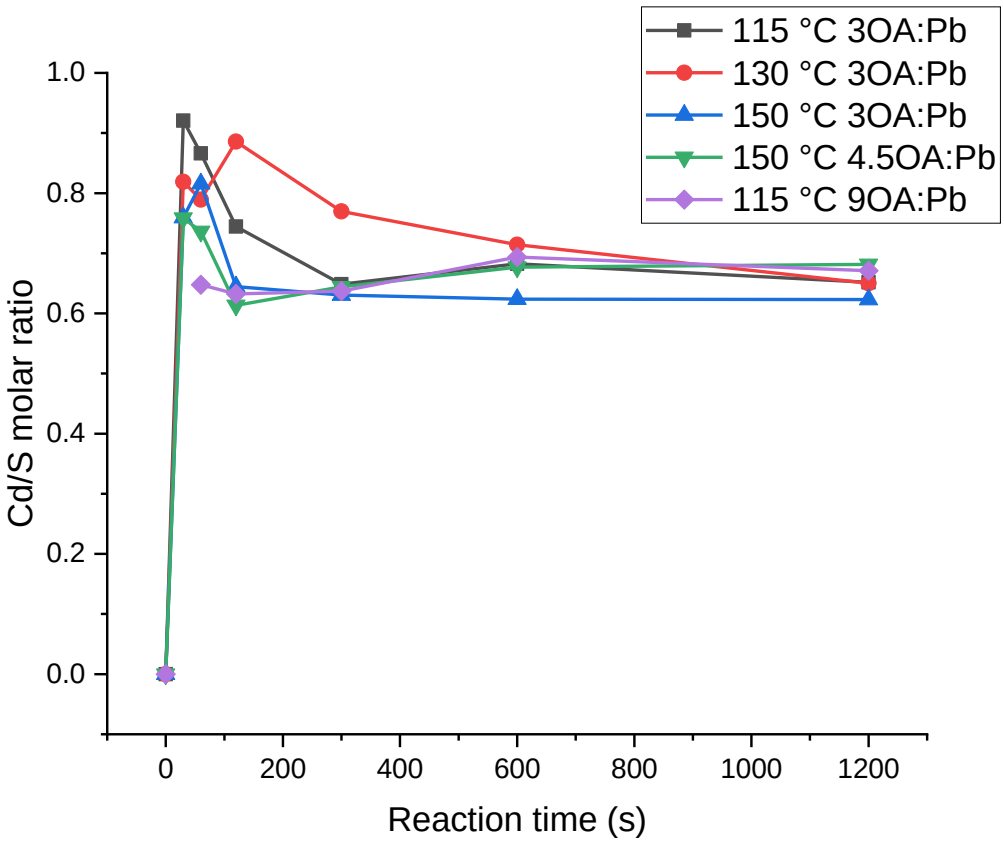

Figure 3-19 - Cd/S molar ratios of PbS and PbS/CdS samples at different synthesis conditions and reaction times obtained via ICP-MS.

Whilst the Cd/S ratio increased significantly after precursor addition, the Pb/S ratio did not decline rapidly, as shown in Figure 3-19 and Figure 3-20. The Pb/S ratio decreased slowly at first up to 2 minutes reaction time, after which it decreased more appreciably with extended reaction time. Given the absence of additional anions introduced, an assumption was made that the total S content remained constant. From the ratios, a negligible decrease in Pb content was observed initially following Cd addition, and only a minority fraction (20-30%) of the Pb had been exchanged and removed from the nanocrystals across all samples by the final time point. However, the overall Cd content greatly increased, from initially a significant fraction of cations (40%) to comparable in molar terms with the Pb content by the final time point (50%), despite the decrease in Cd/S ratio as the reaction progresses. The progression of ion ratios measured with ICP-MS provided insight on the cation exchange reaction kinetics. The reaction was observed to proceed in two phases: initial rapid adsorption of Cd species onto nanocrystal surfaces, evidenced by the initial high Cd content and negligible decrease in Pb content, followed by slower ion exchange of lattice Pb with Cd cations, evidenced by gradual increase in Cd with concomitant decrease in Pb content, along with decrease in overall cation-anion ratio. Previous studies primarily focused on slower processes at extended reaction

times after the penultimate time point shown here. The rapid adsorption processes observed here at early time points have not been shown in other works.

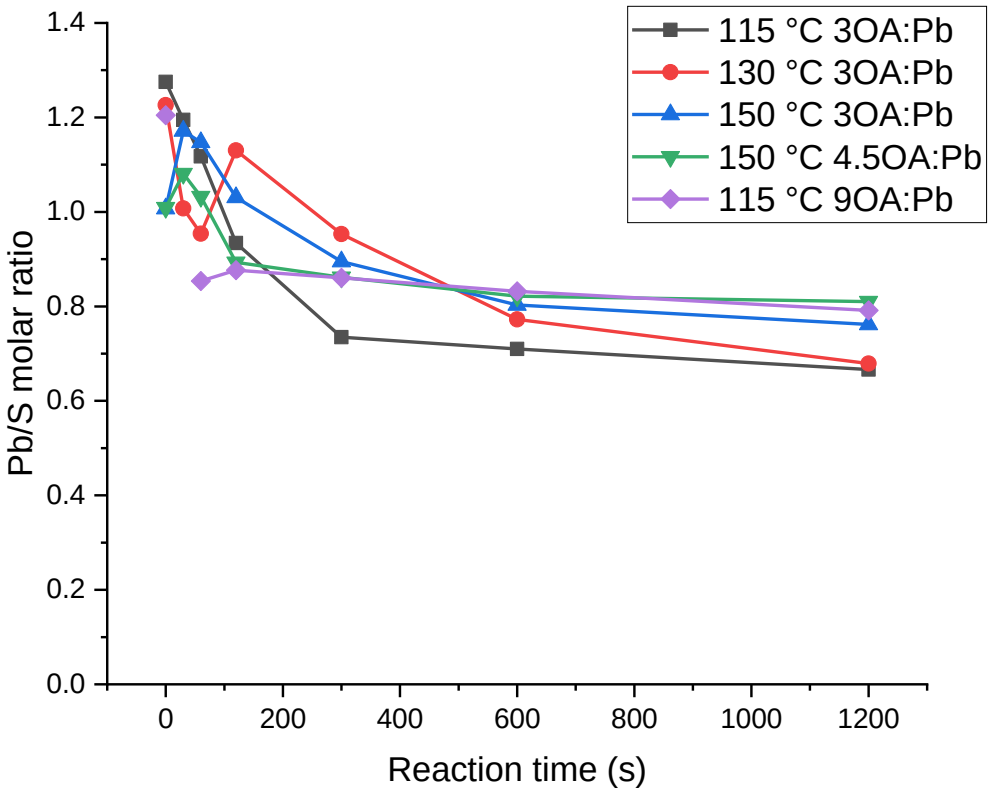

Figure 3-20 - Pb/S molar ratios of PbS and PbS/CdS samples at different synthesis conditions and reaction times obtained via ICP-MS.

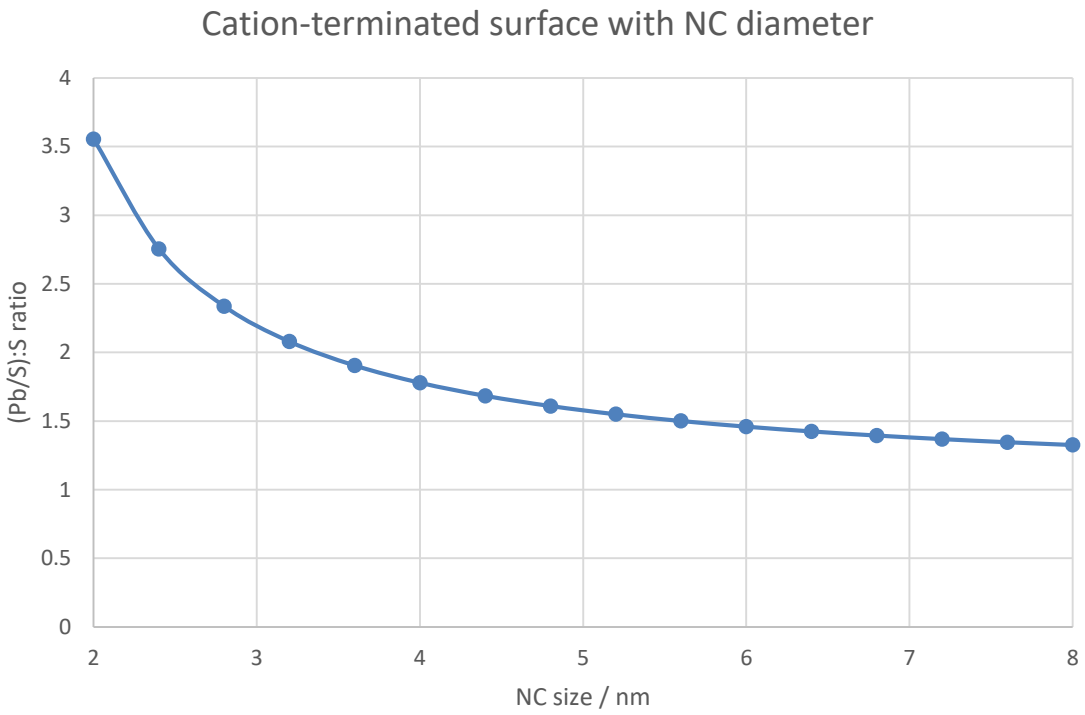

Figure 3-21 – Simple model of size-dependent PbS nanocrystal cation (Pb or Cd) to anion ratios if all surface atoms were cation-terminated. The model was constructed using spherical particles of different radius with the physical properties of PbS: rocksalt structure, lattice parameters and density. The total number of unit cells was calculated from the volume along with the fraction of surface unit cells for each size with the assumption of the (100)-face for simplicity. The surface/bulk atomic ratio was calculated with surface unit cells were Pb-terminated and had the full Pb component but only half the S component according to the rocksalt structure. The excess of Pb to S for the whole nanocrystal was then calculated as a ratio to indicate the cation-anion ratio of nanocrystals of given size if completely cation terminated. The simplistic model does not account for complex factors such as expression of other facets or non-spherical shapes.

Fig 3-21 shows a structural model to help explain the increase in cation-anion ratio at short time points. From a simple structural model of PbS spheres, it can be shown that the large proportion of surface atoms can make a large difference to overall nanocrystal composition. Given that the PbS nanocrystals prior to Cd addition were all Pb-rich, this suggested that surface expression of Pb was preferred to S. This is reasonable given the use of oleic acid ligands and Pb-oleate complexes in the synthesis, allowing for surface binding of native oleic acid ligands. It also shows that there are plenty of sites for adsorption of Cd cations, as the initial ratios are far below the modelled complete-cation coverage ratios, indicating that there are S-terminated surfaces present. Thus the rapid increase of Cd content following addition could be explained by adsorption to S-terminated surfaces, as the overall cation-anion ratios approach the modelled ratios for complete surface coverage in the 2.5-3.5 nm size regime.

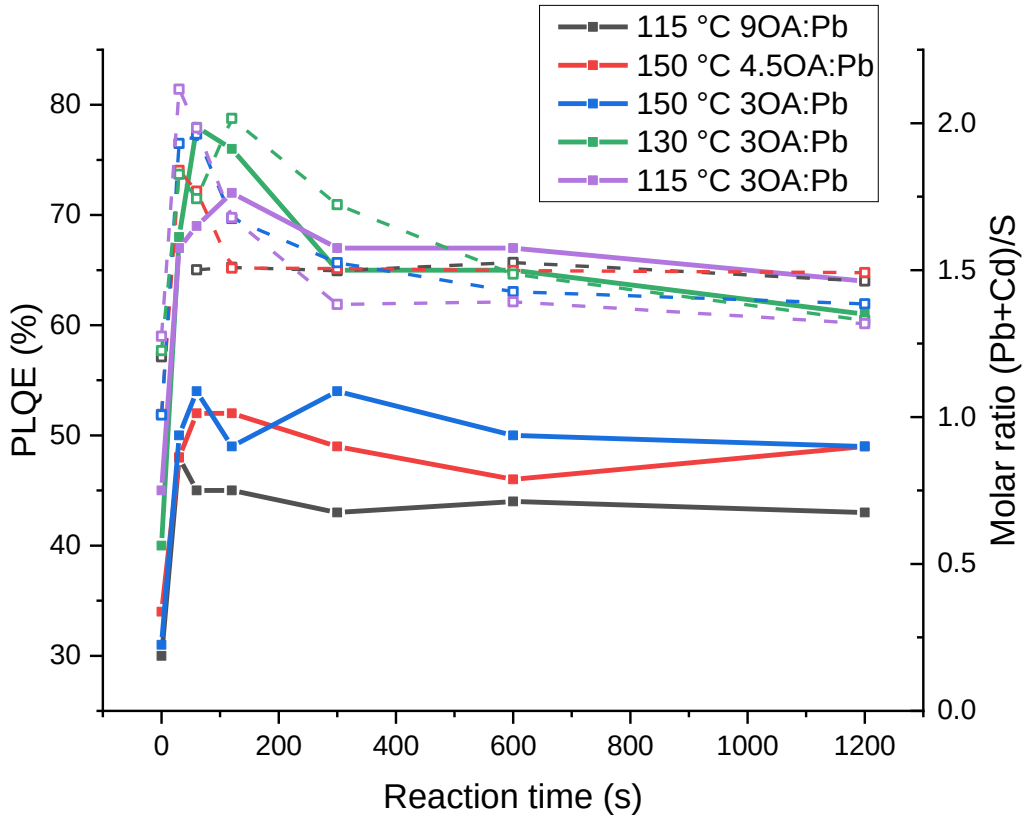

Figure 3-22 – Combined plot of PLQE (solid) and total cation/anion ratios (dashed) obtained via ICP-MS of PbS and PbS/CdS at different synthesis conditions and reaction times.

The rapid adsorption of Cd cation species was associated with increased PLQE for all PbS bandgaps investigated, shown in Figure 3-16 and Figure 3-22. The maximum luminescence efficiency for each PbS size was attained at short reaction times associated with Cd adsorption. The progression of QD PLQE generally followed the trend for total cation fraction (Cd+Pb), with the maximum PLQE associated with the highest cation ratio. A slow decrease in PLQE was associated with the decrease in total cation ratio at longer reaction times, associated with the exchange of Pb with Cd. The observed luminescence behaviour was explained by the passivation of surface sites by rapid initial adsorption of Cd cation species, eliminating traps and increasing photoluminescence efficiency. At longer reaction times, exchange of lattice cations progressed, introducing lattice defect sites, increasing trap states and decreasing luminescence efficiency. The schematic Figure 3-23 illustrates the proposed mechanism explained here.

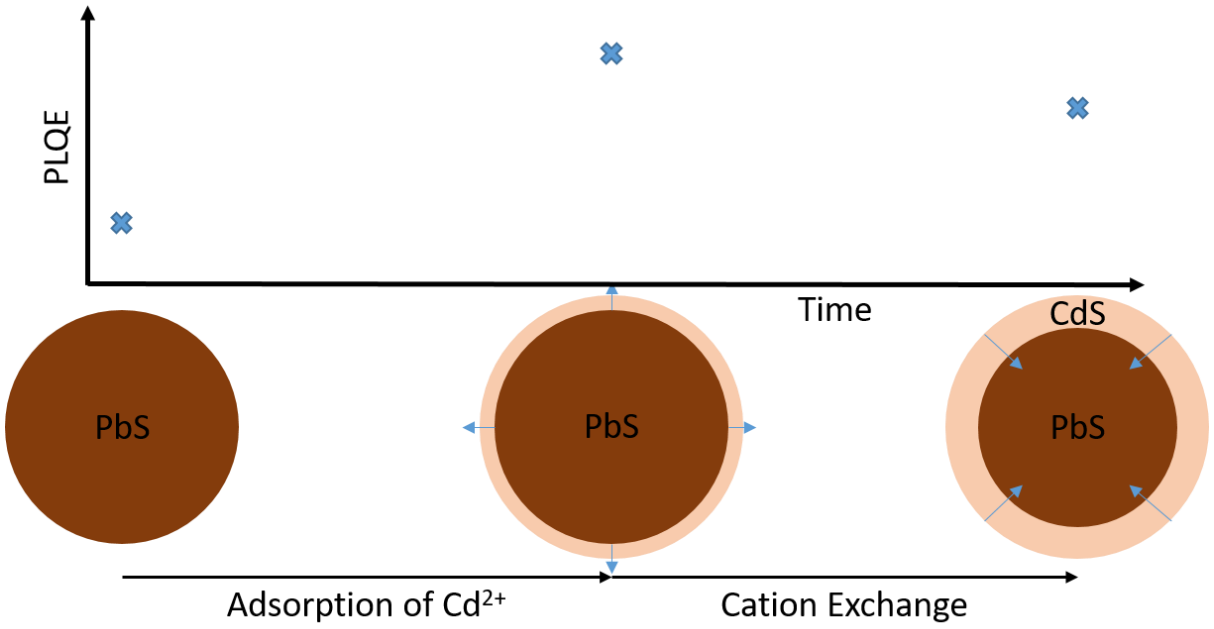

Figure 3-23 – Cartoon of proposed cation exchange process, showing initial fast adsorption of Cd onto the surface with negligible removal of Pb and large improvement in PLQE, followed by slower exchange of Pb by Cd with corresponding shrinking of PbS core, along with slight gradual decrease in PLQE.

For most nanocrystal sizes, the defect trap states introduced from cation exchange was of lower density than the surface sites passivated by initial Cd adsorption, thus the improvement in luminescence efficiency over PbS was largely maintained. The high bandgap, small PbS nanocrystals displayed an initial increase in PLQE following Cd addition at timescales consistent with Cd adsorption, which was unobservable at normal lengthened reaction times. The subsequent drastic drop in PLQE was evident at timeframes associated with cation exchange. The large surface area-volume ratio in the small nanocrystals likely resulted in their disproportionate susceptibility to core-shell interface defect states introduced upon cation exchange. In addition, the higher surface energy of smaller nanocrystals potentially resulted in greater surface reactivity with cation exchange occurring more rapidly compared to other sizes.

3.6 Working Conclusions

Nanocrystal quantum dots are intricately subject to a range of structure-property relationships. The photoluminescence quantum efficiency is particularly sensitive and can be affected by modification of the surface chemistry. Colloidal PbS QDs have previously shown improved photoluminescence efficiencies following Cd cation exchange. In this work, a mechanism for the improved photoluminescence following cation exchange was identified through time-resolved spectroscopic experiments. The cation exchange process resulted an increased photoluminescence lifetime. By combining this result with accurate measurements of the increased photoluminescence quantum

efficiency, it was shown that both the radiative and non-radiative lifetimes were increased following cation exchange. However, the non-radiative lifetime increased to a greater extent than the radiative lifetime, indicating that the increased PLQEs were a result of superior passivation of non-radiative trap states. To identify the nature of these non-radiative trap states, single particle blinking experiments showed suppression of the surface-trap assisted photoluminescence blinking mechanism whilst the Auger-assisted blinking mechanism was not affected following cation exchange. These results clearly showed that elimination of transient surface trap non-radiative pathways by the cation exchange process were the cause for improved photoluminescence efficiencies. Building on this understanding, high PbS QD luminescence efficiencies, comparable to the best reliable literature reports, have been attained through better understanding the mechanism of cation exchange and optimisation of reaction parameters.[13] Unlike previous work where fast reaction kinetics was not identified, cation exchange has been indicated to occur in multiple phases through PLQE and time-resolved elemental composition analysis ICP-MS. A rapid ion adsorption process is gradually followed by slower ion exchange. Limiting the cation exchange process to the rapid adsorption phase, through solvent reaction quenching, has been shown to maximise the luminescence efficiencies of the resulting product. Although cation exchange has long been shown to improve luminescence efficiencies of PbS QDs, striking the delicate balance between the benefits of increased surface passivation and the detriments of introduced additional interfacial defects is crucial in maximising luminescence.[24,25,27,29] Further work utilising these highly luminescent QDs for near-infrared emitter applications is ongoing.

3.7 References

1. Franke, D., Harris, D. K., Chen, O., Bruns, O. T., Carr, J. A., Wilson, M. W. B. *et al. Nature Communications* **7**, 1–9 (2016).

2. Aharoni, A., Mokari, T., Popov, I. & Banin, U. *Journal of the American Chemical Society* 257–264 (2006).

3. Supran, G. J., Song, K. W., Hwang, G. W., Correa, R. E., Scherer, J., Dauler, E. A. *et al. Advanced Materials* **27**, 1437–1442 (2015).

4. Al-Khuzheyri, R., Dada, A. C., Huwer, J., Santana, T. S., Skiba-Szymanska, J., Felle, M. *et al. Applied Physics Letters* **109**, (2016).

5. Davis, N. J. L. K., Allardice, J. R., Xiao, J., Karani, A., Jellicoe, T. C., Rao, A. *et al. Materials Horizons* **6**, 137–143 (2019).

6. Benayas, A., Ren, F., Carrasco, E., Marzal, V., Del Rosal, B., Gonfa, B. A. *et al. Advanced Functional Materials* **25**, 6650–6659 (2015).

7. Bae, W. K., Lim, J., Lee, D., Park, M., Lee, H., Kwak, J. *et al. Advanced Materials* **26**, 6387–6393 (2014).

8. Talapin, D. V, Mekis, I., Go, S., Kornowski, A., Benson, O. & Weller, H. 18826–18831 (2004).

9. Kang, I. & Wise, F. W. *Journal of the Optical Society of America B* **14**, 1632 (1997).

10. Konstantatos, G., Howard, I., Fischer, A., Hoogland, S., Clifford, J., Klem, E. *et al. Nature* **442**, 180–183 (2006).

11. Hines, M. A. & Scholes, G. D. *Advanced Materials* **15**, 1844–1849 (2003).

12. Xu, F., Gerlein, L., Ma, X., Haughn, C., Doty, M. & Cloutier, S. *Materials* **8**, 1858–1870 (2015).

13. Greben, M., Fucikova, A. & Valenta, J. *Journal of Applied Physics* **117**, (2015).

14. Bertasius, V., Mastria, R., Rizzo, A., Gigli, G., Giansante, C. & Gulbinas, V. *Journal of Physical Chemistry C* **120**, 14356–14364 (2016).

15. Liu, H., Zhitomirsky, D., Hoogland, S., Tang, J., Kramer, I. J., Ning, Z. *et al. Applied Physics Letters* **101**, 1–4 (2012).

16. Böhm, M. L., Jellicoe, T. C., Tabachnyk, M., Davis, N. J. L. K., Wisnivesky-Rocca-Rivarola, F., Ducati, C. *et al. Nano Letters* **15**, 7987–7993 (2015).

17. Ma, W., Swisher, S. L., Ewers, T., Engel, J. H., Ferry, V. E., Atwater, H. A. *et al. ACS Nano* **5**, 8140–8147 (2011).

18. Bertolotti, F., Dirin, D. N., Ibáñez, M., Krumeich, F., Cervellino, A., Frison, R. *et al. Nature Materials* **15**, 987–994 (2016).

19. Boercker, J. E., Woodall, D. L., Cunningham, P. D., Placencia, D., Ellis, C. T., Stewart, M. H. *et al. Chemistry of Materials* **30**, 4112–4123 (2018).

20. Lu, H., Joy, J., Gaspar, R. L., Bradforth, S. E. & Brutchey, R. L. *Chemistry of Materials* **28**, 1897–1906 (2016).

21. Ip, A. H., Thon, S. M., Hoogland, S., Voznyy, O., Zhitomirsky, D., Debnath, R. *et al. Nature Nanotechnology* **7**, 577–582 (2012).

22. Kramer, I. J. & Sargent, E. H. *Chemical reviews* **114**, 863–82 (2014).

23. Li, Q., Zhang, T., Gu, H., Ding, F., Qu, F., Peng, X. *et al. Acta Chimica Sinica* **71**, 929 (2013).

24. Justo, Y., Sagar, L. K., Flamee, S., Zhao, Q., Vantomme, A. & Hens, Z. *ACS Nano* **8**, 7948–7957 (2014).

25. Fan, Z., Lin, L.-C., Buijs, W., Vlugt, T. J. H. & van Huis, M. A. *Nature Communications* **7**, 11503 (2016).

26. Neo, M. S., Venkatram, N., Li, G. S., Chin, W. S. & Ji, W. *The Journal of Physical Chemistry C* **114**, 18037–18044 (2010).

27. Neo, D. C. J., Cheng, C., Stranks, S. D., Fairclough, S. M., Kim, J. S., Kirkland, A. I. *et al. Chemistry of Materials* **26**, 4004–4013 (2014).

28. Ren, F., Lindley, S. a, Zhao, H., Tan, L., Gonfa, B. A., Pu, Y.-C. *et al. Physical Chemistry Chemical Physics* **18**, 31828–31835 (2016).

29. Lechner, R. T., Fritz-Popovski, G., Yarema, M., Heiss, W., Hoell, A., Schülli, T. U. *et al. Chemistry of Materials* **26**, 5914–5922 (2014).

30. de Mello, J. C., Wittmannn, H. F. & Friend, R. H. *Advanced materials (Deerfield Beach, Fla.)* **9**, 230 (1997).

31. Greenham, N. C., Samuel, I. D. W., Hayes, G. R., Phillips, R. T., Kessener, Y. A. R. R., Moratti, S. C. *et al. Chemical Physics Letters* **241**, 89–96 (1995).

32. Zhang, J., Crisp, R. W., Gao, J., Kroupa, D. M., Beard, M. C. & Luther, J. M. *The Journal of Physical Chemistry Letters* **6**, 1830–1833 (2015).

33. Abe, S., Capek, R. K., De Geyter, B. & Hens, Z. *ACS Nano* **7**, 943–949 (2013).

34. Peng, X., Wickham, J. & Alivisatos, a. P. *Journal of the American Chemical Society* **120**, 5343–5344 (1998).

35. Peng, Z. A. & Peng, X. *Journal of the American Chemical Society* **124**, 3343–3353 (2002).

36. Grim, J. Q., Manna, L. & Moreels, I. *Chem. Soc. Rev.* **44**, 5897–5914 (2015).

37. Zherebetskyy, D., Scheele, M., Zhang, Y., Bronstein, N., Thompson, C., Britt, D. *et al. Science* **344**, 1380–1384 (2014).

38. Semonin, O. E., Johnson, J. C., Luther, J. M., Midgett, A. G., Nozik, A. J. & Beard, M. C. *Journal of Physical Chemistry Letters* **1**, 2445–2450 (2010).

39. Zhao, H., Chaker, M., Wu, N. & Ma, D. *Journal of Materials Chemistry* **21**, 8898 (2011).

40. Klimov, V., Hunsche, S. & Kurz, H. *Physical Review B* **50**, 8110–8113 (1994).

41. El-Ballouli, A. O., Alarousu, E., Usman, A., Pan, J., Bakr, O. M. & Mohammed, O. F. *ACS Photonics* **1**, 285–292 (2014).

42. Efros, A. L. & Nesbitt, D. J. *Nature Nanotechnology* **11**, 661–671 (2016).

43. Quinn, S. D., Rafferty, A., Dick, E., Morten, M. J., Kettles, F. J., Knox, C. *et al. The Journal of Physical Chemistry C* **120**, 19487–19491 (2016).

44. Galland, C., Ghosh, Y., Steinbrück, A., Sykora, M., Hollingsworth, J. A., Klimov, V. I. *et al. Nature* **479**, 203–207 (2011).

45. Yuan, G., Gómez, D. E., Kirkwood, N., Boldt, K. & Mulvaney, P. *ACS Nano* **12**, 3397–3405 (2018).

46. Correa, R. E., Dauler, E. A., Nair, G., Pan, S. H., Rosenberg, D., Kerman, A. J. *et al. Nano Letters* **12**, 2953–2958 (2012).

47. Zhao, H., Liang, H., Vidal, F., Rosei, F., Vomiero, A. & Ma, D. *The Journal of Physical Chemistry C* **118**, 20585–20593 (2014).

48. Weidman, M., Beck, M., Hoffman, R., Prins, F. & Tisdale, W. A. *ACS Nano* **8**, 6363–6371 (2014).

49. Chantler, C. T. *Journal of Physical and Chemical Reference Data* **29**, 597–1056 (2000).

Chapter 4 III-V and Lead-free Near-Infrared Quantum Dots

4.1 Introduction

III-V materials

Semiconductor materials comprising of compounds of boron group elements and pnictogens are termed III-V materials. These have found extensive use in electronics and optoelectronics as transistors, photovoltaics and LEDs.[1–3] Colloidal nanocrystal quantum dots of III-V materials have also been extensively investigated.[4–7]

For infrared emitter applications such as down-conversion for photovoltaics, the predominant materials currently studied are lead chalcogenides such as PbS, further described in Chapter 3. The bandgap for these materials is well-matched to that of silicon. Significant environmental legislation currently exists restricting the use of lead and other heavy metals in electronic devices. It thus becomes attractive to explore alternative materials as potential substitutes.

InAs

Indium arsenide (InAs) is a direct-bandgap semiconductor material with very low effective electron mass of 0.023 m_0 and correspondingly high electron mobility.[8] InAs has a bulk bandgap of 0.35 eV thus quantum-confined systems of InAs colloidal nanocrystals can be tuned to achieve similar bandgaps and optical properties as lead chalcogenide quantum dot systems. This makes it an excellent candidate as an alternative infrared emitter material.

The synthesis of colloidal InAs quantum dots (QDs) has been relatively well-established and significant advances have been made to increase their photoluminescence efficiency.[6,9–12] Typical synthesis involves the dehalosilylation reaction of tris(trimethylsilyl)arsine and indium(III) chloride, although very recently alternative methods with less reactive and less dangerous precursors have been demonstrated.[9,13] Colloidal InAs quantum dots typically possess bandgaps spanning the near-infrared region and have been shown to possess high photoluminescence quantum efficiencies with sufficient passivation.[10,13] Established passivation techniques for the improvement of InAs QD luminescence typically followed core-shell structural strategies involving the growth of wide-gap semiconductor shells around InAs cores.[10,13] High surface defect densities and the higher valencies of III-V materials impede effective surface passivation with organic and inorganic ligands. As a result, core-only InAs QDs have universally demonstrated poor photoluminescence efficiencies.[7] For infrared emitter

applications where high luminescence efficiency is essential, it is evident core-shell strategies should be explored predominantly.

$CuInSe_2$

Copper indium selenide ($CuInSe_2$) is a ternary chalcopyrite (I-III-VI_2) type semiconductor material that has recently been investigated for use in solar cells.[14] $CuInSe_2$ based nanocrystals have displayed high luminescence efficiencies within the infrared.[15,16] The trap-like nature of the emissive state consists of a Cu-defect site, where a In^{3+} site is substituted for a Cu^+ creating a hole-trap and efficient electron transfer from the conduction band to the trapped hole leads to efficient emissive recombination.[17] The efficient transfer affords greater tolerance of other defects and they have fewer challenges compared to lead chalcogenide and III-V materials in retaining luminescence efficiency when transferred to the solid state. As such they have been demonstrated as effective emitters in luminescent solar concentrator configurations.[18] However, despite the trap-like emissive state in $CuInSe_2$ nanocrystals, they still require substantial passivation and protection from their environment through core-shell structure such as ZnS to prevent rapid non-radiative quenching.

As described in Chapter 2, singlet fission down-conversion applications require energy transfer into quantum dots with high photoluminescence efficiencies in the infrared. This Chapter investigates the growth of core-shell structures to improve luminescence in lead-free infrared nanocrystals. As the shell materials themselves could pose a tunnelling barrier to energy transfer processes, it is necessary to explore optimal shell thicknesses for luminescence efficiency improvement. For down-conversion applications, QDs possessing maximum luminescence with the minimum required shell are ideal.

4.2 Methods

Synthesis of TMS_3As

Tris(trimethylsilyl)arsine (TMS_3As) was synthesised according to a previously published method with the assistance of Callum Benson and Prof. Dominic Wright.[19,20] ***The synthesis of TMS_3As is not trivial and involves significant handling of highly pyrophoric and toxic precursors. Users should have access to extensive experience with inert-atmosphere methods for organometallic materials, along with a suitably-equipped laboratory before attempting synthesis.*** Finely ground arsenic powder (7 g, 99.997%, Strem Chemicals) was placed in a 1 L four-necked round-bottomed flask fitted with condenser, septum cap, overhead stirrer and placed under flowing argon. Anhydrous 1,2-dimethoxyethane (DME, 400 mL, Sigma-Aldrich) was added to the reaction vessel. The vessel was heated to 76 °C in an oil bath with stirring. A glass stirrer blade was used as PTFE decomposes in the reaction mixture. Sodium-potassium alloy (10 g, 44% Na 56% K) was produced by heating Na and K metal chunks together under argon in a dropping funnel with fritted filter. The dropping funnel was attached to the reaction vessel and the filtered liquid NaK alloy was added to the hot reaction mixture

with vigorous stirring. The mixture was heated at reflux (85 °C) for 48 hours, with the solution turning black within 1 hour.

The heat was removed and the vessel cooled with an ice bath. Trimethylsilylchloride (TMSCl, 38.5 g, 99%+, Alfa Aesar) was added slowly with vigorous stirring over 45 minutes. The mixture was then heated at reflux with vigorous stirring for 24 hours before cooling to room temperature.

The condenser was removed under a steady flow of argon and replaced with a fritted filter connected to a three-necked round-bottomed collecting flask. The reaction mixture was transferred to the collecting flask through the filter frit. The salt cake collected on the frit was washed with additional portions of anhydrous DME. The fritted filter was removed from the receiving flask under a strong flow of argon and the vessel was capped. The solvent was removed under vacuum at room temperature to leave a pale yellow liquid, which turned red if exposed to air. Fractional distillation of the impure product was carried out under vacuum (bp 65-71 °C) to produce a colourless liquid in a round-bottomed receiving flask. The product was transferred to a nitrogen glovebox and placed in a J Young flask for storage. The identity of the product was confirmed by ^{1}H and ^{13}C NMR in deuterated toluene (C_7D_8).

InAs synthesis

Synthesis of colloidal InAs nanocrystals was carried out according to a variation on the previously published dehalosilylation reaction between tris(trimethylsilyl)arsine and indium chloride.[7] A typical synthesis is as follows: A concentrated stock solution of indium chloride in trioctylphosphine (TOP) was produced by heating $InCl_3$ (5 g, 99.99%, Sigma-Aldrich) in TOP (15 mL, 99%, Sigma-Aldrich) under nitrogen. The solution was cooled and taken into an argon glovebox for storage. In a three-necked round bottomed flask, TOP (2.4 mL, 2 g) was heated to 300 °C under flowing nitrogen. In an argon glovebox, a syringe was prepared by mixing TMS_3As (0.23 mL) and $InCl_3$:TOP stock solution (0.77 mL) to produce a reaction solution (1 mL, 1 TMS_3As:1.1 $InCl_3$:2.8 TOP by mass). The reaction solution was injected quickly into the flask of hot TOP at 300 °C. The reaction mixture was cooled to 260 °C for further growth. Further injections of reaction solution mix (2nd 0.5 mL, 3rd 0.8 mL) were slowly added as required in intervals to grow larger nanocrystals. Total reaction time for a typical synthesis was 10 minutes, after which the reaction mixture was cooled to room temperature and transferred to an argon glovebox. The nanocrystals were purified twice by successive precipitation, centrifugation and resuspension with acetone/methanol as the non-solvent and toluene/hexane as the solvent. The product was dried and suspended in toluene or octane for final storage in an argon atmosphere.

Shell growth of wider-bandgap semiconductor materials around InAs cores was performed in adaptation of previously published methods.[10,11] The general synthetic method was successive ionic

layer adsorption and reaction (SILAR), with sequential injection and reaction of cation and anion precursor solutions.

InAs/CdSe and InAs/ZnSe

For growth of CdSe and ZnSe shells, Cd, Se and Zn stock precursors were prepared. A stock Zn precursor solution was prepared as follows: 1-octadecene (ODE, 90%, Sigma-Aldrich) was degassed under vacuum at 110 °C for 1 hour then taken into an argon glovebox. A 0.04 M solution of Zn in ODE was prepared in the glovebox by mixing diethylzinc solution (0.19 mL, 15% in toluene, Sigma-Aldrich) with degassed ODE (9.81 mL). A stock 0.04 M Se precursor solution was prepared as follows: selenium powder (190 mg, 99.999%, Alfa Aesar) was added to 1-octadecene in a 3-necked round-bottomed flask and degassed under vacuum at 110 °C for 1 hour. The flask was turned to nitrogen and heated to 200 °C for 3 hours to form a clear pale-yellow selenium solution. The stock solution was then transferred into an argon glovebox for storage. A stock 0.04 M Cd precursor solution was prepared as follows: Cadmium oxide (154 mg, 99.999%, Sigma-Aldrich) was added to a mixture of 1-octadecene (27 mL) and oleic acid (OA, 3 mL, 90%, Sigma-Aldrich) in a 3-neck round-bottomed flask then degassed under vacuum at 110 °C for 2 hours. The flask was switched to nitrogen and heated to 250 °C until all the cadmium oxide had dissolved to form a colourless solution of cadmium oleate complex. The solution was cooled to 110 °C and degassed again under vacuum for 15 minutes then transferred into an argon glovebox for storage.

ODE (6.3 mL) and oleylamine (OLA, 1.8 mL, 70%, Sigma-Aldrich) were added to a three-necked flask fitted with condenser, stirrer bar, temperature probe and connected to a Schlenk line. The mixture was degassed under vacuum at 110 °C for 1 hour then cooled under nitrogen. InAs cores (10-25 mg) in toluene or octane was transferred to a syringe in the glovebox and injected into the reaction solution. The solution was heated again to 100 °C and degassed under vacuum for 10 minutes to remove trace volatile solvents. Next the vessel was switched to nitrogen atmosphere and heated to 260 °C. Upon reaching 260 °C, sequential additions of Cd/Zn and Se precursor solution were injected into the reaction vessel at 10 minute intervals. A typical volume of injections was 0.45 mL each of 0.04 M Cd/Zn and Se precursor for the first layer and 0.65 mL each for the second layer. The reaction mixture was cooled to room temperature 10 minutes after the final injection and transferred into an argon glovebox. The nanocrystals were precipitated with a mix of ethanol, methanol and 1-butanol, centrifuged, re-suspended and re-precipitated using hexane or toluene as the solvent and a mix of ethanol, 1-butanol and methanol as the non-solvent respectively. The product was dried and suspended in octane or toluene for storage in an argon atmosphere.

InAs/CdSe/ZnSe

ODE (6.3 mL) and oleylamine (OLA, 1.8 mL, 70%, Sigma-Aldrich) was added to a three-necked flask fitted with condenser, stirrer bar, temperature probe and connected to a Schlenk line. The

mixture was degassed under vacuum at 110 °C for 1 hour then cooled under nitrogen. InAs cores (10-25 mg) in toluene or octane was transferred to a syringe in the glovebox and injected into the reaction solution. The solution was heated again to 100 °C and degassed under vacuum for 10 minutes to remove trace volatile solvents. Next the vessel was switched to nitrogen atmosphere and heated to 260 °C. Upon reaching 260 °C, sequential additions of Cd and Se precursor solution were injected into the reaction vessel at 10 minute intervals, followed by sequential additions of Zn and Se precursor to grow the second shell. A typical volume of injections was 0.45 mL each of 0.04 M Cd and Se precursor for the first layer, followed by 0.65 mL each of Zn and Se for the second layer, 1.05 mL each for the third, 1.45 mL each for the fourth, 1.9 mL each for the fifth and 2.4 mL each for the sixth. For a typical CdSe/ZnSe shell1/shell2 core-shell preparation, the interlayer of CdSe was a nominal single layer thickness followed by up to nominally 5 layers of ZnSe. Ten minutes after the final injection, the reaction mixture was cooled to room temperature and taken into an argon glovebox. The nanocrystals were precipitated with a mix of ethanol, methanol and 1-butanol, centrifuged, re-suspended and re-precipitated using hexane or toluene as the solvent and a mix of ethanol, 1-butanol and methanol as the non-solvent respectively. The product was dried and suspended in octane or toluene for storage in an argon atmosphere.

InAs/ZnS

Growth of ZnS shells was performed through the decomposition of a single source precursor according to a previously published method for CdSe nanocrystals.[21,22]

A stock reaction medium was prepared by degassing ODE (100 mL), OLA (30 mL) under vacuum at 110 °C for 1 hour in a three-necked flask. The mixture was cooled and put under nitrogen, whereupon TOP (30 mL) was added. The mixture was again degassed at 110 °C for 10 minutes, before cooling to room temperature and transferral into an argon glovebox for storage.

For a typical synthesis, a three-necked flask with stirrer bar, condenser and temperature probe was loaded with zinc diethyldithiocarbamate (80 mg, 97%, Sigma-Aldrich) and put under nitrogen. Stock reaction medium (16 mL, 10 mL ODE: 3 mL OLA:3 mL TOP) was taken from the glovebox and injected into the flask. The contents were heated at 60 °C for 1 hour until all the white solid had dissolved. A solution of InAs cores (25 mg) in toluene was added to the solution and the vessel was degassed under vacuum for 5 minutes to remove volatile solvents. The flask was switched to nitrogen and heated to 120 °C for 2 hours for shell growth. The mixture was cooled to room temperature and transferred into a glovebox. The nanocrystals were precipitated by the addition of anhydrous 1-butanol (25 mL), acetone (20 mL) and methanol (20 mL) and centrifuged. The supernatant was removed and the precipitated nanocrystal pellet washed with 1-butanol (20 mL) and methanol (20 mL). The isolated product was then re-suspended in toluene for storage in an argon glovebox.

$CuInSe_2$

Synthesis of $CuInSe_2$/ZnS nanocrystals was performed from an adaptation of an existing method.[18] In the one-pot method, $CuInSe_2$ cores were synthesised first followed by in-situ growth of the ZnS shell through sequential SILAR-style injections.

A stock Se precursor solution was prepared by dissolving selenium powder (95 mg, 99.999%, Alfa Aesar) in degassed oleylamine (3 mL) and diphenylphosphine (DPP, 0.9 mL, 99%, Sigma-Aldrich) in an argon glovebox. A stock ZnS precursor solution was prepared in a three-necked round bottomed flask loaded with zinc stearate (6.32 g, Sigma-Aldrich), ODE (20 mL), oleic acid (OA, 10 mL, 90%, Sigma-Aldrich) and 1-dodecanethiol (DDT, 10 mL, 99%, Sigma-Aldrich). The flask was heated under nitrogen to 150 °C for 10 minutes until all the zinc stearate had dissolved. The temperature was lowered to 80°C then the solution degassed under vacuum for 1 hour. The vessel was switched to nitrogen and kept at 50 °C to prevent precipitation during the synthesis of $CuInSe_2$ cores.

A three-necked round-bottomed flask was loaded with indium acetate (175 mg, 99.999%, Sigma-Aldrich), copper(I) iodide (114 mg, 99.99%, Sigma-Aldrich), OLA (6 mL) and ODE (6 mL) and heated to 80 °C under vacuum for 1 hour. The flask was switched to nitrogen flow and heated to 210 °C. The stock Se solution was injected into the flask and the temperature maintained for 40 minutes, after which the temperature was reduced to 80 °C to quench the reaction. The as-synthesised $CuInSe_2$ nanocrystal solution was degassed under vacuum for 30 minutes to remove volatile species in preparation for ZnS shell growth. The vessel was heated under nitrogen to 230 °C upon which a portion of the ZnS precursor solution (11 mL) was injected slowly to commence growth of the ZnS shell. Up to three additional injections of equal volume were added at 2 hour intervals as necessary for further growth of the ZnS shell. The temperature was maintained for 4 hours after the final injection. The reaction mixture was cooled and transferred to an argon glovebox, where the nanocrystals were purified by two sequences of precipitation, centrifugation and resuspension with ethanol as the non-solvent and hexane as the solvent. The purified nanocrystals were stored in hexane. For the synthesis of $CuInSe_2$ without shells, the reaction was quenched and purified prior to the ZnS growth stage. Shell thickness variation was achieved with the omission of one or more ZnS precursor injections.

Nanocrystal film fabrication was performed by spin-coating suspensions onto glass substrates through layer-by-layer deposition to increase film thickness and optical density.[23] A solution of 1,4-benzenedithiol in acetonitrile (BDT, 20 mM, 99%, Sigma) was spin-coated onto substrates at 1000 rpm. The substrate was spin-rinsed with acetonitrile to remove excess ligand, followed by an octane rinse to remove excess acetonitrile. The BDT-functionalised substrate was spin-coated with nanocrystal solution from octane or toluene at 1000 rpm. BDT solution was spin-coated to crosslink the nanocrystals on the surface. This was followed by acetonitrile then octane spin-rinses. The

sequential nanocrystal-BDT-acetonitrile-octane deposition was repeated 5 times in total to increase thickness of the films. Films were encapsulated using glass cover slips with two-part epoxy resin. For down-conversion bilayer films, an additional layer of tetracene was evaporated or 5,12-bis(triisopropylsilylethynyl)tetracene (TIPS-tetracene, 1 mg mL^{-1}) in chloroform was spin-coated at 1000 rpm or onto nanocrystal films prior to final encapsulation.[24–26]

Transmission electron microscopy (TEM) imaging was performed with a FEI Tecnai 20 TEM with LaB_6 cathode at 200 kV operating voltage. Samples were diluted and drop cast onto 200-mesh carbon-coated Cu grids (Agar Scientific AGS160).

Photoluminescence quantum efficiency (PLQE) measurements were performed using the integrating sphere method of de Mello.[27,28] The excitation light source was either a Coherent OBIS 405 nm or CNI MGL-III 532 nm diode laser. The optical system was a 6-inch Labsphere integrating sphere with diffusely-reflective $BaSO_4$ coating fibre-coupled into an Andor Shamrock SR-303i imaging spectrograph with iDus InGaAs photodiode array detector. Detailed descriptions of the measurement are described in Chapter 5. All PLQE values explicitly shown were performed to be consistent relative to measurements in this Chapter. However, the measurements were performed during times with possible contamination of the measurement setup. As described in Chapter 5, the likely result of this effect is to cause underestimates in the measured PLQE values. Full random error analysis was not performed as the samples measured in this Chapter were sufficiently absorbing and this was deemed unnecessary.

UV-Vis-NIR absorption measurements were taken with a Perkin-Elmer Lambda 9 spectrophotometer. Samples were diluted in octane and placed in a quartz absorption cuvette (Hellma Suprasil) with 1 cm path length.

Infrared time-correlated single photon counting (TCSPC) was performed on film samples with a pulsed white light Fianum Whitelase SC-400-4 laser at 1 MHz repetition rate. Bandpass notch filters were used to modify excitation wavelength at 670 nm and 450 nm. A 1000 nm long-pass filter was used to remove visible light scatter from reaching the NIR InGaAs/InP avalanche photodiode detector.

Photoluminescence excitation (PLE) was performed with an Edinburgh Instruments FLS980 with 450 W Xe lamp excitation source and Hamamatsu R928P PMT and InGaAs PD detectors.

4.3 Results and Discussion

TMS_3As synthesis

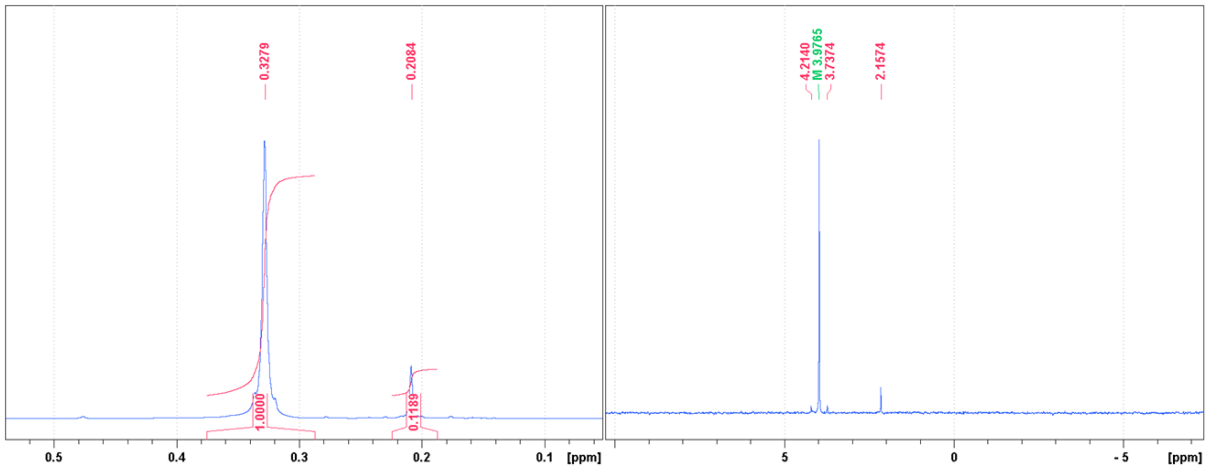

Figure 4-1 – ^{1}H (left) and ^{13}C (right) NMR spectra of synthesised TMS_3As in C_7D_8. The C_7D_8 reference (δ = 2.09) can be observed in the ^{13}C spectrum. The small peak (δ = 0.21) in the ^{1}H spectrum was assigned to silicone grease contamination. NMR was performed with the open-access 400 MHz spectrometer 'Laphroaig' in the Department of Chemistry with Callum Benson.

The identity of the product was confirmed by NMR, shown in Figure 4-1, and compared to the literature. A singlet resonance at δ = 0.30 ppm was observed with ^{1}H NMR and a resonance was observed at δ = 4.31 ppm with ^{13}C NMR in agreement with literature values.[20] The yield was 15 g (56%). The secondary small peaks at δ = 0.21 ppm and δ = 2.1 ppm respectively were attributed to silicone vacuum grease from the synthesis glassware.[29]

The first step of the synthesis of TMS_3As – the reaction of arsenic and NaK alloy – was determined to be critical to the successful synthesis of TMS_3As product. This step consists of the slow sequential attack and breakdown of the arsenic six-membered rings by NaK. Incomplete breakdown of the ring species results in dimer and oligomeric arsenic species which cause side reactions with trimethylsilylchloride and the formation of other organoarsenic compounds with varying degrees of trimethylsilyl-functionalisation. For complete breakdown of arsenic and conversion into the necessary trivalent As^{3-} anion species, the arsenic powder is required to have small particle size thus have a large surface area-volume ratio for NaK attack. To mitigate variations in powder granularity resulting from supplier batch differences, the arsenic was manually crushed with mortar and pestle to a fine powder before addition to the flask. Furthermore, the reaction time of the first step was lengthened to 48 hours under reflux to ensure complete breakdown. The incomplete reaction and formation of side products formed colourless liquid products with vastly different boiling points upon distillation. These side products did not form colloidal products if substituted for TMS_3As in InAs nanocrystal synthesis.

Reaction of small quantities of TMS_3As with air was observed to be relatively slow, with the gradual formation of orange-red salts. The reaction was exothermic enough to ignite surrounding flammable material although pyrophoricity was not observed by itself in small quantities.

InAs core synthesis

The synthesis of colloidal InAs nanocrystals was investigated through variation of reaction conditions: overall reaction time, number of injections and time between injections. The individual samples featured in this section are described in Table 4-1.

Sample	Conditions
InAs 1	Injection at 265°C, reaction at 260°C/60 min
InAs 10	Injection at 300°C, reaction at 260°C/40 min with additional injection at 25 min
InAs 11	Injection at 300°C, reaction at 260°C/15 min
InAs 12	Injection at 300°C, reaction at 260°C/5 min
InAs 14	Injection at 300°C, reaction at 260°C/5 min repeat
InAs 15	Injection at 300°C, reaction at 260°C/10 min with additional injection at 5 min
InAs 16	Injection at 300°C, reaction at 260°C/35 min with additional injections at 10 and 20 min
InAs 17	Injection at 300°C, reaction at 260°C/30 min with additional injections at 10 and 20 min

Table 4-1 – Summary of synthesis conditions for InAs QD cores for samples featured in this chapter. The numerical designation indicates chronological sample preparation. Successive injection volumes (1 mL, 0.5 mL, 0.8 mL) where applicable are identical as described in Methods section.

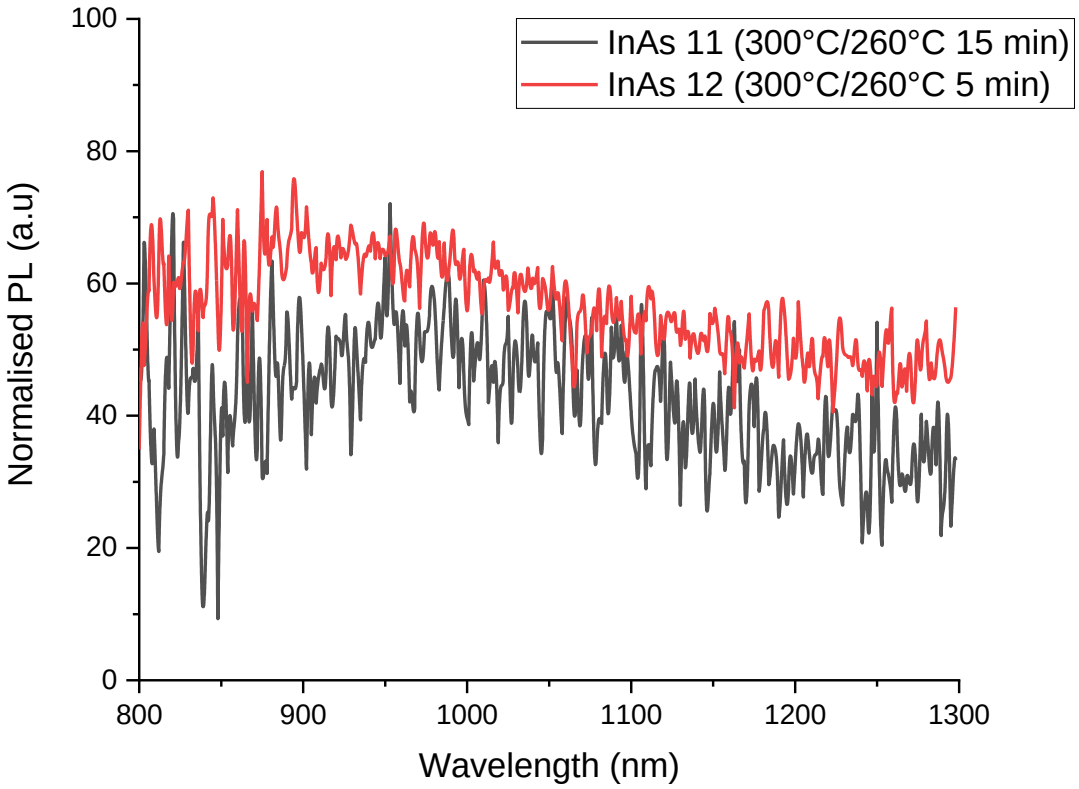

Figure 4-2 – PL spectra of InAs QDs synthesised with one injection at different reaction times. Injection temperature was 300 °C and reaction temperature was maintained at 260 °C. The samples had very low fluorescence yields (<0.3%)

Unlike the synthesis of other semiconductor nanocrystals, the reaction time was found to be less influential on the resulting size and bandgap of the product than the number of injections of precursor material. For a given injection temperature, a single injection produced nanocrystals of similar bandgap at different reaction times, shown in Figure 4-2. However, with extended synthesis times with a single injection, precipitation of the product was observed

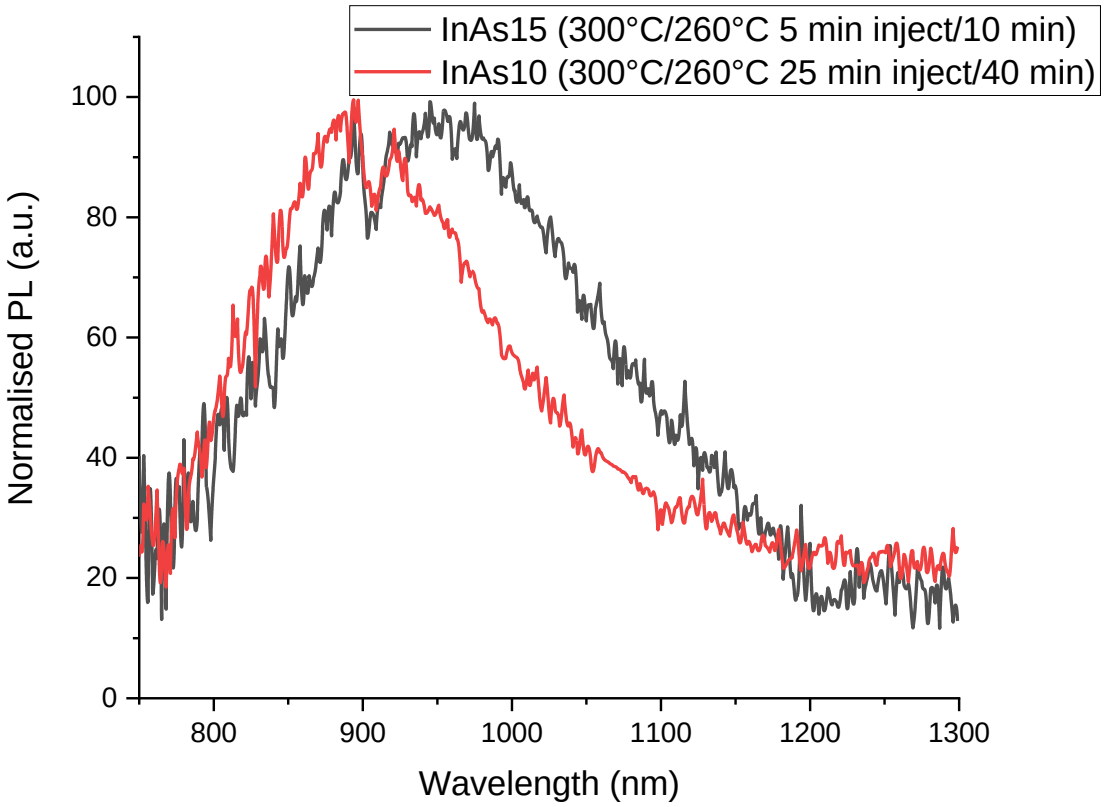

Figure 4-3 – PL spectra of InAs QDs synthesised with two injections at different time intervals with different overall reaction times. Injection temperature was 300 °C and reaction temperature was maintained at 260 °C. The samples had low fluorescence yields (<0.5%).

Figure 4-3 illustrates similar QD bandgaps were synthesised at different reaction times with the same number and amount of precursor injections. Contrary to intuition, the longer synthesis time resulted in a larger bandgap and lower emission wavelength. This was attributed to size defocusing, where the depletion of growth monomer in the reaction medium results in dissolution of smaller crystals coincident with growth of the larger crystals, also termed Ostwald ripening.[6] The smaller crystals with higher surface energy and reactivity are more rapidly dissolved into monomer species than the larger crystals, which do not dissolve as quickly. The net result is the gradual broadening of the size distribution until eventually the larger crystals are unable to be stabilised by surface ligands as a colloid and precipitate out of solution. The luminescent population here thus consisted of the remaining smaller crystals. Rapid nucleation and growth occurs within a short period of time following the initial injection of precursor solution to lead to a relative kinetic equilibrium.[6,13]

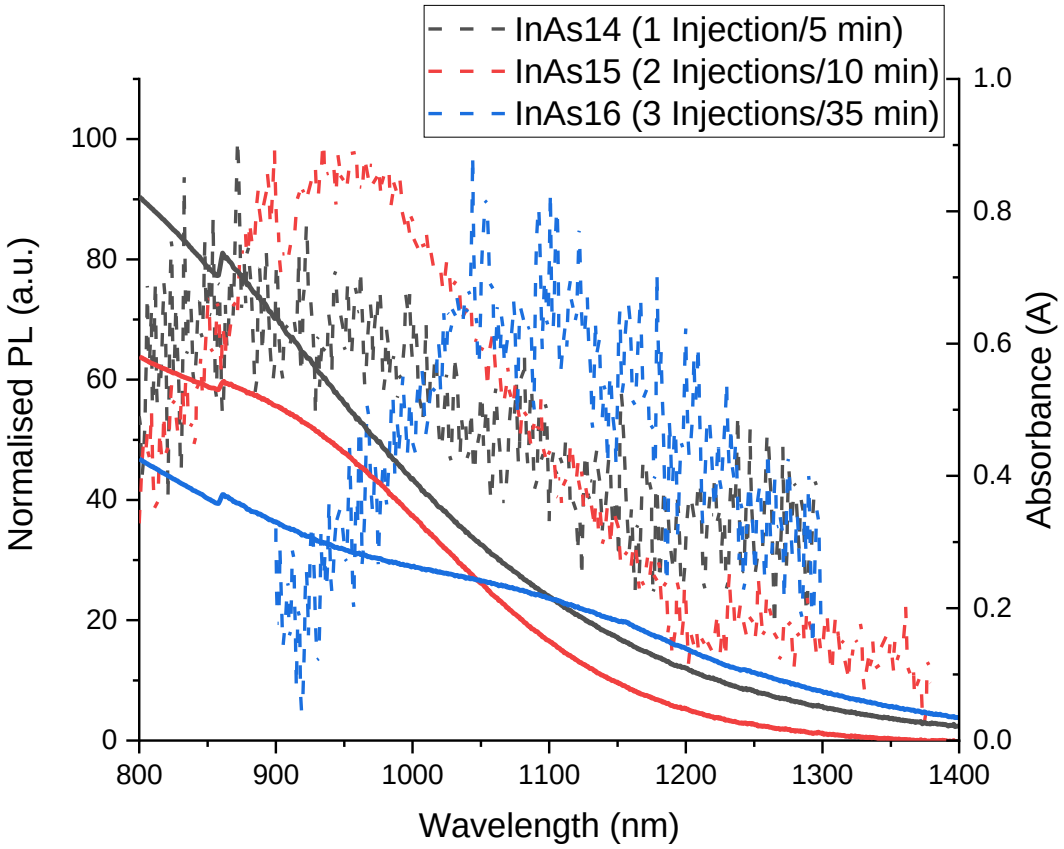

Figure 4-4 – Normalised PL (dashed) and absorption (solid) spectra of InAs QDs synthesised with different numbers of injections. Injection temperature was 300 °C and reaction temperature was maintained at 260 °C. The samples had low fluorescence yields (<0.5%). The bump at 850 nm in the absorption spectra was caused by a detector change in the instrument.

The growth phase may be extended with further injections. The reaction kinetics and resulting size of the nanocrystals was determined by the available pool of growth monomer during synthesis. With increased number of injections, the monomer concentration was replenished allowing further growth around existing nanocrystal cores to greater sizes, shown in Figure 4-4 with absorption spectra included to highlight size differences.[6,7,10] Recent literature reports published since this work was performed also support this observation.[13]

Photoluminescence quantum efficiency measurements of InAs nanocrystals universally showed low emission efficiencies of <1%. However, it was observed that shorter reaction times produced more emissive nanocrystals. Initial attempts in replicating literature efforts featuring long reaction times exceeding 2 hours produced samples with negligible luminescence.[7] Upon reducing reaction times and time between subsequent injections, this was consistently improved to around 0.5% PLQE. The overall poor luminescence may be explained in part by the incomplete passivation of the nanocrystal surfaces by the native trioctylphosphine (TOP) ligands as synthesised in the presence of chloride. The

bulky TOP ligands sterically impede each other and incompletely passivated indium dangling bonds provide non-radiative decay routes via trap states. In addition, synthesis with indium chloride precursor gives rise to halide co-passivation, blocking some coordination sites for ligand attachment and monovalent chloride ions incompletely passivating trivalent indium defects. The extended reaction times leading to poor PLQE may be explained by disproportionation in nanocrystal dissolution and growth leading to creation of additional surface defects at depleted monomer concentrations.

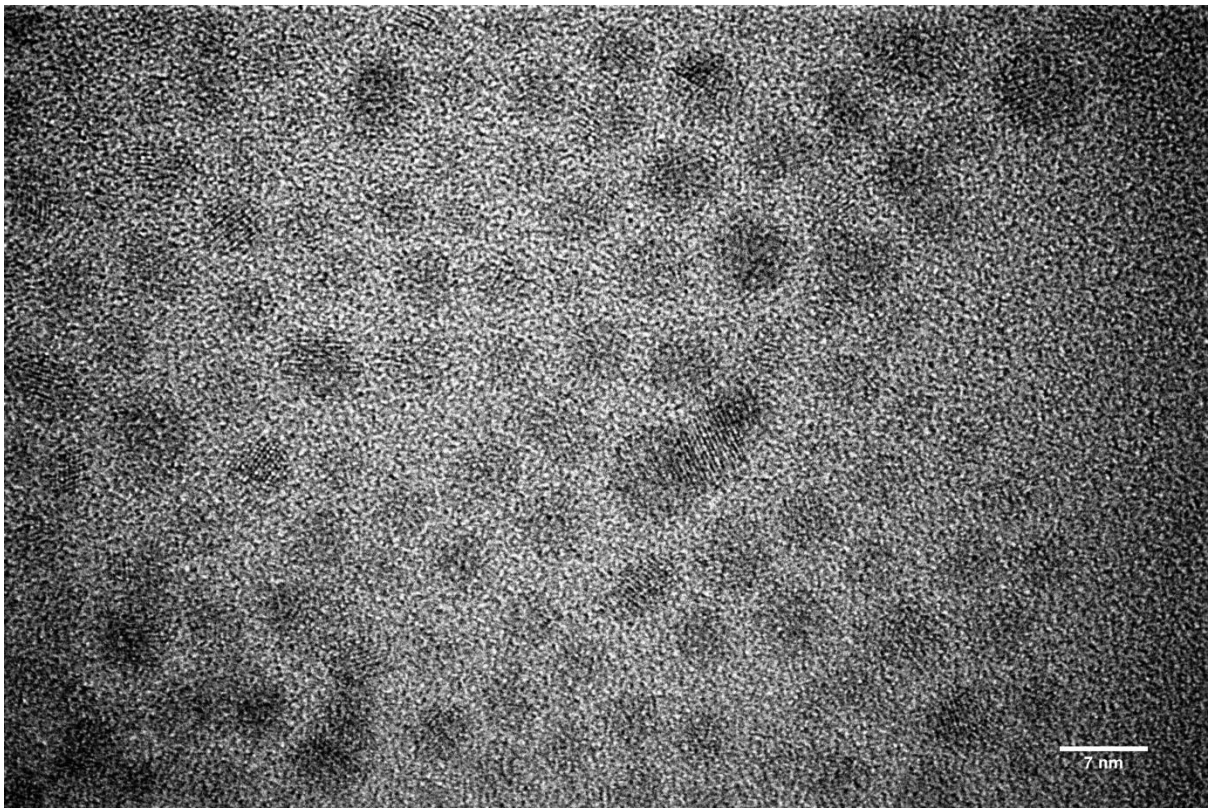

Figure 4-5 – TEM image of InAs nanocrystals. The sample was InAs 1 and did not possess detectable photoluminescence.

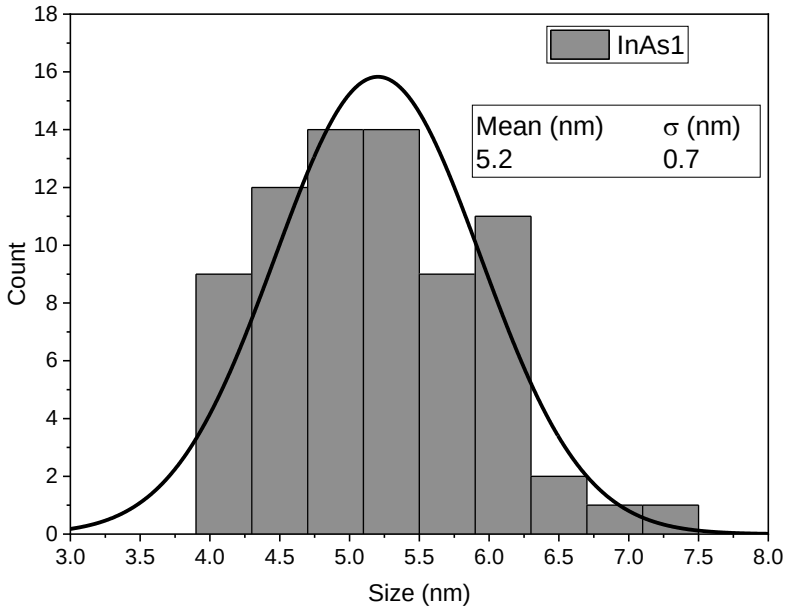

Figure 4-6 – TEM size distribution analysis of InAs 1 QD sample shown in Figure 4-5. Sizes were measured by manually taking the mean length along perpendicular axes. The mean size was 5.2 nm with a standard deviation of 0.7 nm.

Ligand exchanges to less bulky ligands such as oleic acid to improve luminescence were not investigated due to the wealth of literature supporting a core-shell strategy for III-V nanocrystals.[10,30–32] TEM images of InAs 1 nanocrystals, shown in Figure 4-5, showed roughly spherical crystallites with visible lattice fringing with a measured d-spacing of 0.35 nm, consistent with the spacing in the [111]-direction for zincblende InAs.[10] Size distribution analysis was performed on the TEM images of the InAs 1 sample, shown in Figure 4-6, indicating a mean size of 5.2 nm with a standard deviation of 0.7 nm.

Core-shell InAs

The growth of wider-bandgap semiconductors around InAs to form core-shell structures was investigated with several architectures explored. Both simple core/shell and graded core/shell/shell structures were synthesised with CdSe, ZnSe and ZnS as the shell materials of choice. The core-shell growth samples featured in this section are summarised in Table 4-2.

Sample	Conditions
InAs 14/2CdSe	Cores: Injection at 300°C, reaction at 260°C/5 min Shells: Growth of 2 nominal layers of CdSe (2 successive injections each of Cd and Se precursor).
InAs 17/(1-3)ZnSe	Cores: Injection at 300°C, reaction at 260°C/30 min, additional injections at 10 and 20 min Shells: Growth of (1-3) nominal layers of ZnSe (1-3 successive injections each of Zn and Se precursors).
InAs 17/CdSe/(1-5)ZnSe	Cores: Injection at 300°C, reaction at 260°C/30 min, additional injections at 10 and 20 min Shells: Growth of single nominal interlayer of CdSe (1 successive injection each of Cd and Se precursors) followed by growth of (1-5) nominal layers of ZnSe (1-5 successive injections each of Zn and Se precursors).
InAs 16/ZnS	Cores: Injection at 300°C, reaction at 260°C/35 min with additional injections at 10 and 20 min 1 equivalent - 40 mg zinc diethyldithiocarbamate 2 equivalents - 80 mg zinc diethyldithiocarbamate

Table 4-2 – Summary of synthesis conditions for core-shell InAs/shell QDs for samples featured in this chapter. The numerical prefix before a shell material indicates nominal shell thickness. Injection volumes for shell growth are as described in Methods section for a given complete layer (1st 0.45 mL each, 2nd 0.65 mL each etc.)

The established method of successive ionic layer adsorption and reaction (SILAR) was used for growth of CdSe and ZnSe shells.[10,21] The general SILAR strategy involved the sequential introduction of cation and anion precursors to a growth medium containing nanocrystal cores. Separate sequential injection of cation and anion precursor was performed to prevent side nucleation of nanocrystals of the shell material. The aim for this methodology was to ensure complete shell layer growth with fine control of thickness, thus allowing a series of shell thicknesses to be investigated. Complete shell growth was evidenced by substantial relative increases in PLQE. In addition, more complex interlayer shell structures could be formed by separating the introduction of different cation precursors.

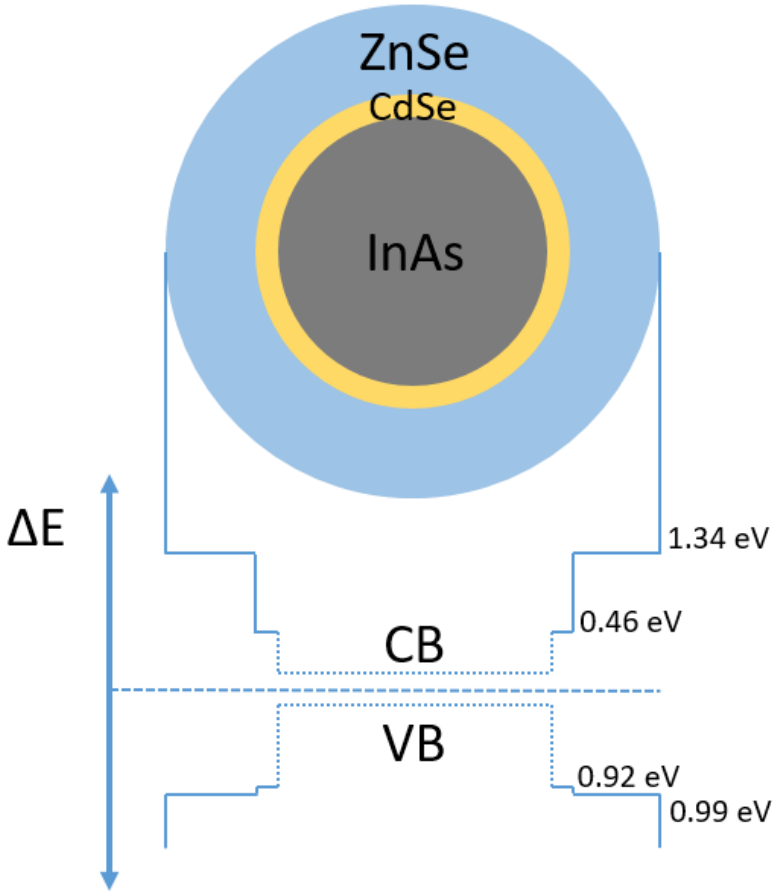

Figure 4-7 – Cartoon band structure diagram for InAs/CdSe/ZnSe core-shell-shell QDs with bulk valence and conduction band offsets for CdSe and ZnSe compared to InAs. While the actual band gap of the InAs core varies, it can be seen that ZnSe is sufficiently large for confinement InAs. However, CdSe does not have a sufficiently large conduction band offset for confinement as the InAs bandgap approaches 1.25 eV and above, allowing wavefunction leakage into the CdSe shell.

Growth of CdSe to form single-shell InAs/CdSe was performed to different thicknesses. Cadmium selenide was initially an attractive candidate because of the similar lattice parameter constants and identical crystal structures of the cubic phase of CdSe and InAs. Both follow the zinc blende crystal structure with lattice constants of 6.08 and 6.05 Å respectively. The small lattice mismatch and compatible crystal structures would ensure epitaxial growth of shell material, ensuring complete surface passivation of the core whilst minimising defect formation between core and shell materials.

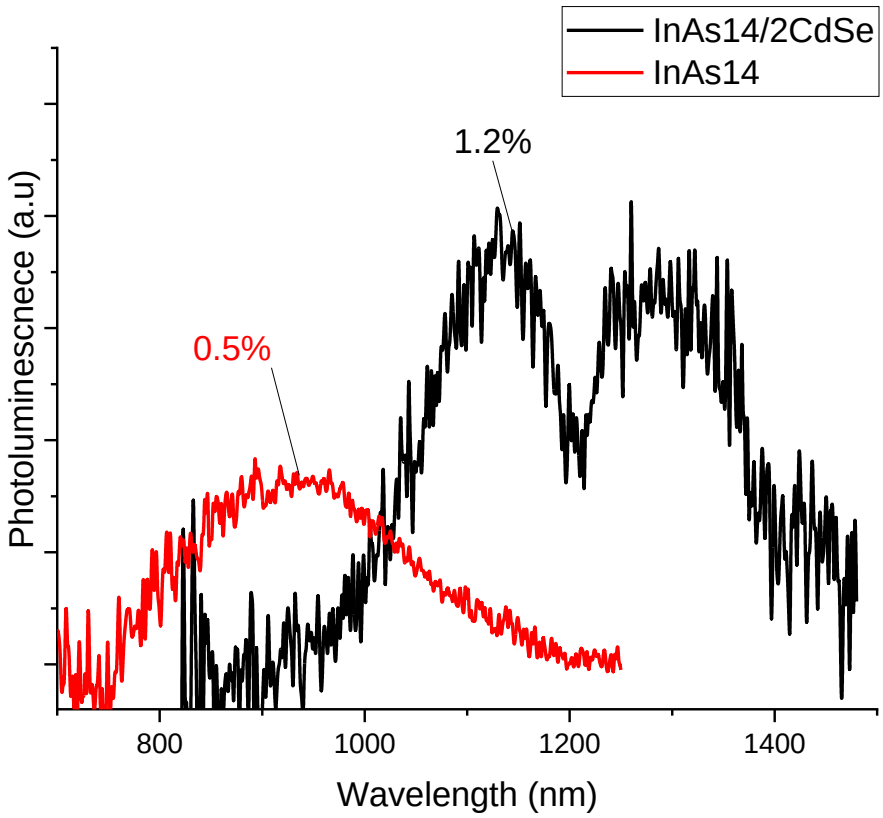

Figure 4-8 – PL spectra of InAs core and InAs/CdSe core-shell QDs with nominal thickness of 2× CdSe layers. Peaks have been scaled to measured PLQE by area. The two peaks may be because of two populations with different thicknesses of CdSe shells. The solvent was octane thus toluene absorption modes at 1150 and 1200 nm were not present.

Nanocrystals with InAs/CdSe core-shell structure displayed a small increase in emission efficiency and a redshift in emission peak position, shown in Figure 4-8. The increase in PLQE was attributed to effective passivation of surface defects by the CdSe shell. The observed redshift was consistent with previous literature reports and may be explained by the leakage of the exciton wavefunction into the CdSe shell.[10] Despite the large difference in bulk bandgap between InAs and CdSe, the alignment between the InAs and CdSe conduction bands results in a low potential barrier for the electron wavefunction to access the CdSe shell, illustrated in the cartoon Figure 4-7, where the conduction band offset of CdSe is only 0.46 eV.[33] This increases the size of the 'box' and effectively decreases confinement of the exciton wavefunction, leading to a smaller bandgap and emission redshift.

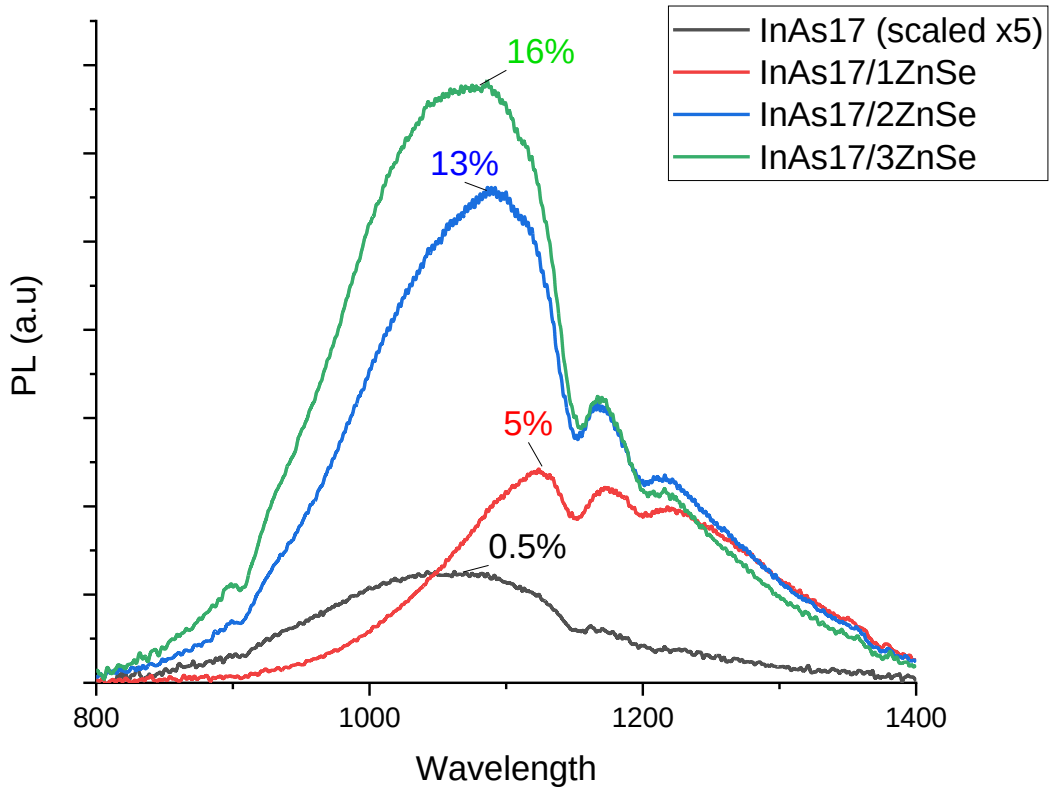

Figure 4-9 – PL spectra of InAs QDs and InAs/ZnSe core-shell QDs with nominal shell thicknesses of 1, 2 and 3 layers. PL has been scaled to measured PLQE by area. Dips in emission at 1150 and 1200 nm are caused by absorption by the toluene solvent.

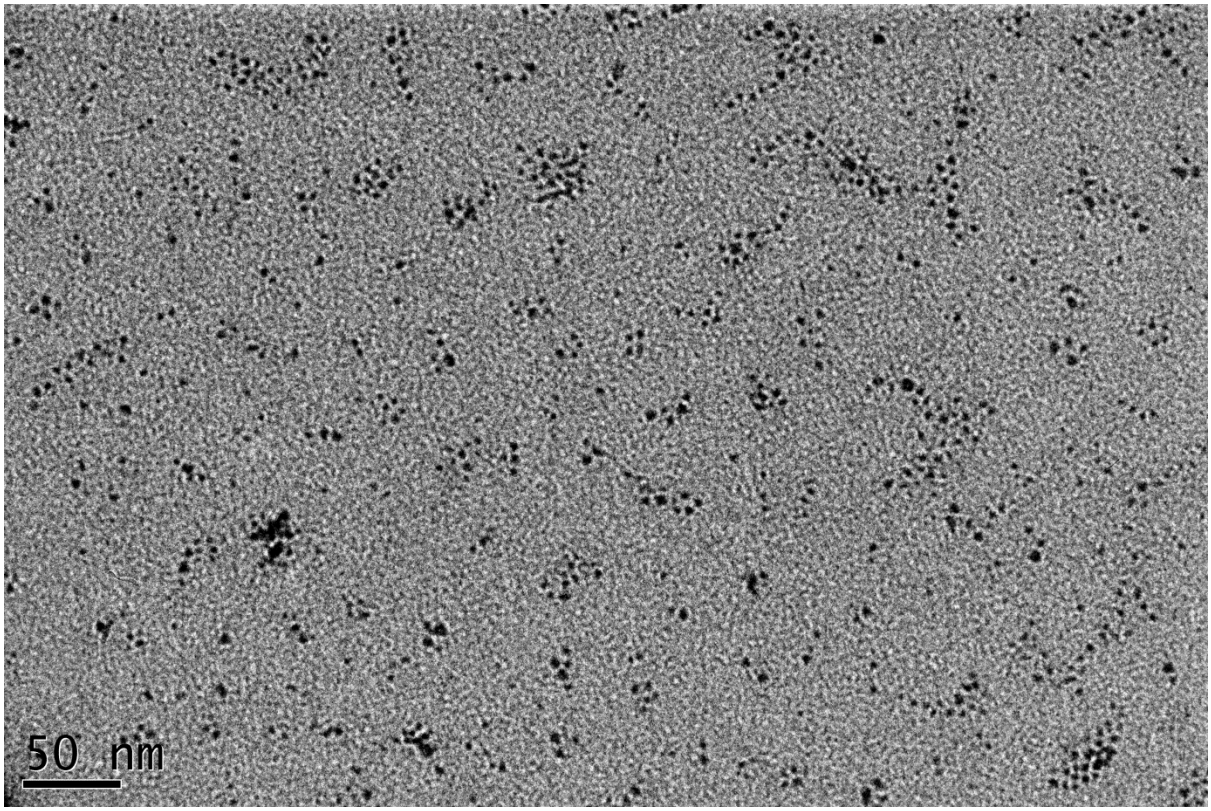

Figure 4-10 – TEM image of InAs17/2ZnSe core-shell nanocrystals. Size distribution analysis of this sample was performed in ImageJ by thresholding because of sufficient image contrast, shown in Figure 4-11.

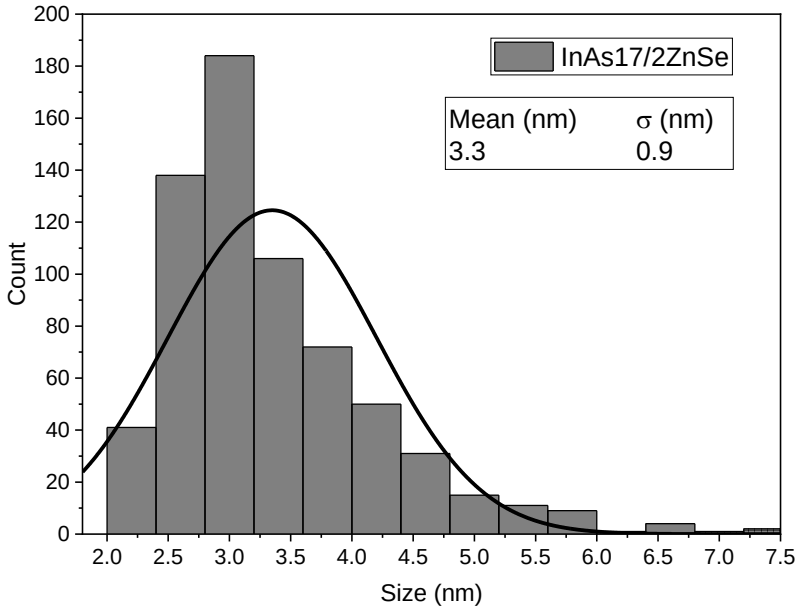

Figure 4-11 – TEM size distribution analysis of InAs17/2ZnSe core-shell nanocrystals emitting at 1100 nm shown in Figure 4-10. Sizes were measured by thresholding the image sets in ImageJ and using the particle size analysis function. The measured mean size was 3.3 nm with a standard deviation of 0.9 nm.

A different semiconductor material, zinc selenide, was used to prevent exciton wavefunction leakage from the core into the shell. Growth of single-shell InAs/ZnSe structures was performed to different thicknesses. The larger bandgap of ZnSe over CdSe, illustrated in Figure 4-6 with a large 1.34 eV conduction band offset, should provide a larger potential barrier to confine the core exciton wavefunction and prevent emission redshift as observed with CdSe shelled nanocrystals. For InAs/ZnSe core-shell structures, a large increase in PLQE was generally observed with similar emission peak positions compared to the core only. Improvement in photoluminescence was observed for thin shells of nominal thickness up to three ZnSe layers corresponding to three complete cation-anion addition sequences, shown in Figure 4-9. TEM imaging of the InAs 17/2ZnSe 2-layer ZnSe is shown in Figure 4-10. The image contrast was sufficient to perform size distribution analysis through image thresholding in ImageJ to obtain a larger sample size. This is displayed in Figure 4-11, showing a skewed size distribution with a modal population of 3 nm smaller particles, with outlier larger particles of up to 7.5 nm, leading to a mean size of 3.3 nm and standard deviation of 0.9 nm. However, insufficient resolution or contrast differences while image thresholding may yield larger particles as individual particles appear twinned. Further additions of shell precursor for the growth of thicker ZnSe shells resulted in a substantial decrease in observed PLQE. This behaviour likely arises because the lattice mismatch between the core and shell material develops strain and introduces defects between the core and shell.[10,11] In the case of thin shells around cores, this strain may be

sustained and epitaxial character between core and shell may be maintained with better passivation of cores. As shell thickness increases, the strain increases to the point where defects are introduced, relieving strain but with loss of epitaxy. These defects cause non-radiative traps states which decrease emission efficiency compared to InAs/ZnSe nanocrystals with thin shells.

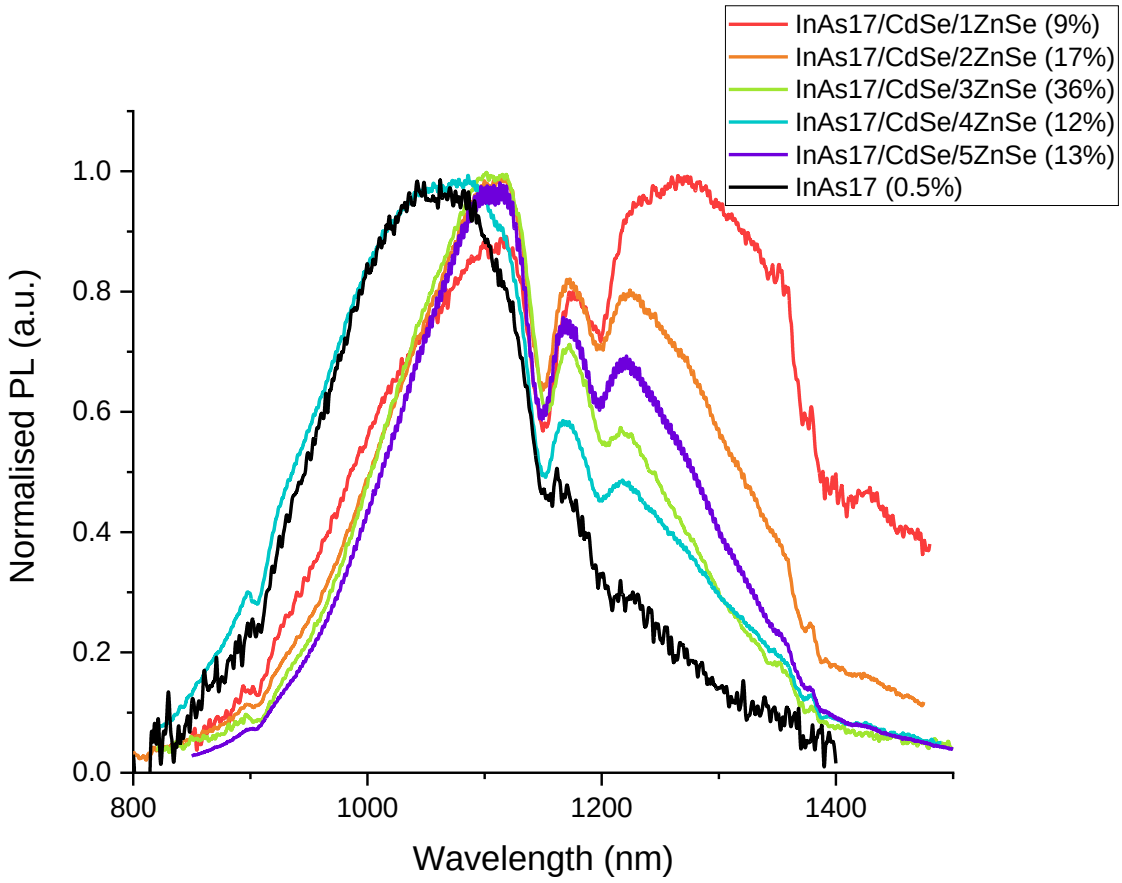

Figure 4-12 – Normalised PL spectra of InAs core and InAs/CdSe/ZnSe core-shell QDs with varying shell thicknesses. The CdSe layer was one nominal layer thickness and the ZnSe layer thickness varied from 1 to 5 nominal layers. Dips in emission at 1150 and 1200 nm are caused by absorption by the toluene solvent.

To achieve higher luminescence efficiencies with InAs QDs, a graded shell strategy with two different shell materials was followed; a thickness series is shown in Figure 4-12. The targeted structure of InAs/CdSe/ZnSe incorporates a thin interlayer shell of CdSe surrounded by a thicker shell of ZnSe. The rationale was to have an epitaxial CdSe shell for low lattice mismatch with the core followed by growth of a thicker ZnSe shell for greater passivation and confinement. This approach was intended to prevent the strain build-up from generating defects at the core-shell interface with the formation of traps; instead transferring strain to the inter-shell interface. The most luminescent sample achieved a PLQE of 36% with a single CdSe layer and 3 ZnSe layers, nearly double the highest luminescence efficiency observed in InAs/ZnSe structures. Starting from an InAs core luminescence efficiency of

around 0.5%, this represented a PL enhancement of 70-fold, with some small observed shifts in emission, shown in Figure 4-13.

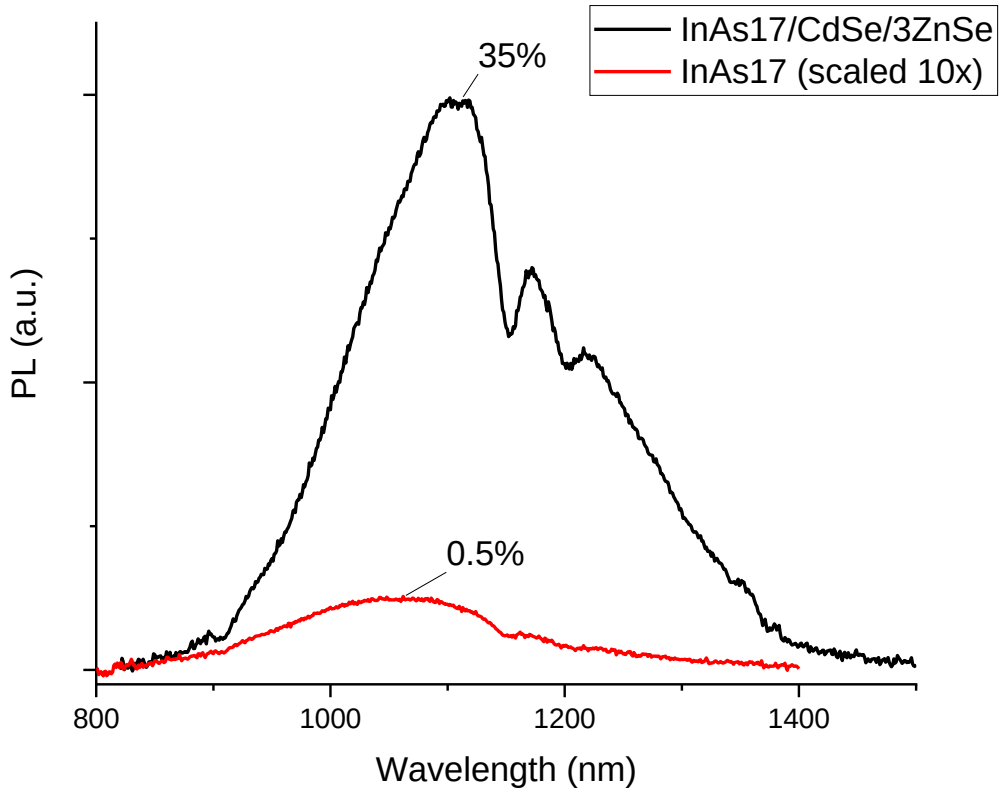

Figure 4-13 – Comparison of luminescence efficiency of core and core-shell InAs QDs. The peaks have been scaled to measured PLQE by area and the InAs emission has been exaggerated by a factor of 10. Dips in emission at 1150 and 1200 nm are caused by absorption by the toluene solvent.

An alternative shell-growth approach was investigated utilising a single-source molecular precursor. Thermal decomposition of zinc diethyldithiocarbamate molecular precursor yields zinc sulfide.[21,22] In a solvent with the presence of ligands and colloidal nanocrystals, the decomposition of the molecular precursor results in growth of ZnS shells around the colloidal nanocrystals. In contrast to SILAR methods which required multiple sequential injections of precursors for shell growth, the single-source molecular precursor route was a simpler procedure. As decomposition rate of the molecular precursor can be controlled by varying the synthesis ligand and reaction temperature, fine control of the shell growth monomer concentration could be achieved. Secondary nucleation of the shell material as a side product could thus be suppressed.

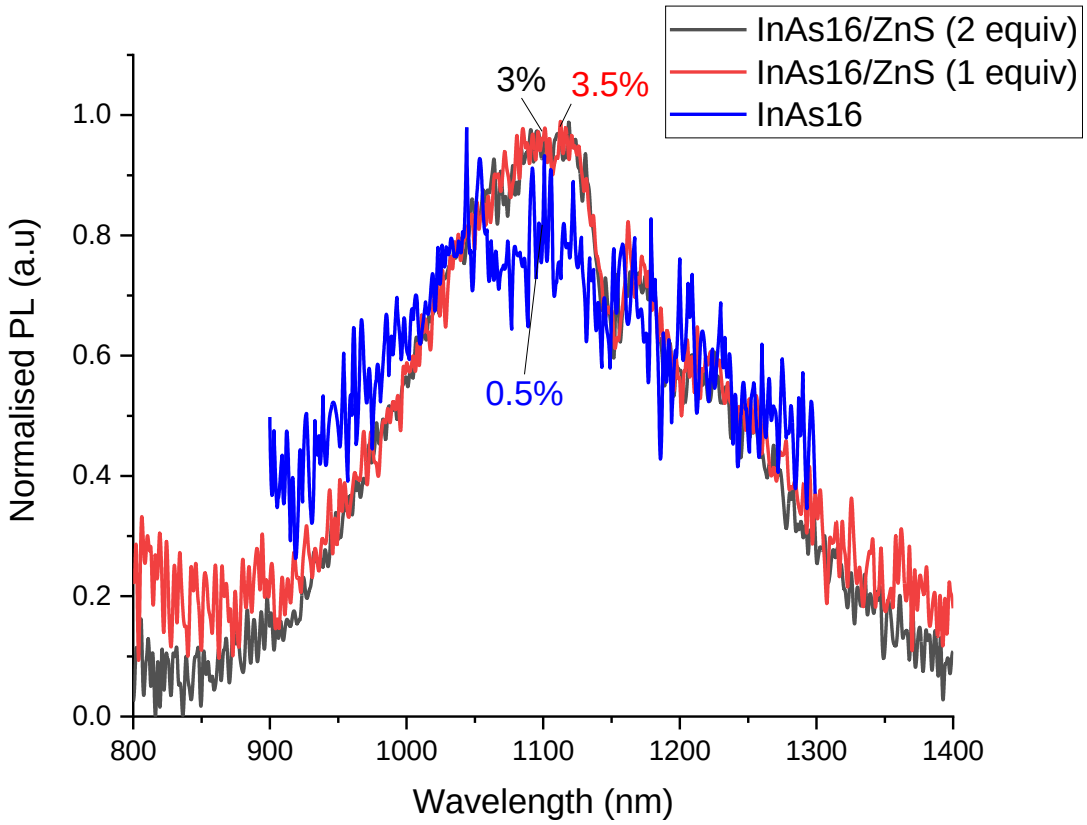

Figure 4-14 – Normalised PL spectra of InAs core and InAs/ZnS core-shell QDs with shell growth through decomposition of a single-source precursor. Dips in emission at 1150 and 1200 nm are caused by absorption by the toluene solvent.

Core-shell InAs/ZnS nanocrystals synthesised using a single-source molecular precursor displayed improved photoluminescence compared to the cores, shown in Figure 4-14. However, luminescence increase was not as large as the for ZnSe SILAR shell with nominal two-layer thickness. In part this may have been due to the greater lattice mismatch between InAs and ZnS compared to ZnSe. Growth of thinner shells resulted in a marginal measured increase in PLQE, although this was within the error of the measurement.

Energy transfer experiments

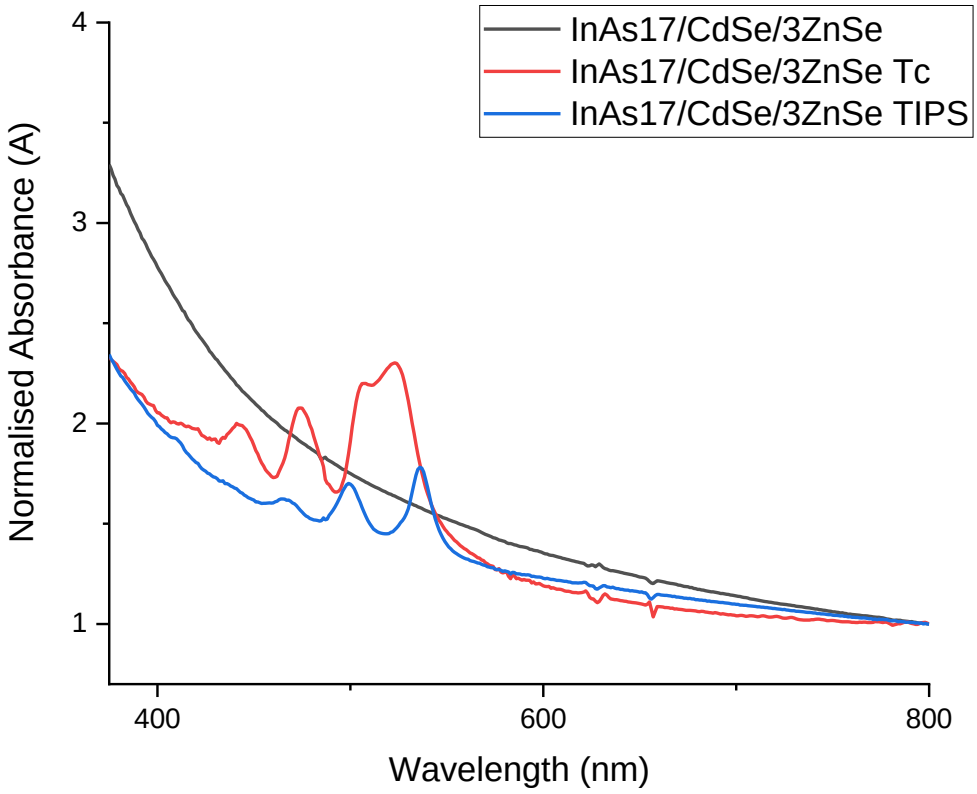

Figure 4-15 – Absorption spectra of encapsulated films of InAs/CdSe/ZnSe QDs fabricated with layer-by-layer deposition and in bilayers with evaporated tetracene and TIPS-tetracene singlet fission molecules. The spectra have been normalised at 800 nm. The evaporation of tetracene procedure for the individual sample was performed by Jesse Allardice.

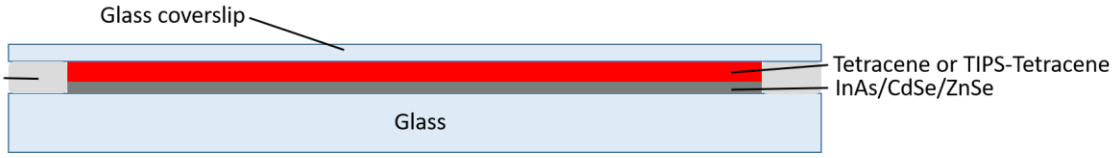

Figure 4-16 – Cartoon schematic of InAs-based QD and organic singlet fission bilayer films.

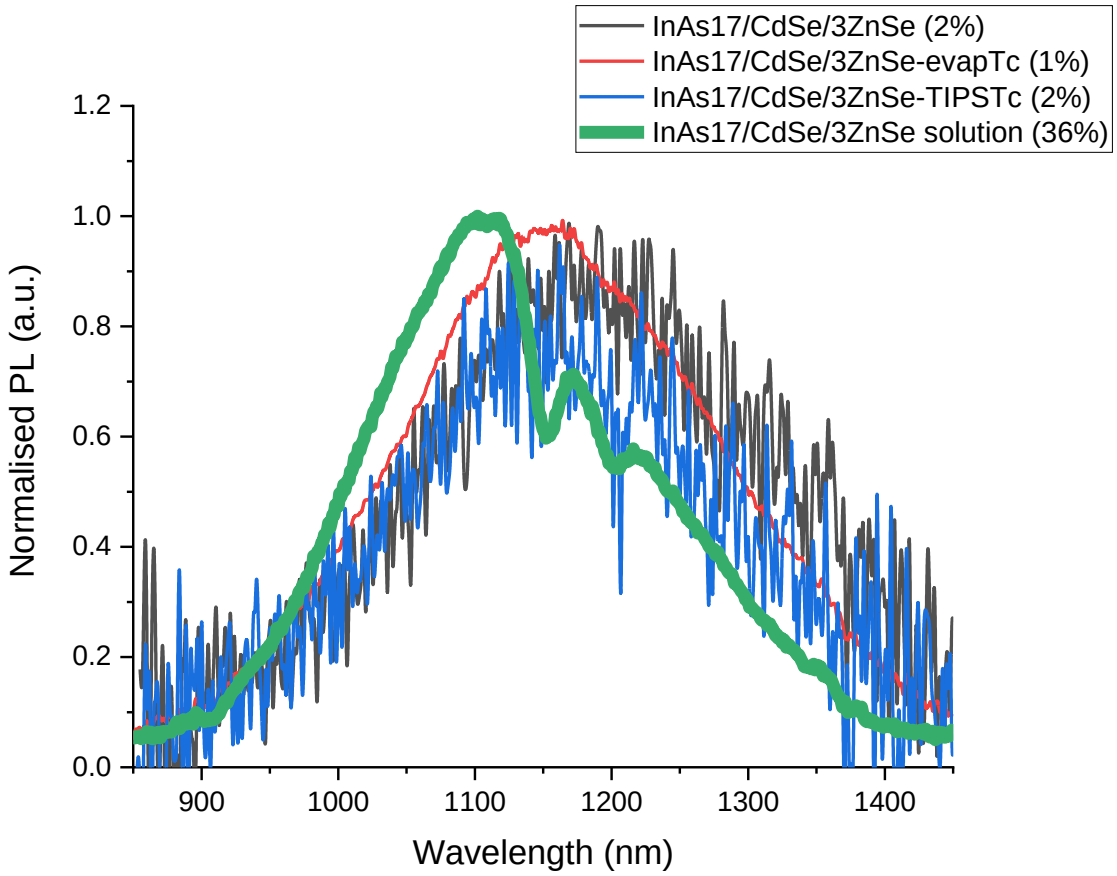

Figure 4-17 – Normalised PL spectra of encapsulated films of InAs/CdSe/ZnSe QDs fabricated with layer-by-layer deposition and in bilayers with evaporated tetracene and TIPS-tetracene singlet fission molecules. The spectrum of the nanocrystal solution is also shown for reference. Dips in emission at 1150 and 1200 nm are caused by absorption by the toluene solvent. Excitation wavelength was 405 nm.

For the targeted application of singlet fission down-conversion, it was necessary to demonstrate luminescence of InAs nanocrystals within the solid state. For these, films of InAs/ZnSe core/shell and InAs/CdSe/ZnSe core/shell/shell were spin-coated onto glass substrates and encapsulated to prevent atmospheric ingress. In addition, bilayers were synthesised with the inclusion of an organic singlet fission material, either tetracene or TIPS-tetracene, shown in Figure 4-15 and as a cartoon schematic in Figure 4-16. In general, photoluminescence efficiency was observed to drop substantially relative to solution, with a notable redshift, shown in Figure 4-17. Spin-coated films of InAs/ZnSe core/shell QDs did not display detectable photoluminescence, indicating less effective passivation. The emission redshift was attributed to the aggregation of nanocrystals in a film, resulting in wavefunction delocalisation across neighbouring nanocrystals. As nanocrystal-nanocrystal spacing is reduced, the exciton wavefunctions overlap, decreasing confinement and observed bandgap. Aggregated nanocrystals also increase the probability of non-radiative decay, as excitons on an emissive QD can decay at a trap on a neighbouring non-emissive QD, contributing to the decrease in observed

luminescence efficiency. As the experiment was intended to demonstrate energy transfer from the singlet fission materials to the InAs-based QDs, attempts to improve the solid state luminescence through dispersion of QDs into polymer matrices were not performed, as this would increase the separation between the organic and QDs.

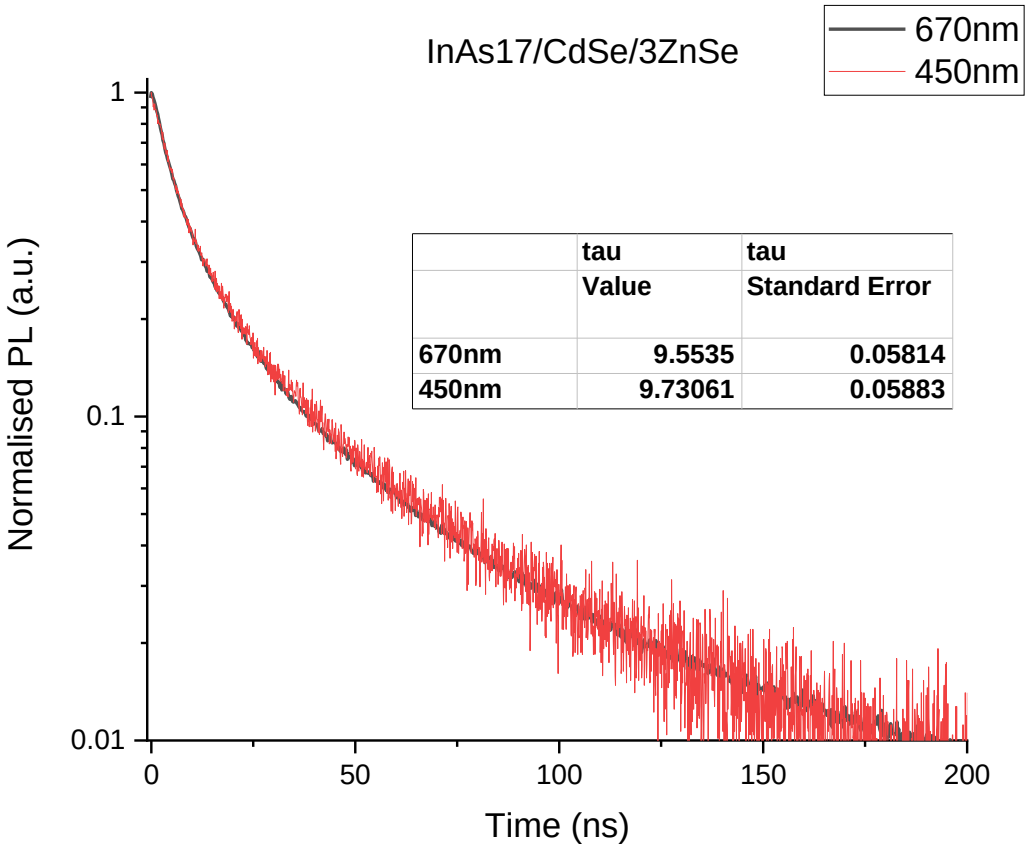

Figure 4-18 – TCSPC of encapsulated films of InAs/CdSe/ZnSe QDs fabricated with layer-by-layer deposition. Excitation was from a white light laser with notch filters at 450 nm or 670 nm at 1 MHz repetition frequency. Lifetime (tau) was obtained by fitting the data to a single exponential decay.

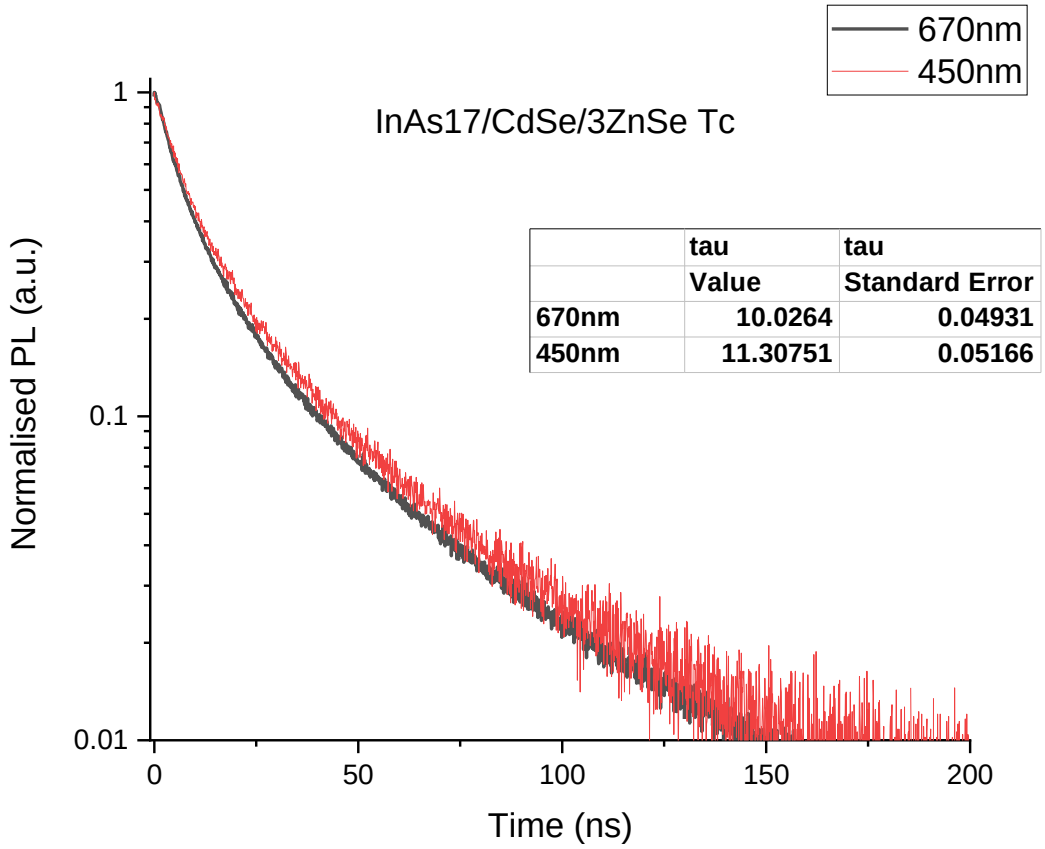

Figure 4-19 - TCSPC of encapsulated films of InAs/CdSe/ZnSe QDs fabricated with layer-by-layer deposition in a bilayer with evaporated tetracene (100 nm). Excitation was from a white light laser with notch filters at 450 nm or 670 nm at 1 MHz repetition frequency. Lifetime (tau) was obtained by fitting the data to a single exponential decay.

Time correlated single photon counting (TCSPC) of InAs/CdSe/ZnSe films was used to investigate the photoluminescence lifetimes of standalone QDs and QDs in bilayers with deposited singlet fission materials. The excitation wavelength was isolated with notch filters to selectively excite the QDs at wavelengths longer than the absorption features in the SF materials (670 nm) or excite both components in the bilayer assembly (450 nm). The films were oriented such that the excitation laser was incident on the singlet fission material where applicable. Luminescence was filtered with a 1000 nm long-pass filter to selectively measure emission from the QDs.

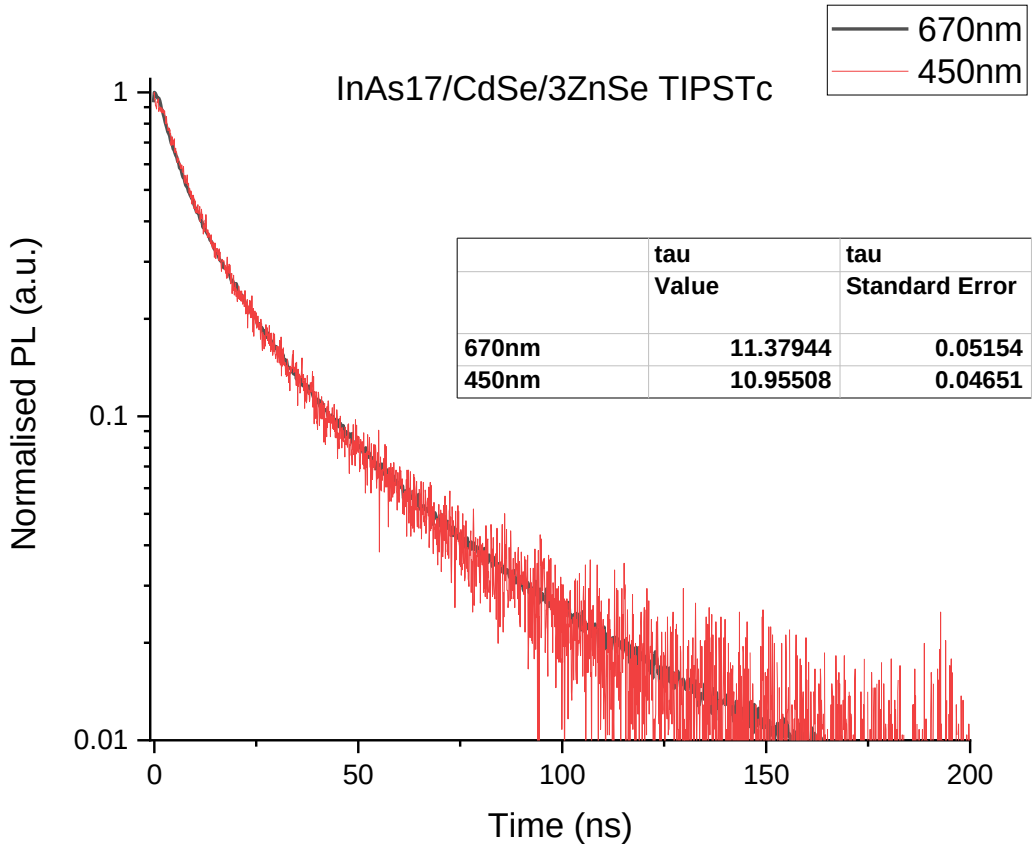

Figure 4-20 – TCSPC of encapsulated films of InAs/CdSe/ZnSe QDs fabricated with layer-by-layer deposition in a bilayer with spin-coated TIPS-tetracene. Excitation was from a white light laser with notch filters at 450 nm or 670 nm at 1 MHz repetition frequency. Lifetime (tau) was obtained by fitting the data to a single exponential decay.

As shown in Figure 4-18 and Figure 4-20, little differences were observed in the photoluminescence lifetimes between selective QD excitation at 670 nm and the ensemble at 450 nm for films containing QD and QD with TIPS-tetracene. In the film containing QDs in tandem with evaporated tetracene, a slight increase, above the fitting error, in photoluminescence lifetime was observed with excitation at 450 nm compared to excitation at 670 nm, shown in Figure 4-19. This indicated that the photoluminescence lifetime of the QDs was increased through interaction with tetracene. To verify any potential energy transfer from the singlet fission organic material to the QDs, photoluminescence excitation (PLE) scans were performed on InAs/CdSe/ZnSe films with and without singlet fission material. However, photoluminescence was not detectable in any of the films, despite displaying photoluminescence during PLQE measurements. This was likely a combination of: poor photoluminescence efficiency of the films, weak excitation intensity of the xenon lamp and poor camera sensitivity with high noise of the InGaAs detector.

4.4 Working conclusions for InAs-based NCs

The luminescence efficiency of quantum dots of the III-V semiconductor material InAs was improved through growth of various core-shell structures. The primary mechanisms for luminescence increase was the passivation of surface defects on InAs nanocrystals and the additional confinement afforded to the QD wavefunction through the formation of type-I semiconductor band structures. However, the luminescence efficiency gained through shell growth was difficult to maintain from transfer from solution to the solid state. Initial investigations into energy transfer using bilayers, or the effect of the tunnelling barrier created by growth of a larger bandgap semiconductor shell were hampered by poor luminescence below facile detection thresholds. More recently, it has been demonstrated that singlet fission ligands can facilitate triplet energy transfer into QDs.[34] This may provide an additional method of studying energy transfer in the InAs QD system without transferral to the solid state and the observed severe losses in luminescence efficiency. Further work through the use of polymer matrices as a host for embedded InAs quantum dots may be attractive to minimise concentration quenching upon transferral to the solid state, as well as providing an additional physical barrier for atmospheric degradation processes. However, the relative inaccessibility of the precursors and the difficult, involved synthetic methods remain, making InAs a less-attractive NIR emitter material compared to the similar-bandgap lead chalcogenide materials such as PbS. As such, the literature remains relatively sparse.

4.5 $CuInSe_2$/ZnS

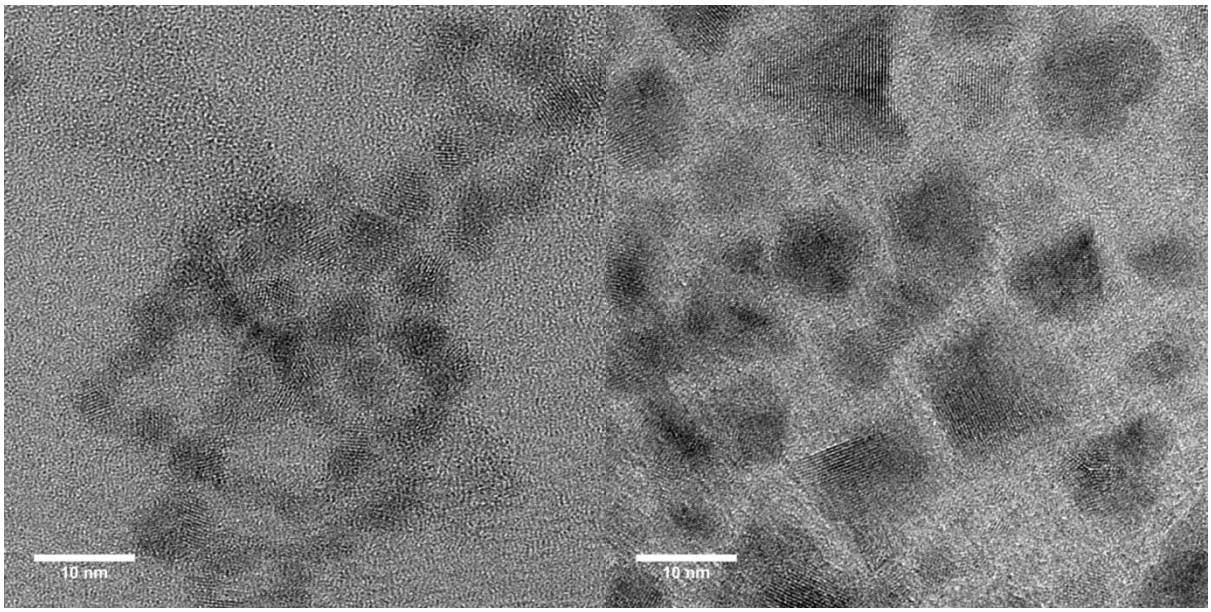

Figure 4-21 – TEM images of $CuInSe_2$ (left) and $CuInSe_2$/ZnS (right) with one growth layer of ZnS.

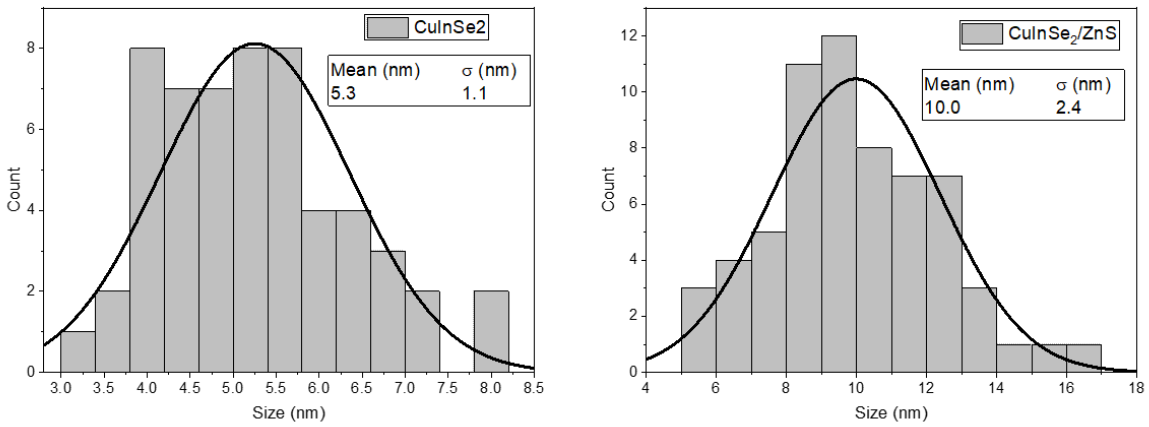

Figure 4-22 – TEM size distribution analysis of $CuInSe_2$ (left) and $CuInSe_2$/ZnS (right). Sizes were measured by manually taking the mean length along perpendicular axes. The mean size of $CuInSe_2$, with negligible photoluminescence was 5.3 nm with a standard deviation of 1.3 nm. The mean size after one ZnS shell growth layer was 10 nm with a standard deviation of 2.4 nm.

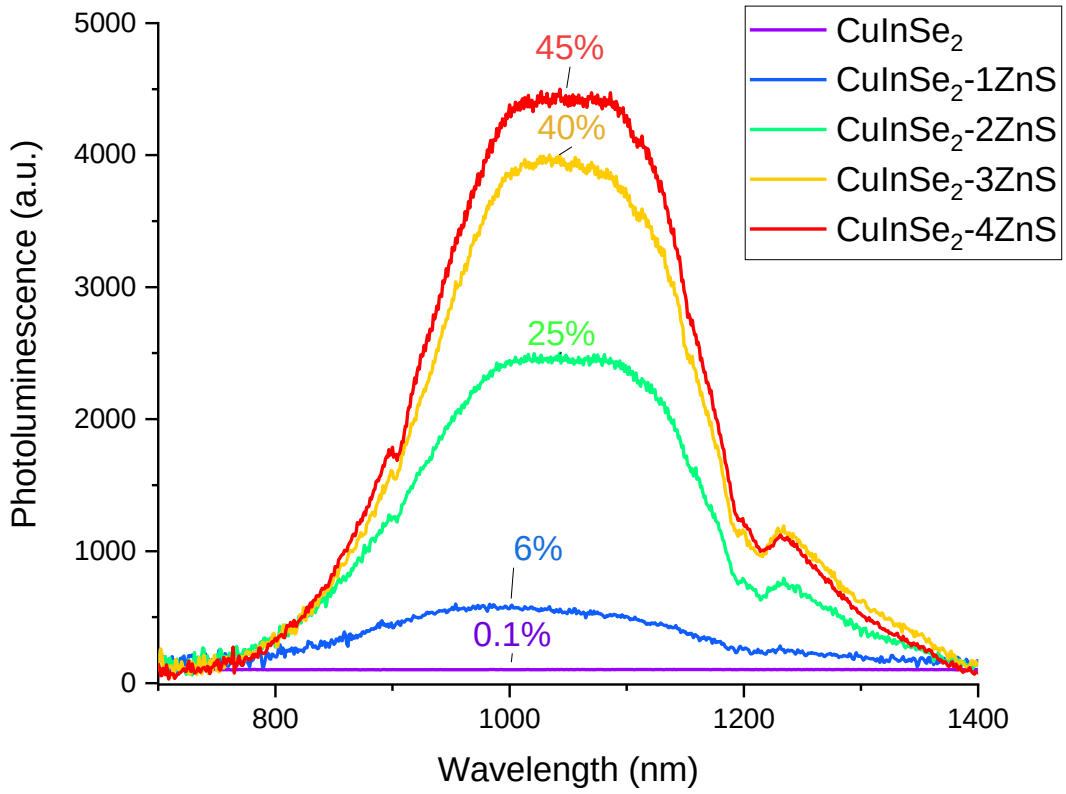

Figure 4-23 – PL spectra of $CuInSe_2$ and $CuInSe_2$ core-shell nanocrystals with varying shell thicknesses indicated by nominal growth stages. The emission peak has been scaled to the measured PLQE by area.

Transmission electron microscopy, shown in Figure 4-21, of $CuInSe_2$ and $CuInSe_2$/ZnS showed differences between core and core-shell structures with a single growth sequence. Size distribution analysis, shown in Figure 4-22, was performed by manually measuring the mean length along perpendicular axes. The mean size of core $CuInSe_2$ was 5.3 nm with a standard deviation of 1.3 nm. The mean size after one ZnS shell growth layer was 10 nm with a standard deviation of 2.4 nm, indicating asymmetric growth across nanocrystals. The unshelled $CuInSe_2$ nanocrystals possessed negligible emission and were colloidally unstable, with large fractions aggregating and precipitating after a few days. Growth of a ZnS shell in one stage resulted in stable colloids and an increase in PLQE to 6%. Increasing ZnS shell thickness with up to four growth stages resulted in PLQE increase up to 45%, shown in Figure 4-23. The nanocrystals were still emissive after exposure to air over several weeks. The emission was observed to be quite broad, indicating a large size distribution. The observed peak width was consistent with other literature reports.[35] The luminescence efficiency was improved through the passivation of surface non-radiative fast traps, as evidenced by the negligible emission from core-only nanocrystals and the immediate improvement with a single growth stage. Increased growth stages resulted in better passivation with implied thicker shells. The exciton Bohr radius of 10.6 nm for $CuInSe_2$ was approached in size by core-shell nanocrystals with a single shell layer observed in TEM.[16,36] Thicker shells with more growth stages thus likely helped to confine the exciton wavefunction away from the surface and within the nanocrystal core. The bulk bandgap of $CuInSe_2$ is around 1 eV, indicating that these nanocrystals possessed weak confinement.[16]

4.6 Working conclusions for $CuInSe_2$-based NCs

Further work on $CuInSe_2$ is required to determine suitability in applications involving energy transfer. The tunnelling barrier of the ZnS shell to triplet energy transfer has not yet been investigated thoroughly in any nanocrystal system. The luminescence efficiency of $CuInSe_2$/ZnS was controllable through the number of ZnS shell growth stages. The implication was increased shell thickness resulted in greater luminescence efficiency through greater surface passivation and also greater exciton confinement. As a non-toxic material with a facile synthesis with readily controllable passivation, it remains attractive to study $CuInSe_2$ based materials as near-infrared emitters.

4.7 References

1. Mimura, T., Hiyamizu, S., Fujii, T. & Nanbu, K. *Japanese Journal of Applied Physics* **19**, L225–L227 (1980).

2. Yamaguchi, M. *Solar Energy Materials and Solar Cells* **75**, 261–269 (2003).

3. Nakamura, S., Mukai, T. & Senoh, M. *Japanese Journal of Applied Physics, Part 2: Letters* **30**, (1991).

4. Liu, W., Lee, J. S. & Talapin, D. V. *Journal of the American Chemical Society* **135**, 1349–

1357 (2013).

5. Kan, S. H., Aharoni, A., Mokari, T. & Banin, U. *Faraday Discussions* **125**, 23–38 (2004).

6. Peng, X., Wickham, J. & Alivisatos, a. P. *Journal of the American Chemical Society* **120**, 5343–5344 (1998).

7. Guzelian, a. a., Banin, U., Kadavanich, A. V., Peng, X. & Alivisatos, a. P. *Applied Physics Letters* **69**, 1432 (1996).

8. Adachi, S. *Optical Constants of Crystalline and Amorphous Semiconductors* 257–267 (Springer US, 1999).

9. Uesugi, H., Kita, M. & Omata, T. *Journal of Crystal Growth* **416**, 134–141 (2015).

10. Aharoni, A., Mokari, T., Popov, I. & Banin, U. *Journal of the American Chemical Society* 257–264 (2006).

11. Cao, Y. & Banin, U. *Journal of the American Chemical Society* 9692–9702 (2000).

12. Yu, P., Beard, M. C., Ellingson, R. J., Ferrere, S., Curtis, C., Drexler, J. *et al. The journal of physical chemistry. B* **109**, 7084–7 (2005).

13. Franke, D., Harris, D. K., Chen, O., Bruns, O. T., Carr, J. A., Wilson, M. W. B. *et al. Nature Communications* **7**, 1–9 (2016).

14. Li, W., Pan, Z. & Zhong, X. *Journal of Materials Chemistry A* **3**, 1649–1655 (2015).

15. van der Stam, W., Bladt, E., Rabouw, F. T., Bals, S. & de Mello Donega, C. *ACS Nano* (2015).

16. Zhong, H., Wang, Z., Bovero, E., Lu, Z., van Veggel, F. C. J. M. & Scholes, G. D. *The Journal of Physical Chemistry C* **115**, 12396–12402 (2011).

17. Li, L., Pandey, A., Werder, D. J., Khanal, B. P., Pietryga, J. M. & Klimov, V. I. *Journal of the American Chemical Society* **133**, 1176–1179 (2011).

18. Wu, K., Li, H. & Klimov, V. I. *Nature Photonics* (2018).

19. Becker, G. *Zeitschrift für anorganische …* **462**, 113–129 (1980).

20. Wells, R. L., Self, M. F., Johansen, J. D., Laske, J. A., Aubuchon, S. R., Jones, L. J. *et al. Inorganic Syntheses* **31**, 150–158 (1996).

21. Chen, D., Zhao, F., Qi, H., Rutherford, M. & Peng, X. *Chemistry of Materials* **22**, 1437–1444 (2010).

22. Dethlefsen, J. R. & Døssing, A. *Nano Letters* **11**, 1964–1969 (2011).

23. Liu, H., Zhitomirsky, D., Hoogland, S., Tang, J., Kramer, I. J., Ning, Z. *et al. Applied Physics Letters* **101**, 1–4 (2012).

24. Thompson, N. J., Wilson, M. W. B., Congreve, D. N., Brown, P. R., Scherer, J. M., Bischof, T. S. *et al. Nature Materials* **13**, 1039–1043 (2014).

25. Ehrler, B., Wilson, M. W. B., Rao, A., Friend, R. H. & Greenham, N. C. *Nano Letters* **12**, 1053–1057 (2012).

26. Tabachnyk, M., Ehrler, B., Gélinas, S., Böhm, M. L., Walker, B. J., Musselman, K. P. *et al. Nature Materials* **13**, (2014).

27. de Mello, J. C., Wittmannn, H. F. & Friend, R. H. *Advanced materials (Deerfield Beach, Fla.)* **9**, 230 (1997).

28. Greenham, N. C., Samuel, I. D. W., Hayes, G. R., Phillips, R. T., Kessener, Y. A. R. R., Moratti, S. C. *et al. Chemical Physics Letters* **241**, 89–96 (1995).

29. Fulmer, G. R., Miller, A. J. M., Sherden, N. H., Gottlieb, H. E., Nudelman, A., Stoltz, B. M. *et al. Organometallics* **29**, 2176–2179 (2010).

30. Kim, S. W., Zimmer, J. P., Ohnishi, S., Tracy, J. B., Frangioni, J. V & Bawendi, M. G. *J. Am. Chem. Soc.* **127**, 10526–10532 (2005).

31. Xie, R., Battaglia, D. & Peng, X. *Journal of the American Chemical Society* **129**, 15432–15433 (2007).

32. Wawrzynczyk, D., Szeremeta, J., Samoc, M. & Nyk, M. *APL Materials* **3**, 116108 (2015).

33. Wei, S. H. & Zunger, A. *Applied Physics Letters* **72**, 2011–2013 (1998).

34. Davis, N. J. L. K., Allardice, J. R., Xiao, J., Petty, A. J., Greenham, N. C., Anthony, J. E. *et al. The Journal of Physical Chemistry Letters* **9**, 1454–1460 (2018).

35. Yarema, O., Bozyigit, D., Rousseau, I., Nowack, L., Yarema, M., Heiss, W. *et al. Chemistry of Materials* **25**, 3753–3757 (2013).

36. Du, C.-F., You, T., Jiang, L., Yang, S.-Q., Zou, K., Han, K.-L. *et al. RSC Adv.* **4**, 33855–33860 (2014).

Chapter 5 Measurement of Photoluminescence Quantum Efficiency

5.1 Introduction

Photoluminescence quantum efficiency (PLQE) is the fraction of photons emitted from the photons absorbed by a luminescent material. A PLQE of 100% means every absorbed photon results in an emitted photon and no non-radiative losses occur. Across the different projects featured within this work, it was necessary to measure PLQE for a variety of materials. Over the course of these projects, it was discovered that satisfactory measurement reproducibility was difficult to achieve, leading to doubts about their accuracy. For singlet fission down-conversion assemblies, described previously and in greater detail within this Chapter, quantitative comparison of PLQE with different excitation wavelengths was required. Prior to the meticulous appreciation of factors affecting the experiment, the uncertainties manifest precluded any firm conclusions from being drawn regarding down-conversion efficiency. In this work, previously unknown potential sources of systematic error have been identified and random errors quantified, to provide accurate values of PLQE with minimised quantifiable uncertainties.

The measurement of absolute photoluminescence quantum efficiencies has been of critical interest in the study of luminescent materials such as semiconductor nanocrystals, with their widespread adoption in light-emitting display and biomedical applications.[1–5] The luminescence efficiency of a material is affected by its form and chemical environment, thus it is necessary to perform characterisation of luminescence efficiency in a range of realistic conditions.

With interest in solid-state luminescent materials, it becomes necessary to measure samples as films with anisotropic emission profiles. Immediately, a problem arises as the angular dependence of the emission become highly dependent on refractive indices of the sample and substrate as well as imperfections such as roughness and non-uniform thickness. For these samples, a means of allowing for the angular dependence of the emission is required. This is typically achieved through the use of an integrating sphere which effectively converts the angle-dependent emission into an isotropic radiance through multiple scattering off a diffusely reflective surface.

As sample complexity increases with multiple intermixed components, additional problems are encountered. In the case of singlet fission down-conversion assemblies, measurements of photoluminescence quantum efficiency require accurate quantitative measurement across a wide spectral and absorbance range. It becomes necessary to measure spectrally distant photoluminescence

emitted by a minority component fraction through selective excitation of both optically dense and optically thin components.

The multitude of interlinked factors affecting the measurement means great care must be placed in the design of the experiment in order to provide meaningful results. With insufficient attention, correct values may only be achievable for a narrow spectral range for excitation and/or emission. In addition, a correct value may be obtained only coincidentally through cancellation of competing systematic errors. This gives the potential for misleading validation of incorrectly-obtained values through naïve agreement with measurements extant in literature or through different measurement methods.[6,7]

5.2 Isotropic emitters – Measurement with fluorescence spectrometer

In the simplest conditions, the measurement of dilute solutions with isotropic emission and negligible self-absorption, the experimental setup may consist of both fluorescence and absorption spectrometers; a cartoon of the former is shown in Figure 5-1. The absorbance and fluorescence of a luminescent species in a known solvent is measured. A reference fluorescence standard of known quantum yield is then measured in both absorbance and fluorescence with the same measurement conditions. The quantum yield may then be calculated by comparing the two materials:

$$\eta = \eta_{ref} \times \left(\left(\frac{PL}{PL_{ref}} \right) \left(\frac{1 - 10^{-A_{ref}}}{1 - 10^{-A}} \right) \left(\frac{n^2}{{n_{ref}}^2} \right) \right)$$

where η is quantum efficiency, PL is the integral of the photoluminescence signal in photon units, A is absorbance and n is the refractive index of the solvent. This formula simply compares the measured photoluminescence intensity for a sample at measured absorbance against a reference standard sample of known PLQE and with measured PL intensity and measured absorbance. The solvent correction factor is used if the refractive index of the solvent is different to the solvent for the reference standard to account for light outcoupling efficiency from the sample to air.

Although a value for PLQE may be obtained from a single measurement from each sample, greater accuracy may be obtained through measurement at multiple concentrations for both materials within the limit of the linear absorbance regime (low concentrations with A much below 0.1). The gradients of the linear fits obtained for photoluminescence against absorbance at different concentrations for both samples is then proportional to the PLQE.[8–12]. The gradient of the PL intensity vs. absorbance fit for the reference standard is proportional to the known PLQE, whilst the unknown PLQE of the sample may be obtained by taking the ratio of its gradient relative to the reference gradient, then multiplying by the known PLQE.

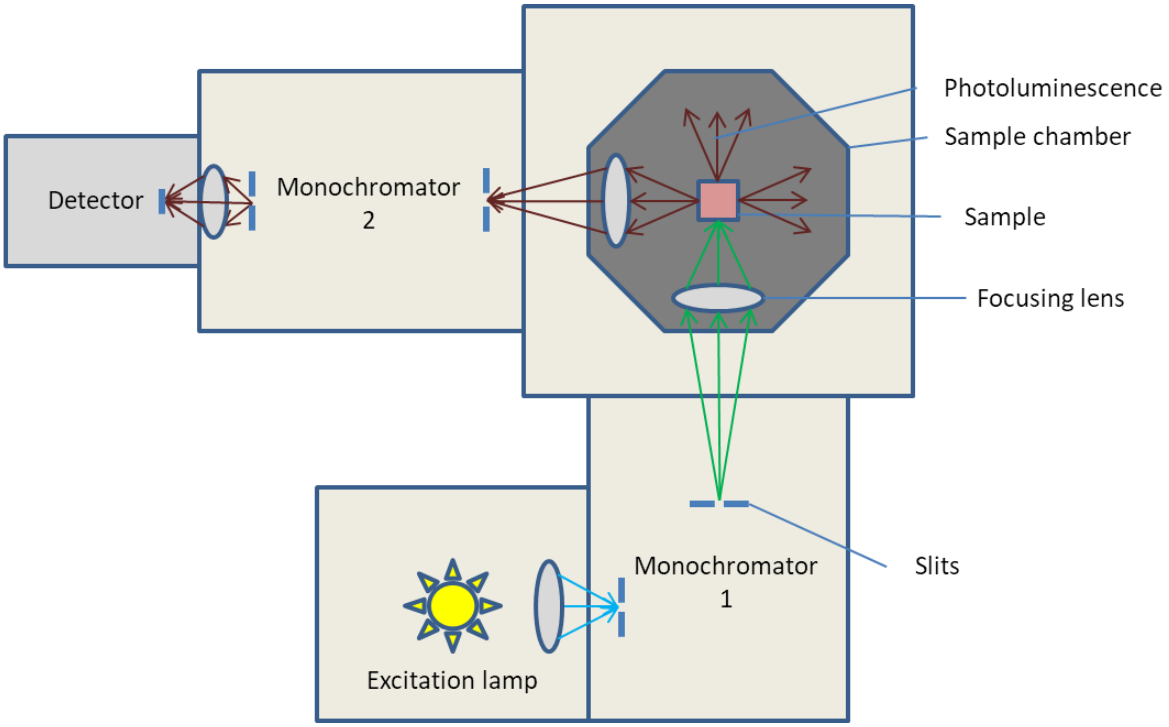

Figure 5-1 – Schematic of fluorescence spectrometer or 'fluorimeter'

The sample is measured in absorbance and fluorescence at each concentration. Ideally dilutions are performed systematically in a series dilution at known concentrations. This minimises compounding of uncertainties arising from detector uncertainty and zeroing errors particularly for the absorbance measurement. In fluorescence, the sample is excited at fixed wavelength and power. The absorption at this wavelength may be determined directly from the absorbance spectrum. In very dilute conditions when the measured absorbance may be within the instrumental sensitivity or noise of the absorbance spectrometer, the value for optical density may be worked out from the known concentration.[12]

As the concentration of the luminescent species increases, a deviation in the linearity of the photoluminescence vs absorbance relationship will be observed. In addition, self-absorption of photoluminescence becomes progressively more significant resulting from the area overlap between PL and absorbance spectra of the sample, which is directly linked to the values of the Stokes shift and emission bandwidth. At higher concentrations, fluorescence quenching effects from intermolecular interactions also decrease the fluorescence quantum yield. Fluorescence reference standards are correct within particular concentration ranges.[9,10,12–14]

The geometry of the fluorescence measurement is typically at a right angle with emission measured at 90 ° to excitation, thus a fluorescence cuvette is transparent on all four faces in a typical 10 mm × 10 mm form factor. The cuvette should preferably possess a wide wavelength transmission range encompassing the regions of interest. Manufacturing tolerances mean each side may be not equivalent, thus care should be taken when using the cuvettes in an absorption spectrometer, where

inconsistent orientation may contribute to zeroing errors, particularly in the blue or UV spectral regions. For fluorescence, the refractive index of the cuvette may be ignored provided the cross-sections of the faces have no thickness variation, meaning they are optically flat and not wedged.

The physical properties of the solvent must also be considered, primarily the refractive index, which is variable with wavelength and the absorption/transmission spectrum within the measurement range. Ideally, refractive index should vary only marginally across the measurement range and absorption should be negligible. Solvatochromic effects arising from different solvent polarity may also change the fluorescence spectral output and emission efficiency of the fluorophore. Reference fluorescence standards are associated with specified solvent environments.[9]

Calibration of spectrometer

The fluorescence spectrometer is required to be calibrated for spectral sensitivity with a source of known spectral shape. Allowing for the limitations of detector sensitivity and saturation, meaning the noise floor and the onset of nonlinearity, this calibration must be performed with the same acquisition settings as the measurement as to not unduly alter the detector response of the spectrometer. In this case with a fluorescence spectrometer, acquisition settings primarily signify monochromator parameters such as slit sizes and other apertures controlling signal intensity. The throughput and slit sizes should be optimised for sufficient signal and spectral resolution for the measurement without saturating the detector during calibration.

For the calibration measurement, the excitation source of the spectrometer is left switched off or blocked with a suitable cover such as black card. The calibrated light source is placed in the position of the sample holder aligned toward the detector. Care must be taken in order to align the source with the collection optics – the correct height and distance from the light source should be maintained in order to minimise any errors from possible angular dependence of lamp emission. Lamps with significant angular-dependent emission should be avoided as the specified ‘calibrated’ output is not readily obtained in use.

Another source of error in these measurements is the stability of the excitation source of the fluorescence spectrometer, usually a xenon arc-lamp. In modern spectrometer systems, a separate reference photodiode may exist which is able to monitor the emission output of the excitation source. This may be used to correct the emission spectrum by removing the effect of transient fluctuations in the lamp’s power and the resulting change in measured photoluminescence.

5.3 Anisotropic emitters – Integrating sphere measurements

When sample configurations produce anisotropic emission profiles or spectrally suitable emission standards become unavailable, an alternative measurement method is required. To eliminate angular dependence of sample photoluminescence, an integrating sphere may be used.

An integrating sphere, illustrated in Figure 5-2 (top), is typically a sphere coated with a diffusely-reflecting material such as barium sulfate or PTFE. One or more removable ports allow the introduction of samples, as well as containing openings for the excitation and collection optical paths. The opening sizes are kept to a minimum in order to minimise light loss and increase the effective radiance in the sphere. The collection optics is typically an optical fibre, which is in turn coupled into a spectrometer. A baffle prevents low-order reflections or direct emission from the sample from reaching the fibre.

Greenham/De Mello method

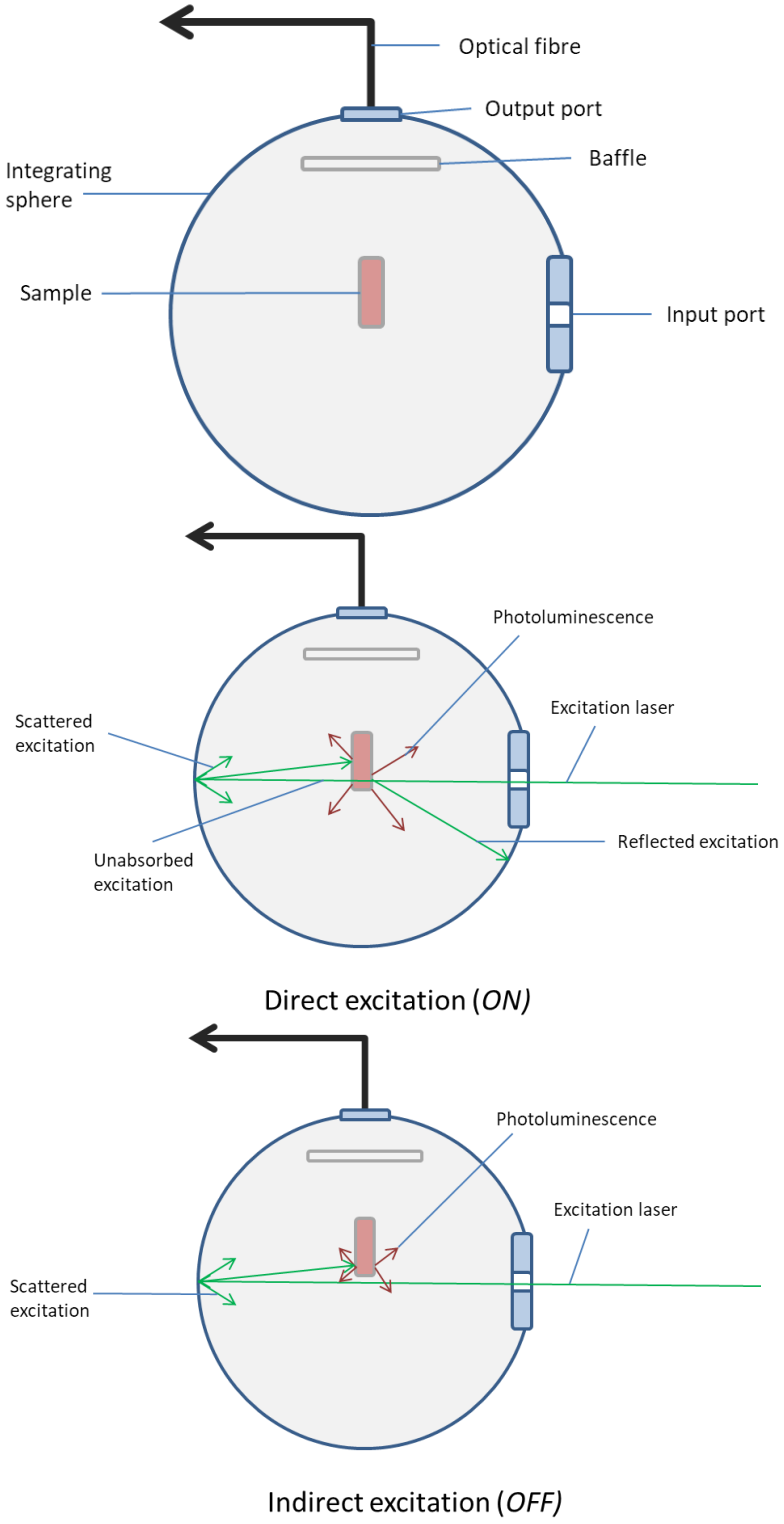

Figure 5-2 – Top: integrating sphere measurement setup for the determination of photoluminescence quantum efficiency. The optical fibre is coupled into an imaging spectrograph or spectrometer. Middle: direct excitation path for photoluminescence measurement. The excitation laser is incident on the sample before scattering on the sphere walls. The sample is illuminated by absorption of incident laser and diffusely-scattered light. Bottom: indirect excitation path for photoluminescence measurement. The

excitation laser is incident on the sphere walls and scattered. The sample is illuminated by diffusely-scattered light only.

The measurement of photoluminescence quantum efficiency in an integrating sphere may be determined from the method of Greenham et al.[15] The subsequent, more commonly used method of de Mello et al. used a CCD spectrograph instead of a calibrated photodiode for measurement as the crucial difference.[7] For the purposes of absolute quantum efficiency measurements, the former is more simple and robust as a quantum counter. However in practice, the simultaneous acquisition of spectral data results in the latter being more commonly employed, despite greater instrumental factors which must be considered to obtain an accurate measurement.[6]

The essence of integrating sphere methods is the measurement of the sample and system in three conditions. Firstly, the excitation laser is allowed to scatter within the sphere with no sample in order to measure the incident laser power. Secondly, the sample is placed within the sphere and excited with the laser directly, illustrated in Figure 5-2 (middle). Finally, the sample is left within the sphere but the laser is allowed to strike the walls of the sphere, illuminating the sample with diffusely scattered light, shown in Figure 5-2 (bottom). For measurements where excitation and emission are spectrally separated, such as with excitation in the visible and photoluminescence in the near-infrared, separate acquisitions in the three conditions at the appropriate measurement window are taken as necessary with appropriate band-pass filters.

The measurement of laser power and PL intensity in these three conditions yields the following expressions:

NO_{LAS} is the measured laser signal, signal meaning photons integrated over the width of the peak, without sample. ON_{LAS} is the measured laser signal with direct sample illumination. OFF_{LAS} is the measured laser signal with diffuse laser excitation.

In the case of direct illumination, portions of the incident laser will be initially reflected, absorbed or scattered. The remainder will be transmitted and scatter on the integrating sphere wall, with another portion of this absorbed by the sample. From this, the measured ON_{LAS} signal can be expressed as a fraction of the incident laser:

$$ON_{LAS} = NO_{LAS}(1 - A)(1 - d),$$

where A is the sum of reflection and transmission and d is the absorption fraction from diffuse illumination. OFF_{LAS} can therefore be expressed as a fraction of the incident excitation:

$$OFF_{LAS} = NO_{LAS}(1 - d).$$

The absorbed fraction A can then be expressed as a ratio of the laser signals from direct and indirect illumination:

$$A = \left(1 - \frac{ON_{LAS}}{OFF_{LAS}}\right).$$

The total light detected from direct illumination, including emitted photoluminescence can be expressed as

$$ON_{LAS} + ON_{PL} = (1 - A)(OFF_{LAS} + OFF_{PL}) + \eta A \times NO_{LAS},$$

where ON_{PL} and OFF_{PL} are photoluminescence signals from direct and indirect excitation respectively and η is the photoluminescence quantum efficiency.

By incorporating the expression for A and rearranging for η, the expression becomes

$$\eta = \frac{ON_{PL} - (1 - A)OFF_{PL}}{A \times NO_{LAS}}.$$

Limitations

A key assumption for this formula is the isotropic radiance within the sphere, or the unimportance of the initial direction of scattering. As this is not entirely true, it is thus critical to ensure the exit port is sufficiently shielded with the baffle and that any laser spot does not strike near the exit port.[16,17]

The method also does not account for self-absorption in the sample. For inhomogeneous samples, the laser striking different regions of the sample when switching between measurement conditions and spectral regions may lead to inconsistently measured absorption and photoluminescence and incorrect values. Undue scattering or guiding of the excitation light by substrate or the sample itself onto other regions may also lead to extraneous absorption or photoluminescence.

5.4 Sources of Systematic Error

The measurement of PLQE is sensitive to a range of potential sources of systematic error. Often in previous literature, insufficient attention has been given to some of these sources, potentially denigrating their importance to the naïve experimenter.[7,8] Throughout the course of this work, these aspects have been identified and detailed progressively to understand their importance and decrease their contribution to systematic errors in the measurement setup. The PLQE measurement setup consisted of integrating sphere (Labsphere 4P-GPS-053-SL), collection fibre (Andor SR-OPT-8019), spectrograph (Andor Kymera-328i) and detectors (Andor iDus 420 and iDus InGaAs 1.7).

Calibration of spectrograph

As with all absolute measurements, calibration of the spectrometer is critical in order to achieve an accurate measurement. The idiosyncratic spectral response of individual instrument setups necessitates this procedure.[8]

For the purposes of calibration, a lamp with a known emission spectrum is required to determine the spectral response of the optical system. Although specified outputs may be provided with all commercial calibration sources, these should not be taken at face value. Care should be taken to recognise the calibration methodology for the light source itself and determine if the specified spectral output is valid for the optical system to be calibrated. This particular problem was encountered extensively with commercial 'calibration lamps' such as the Ocean Optics LS-1-CAL and HL-3P-CAL. In particular, it was found that the provided calibrated output spectra were not applicable by the end user, having been calibrated with a different optical system than supplied with the equipment. The additional optical elements used in calibration were a different optical fibre for coupling into the calibration spectrometer and a different cosine corrector to connect the lamp to the optical fibre. The inclusion of a cosine corrector suggested that the lamp output possessed some angular dependence. Testing the angular dependence by illuminating the integrating sphere input port at different angles demonstrated significant anisotropic emission without cosine corrector, shown in Figure 5-3.

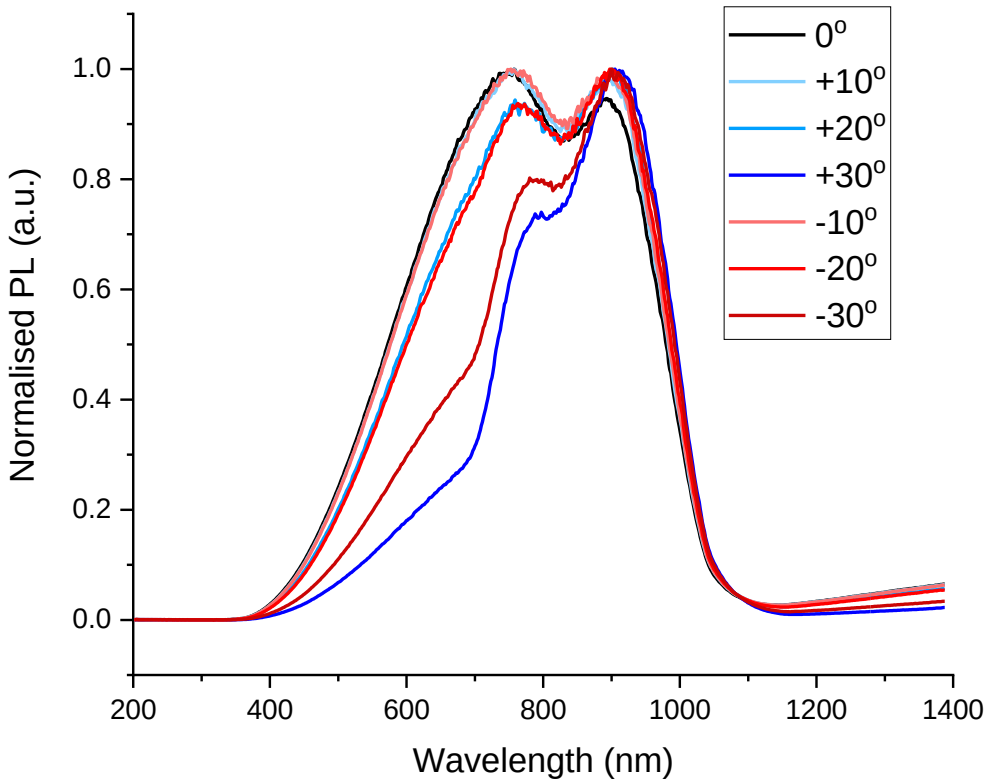

Figure 5-3 – Emission of Ocean Optics HL-3P-CAL lamp without cosine corrector at different observation angles shining into integrating sphere port baffled with two irises. The detector was the silicon iDus 420, with light from the second order diffraction visible at long wavelengths indicated. The angles were roughly measured by hand with an angle measurer.

The difficulties were compounded when it was discovered that the provided cosine corrector, used to homogenise the angular spectral output, dramatically decreased the output intensity and was different to the one used for calibration, invalidating the provided calibration spectrum.

For simplicity and versatility, a light source with isotropic emission is preferred for calibration. The spectral output should then be constant irrespective of observation aspect. For assurance of spectral output matching quoted specifications, accredited calibration certification such as to NIST-traceable standards is essential. In addition, the calibration method and means of measurement should be recognised to ensure the validity of the calibration in the desired usage condition. Sufficient power output across the entire spectral range of instrument sensitivity is required to minimise noise within the calibration spectrum. The small excitation entrance port restricts light input thus a reasonably powerful calibration source may be required. A suitable source is a quartz tungsten halogen-type (QTH) lamp with controlled power supply to minimise output fluctuation. The calibration source will also contain a specified degree of wavelength-dependent uncertainty which is converted into a

systematic error once embedded within a sensitivity curve. For a quality lamp, the expanded uncertainty may be as high as 2% for the extremes of the spectrum and as low as 0.5% for the middle.[18]

If an isotropically-emitting calibration source is not available, it is possible to use a lamp with a different form factor such as the Ocean Optics lamps previously mentioned. However, as directional lamps with a planar emitter have the inherent problem of angular-dependent variable spectral output requiring meticulous alignment and baffling. An optical device such as a cosine corrector may be used to minimise the variability, with the caveat that the lamp calibration will be specific to the individual system, thus the lamp calibration itself must be performed with the same optical fibre and cosine corrector to be used in calibrating the measurement setup.

A 200 W NIST-traceable QTH lamp (Newport 63976-200QC-OA) was obtained for the purpose of calibration following the discovery that the Ocean Optics calibration lamps provided insufficient intensity for calibration in the near-infrared with cosine corrector fitted to reduce angular-dependent emission. The lamp was illuminated into the input port of the integrating sphere with the light pathway baffled with black card to avoid scatter within the room and the spectrum was recorded for a range of spectral regions for each detector as appropriate.

The output of a calibration lamp is typically quoted in units of spectral irradiance mW cm^{-2} nm^{-1}. As counts are a natural unit with photodiode or CCD based detection systems, it is necessary to convert spectral irradiance first into photon flux, then into detected counts, to establish relative detector sensitivity.

The calibrated spectral irradiance of the lamp was provided at discrete wavelengths, thus interpolation was necessary and performed using a spline fit. The photon energy was calculated for each wavelength point, and the irradiance was converted into number of photons at each wavelength. The resulting output was the calibrated lamp spectrum converted into suitable units.

The spectrum of the calibrated lamp, as measured through the optical system, was acquired. The detector counts were linearly interpolated to provide a common wavelength bin and divided by the converted, calibrated lamp spectrum photon count at each wavelength to obtain the relative detector sensitivity at each wavelength. The resulting output was the sensitivity curve for the spectral response of the measurement system, an example is shown in Figure 5-4. For PLQE, arbitrary normalisation of the sensitivity curve is acceptable provided the spectral shape does not change.

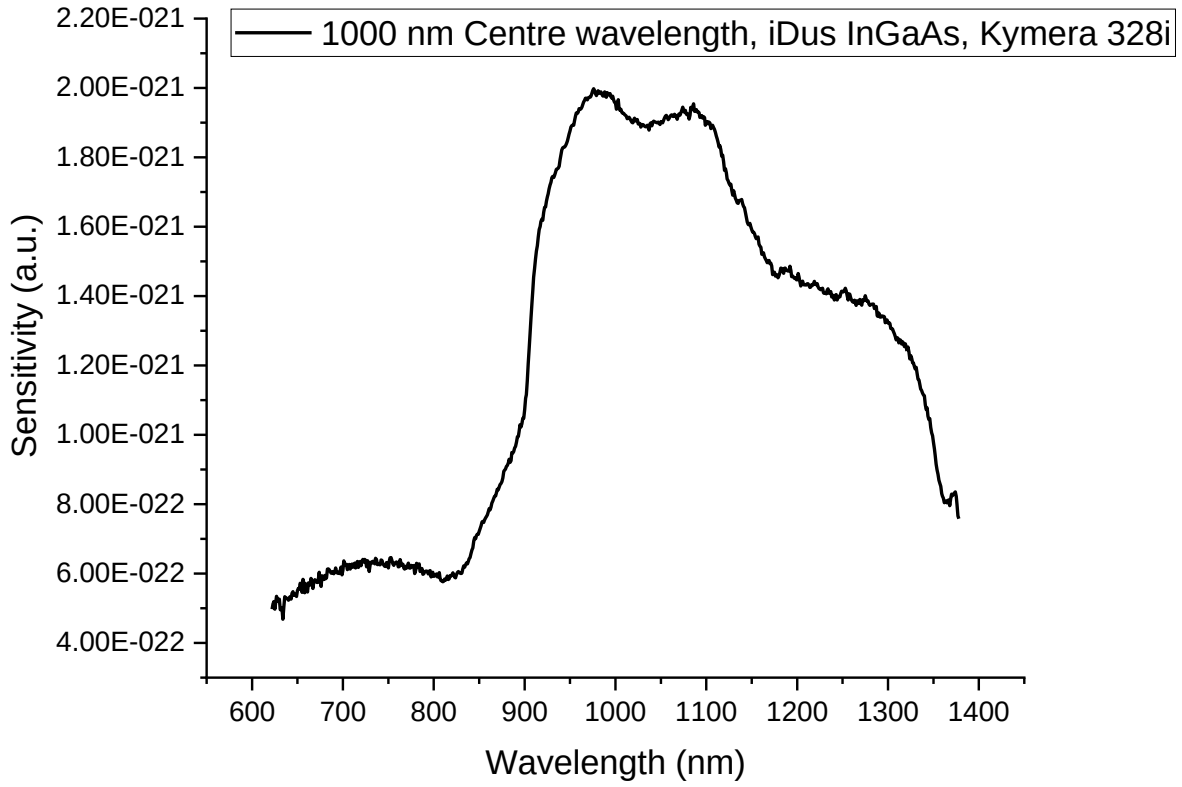

Figure 5-4 – Example sensitivity curve for a measurement setup with Labsphere integrating sphere coupled by Andor fibre optic into a Andor Kymera-328i spectrograph with Andor iDus 1.7 InGaAs. The centre wavelength is 1000 nm. The curve was generated from measurement of Newport 200 W calibration lamp filtered with a 600 nm long-pass filter compared to the NIST-calibrated known spectral output.

Optical path

As all optical elements affect the spectral response of the system, the calibration must be performed with identical optical path as the measurements. As individual optics subject to manufacturing tolerances and errors, a calibration is only valid for a unique system. Thus a recalibration should be performed if any elements are changed or replaced with a nominally-identical element. Thus one should use a particular optical fibre; if it becomes damaged or otherwise unavailable, a replacement optical fibre would require the whole system to be recalibrated, to maintain traceability with the calibration source.

Integrating sphere geometry and baffles

An important consideration for integrating sphere measurements is the geometry between sample mounting and position of the collecting fibre. The collection optics must be shielded from direct excitation and low-order reflections of the incident laser excitation. This is as to not unduly increase the measured fluence of the excitation beam relative to the sphere radiance. The simplest solution to

this is a baffle, a structure to block low-order scattered light with the same diffusely reflective coating. Thus this baffle is required to be sufficiently large as to shield a large solid angle with respect to the collection fibre to ensure collected light is equivalent to the sphere radiance.

The original baffle inside the integrating sphere for the measurement setup was unsuitable as it did not fully shield the initial laser spot within the sphere, illustrated in Figure 5-5a. A larger baffle, to prevent any light from reaching the collection fibre in a single bounce, was 3D printed and spray-coated with barium sulfate paint, illustrated in Figure 5-5c.

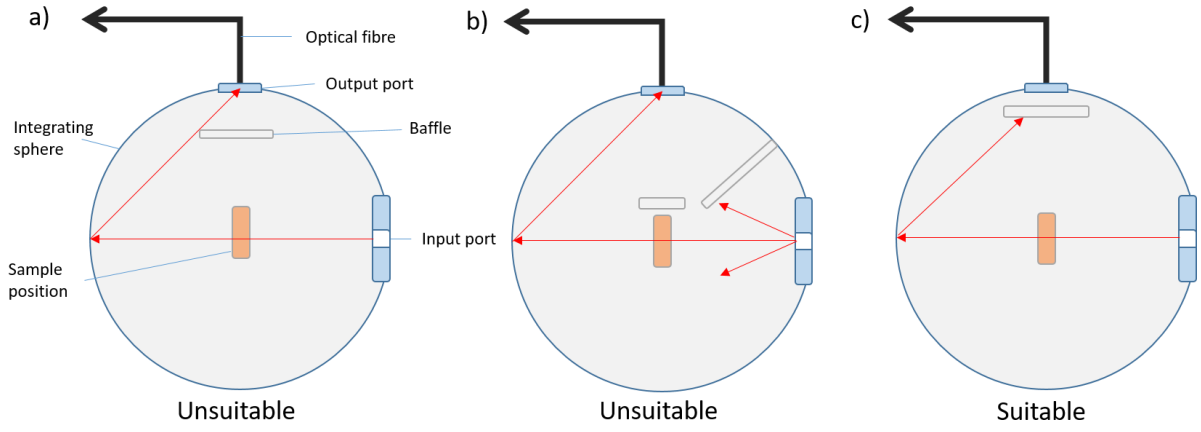

Figure 5-5 – Schematic of different integrating sphere baffle configurations. In configuration a), the baffle shields the sample, but is too small to sufficiently shield the output port from the incident laser spot. Configuration b) is commonly seen on integrating spheres configured for absorption spectroscopy, and does not shield the output port from the incident excitation spot. Configuration c) has a sufficiently large baffle to shield the output port from probable positions of the incident laser spot and is thus suitable.

A recent article has suggested the presence of an artefact arising from integrating sphere PLQE measurements, showing a decrease in measured PLQE values at low single-pass sample absorptions.[17] The article described the artefact as being partly caused by a skewed distribution of measured quantum efficiency resulting from the statistical nature of the experiment, and also partly caused by an overestimation of absorption from an unidentified cause, which was variable between measurement setups. However, the identified cause of skewed distributions in PLQE may simply be mitigated through longer acquisition times or higher excitation intensities to obtain better signal. In addition, the unidentified 'artefact' described in the article may also be explained by a flaw in their experimental setup caused by an improperly-baffled integrating sphere, illustrated in Figure 5-5b. The excitation source described consisted of an LED with a wide input angle, thus the baffles blocked the input port and the sample holder. However, the region of the sphere where the input light was first incident, opposite the input port, was not baffled. Thus as the single-pass absorptance of the sample decreased, the amount of excitation light illuminating the spot increased. Additional excitation light was allowed to reach the output fibre, leading to the disproportionate increase of signal for the excitation light at

low sample absorptances. With disproportionately increased excitation signal, the corresponding calculated PLQE decreased. In addition, the ray-tracing simulations performed in support of the 'artefact' explanation assumed that light was only collected after a minimum of two bounces, which was incorrect for the baffle setup as described. However, poorly absorbing samples do introduce random errors in PLQE determination, which is explained in Section 5.5 describing quantification of random error.

Collecting optics

The selection of optical fibre should consider the light throughput required in the spectral regions of interest. Thus transmission range should be wide enough to encompass both excitation and emission ranges with no undue absorption features within the regions of interest. Initially, the fibre used (Andor SR-OPT-8014) was unsuitable with large absorption features in the near-infrared, resulting from unsuitable material construction (high-OH) and optimised for UV/visible transmission. Switching to a different fibre optimised for visible/NIR transmission (Andor SR-OPT-8019) with low-OH construction eliminated the absorption features. As fibres differ by number of core strands, strand dimensions and spectral windows, ideally all these parameters are maximised as much as possible to maximise signal. Cost and form factor are then limiting concerns, with SMA-type connections common in benchtop integrating spheres. Again, calibration of the instrument is particular to an individual optical fibre.

Spectrograph optics and focusing

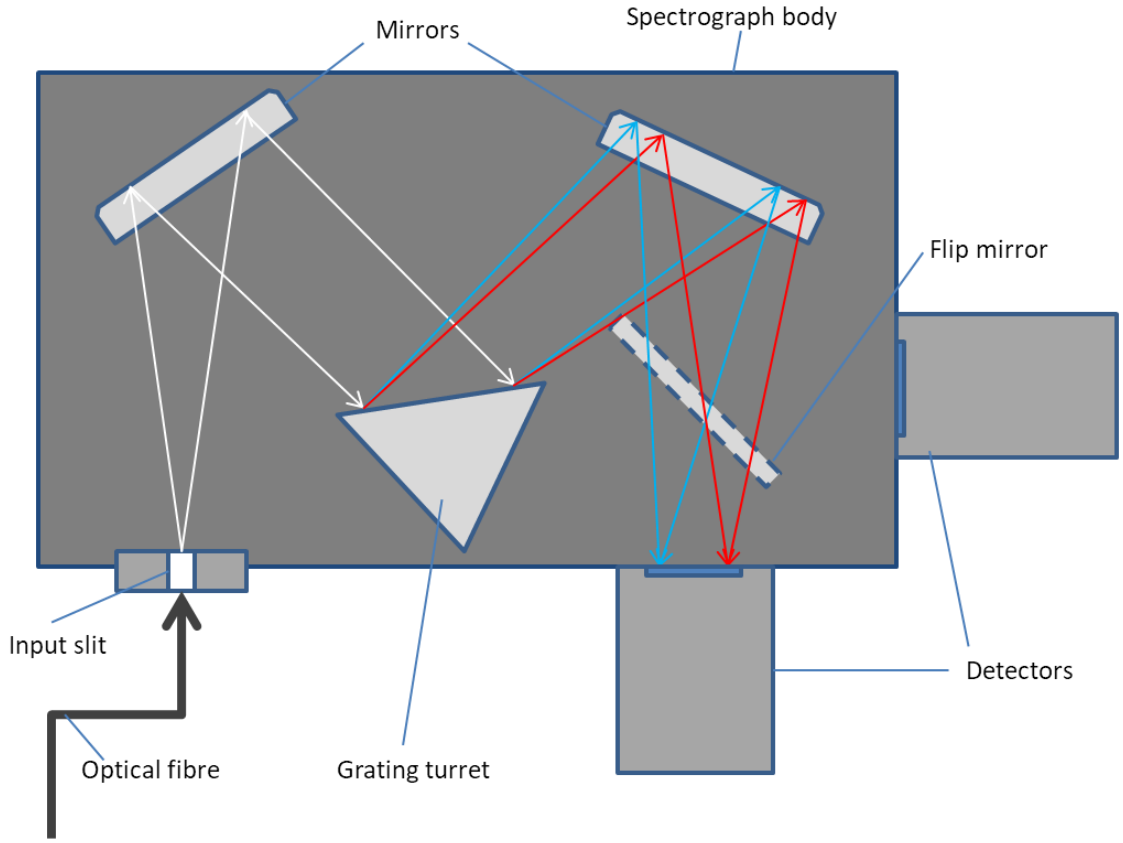

Figure 5-6 – Schematic of Czerny-Turner spectrograph. Rotation of the grating turret allows collection of different spectral regions incident on the detector. The flip mirror allows detector selection.

A spectrograph in the Czerny-Turner optical configuration, shown in Figure 5-6, possesses an input slit, toroidal primary mirror, diffracting grating, secondary mirror and line focal plane array (FPA) for detection.

The input slit is mounted at the focal point of the toroidal primary mirror, which collimates the light off-axis onto the diffraction grating turret. The diffracted, dispersed light is focused by the secondary mirror onto the detector plane. Primarily, the input slit determines the wavelength resolution of the spectrograph, and the slit size should be comparable to the pixel size for maximum resolution. This is because an image of the input slit is formed on the detector plane, apparent by the zero-order reflected mode, so a larger slit will create a larger image on the detector, whilst smaller slits cannot increase the resolution below the pixel pitch of the detector. In the spectrograph used (Kymera 328i) with focal length of 328 mm and 50 lines/mm grating, the reciprocal linear dispersion is approximately 60 nm/mm. The maximum resolution of the system becomes the product of the slit width and the reciprocal linear dispersion. At a slit width equal to the pixel size, 25 µm, the limiting resolution is 1.5 nm, however as sampling theory requires resolution calculation over two pixels, this is doubled to approximately 3 nm.

The optical fibre should be mounted aligned with the slit, and alignment should be performed at small slit sizes, ensuring that the slit is opened symmetrically. Increasing the slit size may allow additional light input and increased signal with a loss of wavelength resolution. If the slit is increased too much, it no longer behaves as a point source for the primary mirror. In addition, stray light from the fibre may enter the spectrograph at an angle greater than the acceptance angle of the primary mirror, leading to scatter within the spectrograph.

Diffraction grating

If there is a wide spectral gap between excitation and emission, it may be necessary to vary the grating position in order to fully capture the regions of interest throughout the measurement. Through variation of the grating angle, different regions of the spectrum may be imaged by the focal plane array detectors. Such flexibility is not without its shortcomings, and several consequences of varying grating angle must be taken into account. Firstly, as dispersion from a grating is wavelength-dependent, wavelength resolution decreases as a function of increasing wavelength i.e. each detector pixel value will correspond to a wider wavelength range. Secondly, light intensity at a given wavelength output changes at different grating angle. Measurement of a monochromatic source at two different grating positions will produce different observed signals. This was initially assumed to be negligible, however was later discovered to potentially contribute a small but significant error, up to 4% in certain conditions. The varying intensity is the result of different light path lengths at different grating angles, as shown in Figure 5-7. Therefore, it is necessary to produce a calibration spectrum for each specific grating position to be used, spanning the full measurement range, and subsequent measurements should only be taken at those grating positions. The relative change in sensitivity and potential relative error is dependent on the properties of the grating and is a nonlinear function of wavelength.

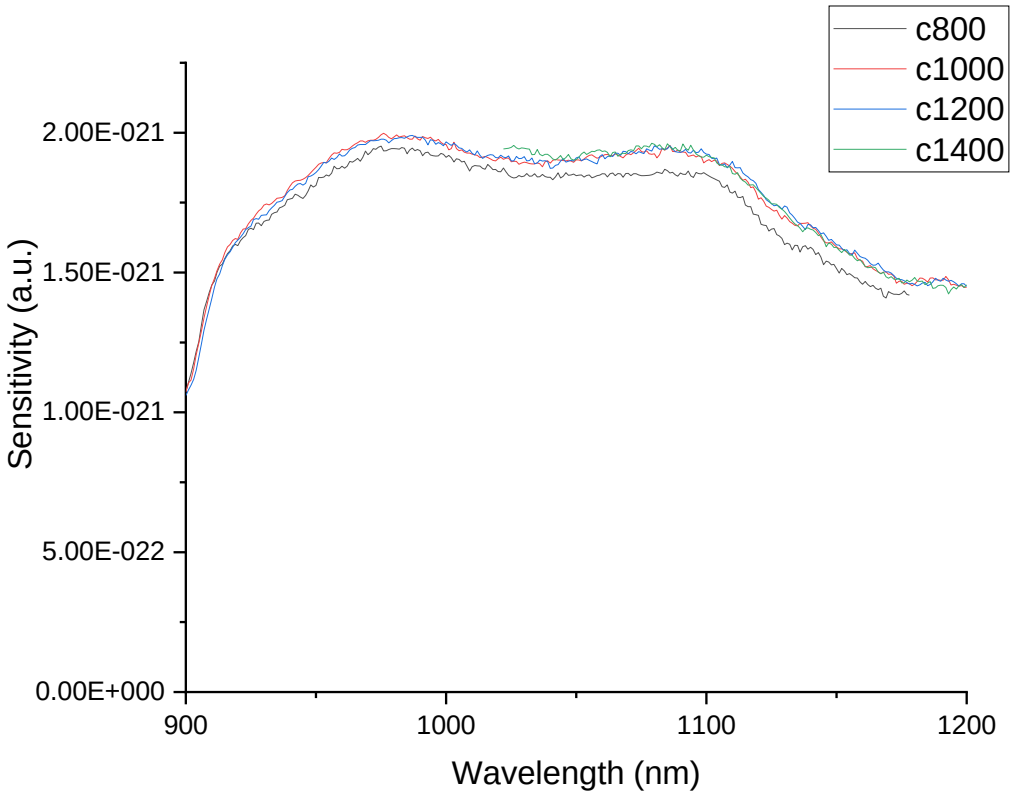

Figure 5-7 – Sensitivity curves at different grating positions for the iDus InGaAs 1.7 photodiode array detector. The magnitude of sensitivity variation depends on multiple factors including grating pitch/blaze, measured spectral region and spectrograph design. The appearance of oscillating noise is the result of alternating pixel sensitivities.

Blaze refers to the construction of a diffraction grating to enhance transmission at a specific wavelength range. As the dispersion of a grating is determined by grating pitch, it is useful to select a grating which can observe the spectral region of interest whilst having optimal transmission properties for that particular region. This is not important however as sub-optimal grating blaze can be compensated with the sensitivity calibration spectra.

Filters and cutoffs

In the diffraction grating spectrograph optical system, higher diffraction orders will be projected onto the detector if the light dispersion at the focal plane is smaller than the length of the detector array. In order to remove higher-order harmonic features from affecting longer wavelength signals, long-pass filters may be placed within the optical path at normal incidence. These filters both introduce a reflective surface for light loss and will have their unique transmission spectra, which can be included as a correction factor. Thus for each measurement range, it is necessary to generate multiple calibration spectra with each relevant filter to enable each excitation wavelength yet remove second order effects. It is also beneficial to use high-quality thin-film filters rather than coloured glass filters,

as the former possess sharper cut-offs and are less likely to possess their own photoluminescence. Sharper cut-offs reduce the effect of bleed-through for higher order diffraction signals whilst measuring at longer wavelengths.

Camera drift and cooling

The dark current of a photodiode or a charge-coupled device detector is proportional to the temperature. This is particularly important as the signal-to-noise ratio is specific for a given operating temperature and is substantially improved with detector cooling. A typical CCD or line FPA in a spectrograph camera is often cooled by a two-stage thermoelectric (Peltier) cooler to reduce dark current and improve sensitivity. As dark current or background counts are highly sensitive to temperature, maintaining a constant detector temperature is highly beneficial to ensure reproducible measurements. As these coolers are controlled by a PID element and are susceptible to perturbations, background count drift may occur during a measurement session.

Pixel-pixel sensitivity variation

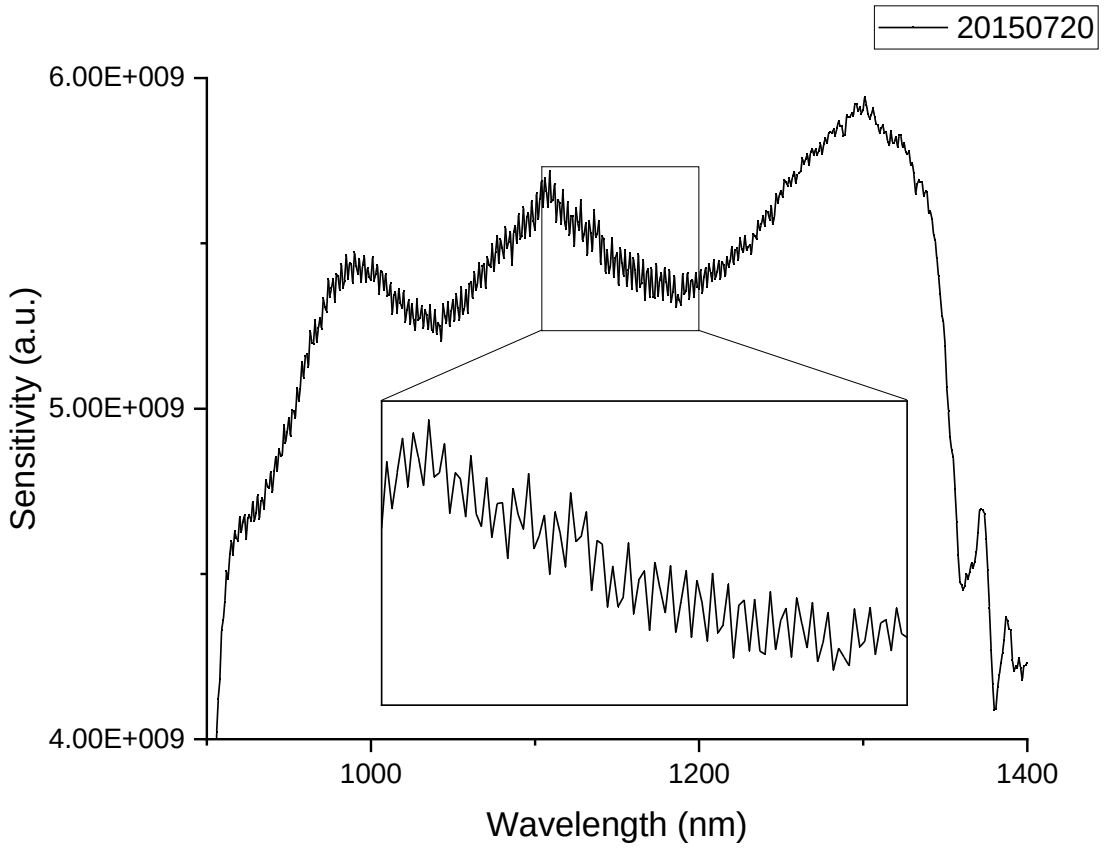

Figure 5-8 - Enlarged section of sensitivity curve for an integrating sphere measurement setup with InGaAs photodiode array detector showing oscillating odd-even pixel sensitivity variation. Zoomed inset for clarity.

The design and construction of the detector element can create inhomogeneity in individual pixel response. As differences are idiosyncratic and arise from manufacturing, these may be unavoidable if cost is a factor. For a photodiode line array of a typical indium gallium arsenide (InGaAs) detector, two factors are of particular importance. First is the thermal insulation of the array along with the thermal interface between the thermoelectric cooler and photodiodes. A non-uniform contact interface between detector and cooler or poor insulation will result in temperature fluctuations across the array, leading to a non-uniform background drift. Secondly, differences in the readout circuitry of each pixel will lead to periodic differences. A line array with two readout circuits will be addressed for odd and even pixels to minimise crosstalk between neighbouring pixels. However, as differences between the component charge amplifiers of each circuit will be present, an oscillatory variation in sensitivity will be observed between odd and even pixels, as seen in Figure 5-8. The oscillating sensitivity gives the appearance of two sensitivity curves overlaid and interlaced. This can be controlled through rigorous calibration and generally contributes negligible absolute errors. The variations become far more significant if x-axis wavelength errors are present, especially at low excitation fluences or for poorly-emissive samples.

Camera sensitivity

As the optical fibre output and spectrograph input are both in the shape of a narrow slit, the wavelength dispersed images of the source projected onto the detector are an array of narrow lines. The detector may either be one- or two-dimensional arrays of pixels whether it is a photodiode array or CCD. In a photodiode line array, the projected image may be larger than the pixel length in the vertical axis thus some signal is not collected. Further secondary reflections of uncollected light can contribute to added light scatter within the spectrograph. For a CCD, the detector area may be increased in the vertical axis with extra pixels. As wavelength resolution is obtained in the horizontal axis, vertical arrays of pixels may be regarded as equivalent. The output signals from each vertical array may be binned (combined) to give a total output signal. As the bit depth of each pixel is defined by the limit of the analogue-digital converter (ADC), far greater signal counts may be attained before saturation with vertically-binned pixels in a CCD compared to a photodiode array with the same ADC. Thus a CCD may take advantage of its greater collection area leading to far greater sensitivity, as demonstrated in Figure 5-9.

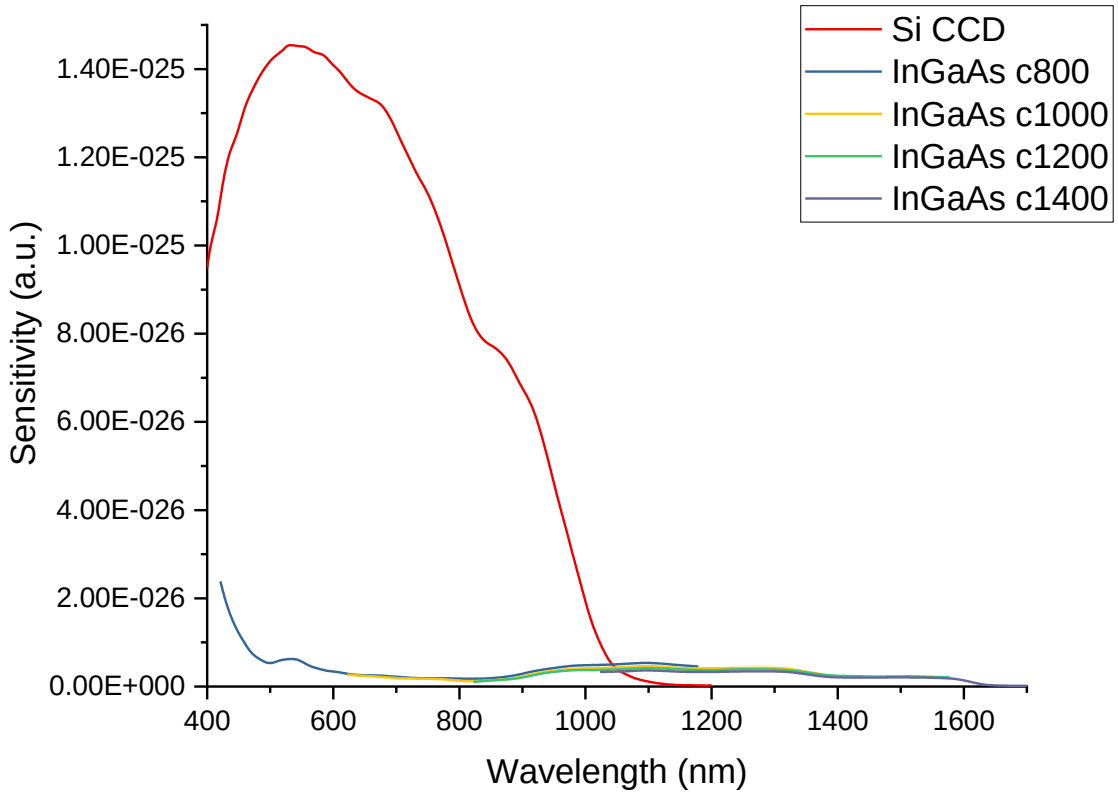

Figure 5-9 - Sensitivity curves of iDus Si CCD and iDus InGaAs 1.7 photodiode array detectors at different grating positions measured with the same light input (HL-3P-CAL lamp) and similar acquisition time. The CCD is able to take advantage of larger collection area from full-vertical binning and provides far greater sensitivity, meaning more signal counts for the same light input.

However with far more pixels, CCD signal readout requires addressing in two axes and is consequently relatively slow. As a result, minimum acquisition times are much longer than with a photodiode line array. The experiment must therefore be designed to avoid the situation of detector saturation at the shortest acquisition time, typically with limitations on excitation power. In addition, variation in detector sensitivity with respect to wavelength means different acquisition settings may be required depending on the location of excitation and emission wavelengths. With linear instrumental response, acquisition settings may be optimised to experimental requirements.

Sample angle – reflection

Attention should be paid to the angle of incidence between the excitation laser and the sample. Care must be taken to prevent the reflection of the laser directly out of the entrance hole in the case of exactly normal incidence. An off-normal incidence should be used to ensure the reflected laser remains within the sphere and scatters. At higher angles of incidence, the effective path length of the

sample increases and also eventually introduces total internal reflection effects within the glass parts of the sample.

Scattering and refractive index change

The sample cuvette or substrate introduces a source of parasitic absorption. The extent of this effect varies for each unique cuvette or substrate; generally negligibly however may become significant for samples in very dilute conditions. Several effects contribute towards the observed parasitic absorption. The quartz or glass material of the cuvette or substrate is not perfectly transparent and possesses variable absorption across wavelengths. Direct absorption from the glass is more prevalent towards shorter wavelengths and the ultraviolet and indeed measurements in the ultraviolet necessitates the use of optical quartz with sufficient transmission and negligible fluorescence. Another effect is the trapping of light within the glass elements from total internal reflection arising from differing refractive index boundaries. This is particularly significant in the case of cuvettes with partially-frosted ground glass construction. Scattered excitation light as well as sample emission is trapped within the thin glass elements by total internal reflection (TIR). The opacity of ground glass sides leads to partial absorption of the waveguided light. As TIR acceptance angle is greater for longer wavelengths, it is generally the case that emission is trapped to a greater degree than scattered excitation light. The net effect manifests as a greater extent of self-absorption within the sample, leading to lower measured quantum efficiency. The total absorption of a blank cuvette can be as high as 15% at 405 nm and depends on excitation wavelength.

This effect was observed as identical samples in similar form-factor cuvettes with differing path lengths gave differing results – it was reasoned that thicker cuvettes (2 mm vs 1 mm) had greater outcoupling and yielded slightly higher PLQE values. It was also observed that varying degrees of partially-filled cuvettes all provided similar results however a minor increase was observed with completely-filled cuvettes. This was likely a result of the different light outcoupling at different solvent-air-glass interfaces.

Sample self-absorption

Sample preparation is paramount in order to measure accurate photoluminescence quantum efficiencies. Especially, the optical density of the sample is required to be sufficiently high at the excitation wavelength to minimise errors in the determination of sample absorption. However, the sample must be either dilute enough or thin enough to minimise reabsorption of emitted light i.e. sample self-absorption. In addition, self-absorption causes an observed concentration-dependent bathochromic shift of emission spectra, as multiple absorption and re-emission events lead to depletion of emission at shorter wavelengths. To minimise self-absorption effects, the sample can be made reasonably dilute and the excitation wavelength selected to correspond to a peak in its

absorption spectrum, however poorly absorbing samples will also introduce random errors as described in the next Section.

Excitation wavelength and sample absorption

For colloidal semiconductor quantum dot solutions, high absorptions may be achieved through excitation at short wavelengths despite very dilute solutions. This is due to the large density of states high in the conduction band. Although it is ideal for these samples to set excitation wavelength as far apart as possible from the emission, this is limited by the spectral sensitivity of the detectors. As the sensitivity of InGaAs detectors diminishes to become negligible in the visible-blue region, excitation wavelength must be selected carefully to enable accurate measurement of laser power, especially for infrared-emitting samples. This may be largely mitigated with a sufficiently-powerful calibration lamp to provide sufficient output at shorter wavelengths. However, larger systematic uncertainties will be propagated resulting from determining detector sensitivity with fewer detector counts compared to regions where the detector is more efficient.

Intrinsic setup absorption

The sample holder is an inherent part of the system thus will contribute some degree of parasitic absorption. To minimise absorption from the holder, all parts should be coated with a diffusely reflective material or PTFE tape. The sample may be fixed with a pair of permanent magnets to minimise wear and contamination through handling and abrasion. The commonly used putty adhesives must be eschewed as they are tantamount to inadvertent contamination with their own absorption and emission properties, and certainly contributed in part to the differing sensitivity curves shown in Figure 5-11 and explained next.

Sphere contamination

Despite meticulous optimisation of the measurement setup and identification of most sources of systematic error, literature values for PLQE for Rhodamine 6G fluorescence standard were not initially achieved, but measured consistently lower (~60%).[13] The culprit was eventually identified as contamination of the integrating sphere with absorbing materials during handling. Following cleaning of the integrating sphere, the measured PLQE values were similar to literature values (~94%). The photoluminescence spectra of dilute Rhodamine 6G solution measured through the integrating sphere is shown in Figure 5-10.

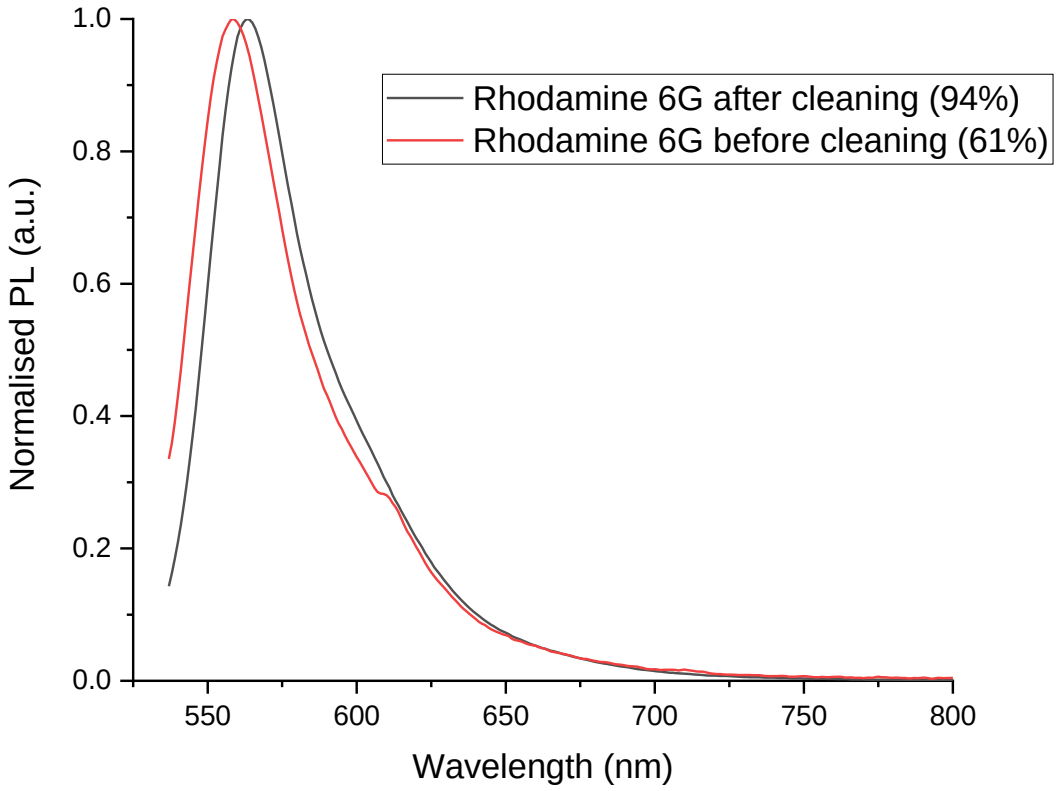

Figure 5-10 – Normalised PL spectra of Rhodamine 6G in ethanol (1×10^{-4} M) before and after integrating sphere cleaning. Low PLQE values were measured with a contaminated integrating sphere (60%). The measured PLQE increased to values comparable to literature following cleaning (94% vs. 95.6%).

Despite strict controls on calibrations and good sample handling techniques, it may be inevitable that with repeated use, contamination of the integrating sphere with foreign materials will occur. As such, these will dramatically change the spectral response of the integrating sphere and render any calibrations invalid. In the least disruptive case, dust or scattering materials may simply reduce the effective radiance of the sphere and reduce measured signals. However, it is generally the case that materials introduced into the sphere have considerably different optical properties to the diffusely-reflective $BaSO_4$ or PTFE coatings. Therefore small patches of absorbing materials can strongly change the shape of the sphere's spectral response, diminishing in some regions but not others. A particularly troublesome situation is any luminescent contamination, as it may prevent the measured PL spectrum being used even qualitatively. Figure 5-11 shows the calibration files generated at different times for an integrating sphere measurement setup showing vastly different spectral response, up to 50%, over time, partly as a result of contamination.

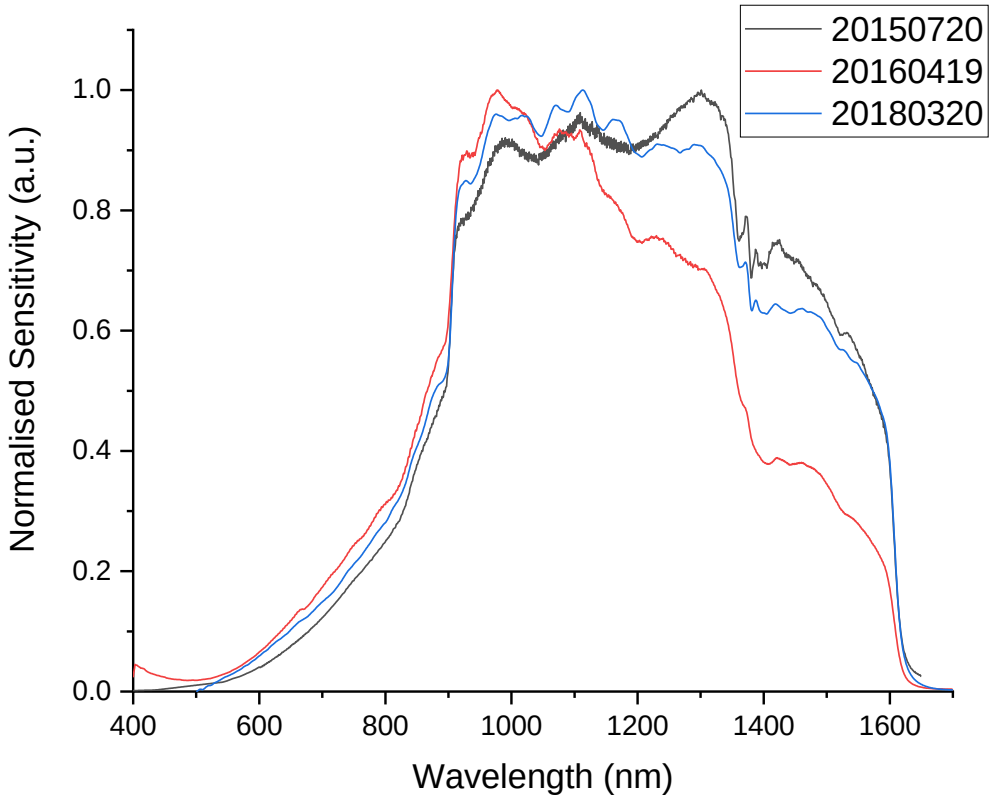

Figure 5-11 – Normalised stitched sensitivity curves of a similar integrating sphere measurement setup with iDus InGaAs 1.7 detector, calibrated at different times, showing change in spectral response as a result of contamination. The integrating sphere was cleaned prior to the 20180320 calibration through abrasion and recoating. Calibrations were performed chronologically by Maxim Tabachnyk, Matt Menke and Emrys Evans.

The net effect of sphere contamination on PLQE measurements is dependent on the spectral region of absorption. Generally, quantum efficiency values are underestimated due to both parasitic absorption of excitation light and emitted PL. In certain cases, if only the narrow excitation region is strongly absorbed, measured incident laser power is unduly reduced. Decrease in measured laser power contributes to an overestimate of the PLQE. This may mean that for an emitter where the PLQE should be largely independent of excitation wavelength, such as quantum dots, different values are obtained at different excitation wavelengths. For singlet fission down-conversion assemblies described in a later section, excitation must occur in spectral regions distant to the emission. It is thus crucial that consistent values for PLQE are obtained across the entire spectrum of excitation wavelengths to be used with a wide range of optical densities.

The cleaning of a contaminated sphere may not be trivial as exposure to solvents to remove contamination may damage the reflective coating or allow the contamination to spread deeper within

the coating. Abrasion of the coating in regions of contamination may effectively clean the sphere. The requirement to remove contamination for the measurement of highly emissive samples may mean sphere recoating and resurfacing becomes necessary. Confirmation of contamination removal may be performed immediately after recalibration by the measurement of highly luminescent dyes such as Rhodamine 6G. Reduced values from the literature number may still indicate the presence of absorbing contaminants.

5.5 Quantification of random measurement error

Having identified and minimised the prevalence of the various sources of systematic error, it was then possible to perform accurate PLQE measurements. However, as with all measurements, the presence of random measurement errors remained. The simple approach for quantifying random error is to repeat the measurement to obtain a spread of values. Figure 5-12 shows measured PLQEs for a sample of PbS/CdS QDs emitting at 1000 nm at a fixed concentration with different excitation wavelengths and respective optical densities inset. The spread of values obtained were similar across all excitation wavelengths and were all overlapping, to be expected of a measurement setup with no absorbing contaminants. The spread displayed deviations of up to approximately ±5 % relative PLQE, which could be taken as an estimate for random measurement error. Allowing for the different sources of random error described in this section, this value is not an unreasonable estimate.

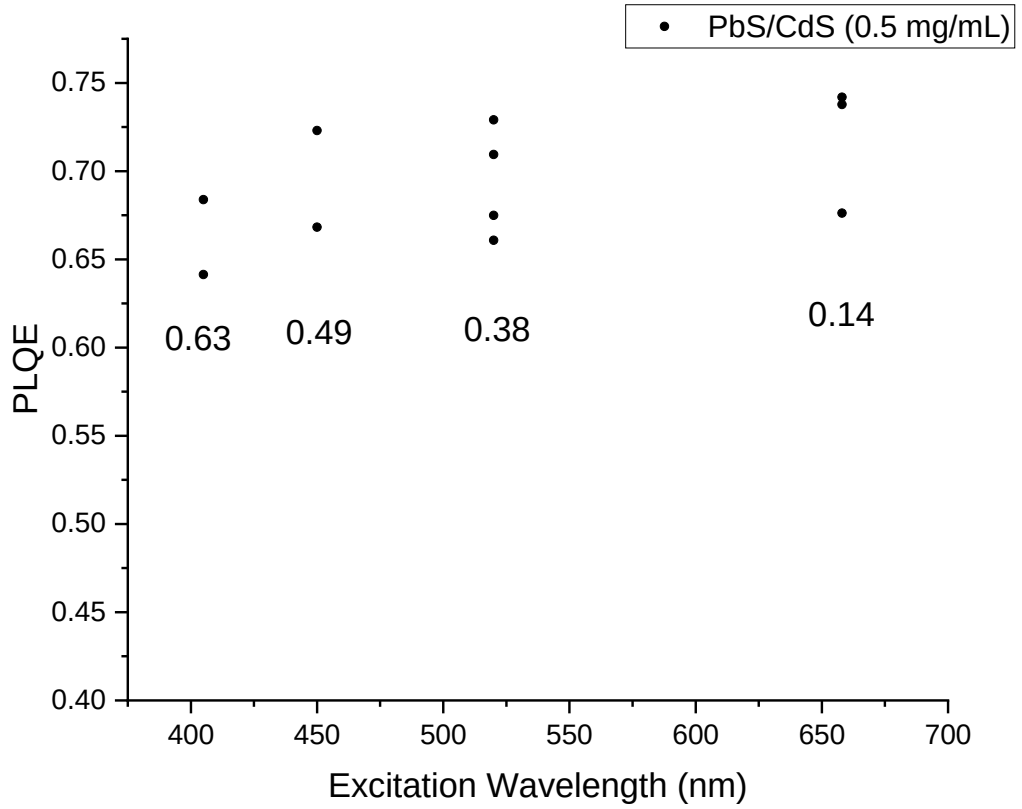

Figure 5-12 – PLQE of PbS/CdS QDs (0.5 mg mL^{-1} in octane) measured at different excitation wavelengths. Dots represent individual measurements of the same batch. Laser power was 1 mW for all excitation sources. Fractional absorption estimated by the expression for *A* in the integrating sphere PLQE formula shown as inset numbers. The values obtained were similar at all excitation wavelengths and the spread of values was reasonably comparable to the statistically-derived estimates of random error as explained in this and the following section, allowing for reasonable assumptions for laser stability.

To statistically quantify the measurement errors within the integrating sphere method, propagation and combination of errors may be performed for each aspect to obtain the final relative error. Assuming a perfect measurement with no additional error factors such as excitation laser fluctuation or calibration source variation, the expression for photoluminescence quantum efficiency is

$$\eta = \frac{ON_{PL} - (1 - A)OFF_{PL}}{A \times NO_{LAS}},$$

where:

$$A = \left(1 - \frac{ON_{LAS}}{OFF_{LAS}}\right).$$

Expansion of the expression to measurable terms gives:

$$\eta = \frac{ON_{PL} - \frac{ON_{LAS}}{OFF_{LAS}} OFF_{PL}}{NO_{LAS} - \frac{ON_{LAS}}{OFF_{LAS}} NO_{LAS}}.$$

Each signal term in this expression is the corrected integral of the detector counts to give the relative photon count Int. This may be expressed as

$$Int = a_1 x_1 + a_2 x_2 + \cdots a_N x_N,$$

where a_i is the spectral sensitivity and x_i is the detected counts at wavelength i. Assuming no error in the spectral sensitivity calibration, the absolute error u_c of the integrated photon count may be expressed from the error in each pixel u_i:

$$u_c(Int) = (a_1^2 u_1^2 + a_2^2 u_2^2 + \cdots a_N^2 u_N^2)^{\frac{1}{2}}.$$

The absolute uncertainty u_i presented here is the combination of detector read noise and shot noise for each pixel. The read noise u_r is dependent on acquisition settings and may be found by taking a background-corrected blank reading. The background correction is a subtraction of two detector outputs with identical acquisition settings to remove the dark-current counts from the measurement. As the subtraction involves two values with associated errors, the measured error is added in quadrature. As the acquisition settings are identical, the standard error may be regarded as the same in both acquisitions and the standard error is multiplied by a factor of $\sqrt{2}$ to give the error present following background subtraction:

$$(u_r^2 + u_r^2)^{\frac{1}{2}} = (2u_r^2)^{\frac{1}{2}}.$$

As the detection method involves the conversion of discrete photons in to photoelectrons, the measured signals will be affected by shot noise, arising from the discrete nature of electric charge. The standard error of shot noise arising from random fluctuations in discrete events is equal to the square root of the number of events. The signal-noise ratio (SNR), the number of events divided by the error, is also equal to the square root of number of events. For imperfect CCD or photodiode detection methods with non-unity quantum efficiencies, the noise is equal to the square root of the number of detected photoelectrons rather than the number of incident photons, having been corrected for quantum efficiency compared to an ideal detector. Thus the absolute value of shot noise error is decreased but the SNR is also decreased. From detector counts, the shot noise error in each pixel u_p is the square root:

$$u_p = (x_i)^{\frac{1}{2}}.$$

Including the uncertainty arising from background subtraction, the combination of shot noise and background-corrected read noise u_r is the quadrature sum of the two parts,

$$u_{r,p} = (2{u_r}^2 + x_i)^{\frac{1}{2}},$$

where

$$u_{r,p} = u_i.$$

The error in the photon count thus becomes

$$u_c(Int) = \left(a_1^2(2{u_r}^2 + x_1)^2 + a_2^2(2{u_r}^2 + x_2)^2 + \cdots a_N^2(2{u_r}^2 + x_N)^2\right)^{\frac{1}{2}}.$$

Commonly used excitation sources for PLQE experiments are diode lasers. Whether these are uncooled or temperature- and current-controlled with PID loops, they will invariably possess some degree of fluctuation in output power and fluence. The fluctuation may be expressed as a percentage deviation from the mean output. If the output is not continuously monitored and corrected for by the detection setup in real time, the fluctuation introduces a percentage error in all measured signals. As any detected signal, laser or photoluminescence, is proportional to the incident excitation fluence, the percentage error in laser output may be converted into an absolute error by multiplying the measured photon count by the percentage error of the laser l, where perfect stability does not introduce any error,

$$u_l = l \times Int.$$

Including the absolute laser error into our expression is the quadrature sum,

$$u_{c,l} = ({u_c}^2 + l^2 Int^2)^{\frac{1}{2}}.$$

We can define the following absolute errors in each integrated corrected signal, where $u_X = u_{c,l}(X)$ as:

u_A is the error in ON_{PL},

u_B is the error in OFF_{PL},

u_C is the error in ON_{LAS},

u_D is the error in OFF_{LAS},

and u_E is the error in NO_{LAS}.

Neglecting covariance (if any) in the error between individual measurements, the standard error in PLQE, u_η becomes the quadrature sum of the absolute errors multiplied by the partial derivative of the PLQE expression for each photon count according to the propagation of error formula:[19,20]

$$u_\eta = \left(\left(\frac{\partial \eta}{\partial ON_{PL}} \right)^2 {u_A}^2 + \left(\frac{\partial \eta}{\partial OFF_{PL}} \right)^2 {u_B}^2 + \left(\frac{\partial \eta}{\partial ON_{LAS}} \right)^2 {u_C}^2 + \left(\frac{\partial \eta}{\partial OFF_{LAS}} \right)^2 {u_D}^2 + \left(\frac{\partial \eta}{\partial NO_{LAS}} \right)^2 {u_E}^2 \right)^{\frac{1}{2}},$$

where:

$$\frac{\partial \eta}{\partial ON_{PL}} = \frac{OFF_{LAS}}{(OFF_{LAS} \times NO_{LAS}) - (ON_{LAS} \times NO_{LAS})},$$

$$\frac{\partial \eta}{\partial OFF_{PL}} = \frac{ON_{LAS}}{(ON_{LAS} \times NO_{LAS}) - (OFF_{LAS} \times NO_{LAS})},$$

$$\frac{\partial \eta}{\partial ON_{LAS}} = \frac{OFF_{LAS} \times (ON_{PL} - OFF_{PL})}{NO_{LAS} \times (ON_{LAS} - OFF_{LAS})^2},$$

$$\frac{\partial \eta}{\partial OFF_{LAS}} = \frac{ON_{LAS} \times (ON_{PL} - OFF_{PL})}{NO_{LAS} \times (OFF_{LAS} - ON_{LAS})^2},$$

$$\frac{\partial \eta}{\partial NO_{LAS}} = \frac{(ON_{PL} \times OFF_{LAS}) - (ON_{LAS} \times OFF_{PL})}{{NO_{LAS}}^2 \times (ON_{LAS} - OFF_{LAS})}.$$

The overall formula thus becomes

$$u_\eta = \left(\left(\frac{OFF_{LAS}}{(OFF_{LAS} \times NO_{LAS}) - (ON_{LAS} \times NO_{LAS})} \right)^2 {u_A}^2 + \left(\frac{ON_{LAS}}{(ON_{LAS} \times NO_{LAS}) - (OFF_{LAS} \times NO_{LAS})} \right)^2 {u_B}^2 + \left(\frac{OFF_{LAS} \times (ON_{PL} - OFF_{PL})}{NO_{LAS} \times (ON_{LAS} - OFF_{LAS})^2} \right)^2 {u_C}^2 + \left(\frac{ON_{LAS} \times (ON_{PL} - OFF_{PL})}{NO_{LAS} \times (OFF_{LAS} - ON_{LAS})^2} \right)^2 {u_D}^2 + \left(\frac{(ON_{PL} \times OFF_{LAS}) - (ON_{LAS} \times OFF_{PL})}{{NO_{LAS}}^2 \times (ON_{LAS} - OFF_{LAS})} \right)^2 {u_E}^2 \right)^{\frac{1}{2}}.$$

The photoluminescence quantum efficiency absolute error thus becomes the quadrature sum of the derivative-factored errors in each signal. Several situations where the measurement noise may contribute to large uncertainty in PLQE arise: low excitation powers, poor photoluminescence quantum efficiency, very high and especially very low absorption can all introduce errors.

Measurements with inadequate signal-noise ratio at low excitation powers and/or poorly emitting samples can be improved by increasing acquisition time through multiple cumulative exposures with longer exposure times, as background-corrected read noise becomes dominated by absolute shot noise or laser fluctuation errors. Extremely absorbing samples can produce low signal for ON_{LAS}, which is compounded if the sample also has low PLQE, resulting in low PL signals and read noise dominance. In addition, highly absorbing samples introduce self-absorption errors which are difficult to quantify. Samples with very low absorption have greater uncertainty, where the difference between ON_{LAS} and OFF_{LAS} terms are small leading to the denominators in their respective derivative terms approaching zero, resulting in inflated factors for their error terms. In practicality, poor absorption can be caused by and is sensitive to sample inhomogeneity or cuvette absorption.

In idealised measurement conditions, the random error uncertainty can be made very small. Application of this error analysis to real data will be shown in the next section. Broadly, however at this stage it can be seen that the luminescence terms are typically dominated by read noise, whilst the laser terms are more susceptible to shot noise, as laser terms typically consist of high number of counts integrated across a small number of pixels, whilst luminescence terms typically consist of fewer counts integrated across a large number of pixels. Practically, shot noise is limited by the dynamic range of the detector, thus there is a maximum number of counts that may be collected before detector saturation. Typically, external sources of error become manifest. Most notably, the stability of the excitation source affects all measurements and increases the minimum uncertainty for the resulting PLQE. Whilst the power output may be continuously monitored and a time-variable correction factor applied to all measurements, this can add extra effort and complexity. The fluctuations may be measured over time and the generalised relative error coefficient may be included. Laser fluctuation increases error for all measurements thus tends to dominate over read noise or shot noise.

With a calibrated, reliable measurement setup and a means for quantifying random error, it was then possible to accurately measure PLQE and their associated uncertainties.

5.6 Measurement of singlet fission down-conversion assemblies

The following work was performed in collaboration with Jesse Allardice, Simon Dowland and Zhilong Zhang. My primary contributions to this work were the calibration and optimisation of the PLQE experiment and setup, described in detail above and the synthesis of some PbS QDs as described in Section 3.2 which were used for earlier experiments leading towards this result. Measurement and analysis of PLQE data was performed with Simon Dowland. Samples were prepared by Jesse Allardice and Simon Dowland. The QDs presented in this dataset were synthesised by Zhilong Zhang.

The characterisation of singlet fission down-conversion assemblies requires accurate measurement of luminescence efficiency of the individual constituents in multi-component systems. In a typical system, a low concentration of PbS quantum dot emitters is dispersed in a high concentration of singlet fission sensitising organic molecules. High concentrations to maximise light harvesting of SF molecules such as TIPS-tetracene result in high component absorptions above the bandgap. Low concentrations of PbS quantum dots to minimise aggregation and luminescence quenching result in relatively low component absorptions compared to the organic material.

To demonstrate photon multiplication in the system, the PLQE of the emitter PbS component is measured through selective component excitation. Direct excitation of the PbS QDs is achieved by a laser wavelength below the bandgap and absorption edge of the organic component. Indirect excitation of PbS is achieved through laser excitation of SF sensitiser material above the bandgap, followed by singlet fission and energy transfer to the QDs. PLQE in the PbS near-infrared spectral region provides an overall measure of down-converter efficiency. As accurate PLQE measurements are critical to demonstrate whether the observed results are valid in this particular system, all aspects of minimising systematic error shown in this Chapter were applied to the measurements performed in this section. In addition, quantification of the random error through the methodology in Section 5.5 was performed to confirm the results obtained were statistically valid.

5.7 Methods

The PLQE measurement setup with integrating sphere (Labsphere 4P-GPS-053-SL), collection fibre (Andor SR-OPT8019), spectrograph (Andor Kymera-328i) and detectors (Andor iDus 420 and iDus InGaAs 1.7) was calibrated for spectral sensitivity with a current-controlled, NIST-calibrated 200 W quartz-tungsten-halogen lamp (Newport 63976-200QC-OA) as described in Section 5.4. PLQE was measured with the integrating sphere method as described in detail in Section 5.3.[7,15] Long-pass filters were used as appropriate for acquisitions in the near-infrared (Thorlabs FGL420, FGL550, FGL630 and FGL830).

TIPS-tetracene-carboxylic acid ligand-functionalised PbS QDs were prepared according to a published method.[21] Singlet fission down-conversion assemblies were fabricated by suspending QDs in solutions of TIPS-tetracene at varying concentrations. The solvent was anhydrous toluene. At high concentrations, TIPS-tetracene was able to undergo singlet fission processes in solution. The mixtures were contained within custom cuvettes of approximate 125 μm path length fabricated by cementing 22 mm square glass coverslips with epoxy resin. A schematic of a singlet fission down-conversion assembly along with pathways resulting in NIR QD emission is shown in Figure 5-13.

Excitation of the TIPS-tetracene was performed with a temperature-controlled 520 nm diode laser (Thorlabs). Excitation of the PbS QDs only was performed using a temperature-controlled 658 nm diode laser (Thorlabs).

5.8 Results and Discussion

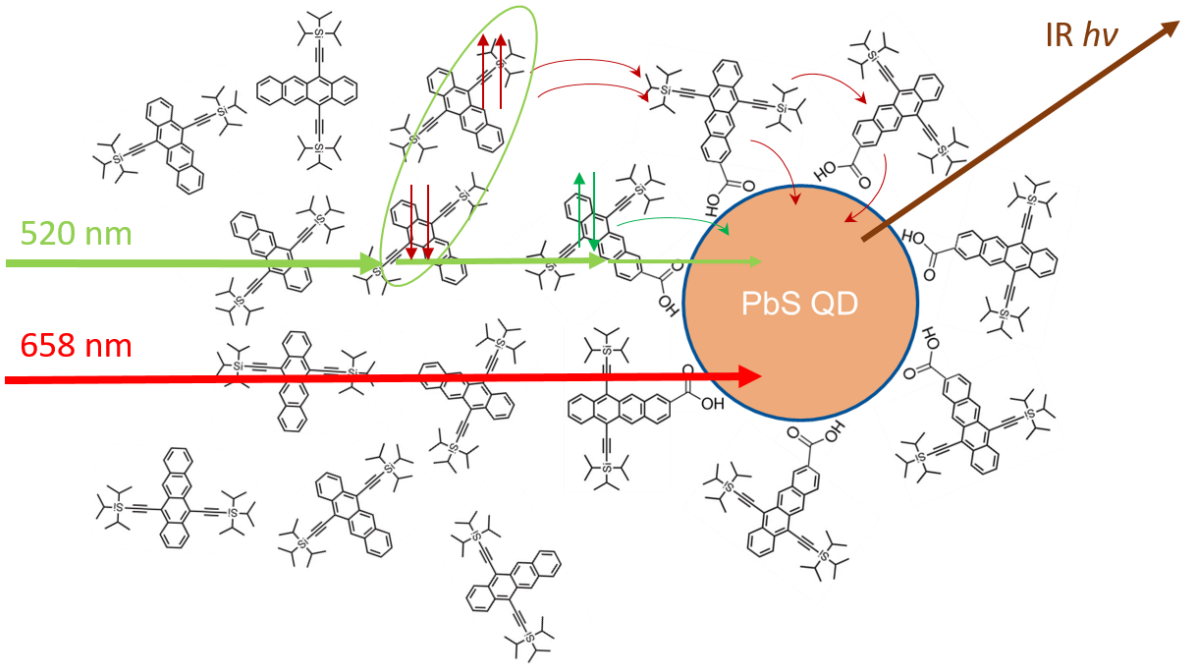

Figure 5-13 – Schematic of solution singlet fission down-conversion assembly. All components are dissolved in toluene. The concentrated TIPS-tetracene is able to perform singlet fission with 520 nm excitation due to random close association of neighbouring molecules of correct orientation. The two generated triplets may dissociate and diffuse onto the TIPS-tetracene-carboxylic acid ligands attached to the QD, then transferring onto the PbS, exciting the QD with resulting IR emission. TIPS-tetracene-carboxylic acid also absorbs 520 nm and can generate a singlet which can transfer onto the QD, with NIR emission. The PbS QD may be directly excited by 520 nm light unabsorbed by the organic tetracene components, or 658 nm light, which is not absorbed by the organic components, both with resulting IR emission.

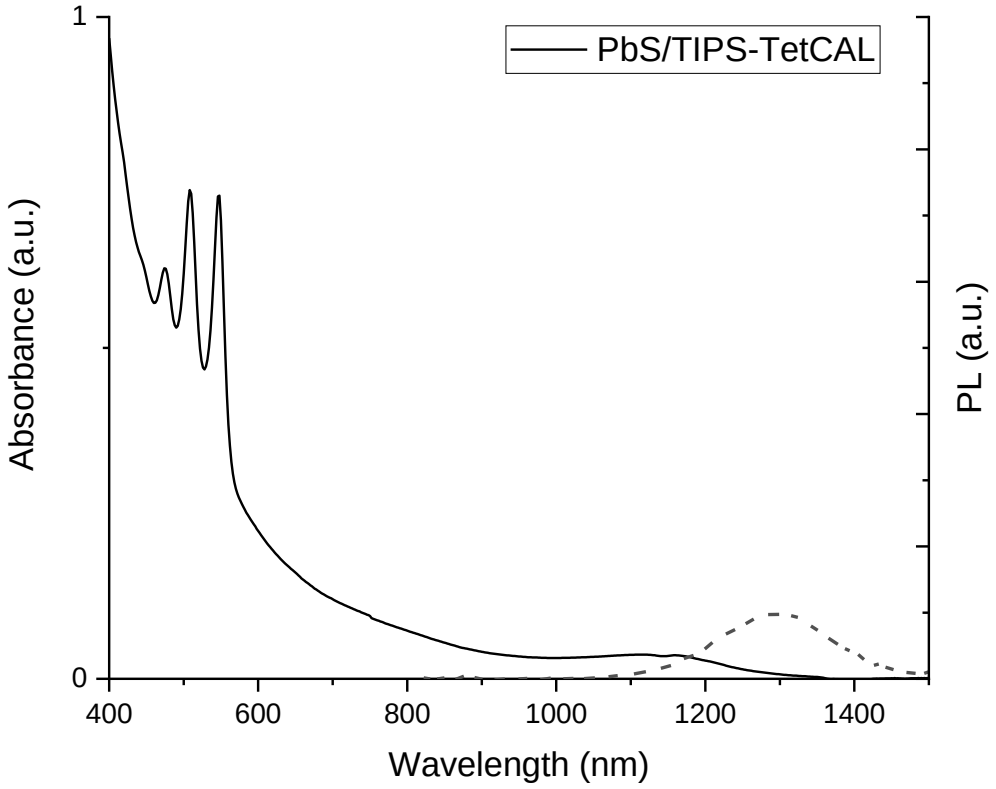

Figure 5-14 – Absorption (solid) and photoluminescence (dashed) spectra of PbS QDs ligand-exchanged with TIPS-tetracene carboxylic acid (TIPS-TetCAL). The ligand absorption peaks are prominent at wavelengths below 550 nm. The absorption between 550 nm and 1250 nm originates wholly from the PbS. Films consisting of varying quantities of TIPS-tetracene and PbS/TIPS-TetCAL possessed component optical densities proportionate to their respective absorption regions – higher TIPS-tetracene content had higher O.D. below 550 nm and higher QD content possessed higher O.D. across the whole spectrum below 1250 nm.

PbS QDs ligand-exchanged with TIPS-tetracene carboxylic acid ligand (TIPS-TetCAL) possessed emission centred at 1300 nm as shown in Figure 5-14. The absorption spectrum displayed peaks associated with the TIPS-TetCAL below 550 nm along with a broad absorption slope up to 1250 nm associated with the PbS QDs. Incorporation into a mixed component film with TIPS-tetracene altered the absorption spectra which could be described as additive components of TIPS-tetracene and PbS QDs. The TIPS-tetracene possessed significant absorption below 540 nm and thus at high relative concentration the optical density was significantly increased at 520 nm with a greater proportion arising from TIPS-tetracene. At high QD concentration, the absorption increased across the entire QD absorption spectrum below 1250 nm and a greater absorption fraction at 520 nm came from QDs. At 658 nm, the QDs were the sole absorbing component and the optical density was entirely a result of QD concentration.

Error analysis

Measurement (10Tc/20QD)	Read noise (counts)	Integrated detector error (rel. photons)	Integrated signal (rel. photons)	Laser fluctuation	Total error (rel. photons)	Derivatives	PLQE error	PLQE	Relative PLQE error (%)	Sample absorption
520 NO LAS	60	4.96E+24	7.21E+27	0.01	7.23E+25	-9.49E-30				
520 ON LAS	60	1.80E+24	3.48E+26	0.01	3.91E+24	1.06E-29				
520 OFF LAS	60	4.69E+24	6.39E+27	0.01	6.40E+25	5.78E-31	0.00104	0.06846	1.52468	0.94556
520 ON PL	60	2.58E+24	4.69E+26	0.01	5.35E+24	1.47E-28				
520 OFF PL	60	2.50E+24	3.16E+25	0.01	2.52E+24	-7.98E-30				
658 NO LAS	60	4.67E+24	1.13E+28	0.01	1.13E+26	-5.13E-30				
658 ON LAS	60	3.51E+24	6.20E+27	0.01	6.21E+25	1.35E-29				
658 OFF LAS	60	4.46E+24	1.02E+28	0.01	1.02E+26	8.18E-30	0.00161	0.05773	2.78246	0.39415
658 ON PL	60	2.55E+24	2.79E+26	0.01	3.78E+24	2.25E-28				
658 OFF PL	60	2.50E+24	3.74E+25	0.01	2.53E+24	-1.37E-28				

Figure 5-15 –Inputs for random error calculation for example down-converter sample excited at 520 nm and 658 nm (10 mg mL^{-1} TIPS-tetracene and 20 mg mL^{-1} PbS-TIPS-TetCAL QDs). Each acquisition time for all measurements was 40 s. Integrated detector error refers to combined shot noise error and read noise error, corrected for spectral sensitivity. Total error is the combined detector error and error from laser fluctuations. Derivatives refer to terms in random error formula previously described. Sample absorption calculated from *A* in PLQE formula.

Following the expressions for propagation of random error within the PLQE measurement, the relative and absolute errors were calculated. Figure 5-15 shows an example of the inputs for error calculation for a down-converter sample with 658 nm and 520 nm excitation. The CCD read error was measured by taking the standard deviation of the background noise for each acquisition setting and was found to be similar for all cases as the total acquisition time was the same for all samples, thus assumed to be the same for simplicity. The shot noise error for each pixel was propagated with the read error to give the total count error per pixel. The count error was factored by the spectral sensitivity in quadrature and integrated to give the photon-count error. The error was then factored with the derivatives for each integrated signal term in quadrature to give the absolute error in PLQE.

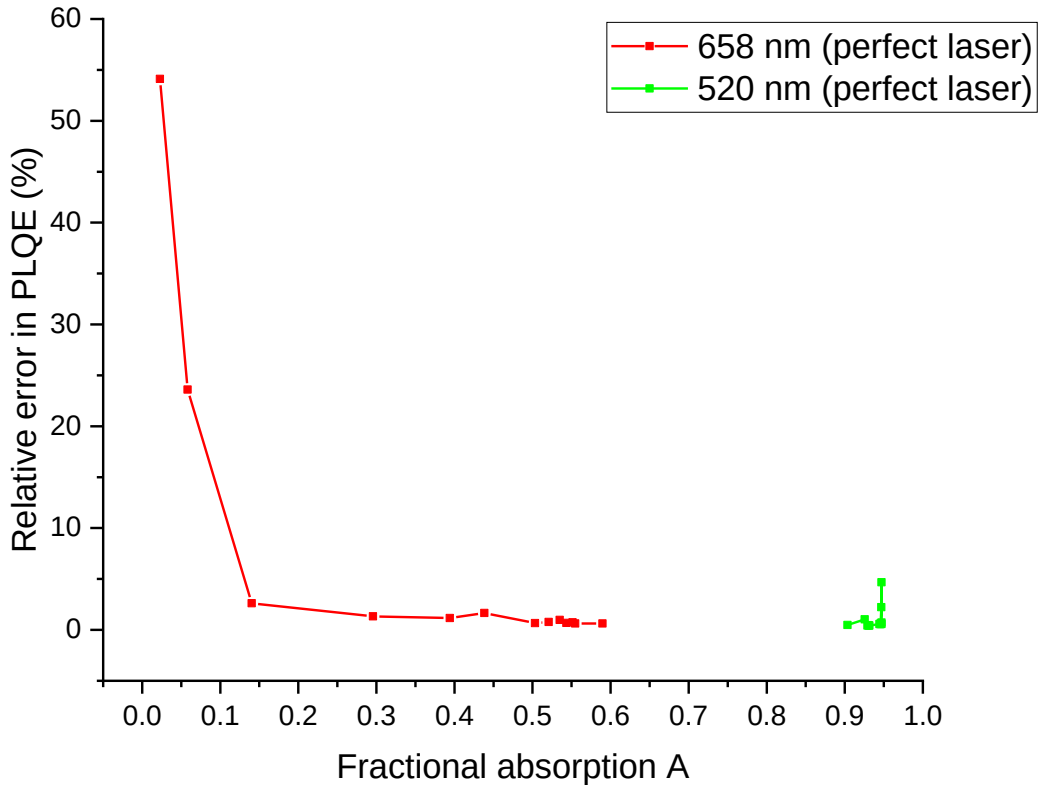

Figure 5-16 – Comparison of relative errors obtained for down-conversion assemblies measured with 658 nm excitation and 520 nm excitation. All samples possessed very high absorption at 520 nm from both QD and TIPS-tetracene. However, only the QD component was able to absorb the 658 nm excitation thus low fractional absorptions were obtained at low QD component concentrations. At low fractional absorption below 0.1, excessive errors become present as a result of large values of the partial derivatives for the ON and OFF laser terms in the error expression. Acquistion time was 2×20 s and 4×10 s for 520 nm and 658 nm excitation respectively.

Figure 5-16 shows the plot of calculated error, plotted as relative error against sample absorption for all down-conversion assemblies assuming perfect excitation stability. It can be seen that all samples were highly absorbing at 520 nm excitation because of high optical densities from both QD and organic components and possessed relatively consistent small errors. At 658 nm excitation, the sample absorption was dependent on the QD concentration thus the absorption was very low at low QD concentration. The relative errors shown in Figure 5-16 were the absolute error divided by the PLQE value, and it can clearly be seen that low sample absorption contributes excessively to errors in PLQE, resulting from the large values of the derivatives of the ON_{LAS} and OFF_{LAS} terms in the error formula. An alternative conceptualisation is to consider the integrals of the excitation peaks at low sample absorption. These large numbers will be similar in magnitude and their resulting small-number

differences are susceptible to the corresponding absolute values of shot noise, i.e. the difference of two large numbers may be comparable in magnitude to their square roots.

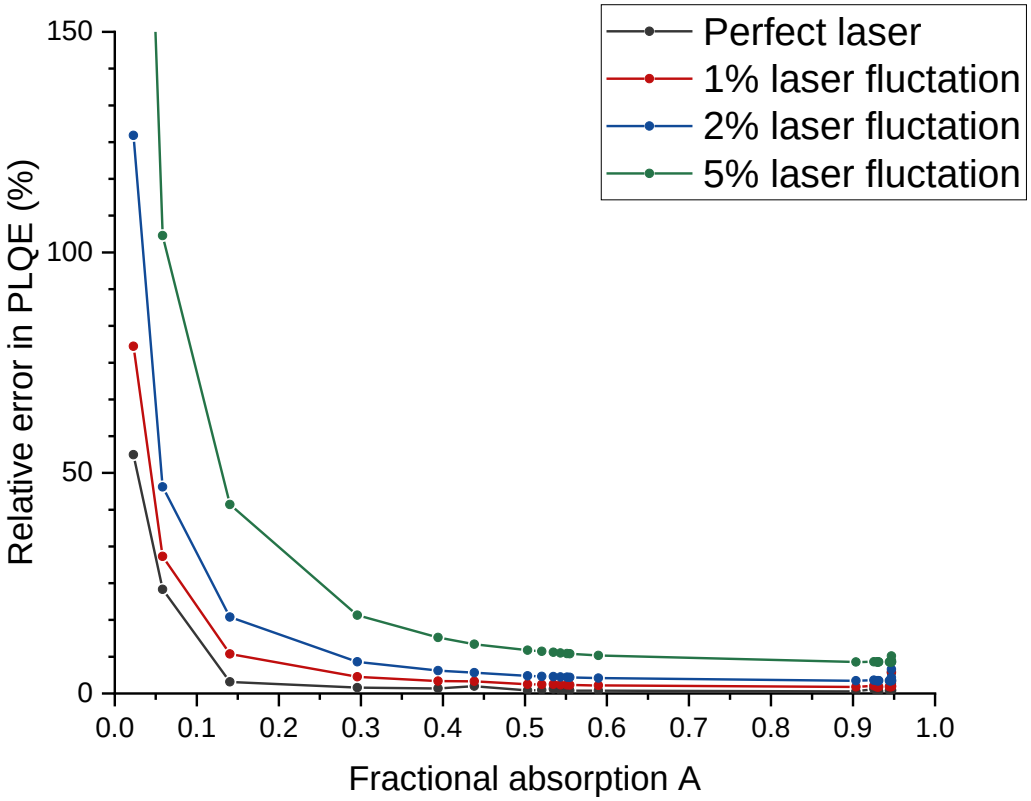

Figure 5-17 - Plot of measured relative error in PLQE for down-conversion assemblies as function of measured fractional absorption A. The simulated laser fluctuation increases the relative error for all sample absorptions. Acquistion time was 2×20 s and 4×10 s for 520 nm and 658 nm excitation respectively.

The error bars included in the plots within this section below were calculated with an assumed laser fluctuation of 1%, shown as the red points in Figure 5-17. The laser output power was not logged for these measurements however an assumed laser fluctuation of 1% was included for all error calculations from previous experience. From Figure 5-17, it can be seen that laser fluctuations greatly increase random errors as an additional factor irrespective of sample absorption. Typically, laser fluctuations of diode lasers were measured at around 0.5-2% in other instances, with >5% observed in very extreme cases caused by degradation of the diode. Fluctuations experienced were typically sinusoidal with periods of ~1 min, or on a similar timescale to the acquisition time. Drift, or a gradual slope to the mean output over time can also be observed with certain lasers, however it is generally negligible for temperature-controlled diodes and power supplies with optimised PID settings.

For plots involving calculation of singlet fission and transfer yields shown below, error bars were calculated by propagating the error between measurements as required.[19]

Down-converter efficiency

The measured PLQE of down-converter assemblies varied according to PbS QD and TIPS-tetracene concentration. The QD concentration was varied for a fixed TIPS-tetracene concentration of 20 mg mL^{-1}. As shown in Figure 5-18, the overall PLQE increased with increasing QD concentration for both excitation laser wavelengths. Direct excitation of the QDs with 658 nm excitation produced higher PLQEs at concentrations below 20 mg mL^{-1}. The QD absorption fraction increased with increasing concentration compared to TIPS-tetracene for 520 nm excitation light. In the absence of SF and energy transfer processes, absorption of excitation light by the TIPS-tetracene component creates a shadowing effect on the QDs. The absorbed light fraction is unable to excite the QDs and the measured photoluminescence quantum yield of the PbS QDs decreases, as the measured emission is lower for the measured overall absorption. As the QD fraction increases, the fraction absorbed by TIPS-tetracene decreases and the shadowing effect diminishes. At 20 mg mL^{-1} QD concentration, the measured PLQE was slightly higher for 520 nm excitation than 658 nm excitation.

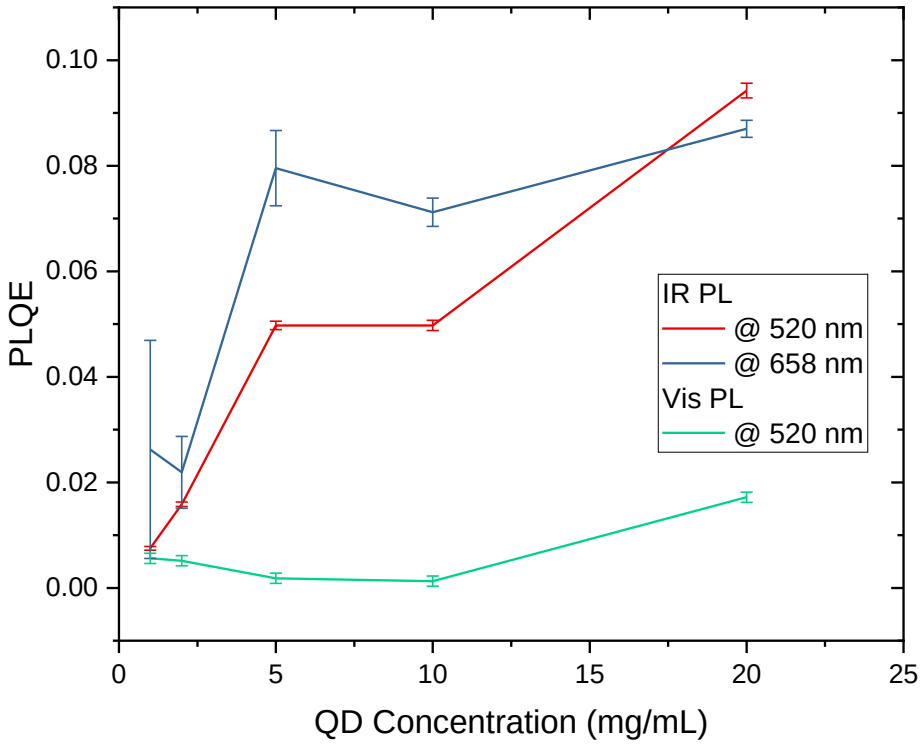

Figure 5-18 – Visible and near-infrared photoluminescence quantum efficiencies of TIPS-tetracene/PbS QD down-conversion assemblies with varying QD concentrations at 520 nm and 658 nm excitation. TIPS-tetracene concentration was fixed at 20 mg mL^{-1}.

Although within error, matching PLQEs for 520 nm and 658 nm excitation was not explained by the shadowing effect. Another scenario was considered: absorption by TIPS-tetracene generates singlet excitons which may transfer directly to QDs through Förster resonance energy transfer (FRET).[21,22] Assuming no singlet fission and complete transfer of TIPS-tetracene singlet excitons into the QDs via FRET, the shadowing effect is eliminated. The measured PLQE for 520 nm and 658 nm excitation would then become consistent and identical to the luminescence efficiency of the QDs. The PLQE limit for the scenario of complete singlet transfer was calculated from the absorption fraction of the TIPS-tetracene multiplied by the luminescence efficiency of the PbS QDs.

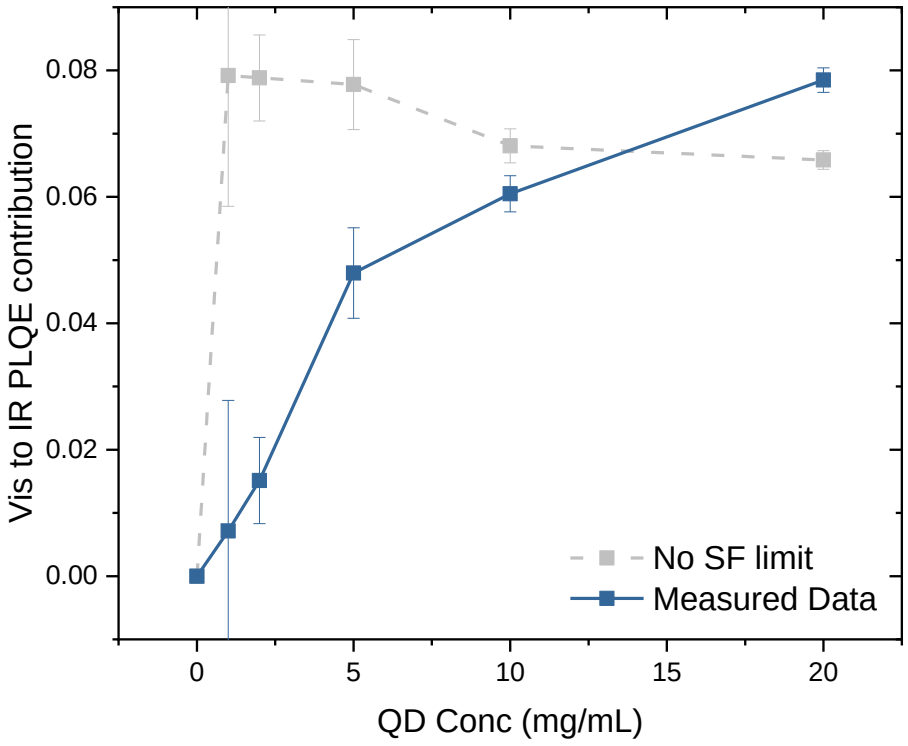

Figure 5-19 – PLQE of down-conversion assemblies with varying QD concentration and 20 mg mL^{-1} TIPS-tetracene concentration at 520 nm excitation compared to PLQE limit assuming complete singlet transfer.

As shown in Figure 5-19, the predicted limit showed that at low QD concentrations, the QD PLQE at 520 nm visible excitation could be explained through the absence of exciton multiplication processes. However, at 20 mg mL^{-1} QD concentration, the measured PLQE appeared to exceed the set limit assuming complete singlet transfer, although within the error of the measurement.

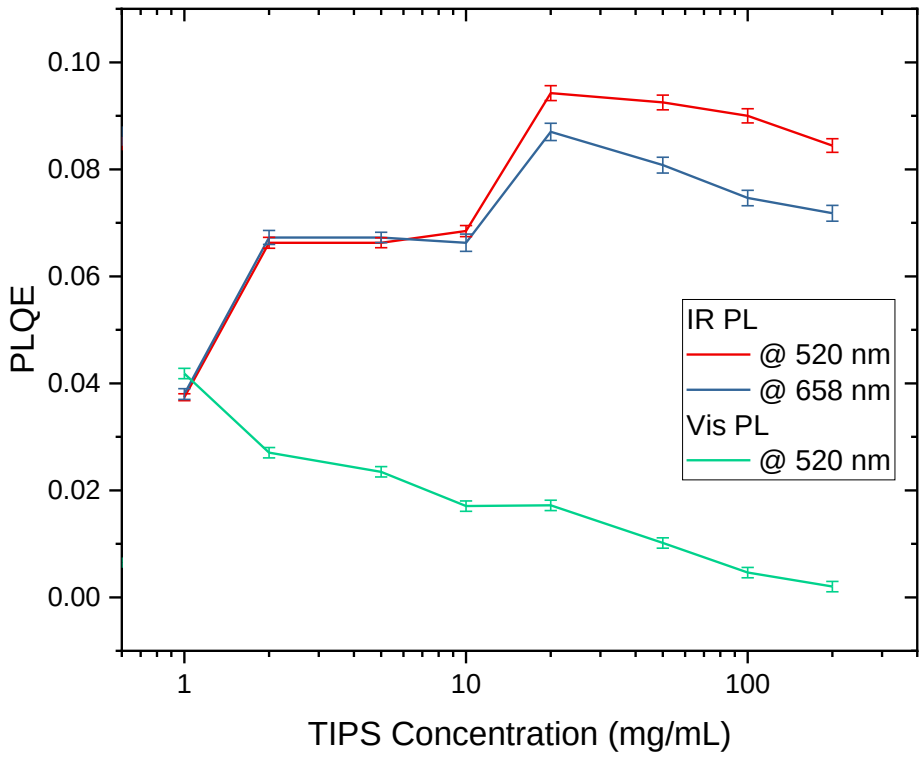

Figure 5-20 - Visible and near-infrared photoluminescence quantum efficiencies of TIPS-tetracene/PbS QD down-conversion assemblies with varying TIPS-tetracene concentrations at 520 nm and 658 nm excitation. QD concentration was fixed at 20 mg mL^{-1}.

To increase the absorption depth of TIPS-tetracene and potentially optimise the efficiency of singlet fission and triplet transfer, the concentration was varied. The QD concentration was fixed at 20 mg mL^{-1}. At low TIPS concentrations, photoluminescence in the visible region from the TIPS-tetracene singlet state was observed. Increase of the TIPS concentration resulted in a decrease of the visible component PLQE. At high TIPS-tetracene concentrations, emission in the near-infrared displayed higher PLQE with 520 nm excitation compared to with 658 nm excitation outside of measurement error as shown in Figure 5-20, indicating enhancement of PLQE through singlet fission and energy transfer.

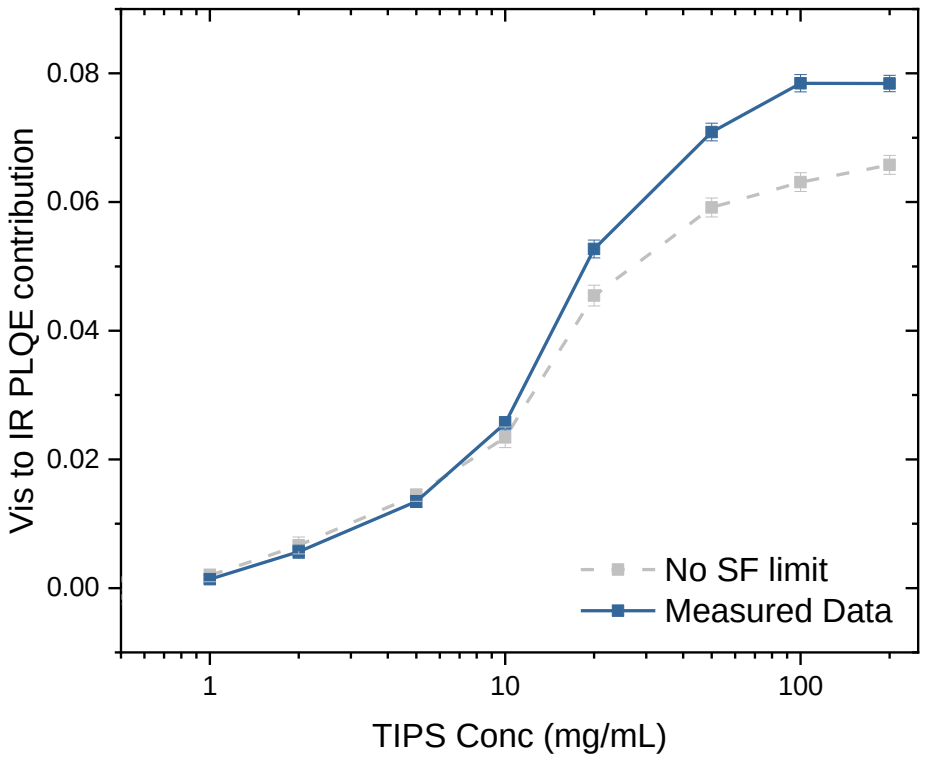

Figure 5-21 – PLQE of down-conversion assemblies with varying TIPS-tetracene concentration and 20 mg mL^{-1} QD concentration at 520 nm excitation compared to PLQE limit assuming complete singlet transfer.

The PLQE was higher than the complete singlet transfer limit for 50 mg mL^{-1} TIPS-tetracene and greater as shown in Figure 5-21. This "No SF limit" represents the condition where no triplets are generated, and all excitations are transferred to the QDs as singlets, i.e. the maximum number of excitons is the number of absorbed photons.

The NIR QD photoluminescence was divided into multiple constituents. At 658 nm excitation, the TIPS-tetracene is transparent and all light is absorbed by the QDs. The NIR PLQE is thus the emission efficiency of the QDs. At 520 nm excitation, a fraction of the excitation light is absorbed by the QDs directly. A fraction of the emission PLQE is thus from direct QD excitation by 520 nm light, quantified by the absorption fraction multiplied by the QD emission efficiency. The remainder of the absorbed excitation light is absorbed by TIPS-tetracene. The fraction of the measured NIR luminescence efficiency as a result of singlet or triplet transfer from TIPS-tetracene to the QDs is calculated by subtracting the direct QD excitation PLQE from the total NIR PLQE.

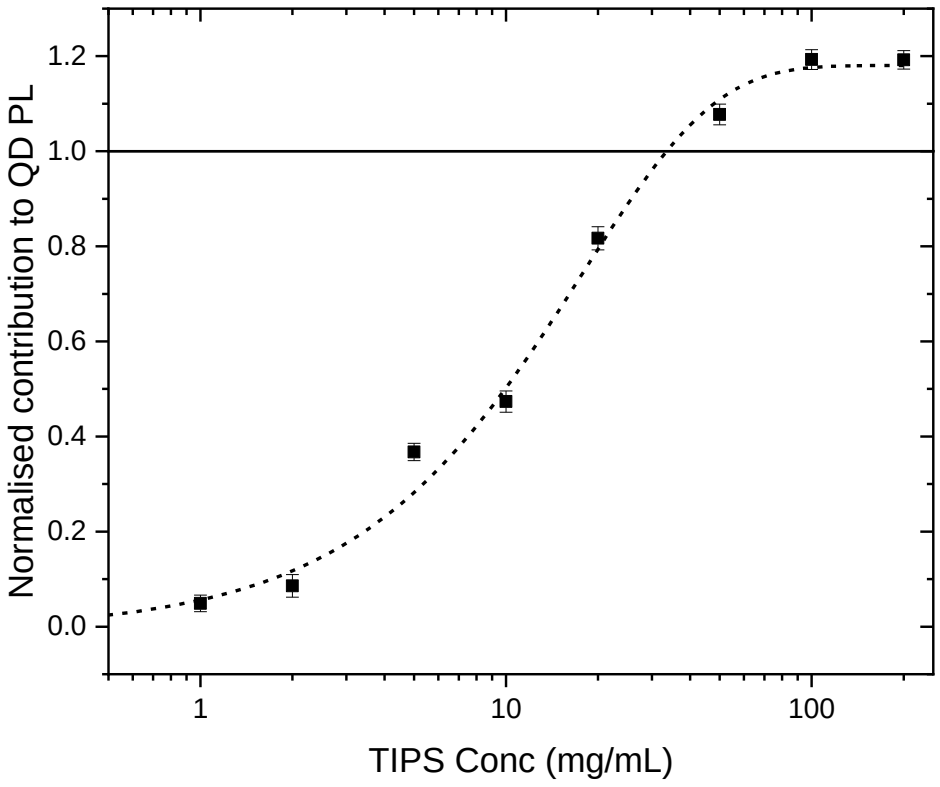

Figure 5-22 – Proportion of PbS QD photoluminescence resulting from TIPS-tetracene transfer at 520 nm compared to QD excitation at 658 nm. A ratio of 1 indicates break-even for luminescence efficiency arising from combined QD absorption and TIPS-tetracene absorption.

Normalising the energy transfer PLQE with the QD emission PLQE provides the fraction of NIR emission resulting from energy transfer into the QDs, as shown in Figure 5-22. By comparing the ratio of PLQE originating from energy transfer processes to the PLQE limit set by complete singlet transfer, the product of the singlet fission and energy transfer efficiency is obtained, as shown in Figure 5-23. At TIPS-tetracene concentrations above 10 mg mL^{-1}, the product of the SF and energy transfer efficiencies is in excess of 1, indicating the occurrence of photon multiplication. The efficiency product reaches a peak of 1.2 at high TIPS-tetracene concentrations.

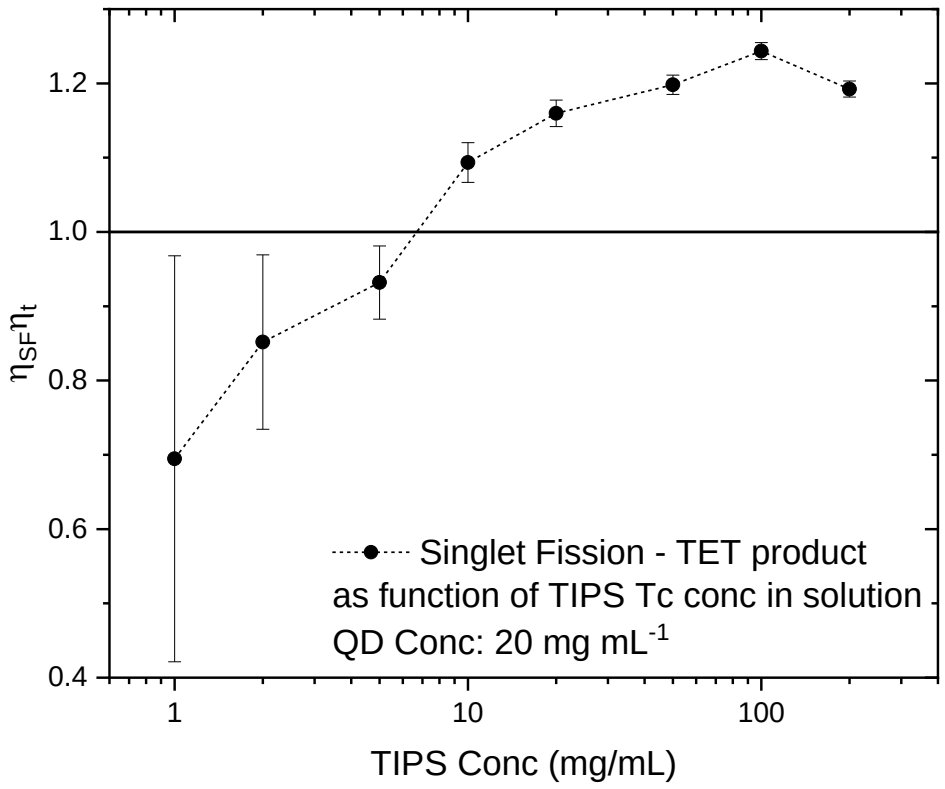

Figure 5-23 – Calculated product of singlet fission and energy transfer efficiencies from TIPS-tetracene to QD. A ratio of 1 indicates break-even for combined singlet fission and triplet energy transfer efficiencies.

5.9 Working Conclusions

The overall down-conversion assembly luminescence efficiency was low at less than 10%, primarily resulting from poor QD luminescence efficiency in these conditions. However, clear demonstration of a photon multiplication process was achieved in the solution-based systems. The crucial factor in demonstrating photon multiplication was accurate measurement of photoluminescence quantum efficiency despite the difficult conditions of high absorption and low quantum yields. Through meticulous identification of the factors and sources of systematic and random error, explained previously in this Chapter, it was possible to maintain a measurement setup and develop a methodology for repeatable and accurate PLQE measurements across a wide spectral range on a multi-component system. These efforts allowed the positive validation of observed photon multiplication with a high degree of confidence.

5.10 References

1. Bae, W. K., Lim, J., Lee, D., Park, M., Lee, H., Kwak, J. *et al. Advanced Materials* **26**, 6387–

6393 (2014).

2. Gerion, D., Pinaud, F., Williams, S. C., Parak, W. J., Zanchet, D., Weiss, S. *et al. The Journal of Physical Chemistry B* **105**, 8861–8871 (2001).

3. Tamang, S., Lincheneau, C., Hermans, Y., Jeong, S. & Reiss, P. *Chemistry of Materials* **28**, 2491–2506 (2016).

4. Davis, N. J. L. K., Allardice, J. R., Xiao, J., Karani, A., Jellicoe, T. C., Rao, A. *et al. Materials Horizons* **6**, 137–143 (2019).

5. Al-Khuzheyri, R., Dada, A. C., Huwer, J., Santana, T. S., Skiba-Szymanska, J., Felle, M. *et al. Applied Physics Letters* **109**, (2016).

6. Valenta, J. *Nanoscience Methods* **3**, 11–27 (2014).

7. de Mello, J. C., Wittmannn, H. F. & Friend, R. H. *Advanced materials (Deerfield Beach, Fla.)* **9**, 230 (1997).

8. Würth, C., Grabolle, M., Pauli, J., Spieles, M. & Resch-Genger, U. *Nature Protocols* **8**, 1535–1550 (2013).

9. Kubin, R. F. & Fletcher, A. N. *Journal of Luminescence* **27**, 455–462 (1982).

10. Rurack, K. & Spieles, M. *Analytical Chemistry* **83**, 1232–1242 (2011).

11. Brouwer, A. M. *Pure and Applied Chemistry* **83**, 2213–2228 (2011).

12. Xu, S., Wang, C., Xu, Q., Li, R., Shao, H., Zhang, H. *et al. The Journal of Physical Chemistry C* **114**, 14319–14326 (2010).

13. Fischer, M. & Georges, J. *Chemical Physics Letters* **260**, 115–118 (1996).

14. Semonin, O. E., Johnson, J. C., Luther, J. M., Midgett, A. G., Nozik, A. J. & Beard, M. C. *Journal of Physical Chemistry Letters* **1**, 2445–2450 (2010).

15. Greenham, N. C., Samuel, I. D. W., Hayes, G. R., Phillips, R. T., Kessener, Y. A. R. R., Moratti, S. C. *et al. Chemical Physics Letters* **241**, 89–96 (1995).

16. Van Dam, B., Bruhn, B., Dohnal, G. & Dohnalová, K. *AIP Advances* **8**, 085313 (2018).

17. van Dam, B., Bruhn, B., Kondapaneni, I., Dohnal, G., Wilkie, A., Křivánek, J. *et al.* 1–14 (2018).

18. Yoon, H. W. & Gibson, C. E. (2011).

19. Ku, H. H. *Journal of Research of the National Bureau of Standards, Section C: Engineering and Instrumentation* **70C**, 263 (1966).

20. Goodman, L. A. *Journal of the American Statistical Association* **55**, 708–713 (1960).

21. Davis, N. J. L. K., Allardice, J. R., Xiao, J., Petty, A. J., Greenham, N. C., Anthony, J. E. *et al. The Journal of Physical Chemistry Letters* **9**, 1454–1460 (2018).

22. Li, X., Slyker, L. W., Nichols, V. M., Pau, G. S. H., Bardeen, C. J. & Tang, M. L. *Journal of Physical Chemistry Letters* **6**, 1709–1713 (2015).

Chapter 6 Applied Synthesis of Luminescent Nanocrystal Quantum Dots

6.1 Electric field modulation of quantum dot photoluminescence in electrolytic environments

In biological applications, colloidal quantum dots have been demonstrated as effective tracer materials for medical imaging applications.[1] Within biological settings, especially in vivo, it is especially important for colloidal quantum dots to be nontoxic and biocompatible to prevent affecting the metabolic processes being studied. Previous studies have utilised various core-shell-structured nanocrystals to achieve biocompatibility by minimising exposure to nanocrystal cores with toxic material compositions.[2–4] Zinc-based semiconductor materials have been commonly featured as shell materials as they have been perceived as being of lower toxicity. Coating of toxic QD cores such with less-toxic shells has been generally followed as a design rule.[5–7] The further ligand functionalisation of the nanoparticle surface has demonstrated potent selectivity for various biological targets.[1,8]

Current applications of colloidal QDs in biological applications have been primarily focussed on their use as photoluminescent centres.[7,9,10] QDs have been highly effective in this role, with near-infrared emission especially effective for transmission through tissue; this approach has often shown insensitivity to changes in local environment, however this is not necessarily disadvantageous. Greater spatial and temporal resolution may be achieved through modulation of photoluminescence by changes in local environment such as voltage within cell systems, providing an additional information channel by utilising the temporally-resolved photoluminescence intensity of the emitter, in addition to their spatial localisation.

Previous research has demonstrated the use of Cd-based QDs as voltage probes and QD response to electric fields has been demonstrated in solid state capacitive devices.[11–13] However, the cytotoxicity of Cd-based QD materials becomes problematic for use in biological systems and solid state devices do not accurately mimic biological environments.[14] Here, core-shell colloidal QDs have been synthesised for the development of a novel voltage probe. Methods of voltage detection in biological systems have been extensively researched for the study of neuronal systems.[15] Previous approaches for neuronal study have involved techniques such as: genetically-encoded voltage indicators, molecular Stark-effect sensors, 2-photon imaging and positron emission tomography.[15–19] In this work, voltage-modulated photoluminescence of biocompatible colloidal QDs with ZnS shells has been investigated. Voltage-sensitive QDs may enable spatially- and temporally-resolved mapping and measurement of voltage in neuronal systems with greater accuracy and sensitivity compared to current

methods. In a biologically-relevant electrolytic environment, the photoluminescence response of quantum dots to fields generated by ion gradients has been demonstrated.

This work was performed in collaboration with Mustafa Calgar and Raj Pandya. My contribution was the synthesis and characterisation of all QDs used.

6.2 Methods

CdSe/CdS core-shell nanocrystals were synthesised in adaptation of a previously published method.[20] In short, CdO (0.128 g, 1 mmol), oleic acid (1.26 mL) and 1-octadecene (20 mL) were degassed under vacuum at 110 °C for 30 minutes. The vessel was switched to N_2 and heated to 300 °C to form a colourless solution. A 1 M solution of Se in trioctylphosphine was prepared in the glovebox and injected (0.25 mL) into the Cd solution at 300 °C. After 90 s 1-dodecanethiol (180 µL) was added dropwise and the reaction was maintained at 300 °C for 30 minutes. The reaction was quenched by cooling to room temperature and the product isolated by repeated precipitation and centrifugation with ethanol and re-suspension in toluene.

ZnS shell growth on CdSe/CdS nanocrystals was performed according to a previously published method.[21] A typical synthesis is as follows: Zinc diethyldithiocarbamate (0.18 g) was loaded into a 3-necked flask and purged with nitrogen. A mixture of 1-octadecene (10 mL), trioctylphosphine (3 mL) and oleylamine (3 mL) was prepared in the glovebox and added to the flask. A solution of CdSe/CdS in hexane (35 mg/mL, 2.5 mL) was added to the flask and then degassed at room temperature under vacuum. The vessel was switched to nitrogen then heated to 120 °C for 2 hours for shell growth. The reaction was quenched by cooling to room temperature and the product isolated by repeated precipitation and centrifugation with acetone and re-suspension with hexane.

InP/ZnS core-shell nanocrystals were synthesised according to a previously published method.[22] A typical synthesis is as follows: $InCl_3$ (0.24 g, 1 mmol) and oleylamine (5 mL) was degassed under vacuum at 140 °C for 1 hour. The solution was switched to nitrogen and heated to 180 °C for injection. Tris(dimethylamino)phosphine (0.18 mL) in oleylamine (0.5 mL) was quickly injected into the solution and maintained for 15 minutes. The reaction was quenched by cooling to room temperature and the product isolated by repeated precipitation and resuspension with acetone and hexane respectively and stored in the glovebox. For growth of ZnS shells, $ZnCl_2$ (0.27 g, 2 mmol) and oleylamine (2 mL) and 1-octadecene (5 mL) was degassed at 120 °C under vacuum. The vessel was switched to N_2 and heated to 200 °C until all solid had dissolved. The solution was cooled to room temperature and a solution of InP cores (20 mg/mL, 3 mL) was injected then degassed under vacuum. The vessel was again switched to nitrogen and heated to 140 °C, whereupon 1-dodecanethiol (0.48 mL, 2 mmol) was added dropwise. The reaction was heated to 250 °C for 1 hour to facilitate

shell growth before cooling to room temperature. The finished product was isolated by repeated precipitation and centrifugation in acetone and re-suspension in hexane.

Ligand exchange of nanocrystals with pyridine was performed with the addition of an equal volume of pyridine to a 20 mg/mL solution of nanocrystals in a glovebox and left at room temperature for 10 minutes. Acetone was added to precipitate the exchanged dots followed by centrifugation. The supernatant was discarded and the dots were re-suspended in toluene. Pyridine-exchanged nanocrystals were dried and redispersed in 1 M aqueous KNO_3 solution for PL measurement in electrolytic conditions without further purification. For device applications, bipyridine was used interchangeably, with poorer colloidal stability but better adhesion to substrate surfaces.

Photoluminescence quantum efficiency (PLQE) measurements were performed according to the method of de Mello.[23] Excitation was provided by a Coherent OBIS 405 nm laser. The optical system was a 6-inch Labsphere with diffusely-reflective BaSO4 coating, fibre-coupled into an Andor Shamrock SR-303i imaging spectrograph with iDus Si CCD detector. Detailed explanations of the measurement are described in Chapter 5, and the therein identified precautions to achieve accurate measurements were performed for all PLQE values explicitly shown in this sub-Chapter. However, full random error analysis was not performed as the samples measured in this sub-Chapter were measured with the low-noise Si detector and were sufficiently absorbing, random error was deemed negligible.

UV-visible absorption measurements were taken with a Hewlett Packard 8453 diode-array spectrophotometer. Samples were diluted in toluene and placed in a quartz absorption cuvette (Hellma Suprasil) with 1 cm path length.

Transmission electron microscopy (TEM) was performed with a FEI Tecnai F20 field-emission scanning/transmission electron microscope (S/TEM) at 200 kV accelerating voltage. Diluted nanocrystal samples were drop-cast onto holey carbon-coated Cu grids (Agar AGS160).

6.3 Results

Synthesis of biocompatible quantum dots

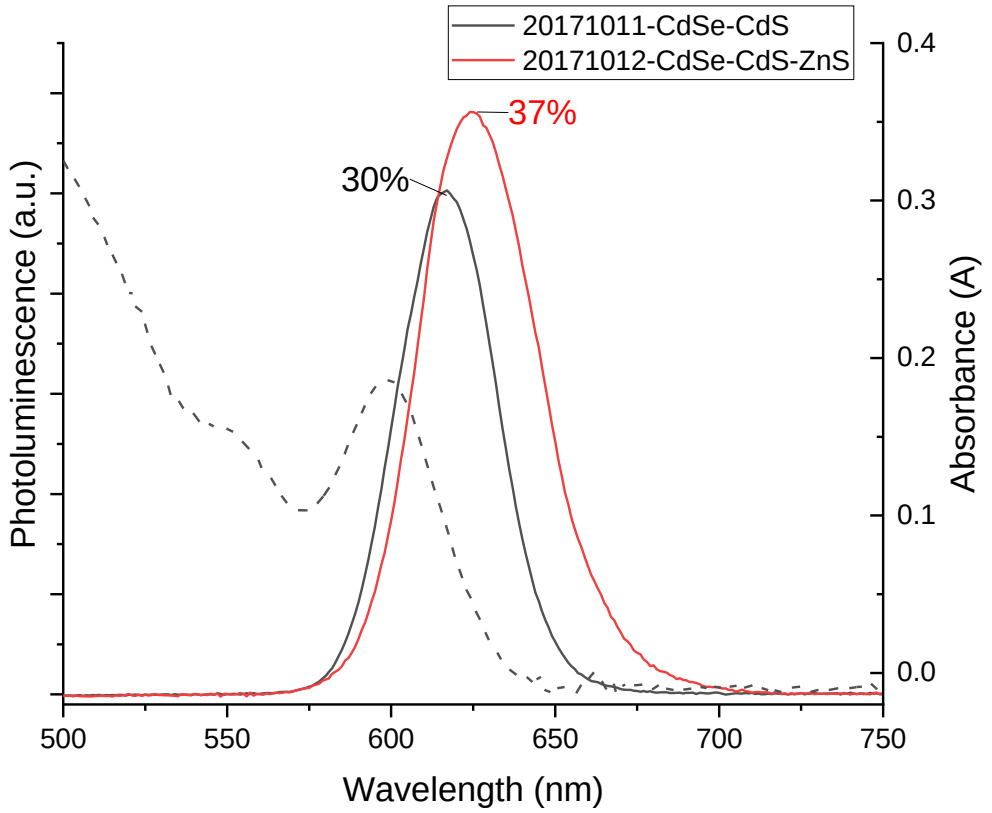

Figure 6-1 – UV-Visible absorption and photoluminescence (PL) spectra of CdSe/CdS core-shell QDs and PL spectrum of CdSe/CdS/ZnS core-shell-shell QDs following growth of ZnS shell. Measured photoluminescence quantum efficiencies labelled. PL spectra normalised and scaled to PLQEs with peak area.

Synthesised CdSe/CdS core-shell nanocrystals demonstrated good photoluminescence quantum efficiencies, shown in Figure 6-1. However, to improve stability, luminescence and reduce potential cytotoxicity, growth of an additional ZnS shell was performed. Following growth of ZnS shells, PLQE improved appreciably, suggesting better surface passivation with the thick shell structures. A slight redshift in emission position and peak broadening were observed, indicating exciton wavefunction leakage into the ZnS shell conduction band and slight increase in size distribution under the high temperature reaction conditions and size defocusing before shell growth.[24]

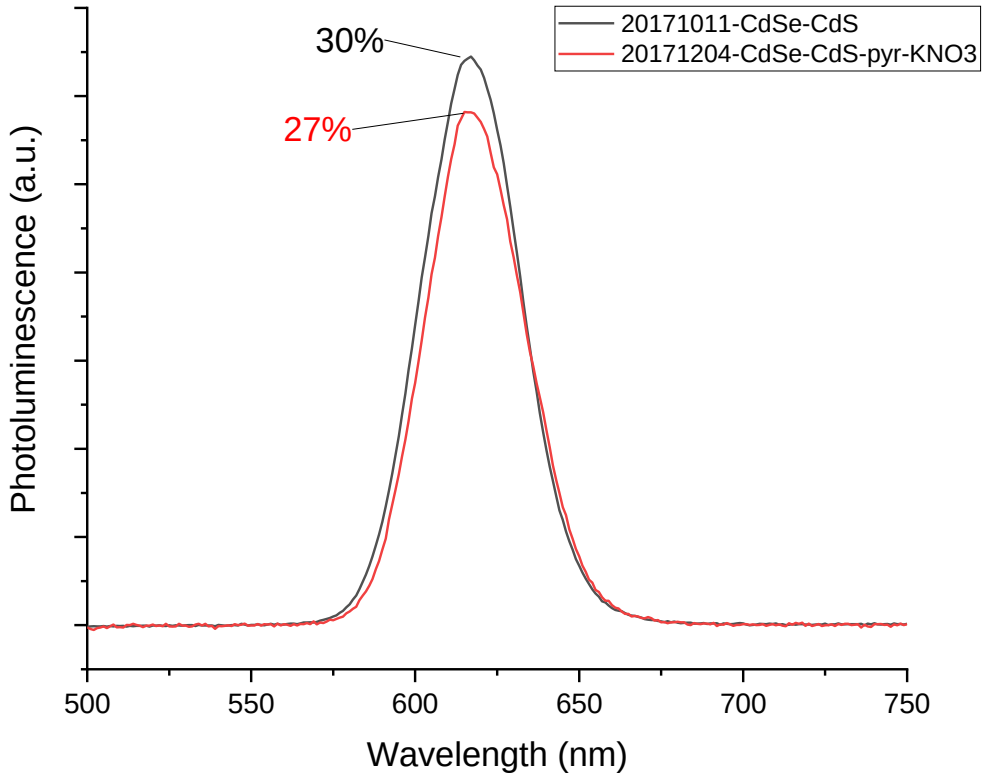

Figure 6-2 – Photoluminescence spectra of CdSe/CdS suspended in toluene or 1 M aqueous KNO_3 solution. Measured PLQE labelled and peaks normalised and scaled to PLQE with area.

Significant photoluminescence was still observed after pyridine-functionalisation and resuspension in aqueous electrolytic solvent for CdSe/CdS without ZnS shells, shown in Figure 6-2. Negligible peak shift was observed in the emission spectrum. As the resuspension was performed after only one purification step following ligand exchange, it was likely excess pyridine ligand was present within the solution, contributing to their solubility within the aqueous electrolytic environment. Prior to deposition on device substrates, the ligand-exchanged QDs were sequentially washed and diluted to decrease the free ligand concentration.

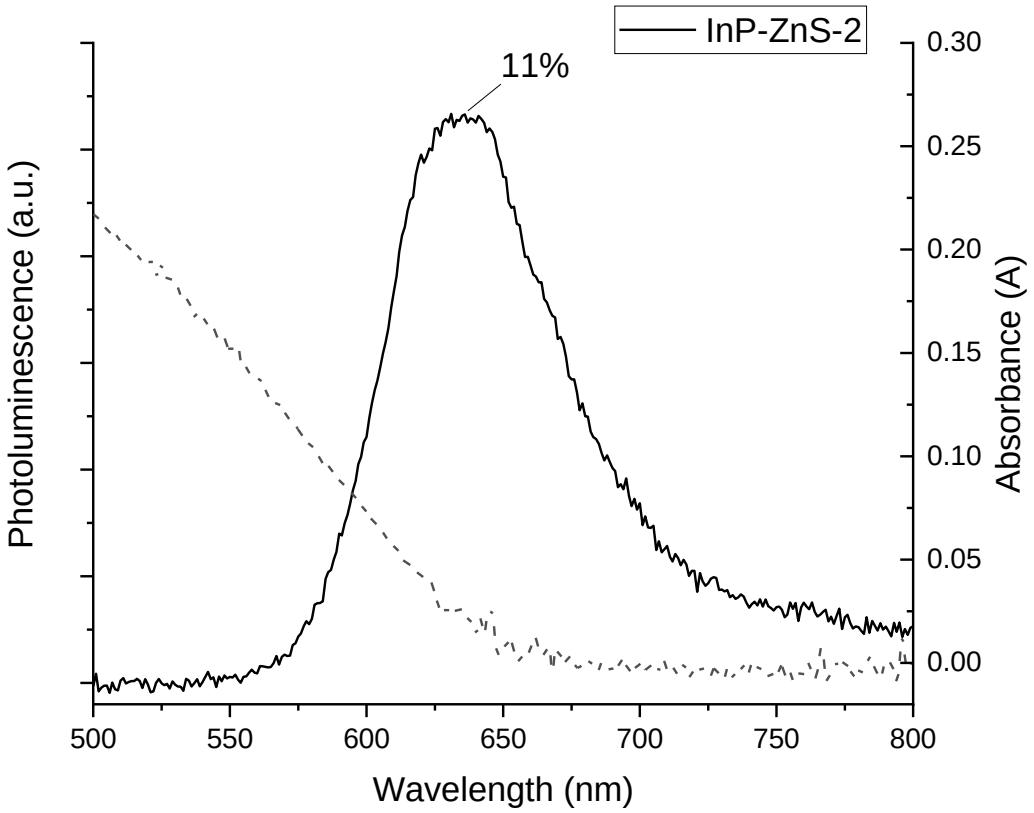

Figure 6-3 – UV-Visible absorption and photoluminescence (PL) spectra of InP/ZnS core-shell QDs. The InP core QDs possessed negligible photoluminescence.

InP QDs synthesised without core-shell structures demonstrated negligible luminescence and stability, with rapid degradation in atmospheric conditions. Upon growth of a ZnS shell, InP/ZnS core-shell-shell nanocrystals demonstrated much greater PLQE than the cores suggesting improved passivation of non-radiative traps on the InP surface was achieved, shown in Figure 6-3. Absorption spectroscopy did not show a well-defined excitonic peak indicating a relatively broad size distribution.[25] Literature reports of InP/ZnS nanocrystals synthesised with a different method have demonstrated higher luminescence efficiencies and stability in aqueous environments.[26–28]

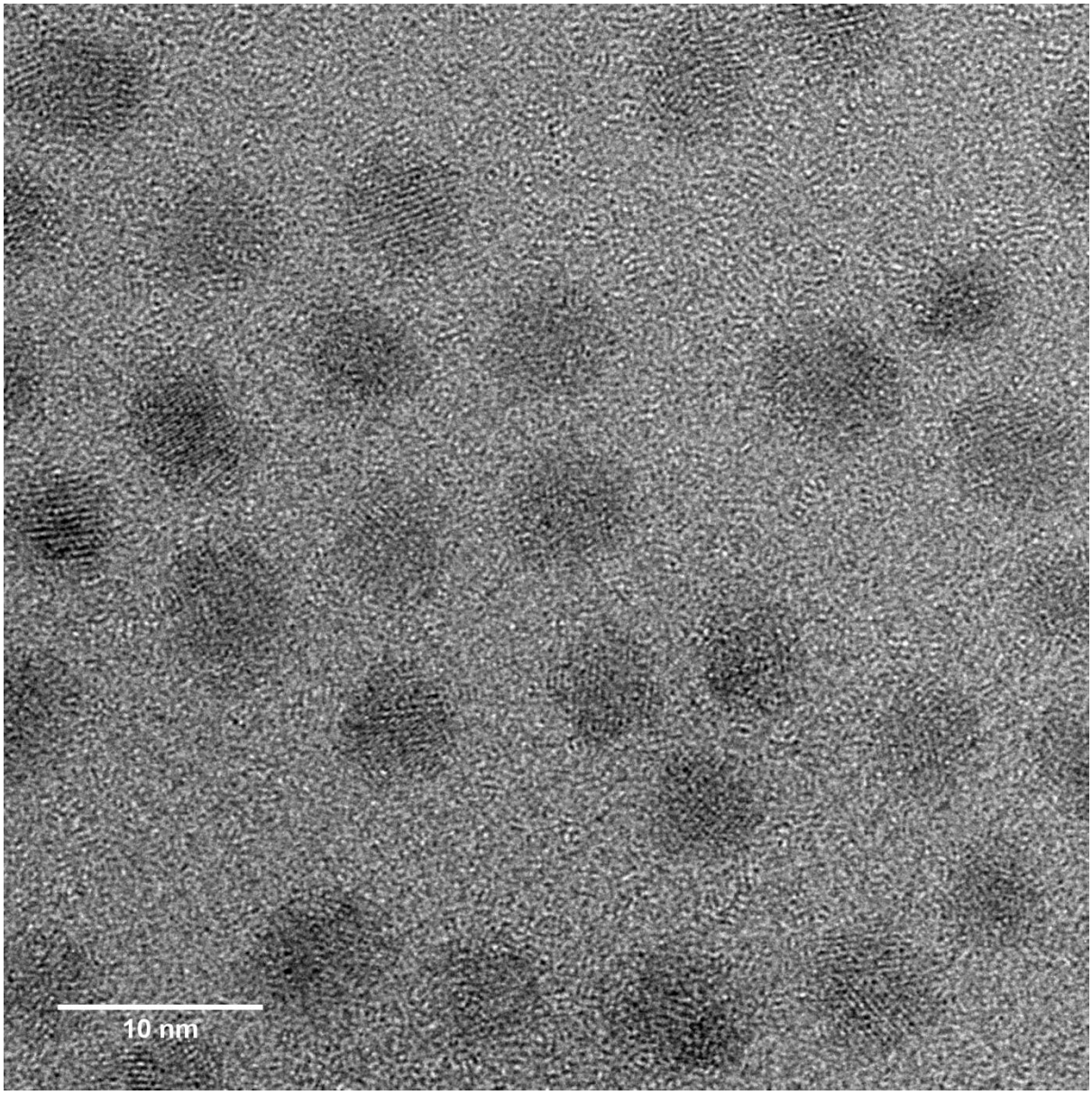

Figure 6-4 – TEM image of CdSe/CdS core-shell nanocrystals.

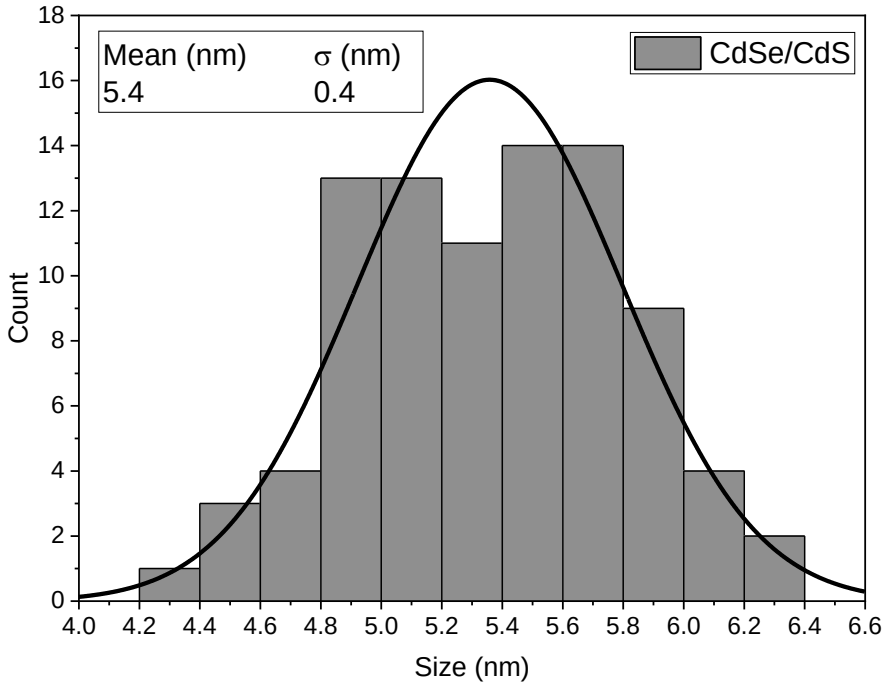

Figure 6-5 – TEM size distribution analysis of CdSe/CdS core-shell nanocrystals. Sizes were measured by manually taking the mean length along perpendicular axes. The mean size was 5.4 nm with a standard deviation of 0.4 nm.

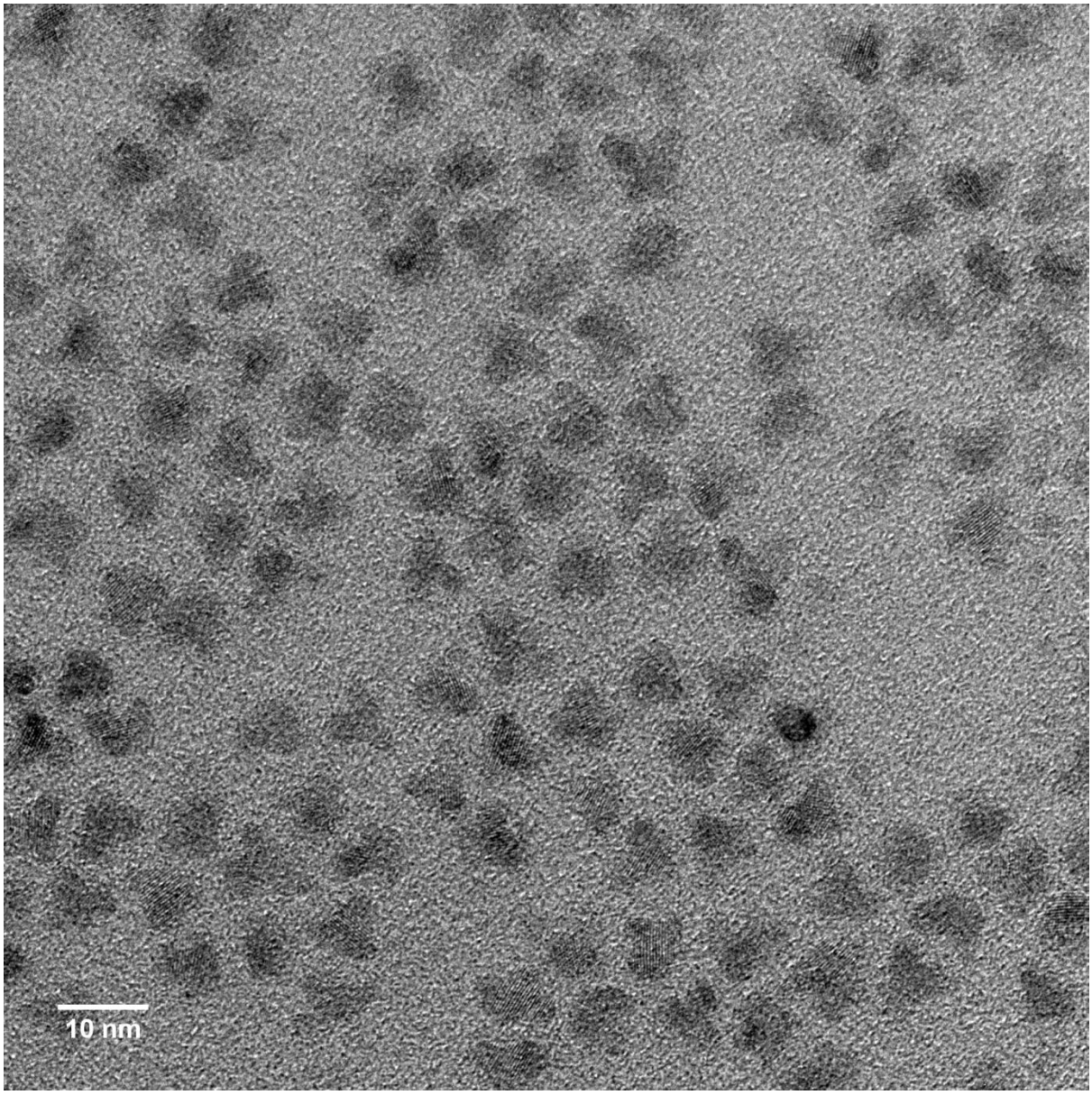

Figure 6-6 – TEM image of CdSe/CdS/ZnS core-shell-shell nanocrystals.

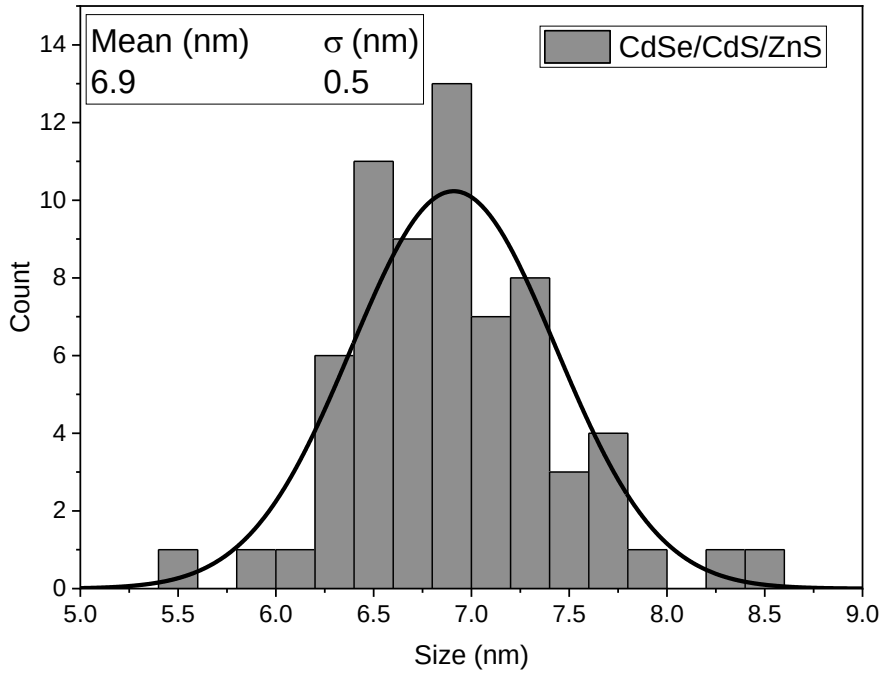

Figure 6-7 - TEM size distribution analysis of CdSe/CdS/ZnS core-shell-shell nanocrystals. Sizes were measured by manually taking the mean length along perpendicular axes. The mean size was 6.9 nm with a standard deviation of 0.5 nm.

Synthesised CdSe/CdS nanocrystals displayed rounded shapes of around 5.4 nm diameter as observed in TEM, shown in Figure 6-4. Upon ZnS shell growth, the observed nanocrystal sizes increased to a mean 6.9 nmand triangular shapes were observed, shown in Figure 6-6. Size distribution analysis, shown in Figure 6-5 and Figure 6-7 showed the standard deviation of CdSe/CdS was ±0.4 nm which increased to ±0.5 nm after ZnS shell growth. However, the size distribution remained at 7% before and after ZnS shell growth. The triangular shapes suggested tetrahedral crystal geometries, indicating anisotropic shell growth preferential along particular crystal facets on the rounded cores.

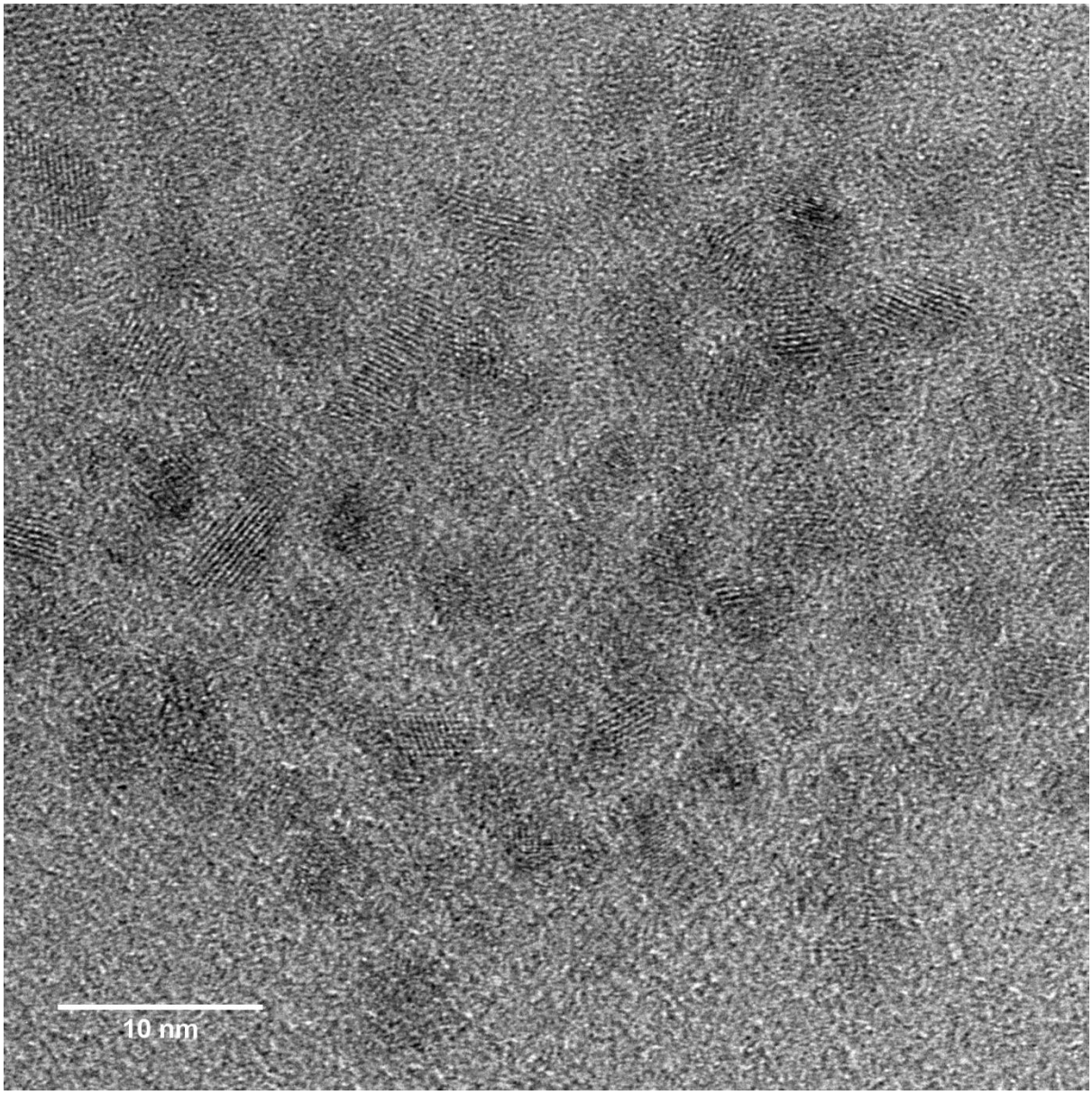

Figure 6-8 – TEM image of InP/ZnS core-shell nanocrystals.

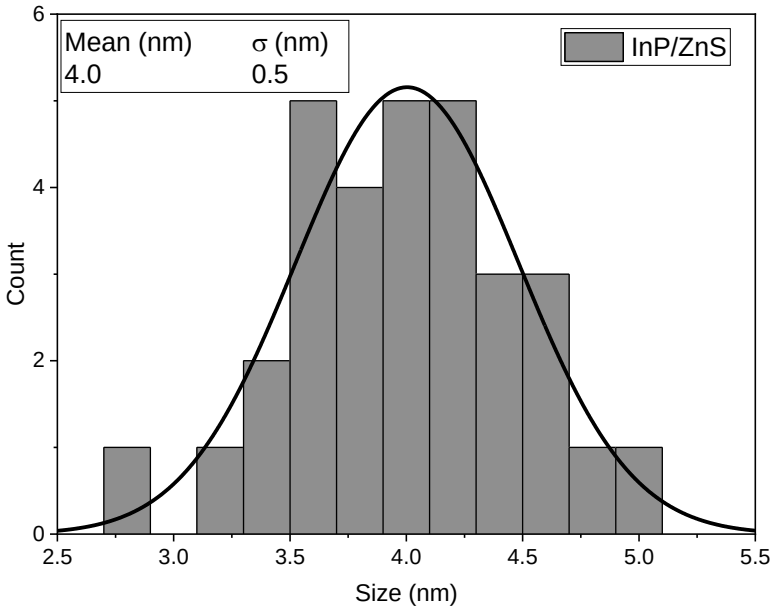

Figure 6-9 - TEM size distribution analysis of InP/ZnS core-shell-shell nanocrystals. Sizes were measured by manually taking the mean length along perpendicular axes. The mean size was 4.0 nm with a standard deviation of 0.5 nm.

InP cores were synthesised using a less reactive phosphine precursor to more common synthesis methods. InP cores synthesised with this method have previously demonstrated tetrahedral shapes, which are less evident after growth of ZnS shells, shown in Figure 6-8.[22] Size distribution analysis, measured manually by taking the mean of perpendicular particle dimensions and displayed in Figure 6-9, showed a mean size of 4.0 nm with a standard deviation of 0.5 nm. Shape selectivity resulted because of the differential reactivity of particular nanocrystal facets during growth. Selective growth of different shapes has been previously demonstrated through modification of synthetic parameters including growth ligands and precursor reactivity.[29,30] Synthesis with the much-more reactive tris(trimethylsilyl)phosphine precursor has been shown to produce round nanocrystals.[28] Shape has been shown to influence the optical and physical characteristics of QDs.[2] The stability and luminescence efficiency of InP QDs may be improved through shape modification with a different synthetic route.

Voltage measurement

Fabrication of devices, measurement of voltage-modulated photoluminescence response and data analysis was performed by Mustafa Calgar and Raj Pandya.

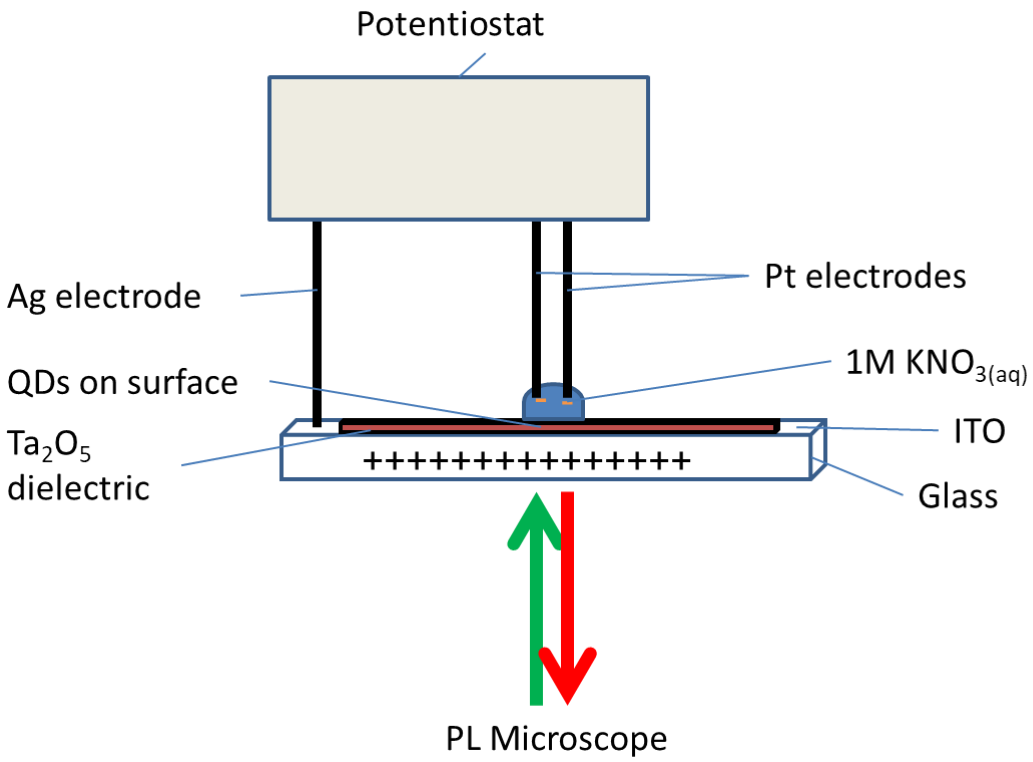

Figure 6-10 – Schematic cartoon of device to measure photoluminescence response of QDs to applied voltage. An electric field is generated by ion gradients in the electrolyte solution.

A device, illustrated in Figure 6-10 was fabricated to measure photoluminescence response of the QDs to an applied electric field. A thin strip of 150 nm dielectric Ta_2O_5 layer was deposited on top of an indium-tin oxide (ITO) glass substrate. A diluted suspension of pyridine- or bipyridine-functionalised core-shell quantum dots was spin-coated on top, with any excess unbound QDs washed away by a toluene rinse. A droplet of degassed aqueous KNO_3 solution was placed on top of the device and two platinum electrodes were immersed within the droplet as working and reference electrodes, ensuring neither was touching. A silver wire electrode was connected to the ITO surface as the counter electrode and all three were connected to a Gamry Ref600 potentiostat for the modulation of voltage and the application of electric fields. Photoluminescence was measured in the reflection mode from the QDs with excitation provided by a 532 nm diode laser and was collected using a combined inverted fluorescence microscope and spectrometer. Simultaneous voltage application and photoluminescence response measurement was thus possible.

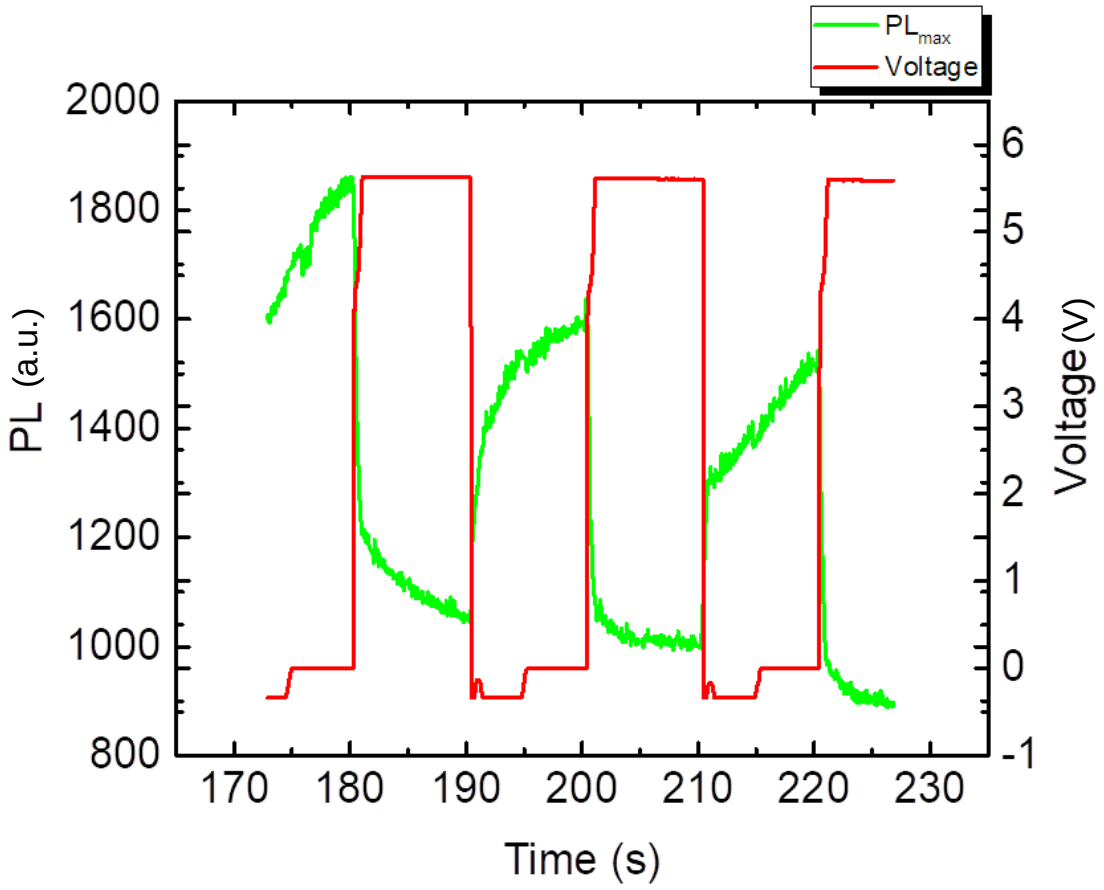

Figure 6-11 – Photoluminescence response of pyridine-functionalised CdSe/CdS QDs in 1 M KNO_3 solution with sequential application of voltage in measurement device illustrated in Figure 6-10.

Voltage-modulated photoluminescence was observed for both CdSe/CdS/ZnS and InP/ZnS QDs. CdSe/CdS/ZnS QDs were relatively stable under measurement conditions, with slow cumulative decay in maximum PL over time. InP/ZnS suffered from relatively rapid photoluminescence bleaching under strong illumination whilst under aqueous ionic conditions over several minutes.

Upon applied voltage, QD photoluminescence intensity dropped significantly, shown in Figure 6-11. Removal of applied voltage resulted in recovery of luminescence towards pre-bias intensities. Despite the slight time lag in intensity during the recovery period, stochastic control of photoluminescence intensity was achieved by cycling the bias between the on/off states.

The electric field in the electrolytic device was generated by the electrophoretic rearrangement of ions upon application of voltage through the Debye-Hückel effect.[32] Application of the voltage induces a polarisation in the dielectric, which causes an accumulation of ions at the surface where the QDs are localised. The field drop is constituted by both the polarization in the dielectric and the screened electric double layer away from the dielectric surface in the electrolyte. By measuring the voltage at counter electrode on the ITO, the reference electrode at the surface and the working electrode within

the droplet, it was possible to estimate the voltage drops across each component and calculate the field generated by the electric double layer, with known droplet size and conductivity.

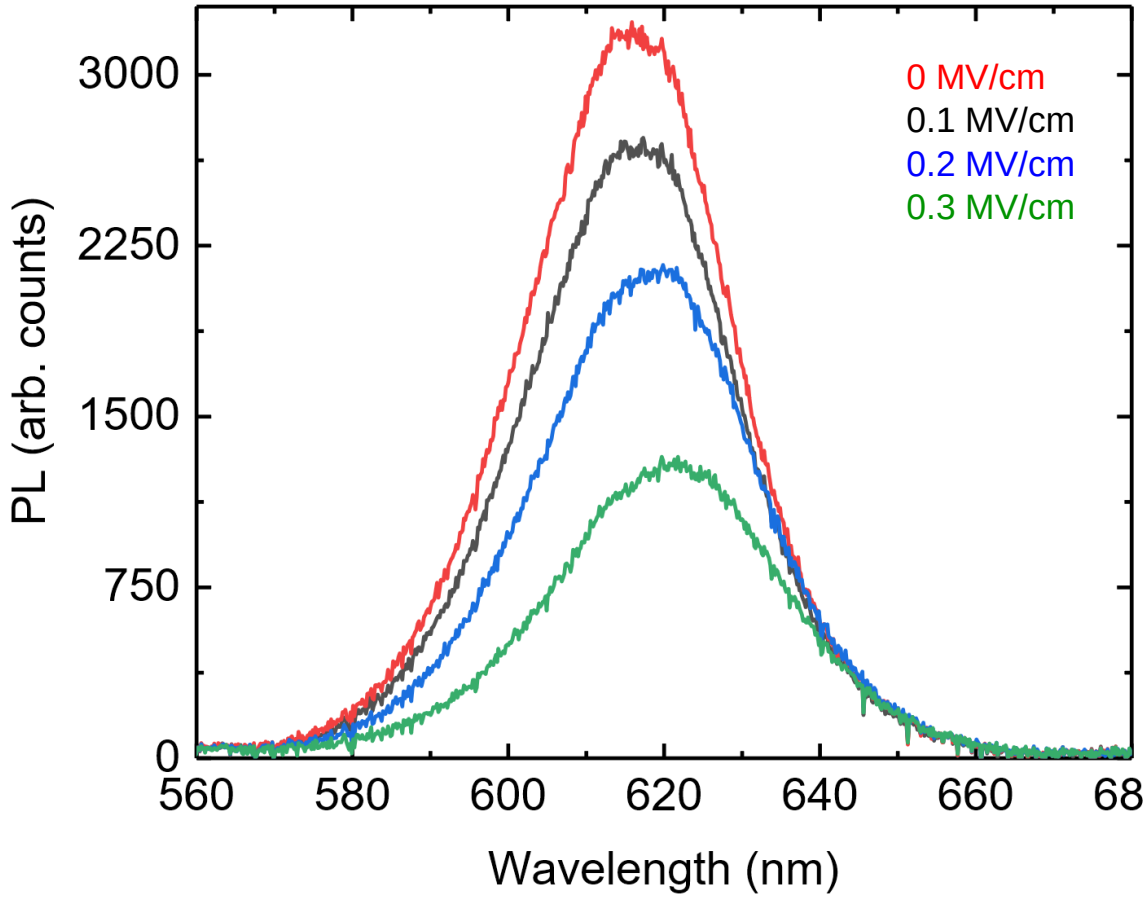

Figure 6-12 – Photoluminescence spectrum of CdSe/CdS/ZnS core-shell-shell QDs upon application of varying potential. Electric field has been calculated based on a Debye-Hückel relationship for the generated electric double layer. A slight peak redshift of 4 nm can be observed with a broadening of the FWHM by 7 nm.

Quantum dots have been shown to respond to electric fields via the quantum-confined Stark effect (QCSE).[31] An applied electric field reduces the QD electron-hole overlap integrals, which decreases the recombination efficiency of photo-generated excitons, in turn reduces photoluminescence quantum efficiency and intensity. The use of deionised water instead of KNO_3 solution did not show any changes to photoluminescence upon application of voltage. The reversible photoluminescence peak broadening and peak position shift of 3 nm, shown in Figure 6-12, were also consistent with previously observed QD response to the QCSE.[11,33] The change in PLQE was the primary contributor for intensity decrease rather than reduction of absorption cross section from QCSE. The rationale being the large density of states within the QD band structures, thus absorption decrease would not have accounted for the magnitude of the PL change. In addition to the observed QCSE effects, the electric fields generated by ions in the aqueous environment likely resulted in some charge generation

on the QDs.[11,34] The charging of QDs allowed Auger non-radiative quenching of photoluminescence in a similar manner to previously observed Auger-assisted QD blinking mechanisms. [35–37] The activation of Auger-assisted blinking in the population of QDs upon voltage application decreased the luminescent population of the ensemble which decreased the observed luminescence. However, the exact mechanism for QD PL decrease in response to electric fields has remained a matter of debate.[11,12,34,35]

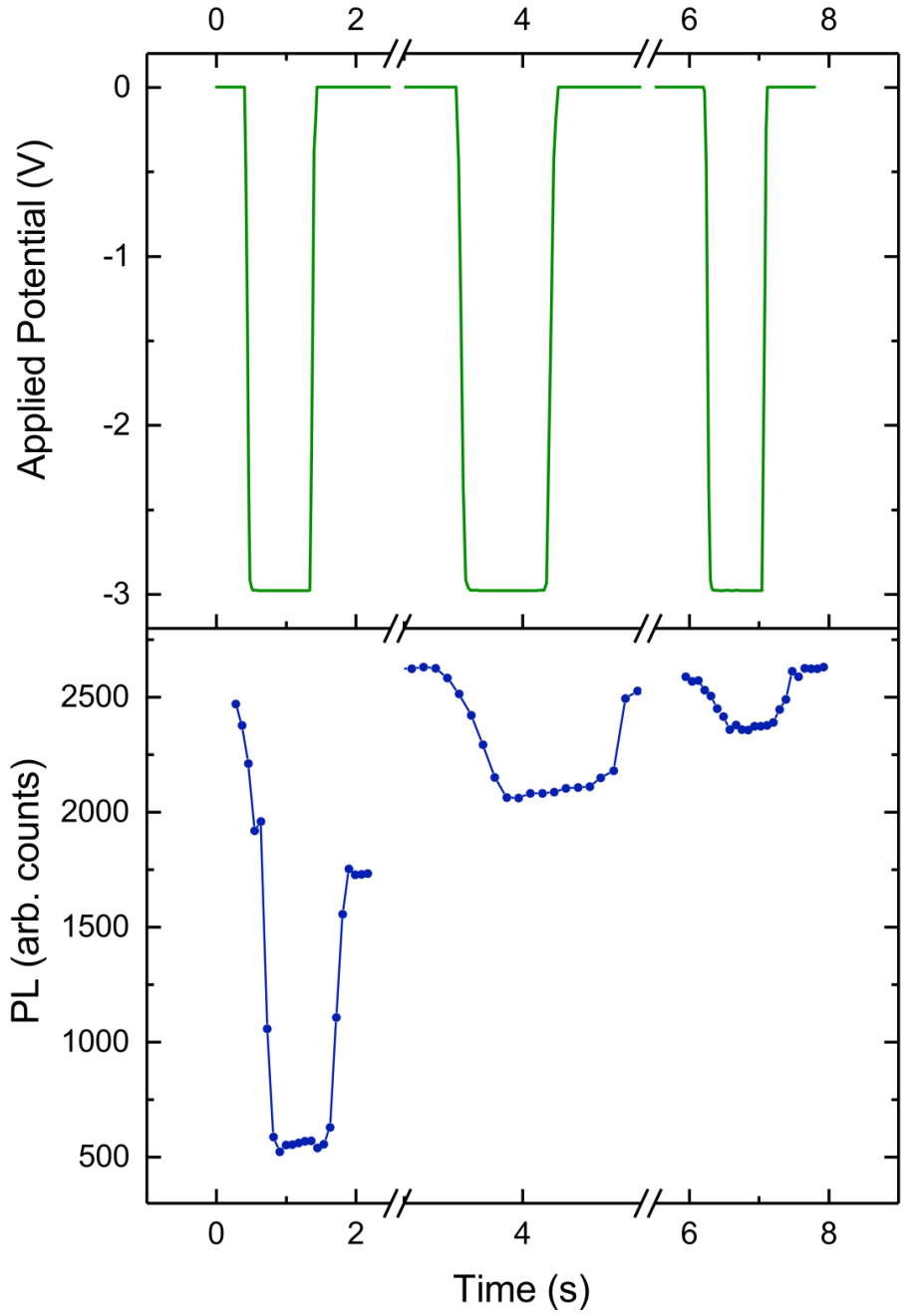

Figure 6-13 –Photoluminescence response of InP/ZnS QDs in aqueous 1 M KNO_3 solution with constant 532 nm excitation to intermittent applied electric field generated by sequential 3 V voltage pulses.

Figure 6-13 shows the photoluminescence response of InP/ZnS QDs in response to an applied voltage within the device, demonstrating a similar effect to that observed in CdSe/CdS/ZnS QDs. The PL drops and recovers following application of the pulse. The magnitude of the response diminishes following repeated cycles, indicating fast photochemical degradation of the QDs in applied voltage. However, this demonstrates the applicability of less-toxic QDs as voltage sensors. Improvements to InP stability may be obtained through optimised synthesis routes and greater control over the shell passivation methods employed.[28]

6.4 Working conclusions

Compared to previous studies performed on solid state capacitive structures, this ongoing work demonstrates the electric field response of QDs in a system mimicking real biological environments. Whilst observing the established QD response to the quantum-confined Stark effect, a greater decrease in luminescence was observed which has been attributed to charging of QDs within the aqueous electrolytic environment and the intensification of Auger-assisted QD non-radiative decay. In addition, a similar effect has been observed in less-toxic InP-based QDs, compared to previous studies focussing on Cd-based QD systems with high cytotoxicity. These results from less-toxic QDs with ZnS shells have demonstrated the applicability of these materials as *in vivo* probes of local electric fields. In addition, the photoluminescence stability of these materials in harsh aqueous environments has so far been demonstrated to be good for CdSe-based materials and adequate for InP-based materials, although there is scope for further improvement for both materials. Further work is ongoing to demonstrate voltage sensing in neuronal systems using these materials as spatially and temporally

6.5 Microfluidic continuous flow synthesis of colloidal PbS quantum dots

As the range of potential applications for colloidal quantum dots has diversified, their industrial relevance has gained greater significance and attention. For applications such as singlet fission down-conversion, large quantities of colloidal QDs of high optical quality are required for successful commercial realisation. A paradigm shift is required in synthetic techniques for the transfer from small-scale laboratory demonstrators to industrial-scale processing.

Established methods for colloidal nanocrystal quantum dot synthesis have commonly involved wet-chemical hot-injection techniques.[38–43] As these are batch processes, they exhibit inherent shortcomings in scalability and reproducibility. For industrial large-scale manufacture, considerable advantages are gained with a continuous process over a batch method. In addition to economic advantages, such as ease of processing and throughput, a continuous flow synthesis process for colloidal QDs may provide far greater control of synthetic parameters. Greater control of reaction conditions results in narrower size distributions, higher luminescence yields and smaller emission bandwidths. In addition, reproducibility is significantly improved with well-defined reaction environments, potentially achievable in laminar fluid flow conditions.

Recently, interest in microfluidic flow synthesis of nanoparticles has greatly expanded with an increasing portfolio of target materials.[3,44,45] Whilst initial research primarily focussed on colloidal metallic and metal-oxide nanoparticles for catalysis and plasmonic applications, more recent investigations have been performed on synthesis of colloidal semiconductor nanocrystals.[46–48] Along with the bulk of previous colloidal quantum dot research, the majority of flow synthesis studies have been performed on materials absorbing and emitting within the visible spectrum. Continuous flow synthesis of near-infrared emitting materials has not been as extensively studied. For synthesis of PbS QDs, a range of routes have been identified including methods analogous to batch techniques. However, the typical use of proprietary commercial flow synthesis apparatuses means developed methods have not been directly transferrable for implementation with different equipment. In addition, challenges in process control and mixing conditions have often resulted in poorer-quality products compared to batch synthesis counterparts.

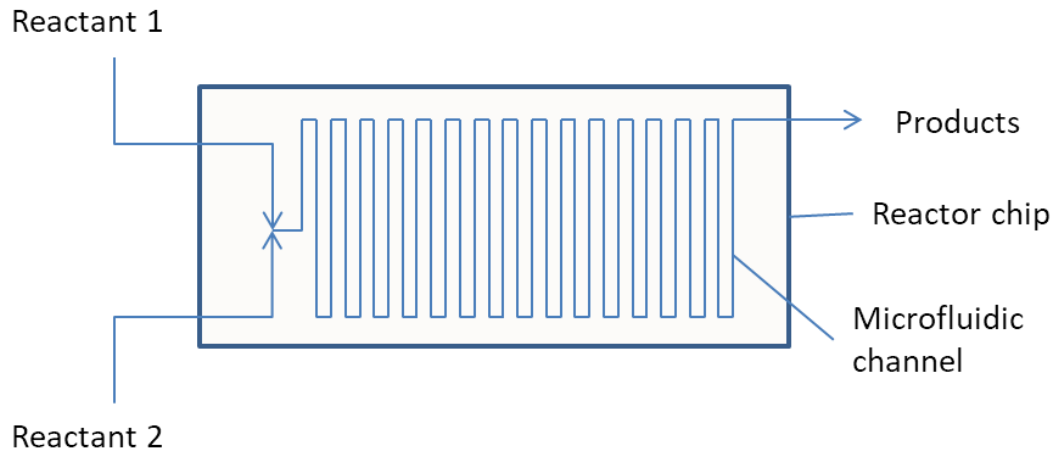

Figure 6-14 – Cartoon of microfluidic flow reactor chip.

The reaction kinetics of semiconductor nanocrystal synthesis has been shown to be highly dependent on experimental conditions such as reaction time, temperature, concentration as well as precursor and ligand ratios.[28,49–52] Within the established hot-injection synthesis framework, these parameters can be easily controlled. However the process of precursor injection itself can introduce major differences in reaction progression within the crucial early phases from factors such as injection speed and mixing. One potential great advantage of microfluidic continuous flow synthesis is the ability to remove these initial mixing differences such that each nucleated nanoparticle experiences the same reaction conditions throughout the synthesis, ideally leading to a population of identical nanoparticles. In addition, processes may be scaled up geometrically through increase of reactor size and tubing capacity.

However, the behaviour of fluid flow does not translate in a straightforward manner from microfluidic systems to plant-scale schemes past the transition from laminar to turbulent flow behaviours. Even on smaller, microfluidic scales, a huge degree of disparity between systems presents itself with variation in channel diameters, arising from interaction between the fluid and the channel walls. Interaction with the channel walls results in a gradient of flow speeds from the walls to the channel centre and combined with restricted mixing between layers in laminar flow, may result in increased product dispersion. As such, it is required to tailor synthetic conditions in a given flow reactor system with defined channel diameter and tubing length.

This work is focussed on the synthesis of PbS using a commercially-available continuous flow microfluidic system with the aim of providing an alternative scalable process for singlet fission down-conversion applications. Various practical considerations faced in the transition from batch to flow processes have been addressed and potential approaches to alleviate emergent problems have been discussed.

6.6 Methods

The synthesis was based broadly on the method of Hines & Scholes; the reaction of lead oleate with bis(trimethylsilyl)sulfide to form PbS nanocrystals.[51] Substantial modifications to the method were required for compatibility with microfluidic flow synthesis. Microfluidic flow synthesis of PbS nanocrystals was performed using a commercial Syrris Asia system with 4 syringe pump channels. Reactors consisted of Dolomite 3-input 1000 µL glass and 250 µL quartz microfluidic chip reactors. A cartoon of a reactor chip is shown in Figure 6-14 and a photograph of the whole system is shown in Figure 6-12.

Figure 6-15 – Photograph of Syrris Asia flow reactor system. 4 pump channels can be seen at the bottom. A single Dolomite 1000 µL glass chip can be seen in the middle heater stage.

A typical synthesis is as follows: A Schlenk flask was loaded with stirrer bar, PbO (0.3125 g, 99.999%, Sigma-Aldrich), oleic acid (OA, 4 mL, 90%, Sigma-Aldrich) and decane (125 mL, Sigma-

Aldrich) and placed under flowing nitrogen. The contents were degassed by bubbling dry nitrogen through the liquid for 3 hours. The flask was heated with a heat gun to 100 °C until the solid had all dissolved into a colourless solution then degassed very gently under vacuum for 10 minutes before being switched to flowing nitrogen. In a nitrogen glovebox, a Schlenk flask was loaded with anhydrous octane (70 mL, Sigma-Aldrich) and bis(trimethylsilyl)sulfide (TMS_2S, 148 µL, 95%, Sigma-Aldrich) then transferred to a Schlenk line and placed under flowing nitrogen. A 1000 µL microfluidic reactor chip was connected to 3 pump inputs and placed on a heating stage. The pump inputs were connected with Luer needles for insertion into rubber septa. The pumps were switched on and connected to precursor solution flasks. The system was sequentially flushed for 20 minutes each with nitrogen, anhydrous octane and again with nitrogen. The chip was heated to 80 °C and the precursor flow was started. Flow rates were 130 µL min^{-1} for the Pb precursor and 70 µL for the S precursor for a reactor dwell time of 5 minutes. The reaction was allowed to stabilise for 15 minutes before collection of the product in a nitrogen-purged Schlenk flask. The synthesis was allowed to proceed for 16 hours before product collection was stopped. The system was flushed sequentially with toluene, acetone, dilute nitric acid (20%) aqueous solution and acetone. The product was transferred into an argon glovebox where the synthesised nanocrystals were precipitated, centrifuged and re-suspended with ethanol and 1-butanol as the non-solvent and hexane then toluene as the solvent. The purified nanocrystals were stored suspended in toluene in a nitrogen glovebox. A cartoon illustration of the overall synthesis system is shown in Figure 6-16.

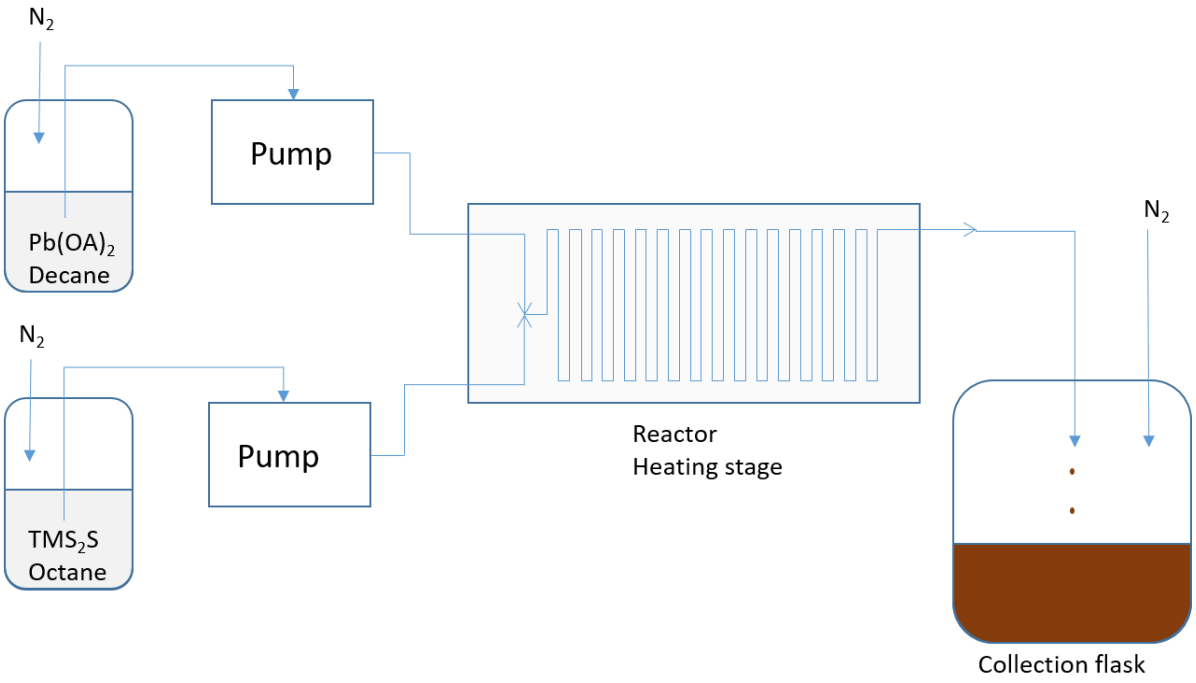

Figure 6-16 – Schematic of flow system for the synthesis of PbS QDs. Nitrogen-purged reagent flasks feed the reactor through two pump channels. The products from the reactor output feed into a nitrogen-purged collection flask.

The continuous flow synthesis of PbS/CdS core-shell nanocrystals was based on the PbS flow synthesis route with immediate follow-up with a continuous-flow cation exchange reaction adapted from the batch process.[53] The reactor setup was modified to include a second 250 µL reactor chip with associated heating stage. The output from the first chip was directed into one input on the second chip, with a second input connected to a fourth pump channel. The output for the second chip was arranged for product collection.

A typical synthesis is as follows: A three-necked round-bottomed flask was loaded with cadmium oxide (0.104 g, 99.999%, Sigma-Aldrich), OA (0.63 mL) and 1-octadecene (ODE, 25 mL, 90%, Sigma-Aldrich) and degassed under vacuum at 110 °C for 1 hour. The flask was switched to nitrogen and heated to 250 °C for 1 hour until all the red CdO had dissolved forming a colourless solution. The temperature was lowered to 110 °C and degassed under vacuum for 30 minutes. The vessel was switched to nitrogen and the Cd precursor contents transferred to a Schlenk flask and placed under flowing nitrogen. A Schlenk flask was loaded with stirrer bar, PbO (0.3125 g, 99.999%, Sigma-Aldrich), oleic acid (OA, 4 mL, 90%, Sigma-Aldrich) and decane (125 mL, Sigma-Aldrich) and placed under flowing nitrogen. The contents were degassed by bubbling dry nitrogen through the liquid for 3 hours. The flask was heated with a heat gun to 100 °C until the solid had all dissolved into a colourless solution then degassed very gently under vacuum for 10 minutes before being switched to flowing nitrogen. In a nitrogen glovebox, a Schlenk flask was loaded with anhydrous octane (70 mL, Sigma-Aldrich) and bis(trimethylsilyl)sulfide (TMS_2S, 148 µL, 95%, Sigma-Aldrich) then transferred to a Schlenk line and placed under flowing nitrogen. A 1000 µL microfluidic reactor chip was connected to three pump inputs and placed on a heating stage. A 250 µL microfluidic reactor chip was connected to one pump input and the output of the 1000 µL reactor. The pump inputs were connected with Luer needles for insertion into rubber septa. The pumps were switched on and connected to precursor solution flasks. The system was sequentially flushed for 20 minutes each with nitrogen, anhydrous octane and again with nitrogen. The first stage chip was heated to 80 °C and the second stage chip heated to 100 °C. The precursor flow was started at flow rates were 130 µL min^{-1} for the Pb precursor, 70 µL for the S precursor and 16 µL for the Cd precursor for a dwell time of approximately 5 minutes and 1 minute for the first and second stages. The reaction was allowed to stabilise for 20 minutes before collection of the product in a nitrogen-purged Schlenk flask. The synthesis was allowed to proceed for 16 hours before product collection was stopped. The system was flushed sequentially with toluene, acetone, dilute nitric acid (20%) aqueous solution and acetone. The product was transferred into an argon glovebox where the synthesised nanocrystals were precipitated, centrifuged and re-suspended with a mix of ethanol and acetone as the non-solvent and hexane then octane as the solvent. The purified nanocrystals were stored suspended in octane in a nitrogen glovebox.

Photoluminescence quantum efficiency measurements were performed according to the method of de Mello.[23] Excitation was provided by a Coherent OBIS 405 nm laser. The optical system was a 6-inch Labsphere with diffusely-reflective $BaSO_4$ coating, fibre-coupled into an Andor Shamrock SR-303i imaging spectrograph with iDus InGaAs photodiode-array detector. Detailed explanations of the measurement are described in Chapter 5. The precautions identified therein were taken to achieve accurate measurements, however full error analysis was not performed as the samples were sufficiently absorbing and the error was not determined to be critical for comparative purposes.

6.7 Discussion and Results

The continuous flow synthesis of PbS quantum dots eventually resulted in achieving luminescence efficiencies comparable to hot-injection batch methods. Initial experiments for PbS synthesis focussed on small-scale validation attempts to probe the reaction parameter space including different reactor arrangements.

Reactor idiosyncrasies

Literature reports of continuous flow PbS synthesis have shown significant differences between varying reactor arrangements.[48] In the work, comparison between single and two-stage reactor assemblies was highlighted to illustrate advantages of separation between nucleation and growth stages. In addition, a mixing stage to ensure reactant homogeneity was utilised.

Initial attempts for synthesis utilised a cooled mixing stage followed by a heated growth reaction stage. Operating at the same precursor concentrations and carrier solvents as the batch method, it was quickly discovered that the precursors were reactive at the minimum practical temperature in the system at the freezing point of the solvent, 1-octadecene at 14 °C. The spontaneous reaction within the mixing stage resulting in nucleation and accumulation of PbS material within the channels, quickly resulting in blockages. This was contrary to previous literature where premature reaction at similar reagent concentrations was not observed.[48]

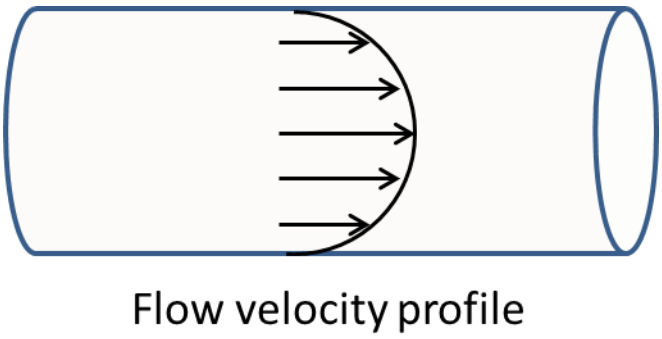

Figure 6-17 – Schematic of velocity profile in channel under laminar flow conditions and interaction between fluid and walls. The profile is parabolic with fastest flow in centre and slowest at walls, approaching zero.

Several general aspects have been identified to explain the accumulation of material and the deviation from published literature.[54] Key characteristics for flow reactor design include channel dimensions, geometry and material composition. In the ideal situation, interaction between the fluid flow and channel walls are minimised, with no variation in flow speeds across the fluid front. Adhesion by the flowing solvent, solute or suspensions on the reactor walls may be mitigated to an extent with suitable construction materials. PTFE is commonly favoured due to its chemical resistance and non-stick properties. The flow characteristics are also sensitive to channel dimensions and geometry. In instances of strong fluid-wall interaction and laminar flow, smaller channel sizes increases the proportion of mass flow in contact with the reactor walls, increasing the gradient of flow rates and variation in reaction conditions between edge and centre flow, presented in Figure 6-17. A non-circular channel cross-section results in greater contact area with walls and in the case of rectangular cross-sections, corners provide regions of stagnated flow allowing precipitated material accretion.

Here, the reactors are constructed of glass or quartz, which allows adhesion by the solvent and nucleated solid material. The mixing chip possesses very restricted channel sizes as narrow as 50 µm, whilst the 1000 µL reactor has channels of rectangular cross-section with widths as narrow as 161 µL at certain sections, shown in Figure 6-18. Although these narrow channels can allow greater mixing by introducing sections of turbulent flow at higher flow rates, they allow more accumulation of material and have lower blockage thresholds.

Deposition may be partly mitigated using higher flow rates, for shorter residence times. However, flow rate is limited by the maximum supply pressure of the pumps. Through lowering the fluid viscosity, less back pressure is produced through constricted channels thus higher rates may be achieved. Viscosity can be reduced by changing the solvent or increasing temperature.

Accumulation of PbS deposits within channels changes both physical and chemical interaction at the fluid-wall interface. Surface roughness is modified and a crystalline PbS surface is exposed to the fluid flow. Surface deposits exacerbate and accelerate the deposition process by presenting nucleation sites for further deposition of PbS on the walls and modifying the nanocrystal growth through seeded growth. From these, it is evident deposition and fouling of the reactor is detrimental to continuous operation of the reactor as well as product qualities, especially size distribution.

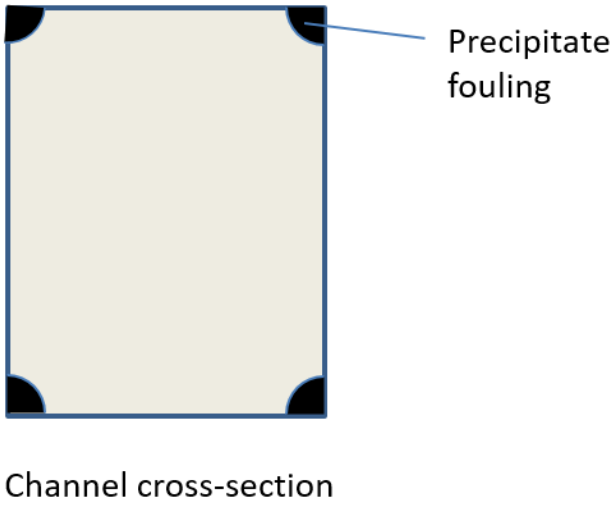

Figure 6-18 – Schematic of microfluidic channel cross-section showing rectangular geometry with corners. Initial nucleated and precipitated PbS fouling shown in corners.

The synthesis scheme was significantly modified in order to slow down reactor fouling and prevent blockage: the synthesis solvents were changed from viscous 1-octadecene to a mixture of n-decane and n-octane. The precursor concentrations were reduced tenfold to slow down the reaction process to reduce premature nucleation. The synthesis temperature was decreased to slow down reaction rates and deposition at the channel surface. To counteract the slower growth rates, oleic acid ligand concentration was increased to achieve larger nanocrystals. The reactor pathway was simplified to a one-stage reactor step and the mixer step was removed.

Synthesis parameters

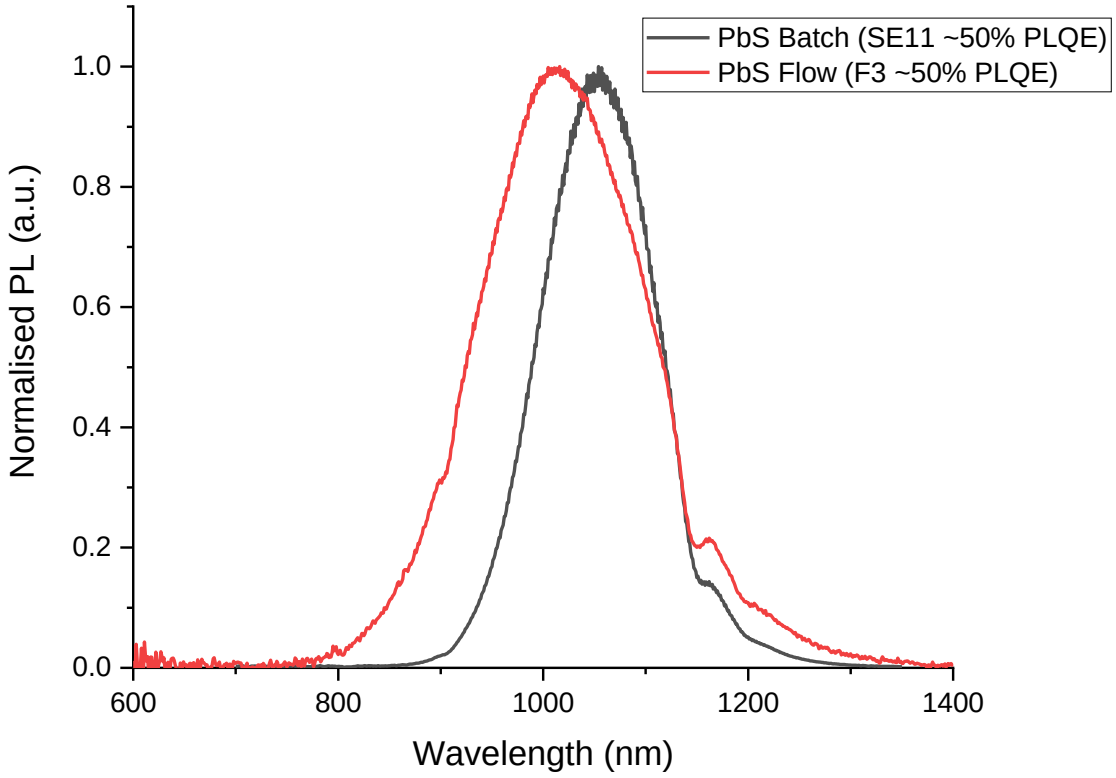

Figure 6-19 – Normalised PL spectrum of PbS with targeted PL energy of ~1.2 eV. The overall PLQE was similar for both however the flow-synthesised QDs possessed a larger emission bandwidth, indicating larger size distribution. The dips at 1150 nm and 1200 nm are from absorption of the toluene solvent.

Synthesis at reduced concentration was successful in achieving luminescent PbS quantum dots. Photoluminescence quantum efficiencies of PbS QDs from a good flow synthesis attempt were comparable to PbS QDs produced via hot-injection synthesis, shown in Figure 6-19. However, PLQEs were less reproducible than with batch synthesis, occasionally the resulting PLQEs being less than half of the value expected. An increase in emission bandwidth was observed compared to batch-produced QDs, which was attributed to increased size polydispersity.

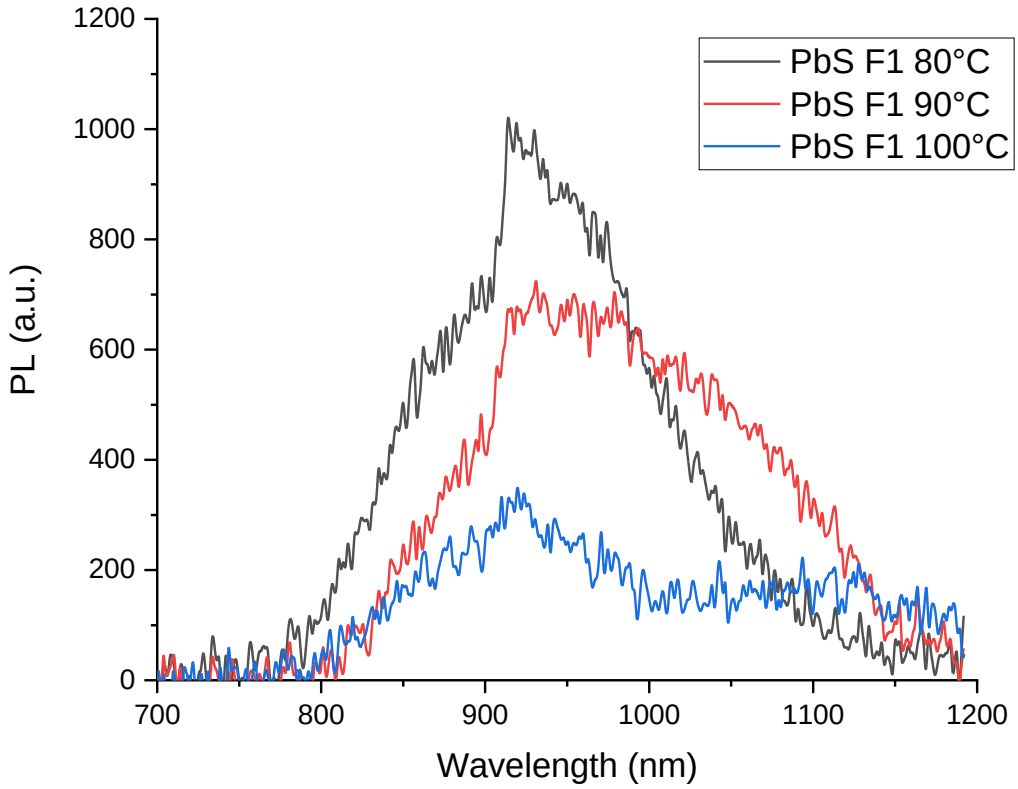

Figure 6-20 – PL spectra of flow synthesis PbS QDs at different reactor temperatures. A decrease in PLQE was observed with increasing temperature.

The resulting nanocrystal bandgap was tuneable through altering modification conditions. However, synthesis temperature variation was observed to have a smaller effect compared to the batch process, shown in Figure 6-20. This was explained as a consequence of the fixed dwell time within the reactor. In hot-injection synthesis, the higher thermal mass of the entire contents of the flask result in correspondingly longer cooling and reaction times at higher temperatures in the absence of quenching. In a microfluidic flow system, the thermal mass is very low thus cooling is very rapid upon fluid exit of the reactor chip. Increased reactor temperature thus becomes largely independent of reaction time.

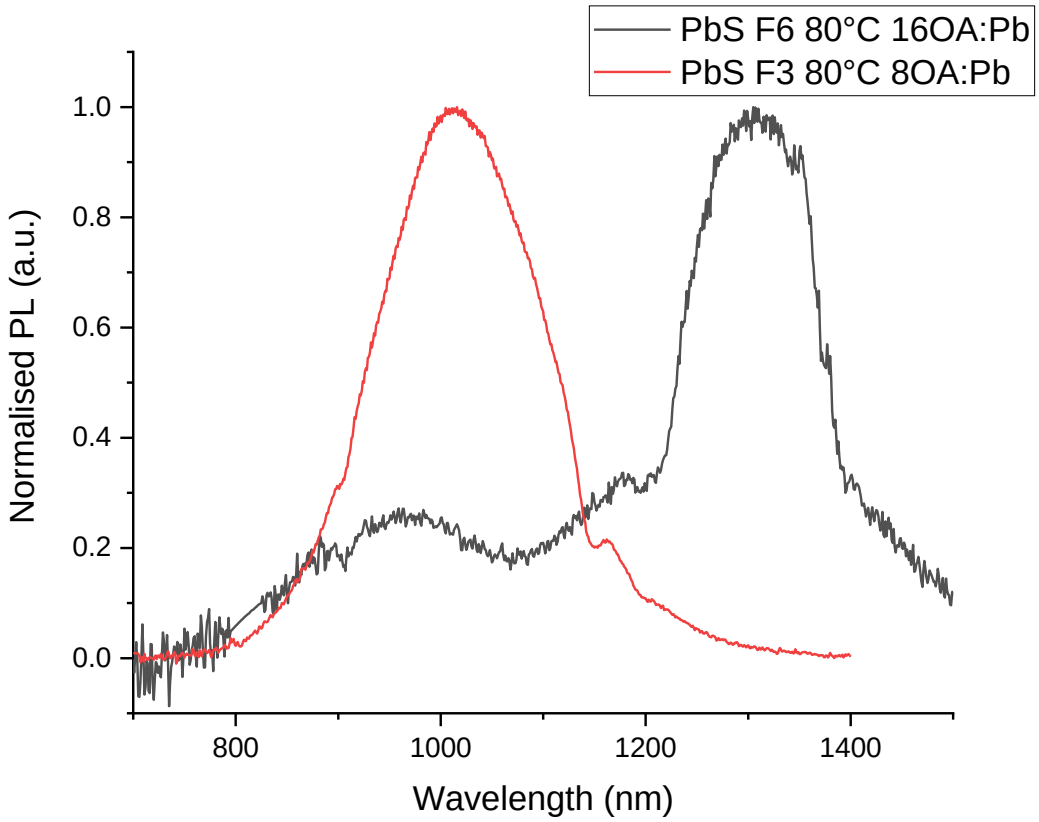

Figure 6-21 – Normalised PL spectra of flow synthesis at different oleic acid concentrations.

Ligand concentration was determined to be the most effective and practical means of modifying the bandgap, demonstrated in Figure 16. The synthesis ligand was oleic acid, which coordinated to Pb to form a lead oleate complex. Higher concentrations of oleic acid increased the reactivity of the lead species leading to increased reaction rate. Faster reaction rates resulted in faster growth of nanocrystals to larger sizes and thus smaller bandgaps. Other typical methods of nanocrystal size control such as dwell time and temperature were kept constant at optimised values. Dwell time was kept constant because flow characteristics were sensitive to absolute flow rate through the restricted channel dimensions. The flow rate was kept constant at an optimised value to provide sufficient reactor dwell time and maintain similar flow profiles during synthesis of different bandgaps. Synthesis at higher temperatures increased the reaction rate and resulting nanocrystal size. The rate increase is exponential with linear increase in temperature according to the Arrhenius equation. The reactor operation at higher temperature also resulted in faster undesirable surface reactions, leading to fouling. The faster fouling limited maximum reactor operation times before blockages occurred, which limited product quantity. The ligand concentration was the primary method of modifying the product bandgap. The other methods of dwell time and temperature resulted in reduced control and were associated with difficulties such as reactor blockages.

At low precursor concentration, reactor fouling was significantly reduced. However, product throughput was slow with a production rate of ~25 mg h^{-1} at 200 µL min^{-1} flow rate. Synthesis scale up was achieved through lengthening process run time, extended to 16 hours through increase in precursor reservoir sizes. Increased visible fouling was observed with increased process run time. Thus for this reactor system, simple lengthening of run time possessed significant limitations for production scale-up.

Precursor concentration was increased to improve throughput for a set run time whilst preventing blockages. The maximum practicable reagent concentration was found to be 5 times less than the original batch synthesis concentration. This allowed for synthetic runs of 16 hours without blockage, although with heavy reactor fouling; further increases were not feasible without additional optimisation of other synthetic conditions. The quantity of the resulting product was comparable to the yield of a typical batch synthesis procedure. Whilst the overall reaction yield of flow synthesis was similar to batch synthesis, the throughput was much slower. The same 312 mg of PbO reagent would produce approximately ~300 mg of finished PbS QDs in both batch and flow methods, however, the batch synthesis could be completed in 3 hours, whereas the flow synthesis would take over 16 hours on this particular reactor system.

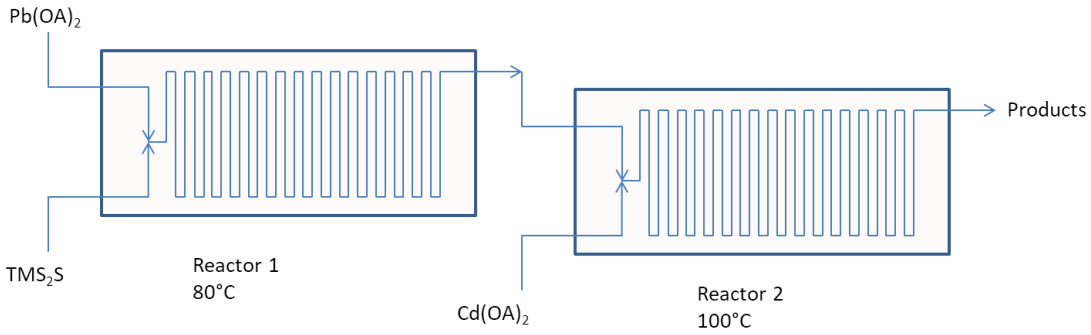

Figure 6-22 – Cartoon schematic of reactor geometry for single pass synthesis with in-flow cation exchange of PbS/CdS core-shell QDs.

The incorporation of additional reaction stages to reduce post-synthesis processing steps was investigated. In particular, immediate cation exchange with Cd to form PbS/CdS core-shell QDs was attempted, shown in Figure 6-22. Photoluminescence quantum efficiency was observed to be significantly lower than PbS/CdS from batch cation exchange. The batch cation exchange is described in detail in Chapter 3.

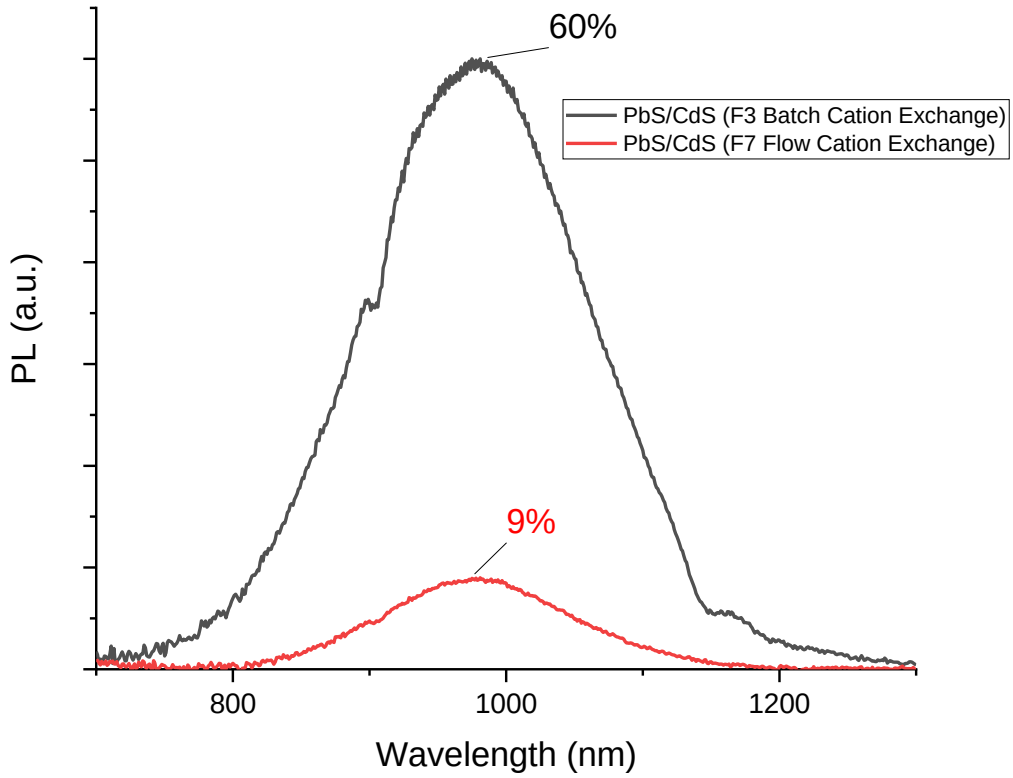

Figure 6-23 – PL spectra of cation exchanged PbS/CdS QDs from PbS synthesised in flow following batch cation exchange and in-line single pass in-flow cation exchange. Measured PLQE shown as labelled. Peak area has been scaled to PLQE.

Batch-process cation exchange of both batch-synthesised and flow-synthesised PbS QDs resulted in a blue-shift and photoluminescence enhancement in the resulting PbS/CdS QDs. Immediate flow-processed cation exchange resulted in a similar blue-shift but a significant reduction in photoluminescence quantum yield, shown in Figure 6-23. The exact cause for the luminescence drop is unknown but could be a result of several factors. The excess synthesis reagents and ligands in the reaction suspension were still present during the cation exchange procedure instead of being removed through precipitation purification steps. Excess unreacted precursors may have resulted in side reactions with products such as nucleation of CdS nanocrystals. The greater reaction temperature compared to the PbS synthesis stage may have also increased the rate of side reactions. In addition, the product was left stagnant in the collection flask for extended periods of time in the presence of synthesis mixture, as an in-line purification system without feeding into a fixed collection flask was difficult to envisage and could not be practicably implemented. The cation exchange reaction rate or ion mobility may have been significant at room temperature and resulted in excess shell growth or structural rearrangements of the shell material, as reported in literature.[55,56]

To mitigate the presence of additional ligand and precursors, two obvious approaches appear. Firstly, optimisation of the PbS synthesis stage to minimise the precursor concentration in the reactor efflux may be performed to minimise side reactions within the second stage. Optimisation may occur through multiple approaches, such as more complex thermal profiles with staged temperature zoning or longer reactors with longer dwell times. Secondly, a reaction quench or purification step may be incorporated within the collecting vessel. The simplest method is a pool of polar anti-solvent to precipitate and separate nanocrystals from the reaction mixture. Polar aprotic solvents would be necessary to prevent stripping of passivating ligands from nanocrystal surfaces.[57]

Scale up

A significant hindrance to practical application of continuous flow routes has been product collection and processing methods. Despite synthesis occurring within a flow process, the product required processing and purification in a similar manner as batch procedures. In addition, diluted precursor concentrations have resulted in large processing volumes for small amounts of product, in turn leading to large quantities of purification non-solvents required. Recent literature reports have demonstrated process-incorporated continuous purification methods utilising electrodes in electrophoretic techniques.[58] For larger-scale syntheses, such methods would be required for both process streamlining and economic cost reductions.

Product throughput was limited by reactor size and pump capacities. Significant scale-up would have required larger reactor channels to allow greater mass flow rates. The challenges of reactor fouling would be less pronounced with larger channel sizes. In addition, mitigation of fouling may be achieved through PTFE material construction to provide non-wettable channel wall surfaces. With reduced reactor fouling, syntheses could be optimised at higher precursor concentrations, further improving throughput.

6.8 Working conclusions

The continuous flow synthesis of colloidal PbS quantum dots has demonstrated the production of high quality materials. Numerous practical issues were encountered unique to microfluidic flow synthesis techniques such as reactor fouling and incomplete mixing. These issues persisted primarily at the small synthesis volumes investigated and limited the attractiveness of flow methods compared to existing batch procedures. One major shortcoming was the low production capacity of the microfluidic flow system compared to the faster, facile synthesis of larger quantities at typical batch scales. However, the problems identified are not generalised across flow methods and do not preclude the viability of flow chemistry to synthesise QDs. The Syrris Asia system investigated would be more suitable for smaller-scale syntheses to investigate reaction conditions, where problems encountered in extended run times would be less problematic and where smaller-scale batch syntheses are more

difficult to effectively perform reproducibly. For larger scales, including the intended use-case here, different mitigation approaches have been identified including optimisation of reactor construction. The scale-up of the synthesis by transitioning to larger flow reactors and flow regimes potentially removes many of the difficulties encountered by microfluidic systems. Flow chemistry thus remains a viable alternative for the large-scale production of high-quality quantum dots, despite complications encountered at the small-scale.

6.9 References

1. Medintz, I. L., Uyeda, H. T., Goldman, E. R. & Mattoussi, H. *Nature Materials* **4**, 435–446 (2005).
2. Pietra, F., Van Dijk - Moes, R. J. A., Ke, X., Bals, S., Van Tendeloo, G., De Mello Donega, C. *et al. Chemistry of Materials* **25**, 3427–3434 (2013).
3. Jiao, M., Zeng, J., Jing, L., Liu, C. & Gao, M. *Chemistry of Materials* **27**, 1299–1305 (2015).
4. Gerion, D., Pinaud, F., Williams, S. C., Parak, W. J., Zanchet, D., Weiss, S. *et al. The Journal of Physical Chemistry B* **105**, 8861–8871 (2001).
5. Xie, R., Chen, K., Chen, X. & Peng, X. *Nano Research* **1**, 457–464 (2008).
6. Grim, J. Q., Manna, L. & Moreels, I. *Chem. Soc. Rev.* **44**, 5897–5914 (2015).
7. Benayas, A., Ren, F., Carrasco, E., Marzal, V., Del Rosal, B., Gonfa, B. A. *et al. Advanced Functional Materials* **25**, 6650–6659 (2015).
8. Parak, W. J., Pellegrino, T. & Plank, C. *Nanotechnology* **16**, R9–R25 (2005).
9. Zimmer, J. P., Kim, S., Ohnishi, S., Tanaka, E., Frangioni, J. V & Bawendi, M. G. 2526–2527 (2006).
10. Zhu, C. N., Jiang, P., Zhang, Z. L., Zhu, D. L., Tian, Z. Q. & Pang, D. W. *ACS Applied Materials and Interfaces* **5**, 1186–1189 (2013).
11. Rowland, C. E., Susumu, K., Stewart, M. H., Oh, E., Mäkinen, A. J., O'Shaughnessy, T. J. *et al. Nano Letters* **15**, 6848–6854 (2015).
12. Bar-Elli, O., Steinitz, D., Yang, G., Tenne, R., Ludwig, A., Kuo, Y. *et al. ACS Photonics* **5**, 2860–2867 (2018).
13. Marshall, J. D. & Schnitzer, M. J. *ACS Nano* **7**, 4601–4609 (2013).
14. Oh, E., Liu, R., Nel, A., Gemill, K. B., Bilal, M., Cohen, Y. *et al. Nat Nano* **11**, doi:10.1038/nnano.2015.338 (2016).
15. Peterka, D. S., Takahashi, H. & Yuste, R. *Neuron* **69**, 9–21 (2011).
16. Kornblum, H. I., Araujo, D. M., Annala, A. J., Tatsukawa, K. J., Phelps, M. E. & Cherry, S. R. *Nature Biotechnology* **18**, 655–660 (2000).

17. Svoboda, K. & Yasuda, R. *Neuron* **50**, 823–839 (2006).

18. Kuhn, B. & Fromherz, P. *The Journal of Physical Chemistry B* **107**, 7903–7913 (2003).

19. Peleg, G., Lewis, A., Linial, M. & Loew, L. M. *Proceedings of the National Academy of Sciences of the United States of America* **96**, 6700–4 (1999).

20. Bae, W. K., Lim, J., Lee, D., Park, M., Lee, H., Kwak, J. *et al. Advanced Materials* **26**, 6387–6393 (2014).

21. Dethlefsen, J. R. & Døssing, A. *Nano Letters* **11**, 1964–1969 (2011).

22. Kim, K., Yoo, D., Choi, H., Tamang, S., Ko, J.-H., Kim, S. *et al. Angewandte Chemie International Edition* **55**, 3714–3718 (2016).

23. de Mello, J. C., Wittmannn, H. F. & Friend, R. H. *Advanced materials (Deerfield Beach, Fla.)* **9**, 230 (1997).

24. Aharoni, A., Mokari, T., Popov, I. & Banin, U. *Journal of the American Chemical Society* 257–264 (2006).

25. Guzelian, a a, Katari, J. E. B., Kadavanich, a V, Banin, U., Hamad, K., Juban, E. *et al. Journal of Physical Chemistry* **100**, 7212–7219 (1996).

26. Li, L. & Reiss, P. *Journal of the American Chemical Society* **130**, 11588–11589 (2008).

27. Ziegler, J., Xu, S., Kucur, E., Meister, F., Batentschuk, M., Gindele, F. *et al. Advanced Materials* **20**, 4068–4073 (2008).

28. Tamang, S., Lincheneau, C., Hermans, Y., Jeong, S. & Reiss, P. *Chemistry of Materials* **28**, 2491–2506 (2016).

29. Kan, S. H., Aharoni, A., Mokari, T. & Banin, U. *Faraday Discussions* **125**, 23–38 (2004).

30. Peng, Z. A. & Peng, X. *Journal of the American Chemical Society* **124**, 3343–3353 (2002).

31. Empedocles, S. A. *Science* **278**, 2114–2117 (1997).

32. Jing, Y., Jadhao, V., Zwanikken, J. W. & Olvera de la Cruz, M. *The Journal of Chemical Physics* **143**, 194508 (2015).

33. Park, K., Deutsch, Z., Li, J. J., Oron, D. & Weiss, S. *ACS Nano* **6**, 10013–10023 (2012).

34. Park, K. & Weiss, S. *Biophysical Journal* **112**, 703–713 (2017).

35. Quinn, S. D., Rafferty, A., Dick, E., Morten, M. J., Kettles, F. J., Knox, C. *et al. The Journal of Physical Chemistry C* **120**, 19487–19491 (2016).

36. Efros, A. L. & Nesbitt, D. J. *Nature Nanotechnology* **11**, 661–671 (2016).

37. Yuan, G., Gómez, D. E., Kirkwood, N., Boldt, K. & Mulvaney, P. *ACS Nano* **12**, 3397–3405 (2018).

38. Nurmikko, A. *Nature Nanotechnology* **10**, 1001–1004 (2015).

39. Guzelian, a. a., Banin, U., Kadavanich, A. V., Peng, X. & Alivisatos, a. P. *Applied Physics Letters* **69**, 1432 (1996).

40. Peng, Z. a. & Peng, X. *Journal of the American Chemical Society* **123**, 183–184 (2001).

41. Wei, H., Guo, W., Sun, Y., Yang, Z. & Zhang, Y. *Materials Letters* **64**, 1424–1426 (2010).

42. Zhang, L. J., Shen, X. C., Liang, H., Guo, S. & Liang, Z. H. *Journal of Colloid and Interface Science* **342**, 236–242 (2010).

43. Murray, C. B., Norris, D. & Bawendi, M. G. *Journal of the American Chemical Society* **115**, 8706–8715 (1993).

44. Sebastian Cabeza, V., Kuhn, S., Kulkarni, A. A. & Jensen, K. F. *Langmuir* **28**, 7007–7013 (2012).

45. Roberts, E. J., Habas, S. E., Wang, L., Ruddy, D. A., White, E. A., Baddour, F. G. *et al. ACS Sustainable Chemistry & Engineering* **5**, 632–639 (2017).

46. Mirhosseini Moghaddam, M., Baghbanzadeh, M., Sadeghpour, A., Glatter, O. & Kappe, C. O. *Chemistry - A European Journal* **19**, 11629–11636 (2013).

47. Ippen, C., Schneider, B., Pries, C., Kröpke, S., Greco, T. & Holländer, A. *Nanotechnology* **26**, (2015).

48. Pan, J., El-Ballouli, A. O., Rollny, L., Voznyy, O., Burlakov, V. M., Goriely, A. *et al. ACS Nano* **7**, 10158–10166 (2013).

49. Mourdikoudis, S. & Liz-Marzán, L. M. *Chemistry of Materials* **25**, 1465–1476 (2013).

50. Ushakova, E. V., Cherevkov, S. A., Litvin, A. P., Parfenov, P. S., Volgina, D.-O. A., Kasatkin, I. A. *et al. The Journal of Physical Chemistry C* **120**, 25061–25067 (2016).

51. Hines, M. A. & Scholes, G. D. *Advanced Materials* **15**, 1844–1849 (2003).

52. Peng, X., Wickham, J. & Alivisatos, a. P. *Journal of the American Chemical Society* **120**, 5343–5344 (1998).

53. Neo, M. S., Venkatram, N., Li, G. S., Chin, W. S. & Ji, W. *The Journal of Physical Chemistry C* **114**, 18037–18044 (2010).

54. Lignos, I., Protesescu, L., Stavrakis, S., Piveteau, L., Speirs, M. J., Loi, M. A. *et al. Chemistry of Materials* **26**, 2975–2982 (2014).

55. Lechner, R. T., Fritz-Popovski, G., Yarema, M., Heiss, W., Hoell, A., Schülli, T. U. *et al. Chemistry of Materials* **26**, 5914–5922 (2014).

56. Justo, Y., Sagar, L. K., Flamee, S., Zhao, Q., Vantomme, A. & Hens, Z. *ACS Nano* **8**, 7948–7957 (2014).

57. Song, J. H., Choi, H., Kim, Y.-H. & Jeong, S. *Advanced Energy Materials* **7**, 1700301 (2017).

58. Lim, H., Woo, J. Y., Lee, D. C., Lee, J., Jeong, S. & Kim, D. *Scientific Reports* **7**, 43581 (2017).

Chapter 7 Summary

7.1 Enhancing Photoluminescence in Colloidal Quantum Dots

This thesis aimed to investigate different approaches for enhancing photoluminescence in colloidal quantum dots across a wide variety of materials. A recurring strategy for photoluminescence enhancement was the implementation of core-shell structures. However, the exact approach differentiated depending on the target material.

PbS/CdS Nanocrystals

In Chapter 3, enhancement of photoluminescence in near-infrared emitting oleic acid-capped PbS was explored in-depth. Though the native PbS PLQEs were in excess of 50% PLQE at 1.2 eV emission, this was improved through cation exchange with Cd to form nominally PbS/CdS core-shell structures, reaching nearly 80% for 1.2 eV emission, comparable to the best reported in literature. This was enabled through understanding the mechanism of enhancement, which was identified to be elimination of transient trapping through passivation of the associated surface sites. An understanding of the exchange dynamics was achieved through time-resolved compositional analysis, where the reaction was discovered to proceed first with rapid cation adsorption, followed by slower cation exchange. Fine optimisation of the exchange reaction enabled the greatest degree of passivation and photoluminescence efficiency with maximal Cd adsorption, which was achieved at previously-unknown short reaction times of less than 1 minute under the explored reaction conditions.

III-V and Lead-free Nanocrystals

In Chapter 4, lead-free nanocrystals were considered as alternative near-infrared emitters to PbS. The III-V material InAs was examined, along with shell growth of different candidate materials to improve its poor native luminescence. A method of successive-ionic-layer adsorption and reaction (SILAR) was used extensively for shell growth of both single and complex graded shells of CdSe and ZnSe and ZnS to provide exciton wavefunction confinement and minimisation of interfacial defects generated by inter-shell strain. However, whilst it was possible to improve the solution PLQEs to approach a respectable 40% at 1.2 eV with the strategies employed, attempts to exploit them in the solid state resulted in severe photoluminescence quenching. Different synthetic approaches, along with extensive work, may have resulted in a practicable system.

The material $CuInSe_2$ was also briefly appraised as an alternative lead-free near-infrared emitter. Whilst of negligible native luminescence, good photoluminescence efficiencies of up to 45% were achieved at 1.2 eV emission following layered growth of ZnS shells, making it attractive for further

study. A clear monotonic increase in photoluminescence efficiency was observed with increasing ZnS shell thickness up to the 4-shell equivalents studied.

7.2 Validation for Measurements of Figure of Merit

As the dominant figure of merit, measurement of photoluminescence quantum efficiency is critical for the comparison of photoluminescent materials, especially quantum dots. However, this key measurement has often been overlooked as routine, without particular attention to its nuances.

In Chapter 5, the key principles of the measurement are presented, along with a comprehensive breakdown of the commonly used integrating sphere method. Sources of systematic error, such as improper calibration of spectral response to contamination of the measurement setup are described in detail, along with mitigation strategies. Having minimised systematic errors, a statistical treatment of the sources of random measurement errors is presented, elucidating the separate, non-mutually exclusive conditions where random errors become significant: low sample absorption, significant fluctuations in excitation laser intensity and exceptionally poor-emitting samples.

7.3 Colloidal Quantum Dots in Luminescent Optoelectronics

An overarching focus of this thesis has been the aim of incorporation of luminescent quantum dots into applied systems, such as singlet fission down-conversion.

Verification of a singlet fission down-conversion assembly

In Chapter 5, the identified idiosyncrasies of photoluminescence quantum efficiency measurements have been accounted for in order to validate a functional solution down-conversion system incorporating PbS quantum dots functionalised with TIPS-tetracene-carboxylic acid and TIPS-tetracene singlet fission material. Although the overall PLQE was low at 9%, this value was determined to be only possible through contribution of additional excitons generated through singlet fission, with the product of singlet fission and triplet transfer efficiency being up to 120%, to a high degree of confidence.

Electric field modulation of QD photoluminescence

In the first half of Chapter 6, visible-emitting QDs were explored with the aim of incorporating them as *in vivo* fluorescent probes. The classically toxic CdSe and the less-toxic InP were both candidate materials. Whilst core-shell CdSe/CdS could be synthesised in a one-pot method with good luminescence of 30% PLQE and stability, its inherent toxicity required additional passivation through growth of less-toxic shell. InP, however, possessed negligible native photoluminescence, and required shell growth to improve luminescence and stability. ZnS shell growth proved suitable for both materials, improving the PLQE of CdSe/CdS to 37% and InP to 11%. Both CdSe/CdS/ZnS and InP/ZnS displayed modulated photoluminescence response to local electric fields in aqueous

electrolytic environments with sufficient stability to enable future experimentation as *in vivo* neuronal voltage probes.

Continuous flow synthesis of PbS

In the second half of Chapter 6, an exploration into the flow chemistry approach to QD synthesis was performed, with the aim of investigating continuous synthesis of the large quantities of PbS required for commercial application of singlet-fission down-converters. Working with a commercial microfluidic reactor system, it was found that it was possible to synthesise PbS of good quality, with 50% PLQE achieved at 1.2 eV. However, the vaunted benefits of flow chemistry, such as its scalability and reproducibility, were not achievable with the specific system used, and it was not competitive with batch synthesis at the intended scale. Several intractable difficulties were encountered, such as the unsuitable geometry and material construction of the reactor channels. In addition, it was realised that flow characteristics are distinctly specific to different systems, thus generalised procedures to fit different systems were not possible, unlike in batch synthesis. However, it was concluded that a simple complete scale up could solve many of the problems inherent to a small-scale system.